Department of Chemical Engineering

Study on adsorption behavior of rare earth elements onto magnetic nanocomposites of carboxymethyl chitosan, alginate and novel biodegradable polyamide

by

Hamedreza Javadian

in fulfilment for the award of the degree of

DOCTOR

by

Universitat Politècnica de Catalunya

Supervised by:

Dr. Ana Maria Sastre Requena

Dr. Montserrat Ruiz Planas

Barcelona, 2020

Thesis presented by compendium of publications

ACKNOWLEDGEMENT

I would like to express my sincere gratitude and heartfelt thanks to my supervisor **Prof. Ana Maria Sastre Requena** for giving me the opportunity to do the research work in Department of Chemical Engineering, Universitat Politècnica de Catalunya, and her sincere guidance and efforts towards the successful completion of the research work, apart from being a great source of support and motivation for me.

My heartfelt thanks go to **Prof. Montserrat Ruiz** for her constant help and providing necessary laboratory facilities to perform the research work. Profound thanks for her kind heart and great constant support to solve my private problems outside the research work.

I express my sincere thanks to **Prof. Mehdi Taghavi**, Department of Chemistry, Faculty of Science, Shahid Chamran University of Ahvaz, 61357-43337, Iran, for his interest to contribute in the research work by his continuous support and valuable suggestions.

Last but not the least; I would like to dedicate my thesis to my beloved parents for their constant inspiration and encouragement not only during the research work but also at all the moments of my life.

The thesis is developed in the frame of the project entitled *"Separacion/recuperacion de tierras raras mediante procesos de sorcion en biopolimeros, composites y membranas. (ReRarE)*" (Ref.: CTM2014-52770-R), "Estrategias de reciclado de residuos que contienen tierras raras: procesos de sorción mediante nanocomposites magnéticos y membranas liquidas para su separación y recuperación"(ReciRar) (Ref.: CTM2017-83581-R) and the contract 2015 BES-2015-072506 financed by the Spanish Ministry of Industry and Competitiveness.

LIST OF ACRONYMS

CA	Calcium alginate
CCD	Central composite design
CMC	Carboxymethyl chitosan
CTAB	Cetyltrimethylammonium bromide
DMF	N,N-dimethylformamide
DMSO	Dimethyl sulfoxide
DW	Deionized water
EDX	Energy-dispersive X-ray spectroscopy
FE-SEM	Field emission scanning electron microscopy
FT-IR	Fourier transform infrared
HREEs	Heavy rare earth elements
ICP	Inductively coupled plasma
ILs	Ionic liquids
LREEs	Light rare earth elements
MREEs	Middle rare earth elements
NMR	Nuclear magnetic resonance
P(PTA)	Poly(pyrimidine-thiophene-amide)
PAs	Polyamides
REEs	Rare earth elements
REOs	Rare earth oxides
RSM	Response surface methodology
TGA	Thermogravimetric analysis
TMAPD	5,5'-(thiophene-2-ylmethylene)bis(2-aminopyrimidine-4,6-diol)
TPP	Triphenyl phosphite
US EPA	United States Environmental Protection Agency
VSM	Vibrating sample magnetometer
XRD	X-ray diffraction

INDEX

SUMMARY

Rare Earth Elements (REEs) are known as the remarkable components in many technologies that are driving the modern world. They are widely used in chemical engineering, permanent magnets, fluorescent lighting, sensors, cell phones, lasers, electronics, rechargeable batteries, etc., because of their unique physicochemical properties. In order to supply the required amounts of these elements and fulfil their increasing demands, it is necessary to recover this elements from secondary sources. Despite many efforts that have been done on recycling REEs, only less than 1% of REEs is recycled which can be due to the numerous challenges, such as collection of different final products and separation of REEs from other contaminants/metals.

Among the different techniques used for separation and purification of REEs from aqueous solution, biosorption has received great attention in recent decades. In this sense, biopolymers have been vastly utilized for the treatment of solutions containing metals. Alginate and chitosan are two kinds of biopolymers that have been utilized by many researchers due to being environmentally-friendly and effective.

The purpose of this work was to study the adsorption of Nd^{+3}, Tb^{+3}, and Dy^{+3} ions from aqueous solutions by using new magnetic nanocomposites based on calcium alginate (CA) and carboxymethyl chitosan (CMC) biopolymers, as well as novel synthetic biodegradable polyamide named poly(pyrimidine-thiophene-amide) (P(PTA)), and magnetic nanoparticles ($Ni_{0.2}Zn_{0.2}Fe_{2.6}O_4$).

The synthesis of the P(PTA) was performed in two steps. Firstly, a diamine-phenol monomer (TMAPD) was synthesized. Secondly, the polymer was obtained by polycondensation of TMAPD in 1,3-dipropyl imidazolium bromide ionic liquid as a solvent to avoid the use of the toxic triphenyl phosphite/N-methylpyrolidone/pyridine/LiCl that is required in the conventional direct polycondensation. The magnetic nanoparticles ($Ni_{0.2}Zn_{0.2}Fe_{2.6}O_4$) were synthesized by hydrothermal technique. The magnetic nanocomposites named CA/CMC/$Ni_{0.2}Zn_{0.2}Fe_{2.6}O_4$, CA/P(PTA)/$Ni_{0.2}Zn_{0.2}Fe_{2.6}O_4$, CMC/P(PTA)/$Ni_{0.2}Zn_{0.2}Fe_{2.6}O_4$ were synthesized by gelation method, and P(PTA)/$Ni_{0.2}Zn_{0.2}Fe_{2.6}O_4$ was synthesized by hydrothermal method.

Different techniques were used to analyze the synthesized materials. XRD was used to confirm the formation of the $Ni_{0.2}Zn_{0.2}Fe_{2.6}O_4$ and determine the size of the particles. The P(PTA) synthesis was confirmed by NMR analysis. The morphologies of the $Ni_{0.2}Zn_{0.2}Fe_{2.6}O_4$

and magnetic nanocomposites was investigated by FE-SEM technique. TGA was used for determining the thermal stability of the P(PTA) and magnetic nanocomposites. EDX was used for elemental analysis of the $Ni_{0.2}Zn_{0.2}Fe_{2.6}O_4$, P(PTA), and magnetic nanocomposites. VSM analysis was applied to determine the magnetic properties of the $Ni_{0.2}Zn_{0.2}Fe_{2.6}O_4$ and the magnetic nanocomposites. To determine the functional groups of all products, FT-IR analysis was applied.

Finally, the adsorption of the REEs was investigated in single and ternary batches, and column experiments. For the batch experiments, the effects of main parameters such as pH, contact time, adsorbent dosage, initial concentration, ionic strength, and temperature on the adsorption of the REEs were investigated in details. In addition, ΔG°, ΔH°, ΔS° as thermodynamic parameters were determined. In ternary system, response surface methodology based on central composite design (RSM-CCD) was used for the ternary system to predict the adsorption efficiency of the REEs and the interactions among different parameters. The kinetic and isotherm models were applied to fit the experimental data of the REEs adsorption in batch system. Besides, the obtained data from column system were fitted by the models.

CHAPTER I

INTRODUCTION

Importance of REEs

In recent decades, the application of rare-earth elements (REEs) has become apparent in numerous technological sectors. The relevance of the REEs was increasing to reach a peak in recent years since these metals play an important role in the emerging clean technologies because of their excellent electronic optic, magnetic and catalytic properties. Currently, there are about 132 million tons of REEs reserves around the world (Gambogi, 2016). Considering the mine production, China is nowadays known as the biggest REEs producer while its mine production rate is about 79%. In the following, Australia is known as the second biggest producer with a mine production rate of 15%. Russia, Brazil, and India with mine production rates of 2.2%, 1.5%, and 1.1% are respectively known as the other countries that have the largest amounts of REEs production (Gambogi, 2016). Since China has reduced its amount of export, the other countries in the world are confronting with a risk of supplying their required REEs. Due to the gap in supplying the required amounts of these elements and fulfilling their increasing demands, as well as the increasing pollution of REEs, it is not only quite necessary to recycle the REEs from secondary sources but also to recover them from waste streams.

1.1. What are Rare Earth Elements?

Lanthanides together with scandium and yttrium in the periodic table are known as REEs that are usually assorted into three classes, excluding promethium and scandium. These three classes are as follows: (1) lanthanum (La-57), cerium (Ce-58), praseodymium (Pr-59) and neodymium (Nd-60) as Light Rare Earth Elements (LREEs), (2) samarium (Sm-62), europium (Eu-63) and gadolinium (Gd-64) as middle rare earth elements (MREEs) and (3) the rest of lanthanides and yttrium as heavy rare earth elements (HREEs) (Yanfei et al., 2016). There is another classification that divides REEs to LREEs and HREEs as shown in **Fig. 1.1**.

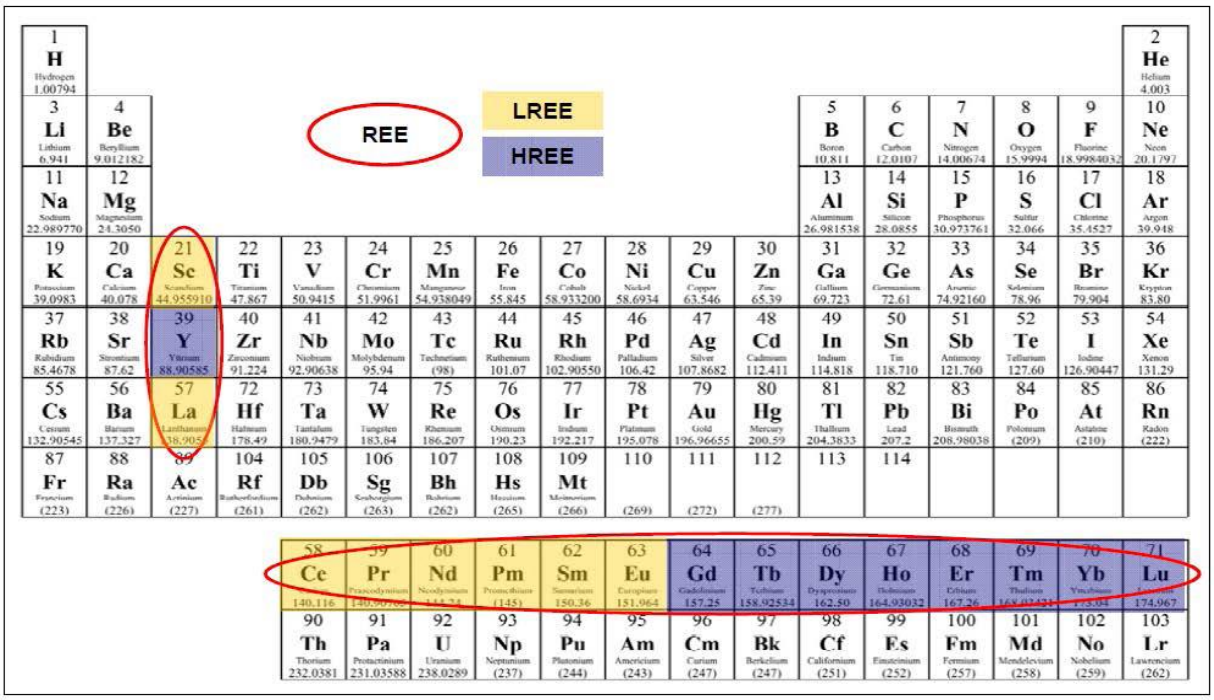

Fig. 1.1. Rare earth elements division as LREEs and HREEs (Schuler et al., 2011).

Gadolinium and dysprosium are sometimes classified as medium-weight lanthanides because of their physicochemical attributes. Notably, the word "rare" has come from metallurgical chemists around the 1940s (Gupta and Krishnamurthy, 2004). Due to the fact that most of them are commonly sold as oxide compounds, they are also known as "rare earth oxides". However, it can be claimed that they are hardly found in sufficient abundance in a single place to be economically feasible for mining (Chakhmouradian and Wall, 2012) since most of these elements are not rare with regards to the general amount of these elements in the earth's crust while their levels in the earth's crust are generally equal to or more than some physiologically important elements like platinum, cobalt, gold, silver, and selenium (Brzyska 1996). **Fig. 1.2** indicates the worldwide distribution of REEs while **Table 1.1** presents the REEs abundance in the earth's crust relative to other ordinary metals. Noteworthy, although these abundances from Wedephol (1995) that are presented here are only one of the several interpretations, they can be considered as a general representative.

As can be seen, the lanthanides content relative to other REEs in rock-forming minerals is not anywise rare. Moreover, as depicted in **Table 1.1**, cerium (60 mg/kg), lanthanum (30 mg/kg), neodymium (27 mg/kg), yttrium (24 mg/kg) and scandium (16 mg/kg) can be considered

as the most common ones. Lutetium (0.4 mg/kg) and thulium (0.3 mg/kg) are respectively the rarest elements while the concentrations of the remainders are in the range of 0.7 to 6.7 mg/kg.

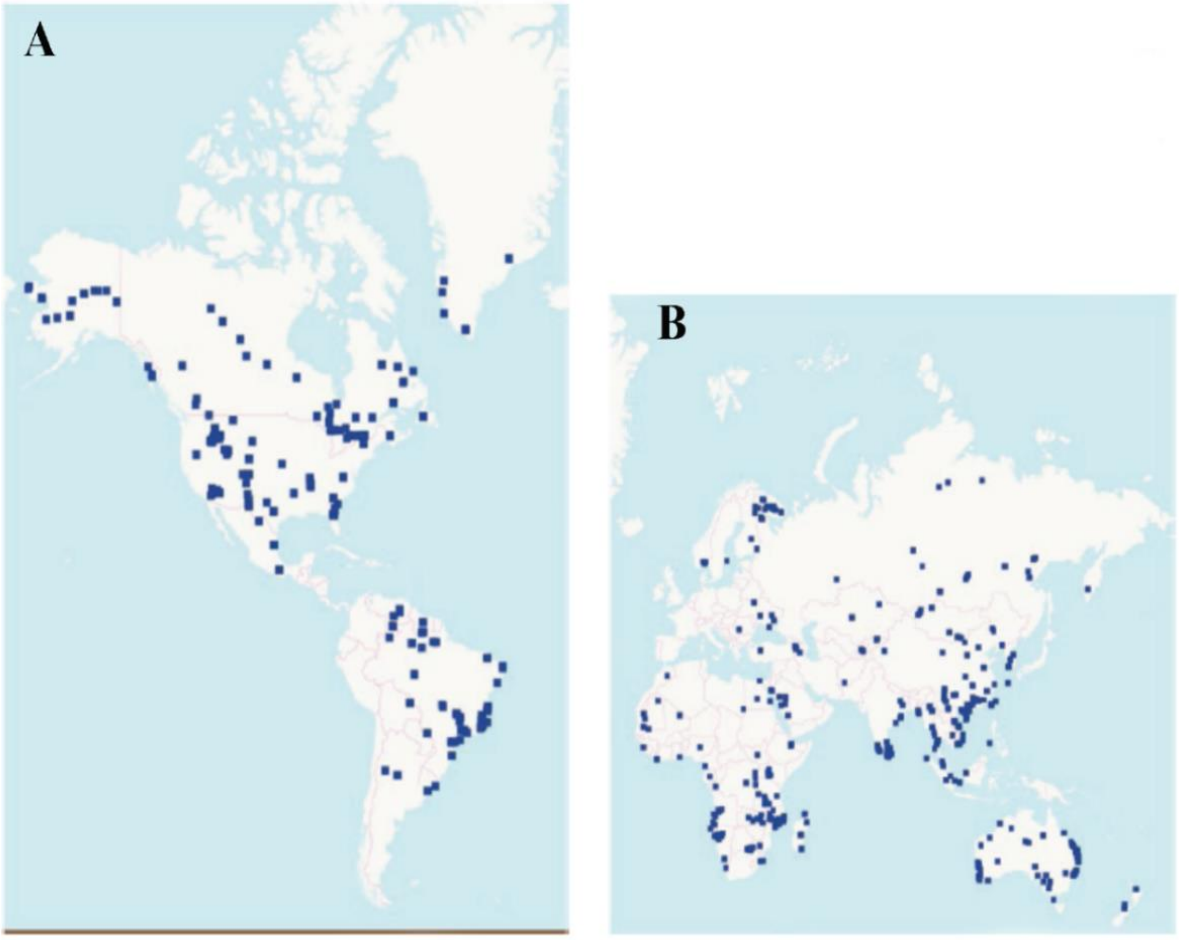

Fig. 1.2. (A) Deposits of REEs in the Greenland and Americas and (B) Deposits of REEs in the rest of the world (Ganguli and Cook, 2018).

Table 1.1. The abundance of elements in the Earth's crust (Wedepohl, 1995) (Bold: Lanthanides, scandium, and yttrium).

Elements	Abundance (parts per million)
Nickel ($_{28}$Ni)	90
Zinc ($_{30}$Zn)	79
Copper ($_{29}$Cu)	68
Cerium ($_{58}$Ce)	60
Lanthanum ($_{57}$La)	30
Cobalt ($_{27}$Co)	30
Neodymium ($_{60}$Nd)	27
Yttrium ($_{39}$Y)	24
Scandium ($_{21}$Sc)	16
Lead ($_{82}$Pb)	10
Praseodymium ($_{59}$Pr)	6.7
Thorium ($_{90}$Th)	6
Samarium ($_{62}$Sm)	5.3
Gadolinium ($_{64}$Gd)	4
Dysprosium ($_{66}$Dy)	3.8
Tin ($_{50}$Tn)	2.2
Erbium ($_{68}$Er)	2.1
Ytterbium ($_{70}$Yb)	2
Europium ($_{63}$Eu)	1.3
Holmium ($_{67}$Ho)	0.8
Terbium ($_{65}$Tb)	0.7
Lutetium ($_{71}$Lu)	0.4
Thulium ($_{69}$Tm)	0.3
Silver ($_{47}$Ag)	0.08
Gold ($_{79}$Au)	0.0031
Promethium ($_{61}$Pm)	10^{-18}

Based on the ordinary pattern of the periodic table, it can be stated that the lanthanides with even atomic numbers are generally more typical in nature. Moreover, a pattern in the occurrence and crustal abundance of some lanthanides has been observed by geochemists (McLeod and Shaulis, 2018). It is worth mentioning that lanthanides having lower atomic numbers were not only known as typical ionic constituents in REEs mineral ores but also generally happened in more considerable abundance compared to the lanthanide elements having more atomic numbers (Dostal, 2017).

REEs were named “rare” due to the fact that just after they were discovered, it was thought that only small amount of them was present in the Earth’s crust and the term “earths” also refers to the fact that their oxides have an earthy appearance. These metals are generally found together in geologic deposits because of having many identical attributes that are used in an extensive range of applications. For instance, magnets that are made using REEs are not only much more powerful and weigh less but also smaller compared to standard magnets. Moreover, some REEs can withstand severe heat as well as giving off intense white light when heated besides having great electrical conductivity. The REEs elemental forms, extracted from mineral ores as oxides (i.e., REOs), are iron-gray to silvery lustrous metals that are normally malleable, ductile soft and generally reactive, particularly when they are finely divided or at elevated temperatures (Hedrick, 2004). As they are not naturally present as pure elements, refinement processes are needed to separate these elements from ores. However, more than 200 REEs-bearing minerals are known. Phosphates (xenotime, monazite, rhabdophane, ningyoite, and florencite) followed by carbonates (synchysite, bastnasite, parasite, and lanthanite) are known as the most common rare elements that contain ores (Oliveira and Inverno, 2014).

The main REEs mineral ores that are most practical for the REEs extraction are xenotime monazite and bastnasite according to the following description: Bastnasite, which is the most abundant one compared to the other three REEs mineral ores, is a carbonate mineral that is mostly found in enriched LREEs (like lanthanum, yttrium, and cerium). Bastnasite is mainly found in pegmatites, vein deposits, and contact metamorphic zones and forms in rocks of carbonate-silicate associated to alkaline intrusions (Gupta and Krishnamurthy, 2004). Although LREEs cerium, neodymium, and lanthanum are generally used to enrich monazite, they can also include HREEs, especially yttrium (Ni et al., 1995). The LREEs predominance is because of the lower pressures and crystallization temperature of this mineral while it also has more HREEs compared to the bastnasite ore deposits. It must be noted that it generally happens in metamorphic rocks, acidic igneous rocks (mainly pegmatites) and some vein deposits. Monazite is not only resistant to weathering but also happens in several placer deposits while the host rocks are eroded. Thorium can be also related to monazite in different amounts (Chen et al., 2017). While xenotime is crystallized under higher pressures and temperatures compared to monazite, its crystalline structure can readily accommodate a higher ratio of HREEs (terbium through yttrium and lutetium) compared to the one that is generally found in monazite. It is

basically a yttrium phosphate mineral and happens as a minor element of gneissic and granitic rocks. In spite of the fact that it is not always present in remarkable quantities, thorium and uranium can also happen as elements of xenotime (Peiró and Méndez, 2013). Moreover, it has been seen that light rare earths (generally with coordination numbers of 8 to 10) concentrate on phosphates and carbonates. On the other hand, heavy rare earths (generally with coordination numbers of 6 to 8) concentrate on oxides and phosphates (Evans 1997).

1.2. Chemical characteristics and solution chemistry of REEs

In order to illustrate the resemblance of the rare earth metals, it is necessary to consider the structure of their atoms. In this regard, all of them have three electrons in their outermost shell while their chemical behavior is also determined using these electrons. Their difference refers to their inner shell -4f, with the systematic filling of **f** orbital, as well as 5d, 6s and 6p are empty. In spite of cerium that can exist as Ce^{+4} and Eu^{+2}, happening in both the trivalent and divalent states, all lanthanides happen as Ln^{+3} in aquatic systems. In contrary to the divalent ions, trivalent ones are enough stable (Topp, 1965). These ions are specified using large ionic radii which means that substitution reactions not only require large cations, like strontium or calcium jointly with their high valence but also tend to be separated from other trivalent ions. Furthermore, the ionic radii of lanthanides reduces from La^{+3} to Lu^{+3}. These ions are fundamentally spherical and able to form complexes that are similar to alkaline and alkaline earth ions besides being very electropositive. Therefore, their bonding attributes are mostly ionic (Henderson, 1996). The ions have low polarizability due to their high z/r ratio. They are usually found in solids with coordination number 8, while the smaller Sc^{+3} is found in coordination number of 6. However, $Ln(H_2O)_6^{3+}$ is the most common lanthanide which tends to bind the water molecules (Brookins, 1989). Although the hydrolysis of these ions is slight, their hydration is increased with the atomic number. In this regard, the hydrated ion size is increased from La to Lu while hydrolysis below pH 5 seems to be insignificant. Consequently, the lanthanide species are not easily hydrolyzed. The $Ln(OH)^{2+}$, $Ln(OH)_3$ and $Ln(OH)_4^-$ stepwise formational constants are significantly decreased while Ln^{+3} may be the dominant form in the water at acidic to neutral pH media.

Several complexes are important and pH-specific, depending on the ionic media and pH range. MEDUSA software is applied to understand the speciation of metals in dilute solutions

(Puigdomenech, 2000). For instance, in **Fig. 1.3A**, when the solution contains multi-metals in the presence of H_2SO_4, at the pH near 6, Tb^{3+} and $TbSO_4^+$ are the important ionic species while in the case of Dy^{3+} and Nd^{3+}, the formation ranges of ionic species are different depending on the type of REE. By increasing pH of the solution from around 6 for Tb^{3+} and Dy^{3+} and around 7 for Nd^{3+}, $Tb(OH)_3$ (s), $Dy(OH)_3$ (s) and $Nd(OH)_3$ (s) are formed and their amounts are increased by increasing pH of the solution up to 12. As depicted in **Figs. 1.3B** and **3C**, when the concentration of SO_4^{2-} increases in the solution, Tb^{3+} is changed to $TbSO_4^+$, $Tb(SO_4)^{2-}$ and $Tb(OH)_3$ depending on the pH of the solution. Similar results are seen for Tb^{3+} and Dy^{3+} which demonstrate that the concentration of reagent can affect the types of complexes, their formation ranges, and fractions in the solution. In **Figs. 1.3D-F**, by changing the reagent to HNO_3, different conditions are obtained when other conditions are constant that indicates the type of reagent has an important effect on the type of ions in the solution. It can be concluded that the type of reagent and its concentration is important as it can affect on the complex types and their formation ranges according to the pH value, also their fractions in the solution. It can be observed from the **Figs. 1.3A-F** that pH $\leq$ 5.5 and low concentration of NO_3^- prevent the formation of complexes. The importance of the halide complexes of the lanthanides is minor, even at low pH. Generally, at basic pH, hydrolysis becomes more significant for trivalent ions, $Ln(OH)_3$ and $Ln(OH)^{2+}$ (Topp, 1965). In the terminology of Pearson, the lanthanides are known as hard acids and can preferentially bond with hard bases containing oxygen as donor atoms. The major ligands generally include at least one donor oxygen atom, and kinetically, rare earths react quickly to form complexes. **Table 1.2** contains some characteristics of REEs.

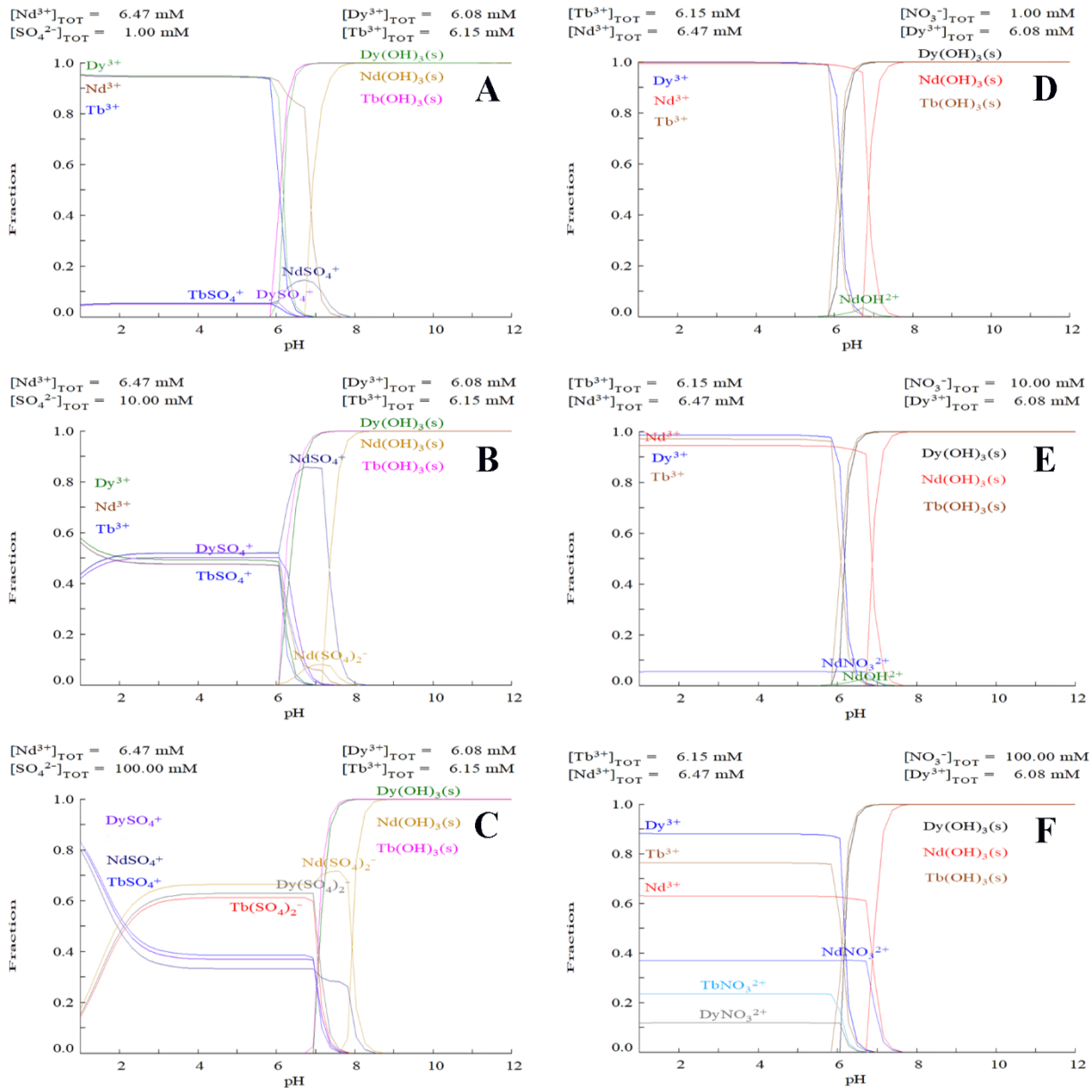

Fig. 1.3. Species of Nd^{3+}, $Tb^{3+,}$ and Dy^{3+} (**A**) in the concentration of 1 mM SO_4^{2-}, (**B**) in the concentration of 10 mM SO_4^{2-}, (**C**) in the concentration of 100 mM SO_4^{2-}, **(D)** in the concentration of 1 mM NO_3^-, **(E)** in the concentration of 10 mM NO_3^-, and (**F**) in the concentration of 100 mM NO_3^-.

Table 1.2. Some characteristics of REEs.

Symbol	Element	Atomic number	Molecular weight	Ionic radii (pm) Coordination number=6	Electronic configuration
Y	Yttrium	39	88.91	104	$[Kr]4d^15s^2$
La	Lanthanum	57	138.9	117.2	$[Xe]5d^16s^2$
Ce	Cerium	58	140.1	115	$[Xe]4f^26s^2$
Pr	Praseodymium	59	140.9	113	$[Xe]4f^36s^2$
Nd	Neodymium	60	144.2	112.3	$[Xe]4f^46s^2$
Sm	Samarium	61	147	109.8	$[Xe]4f^56s^2$
Pm	Promethium	62	150.4	111	$[Xe]4f^66s^2$
Eu	Europium	63	152	108.7	$[Xe]4f^76s^2$
Gd	Gadolinium	64	157.3	107.8	$[Xe]4f^7d^16s^2$
Tb	Terbium	65	158.9	106.3	$[Xe]4f^96s^2$
Dy	Dysprosium	66	162.5	105.2	$[Xe]4f^{10}6s^2$
Ho	Holmium	67	164.9	104.1	$[Xe]4f^{11}6s^2$
Er	Erbium	68	167.3	103	$[Xe]4f^{12}6s^2$
Tm	Thulium	69	168.9	102	$[Xe]4f^{13}6s^2$
Yb	Ytterbium	70	173	100.8	$[Xe]4f^{14}6s^2$
Lu	Lutetium	71	175	100.1	$[Xe]4f^{14}5d^16s^2$
The ionic radii for Ce^{4+} and Eu^{2+} is 101 and 131 pm, respectively.					

1.3. Refinement and production of REEs

REEs are separated as recognizable elements due to the physical similarities in the atomic radius and charge between them. It is worth mentioning that before recent advances that made separation economically practical, no common technological use was found for REEs (Hatch, 2012). Due to the fact that these REEs are low in abundance in rock deposits, their separation is very difficult. Therefore, it can be concluded that besides their low abundance in many rock deposits, REEs were not able to find common use in technologies before recent developments that made separation economically practical. Their similarity signifies that although they can make good substitutes for one another while their applications differ considerably for the overall group (Koerth-Baker, 2012).

Generally, production of REEs includes some steps as follows: extraction of REEs that contain mineral, milling, flotation, purification and subsequent processing of the ore (Schüler et al., 2011). Moreover, REEs are principally available as oxidic compounds and the resources are mostly represented as REOs because of their strong affinity with oxygen. Processing REOs into

utilizable products is not only a very complicated procedure but also significantly different between deposits. The main factors that affect the selection of treatment processes are mentioned as following (Ferron et al., 1991):

- Nature and type of the deposits (like vein type, beach sand, complex ores and igneous) and their complexity.
- Nature and type of other precious minerals that are available with REOs.
- Nature and type of gangue minerals that are available in the deposit (like clay, slimes and soluble gangue).
- Composition and type of the exclusive REO minerals.
- The accessability of the process in environmental and social terms.

Different chemical techniques and sometimes thousands of steps are required to occur refinement via physical separation of the REEs. Unluckily, all REEs and their particular ores are various and therefore need various chemical methods for refining (according to the vapor pressure and melting point along with other physical attributes of the element) (Tiesman, 2010). Generally, separation and concentration from the host material in alkaline or acidic solutions, the individual REOs reduction into pure metals, and REO separation utilizing ion exchange or solvent extraction are known as the fundamental steps in REOs processing (Gupta and Krishnamurthy, 2004). The primary step commonly contains grinding and crushing where ore is reduced to fine particles and REO is separated using different methods like magnetic, flotation or gravimetric separation. The percentage of REOs in the working material is dramatically increased along with the separation process.

The aim of the following steps in the process is to change the concentrated mineral into a more precious chemical that is formed via different chemical and thermal reactions. The mineral concentrates are typically separated into utilizable oxides by employing hydrometallurgy methods (like precipitation, leaching, and extraction). Moreover, the oxides or metal mixtures can be refined into high-purity rare earth metals using methods like the metallothermic reduction for further processing (Suli et al., 2017).

Hydrometallurgy is the most typical chemical extraction technique that is used for the separation of individual REOs from the mineral concentrate. Basicity variations between the different rare earths affect the hydrolysis of ions, the solvability of their salts and the creation of complicated species (Gupta and Krishnamurthy, 2004). In this regard, fractional crystallization,

ion exchange, fractional precipitation, and solvent extraction exploit the differences in these attributes for separating the individual REOs. In spite of the fact that some of the rare earth chlorides and individual REOs yielded from these processes can be used in markets, further refining and processing are necessary for producing high-quality pure metal end products to maximize their value. These processes can be used for recovering REEs from recycled materials. Several technologies can be used to separate and recovery REEs such as liquid-liquid extraction, solid-liquid extraction, solid phase, ion exchange, super critical extraction, electrowinning, electrorefining, electro slag refining (Meyer and Bras, 2011).

1.4. Health impacts and environmental effects of REEs exposure

The particular waste streams in REEs processing and their dangerous waste potential were previously identified and assessed by the US EPA (United States Environmental Protection Agency) (1991) (**Table 1.3**). Based on REEs processing, these elements are able to find their way into the various environmental paths, particularly those that are associated with surface waters and the ground, perhaps have their own contribution to human health and environmental pollution. As a result, based on the function of elements in the environment and their toxicity with regard to human health, a new group of elements REE, viz. and PGE has been included to the already existing elements' classification (**Fig. 1.4**) (Balaram, 2016). Although REEs may only become accessible in small amounts through the atmosphere and the groundwater under natural conditions, their growing use has not only increased the amount of REEs but also formed several new routes for bioaccumulation (in animals, plants, and human beings). It is worth mentioning that the background level of REEs content in waters, both subsoil and surface, is remarkably different and generally dependent on the local geology. Unluckily, the REEs maximum plausible limits in drinking water have not been reported by any international health organization while, as previously mentioned, there is not enough available information about their toxicity to human health (Balaram, 2019). Noteworthy, while REEs must go through a large number of steps to be purified and many various reagents and chemicals are required for these processes, a large amount of radioactive and toxic waste is generated from by-products that must be controlled either via recycling, or pumping it to a holding tank. Additionally, due to the amount of processing that is required for purifying REEs, not only a huge cost is incurred but also the price of the element is significantly increased (Long et al., 2010).

Table 1.3. The waste streams of REEs processing and their hazardous waste potential.

Process Waste Stream	Hazardous Waste Potential
Off-gases from dehydration	None
Spent hydroxide cake	None
Spent monazite solids	None
Spent off-gases from electrolytic reduction	None (after appropriate treatment)
Spent sodium fluoride	None
Waste filtrate	None
Waste solvent	Ignitability
Spent lead filter cake	Toxicity
Lead backwash sludge	None
Waste zinc contaminated with mercury	Toxicity
Solvent extraction crud	Ignitability

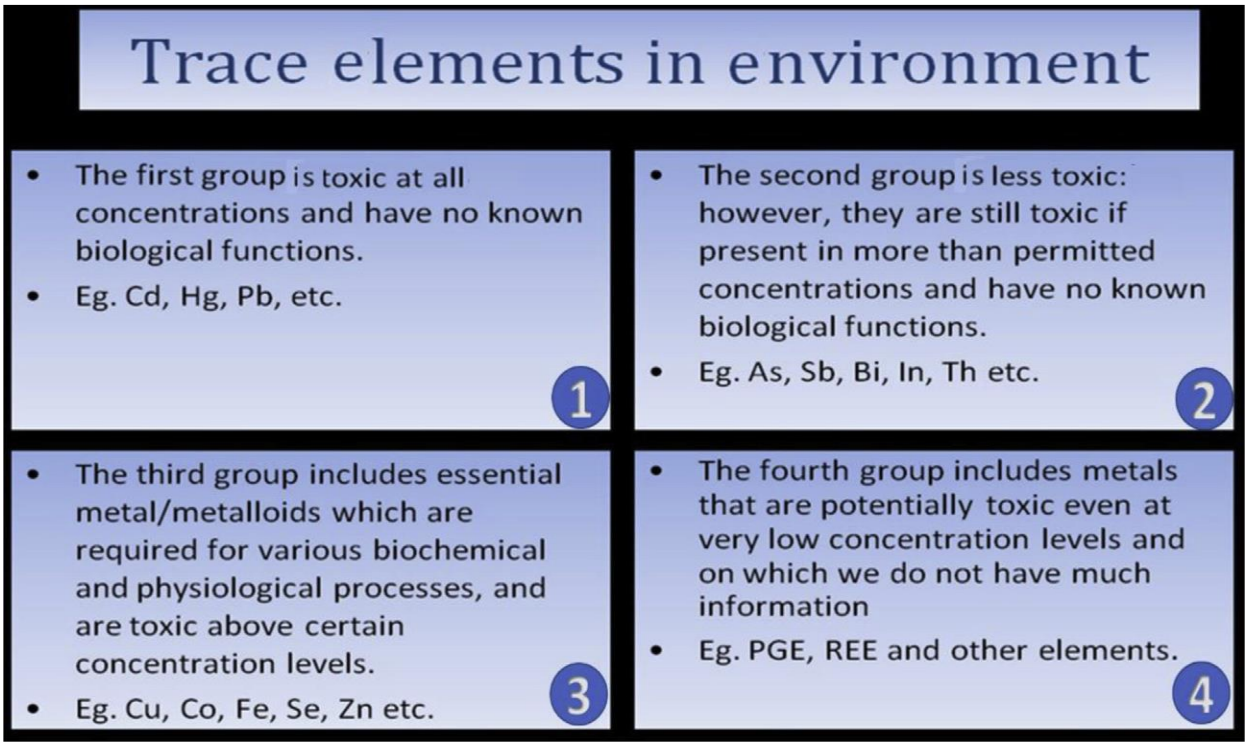

Fig. 1.4. Trace elements are divided into four categories based on their environmental function (Balaram, 2016).

1.5. Applications of REEs

Recently, increasing attention has been focused on REEs as highly precious ingredients for innovation, particularly because of the sustainable energy technologies development. REEs are applied in many advanced technologies that people employ daily, like permanent magnets, fluorescent lighting, sensors, cell phones, lasers, electronics, rechargeable batteries, DVDs, catalysts, alloys and communications, and other green economy applications (Zhao et al., 2016). Along the past twenty years, the requirement for many items that need rare earth metals has been considerably increased. In fact, about twenty years ago only a few numbers of cellphones were in use while this number has increased to over 7 billion nowadays. Using REEs in computers has increased almost as rapidly as cell phones. They are used for making many rechargeable batteries. In other words, by increasing the requirement for portable electronic devices, like readers, cell phones, cameras, and portable computers, the demand for batteries has been also increased. Several grams of rare earth compounds are used in batteries that are employed for powering electric and hybrid-electric vehicles. Considering the issues like energy independence, climate change, and so on that are driving the sale of electrical and hybrid vehicles, the demand for batteries that are made with rare earth compounds will increase even faster. Generally, rare earths are employed as phosphors, catalysts, and polishing compounds. These are employed for controlling air pollution, polishing optical-quality glass and illuminating screens on electronic tools (Long et al., 2010).

Moreover, REEs provide an enormous advantage as they play a key role in national defense. For instance, the United States military employs precision-guided weapons, night-vision goggles, communications tools, batteries, GPS tools, and other defense electronics. Notably, rare earth metals are known as essential ingredients for creating very hard alloys that are utilized in projectiles and armored vehicles that break upon effect. Although there are some substitutes that can be utilized instead of REEs in some defense applications, they are not generally enough efficient and may diminish the superiority of the military (Gambogi, 2011; United States Geological Survey, Fact Sheet 087-02).

The employment of REEs in the United States in 2013 is depicted in **Fig. 1.5.** As it is clear, rare earth catalysts are used in exhaust systems of many vehicles for controlling air pollution. Moreover, the addition of rare earth metals can make a large number of alloys more durable. Granite glass, gemstones, and marble are usually polished using cerium oxide powder. REEs are

also utilized in plenty of motors and generators containing magnets. Furthermore, phosphors that are utilized in monitors, digital displays, and televisions are made with rare earth oxides. Most cell phones, computer and electric vehicle batteries are also created using rare earth metals (Gambogi, 2017; United States Geological Survey, Fact Sheet 087-02). **Table 1.4** presents more information about the key usage of each REE separately.

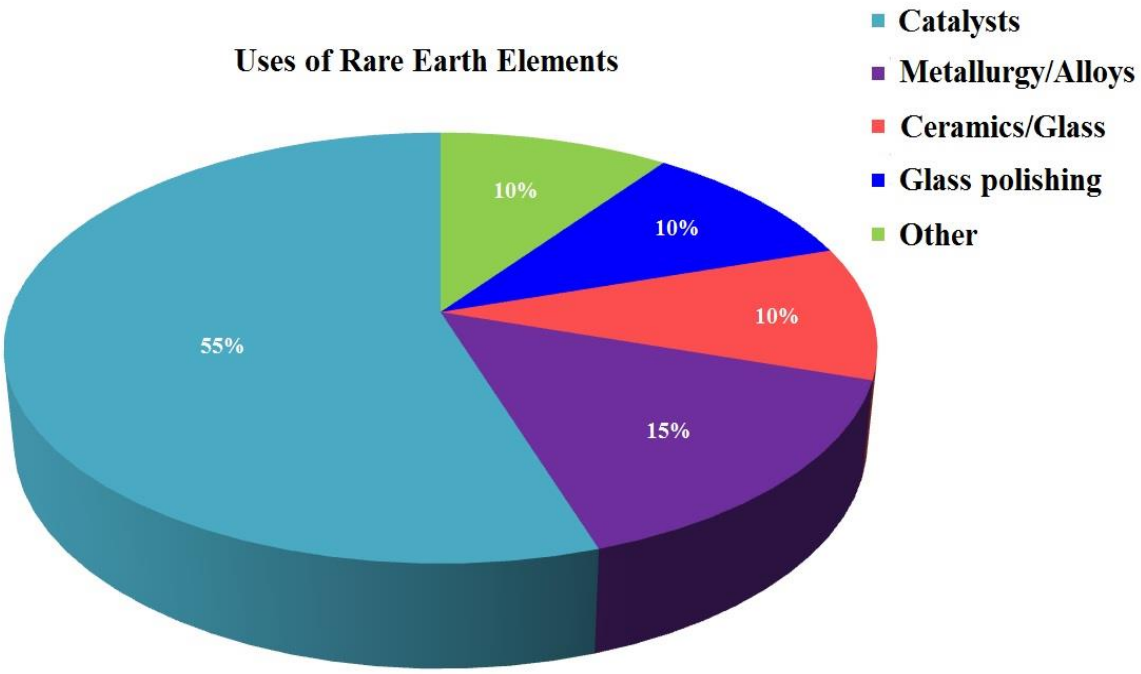

Fig. 1.5. The employment of REEs in the United States, reported by the United States Geological Survey Mineral Commodity Summary, 2017.

Table 1.4. REEs and their usages (EPA, 2012).

Element	Usages
Scandium	Metal alloys for the aerospace industry.
Yttrium	Metal alloys, Ceramics;; lasers; microwave communication for satellite industries; fuel efficiency; color televisions; temperature sensors; computer monitors. Utilized by DoD* in weapon systems and targeting and communication tools. Specified by DOE** as crucial in the short- and mid-term according to the projected supply risks and significance to clean-energy technologies.
Lanthanum	Catalysts for petroleum refining; Batteries; high-tech digital cameras; electric car batteries; video cameras; X-ray films; laptop batteries; lasers. Utilized by DoD in communication tools. Specified by DOE as near crucial in the short-term according to the projected supply risks and significance to clean-energy technologies.
Cerium	Metal alloys; catalysts; polishing; lens polishes (for mirrors, glass, optical glass, television faceplates, disk drives, and silicon microprocessors). Specified by DOE as near crucial in the short-term according to the projected supply risks and significance to clean-energy technologies.
Praseodymium	Enhanced magnet corrosion resistance; searchlights; pigment; photographic filters; airport signal lenses. Utilized by DoD for guiding and controlling systems and electric motors.
Neodymium	Fluid-fracking catalysts, lasers, high-power magnets for laptops. Utilized by DoD for guiding and controlling systems, communication devices and electric motorsSpecified by DOE as crucial in the short- and mid-term according to the projected supply risks and significance to clean-energy technologies.
Promethium	Fluid-fracking catalysts, beta radiation source.
Samarium	Reactor control rods, high-temperature magnets. Utilized by DoD for guiding and controlling electric motors and systems
Europium	Liquid Crystal Displays (LCDs), glass additives, fluorescent lighting. Utilized by DoD in weapon and targeting systems and communication tools. Specified by DOE as crucial in the short- and mid-term according to the projected supply risks and significance to clean-energy technologies.
Gadolinium	Glass additives, magnetic resonance imaging contrast agent.
Terbium	Phosphors for display and lighting. Utilized by DoD in control and guidance systems, weapon and targeting systems, and electric motors. Specified by DOE as crucial in the short- and mid-term according to the projected supply risks and significance to clean-energy technologies.
Dysprosium	High-power magnets, lasers. Utilized by DoD in control and guidance systems and electric motors. Specified by DOE as crucial in the short- and mid-term according to the projected supply risks and significance to clean-energy technologies.
Holmium	The highest power magnets that are known.
Erbium	Glass colorant, lasers.
Thulium	High-power magnets.
Ytterbium	Solar panels, Fiber-optic technology, lasers alloys (stainless steel), radiation source for portable X-ray units.
Lutetium	X-ray phosphors.

*DoD: Key categories of employments by the U.S. Department of Defense
**DOE: Classification of the elements specified to be crucial or near crucial owing to the projected supply risks and their significance to clean-energy technologies.

It should be noted that the quantity of the required REEs in most of the crucial uses is not considered. REEs are generally utilized in small quantities and can significantly enhance the efficiency of the product in most cases. In other words, if they play the needed role, they are simply effective. The quantities of REEs that is used in some products is presented in **Table 1.5**. **Table 1.6** presents an overview of REEs demands in green modern technologies. The data shows a continuous increase in REEs demands in the coming years since their usage is in the center of attention for the producers.

Table 1.5. Amounts of REEs in some products (Ganguli and Cook, 2018).

Mobile phone	0.0005 kg
Air conditioner	0.12 kg
Toyota Prius	15 kg REE per unit
Lockheed-Martin F-35	416 kg
Navy surface ships	1818 kg
Navy submarines	3636 kg

Table 1.6. An overview of the world demand of REEs for modern technologies (zhou et al., 2017).

Year	Wind power (MW)	Lighting LED (Million Cps)	Electric vehicles (Million Cars)	NiMH batteries (Million Batteries)	Catalytic converter (Million Cars)
2016	63350	2675	35.7	0.6	95
2020	79005	4828	37.6	1.3	100
2025	76810	5874	44.2	0.7	111
2030	107488	7146	66.5	2.7	117

1.6. Critical issues related to REEs

Production of REEs contains REEs extraction having milling, mineral, purification, flotation, and more processing of the ore (Schüler et al., 2011). Pollution standards and monitoring options were implemented by the Chinese Ministry of Environmental Protection while the United States and Australia presumably utilized the newest mining technologies (Ministry of Environmental Protection, 2011a). Nevertheless, environmental pollution, generated because of radioactive waste and other chemicals, is still remained as a crucial issue for the production of REEs. In spite of the environmental risks that are generally because of unregulated illegal mining (Wübbeke, 2013), flotation is also really dangerous for our surrounding

environment. Flotation involves chemical beneficiation in ponds, known as tailings. The reminders, like radioactive thorium or uranium other chemicals, are left in the wastewater. Considering the fact that this water is exposed to disruptions or natural environmental conditions, it can pose critical risks of environmental pollution (Schüler et al., 2011). Moreover, although purification is costly and energy-intensive, it is crucial due to the purity of 99% that is almost required (Hatch, 2012). The problem in the production step of REEs is not the only one.

Although REEs are extensively utilized in plenty of applications around the world, supplying them is considerably limited to only a few large mining districts (Chakhmouradlan and Wall, 2012). In spite of the fact that REEs occur around the world, the largest mining fields of ores, such as monazite, bastnäsite, and xenotime having essential REEs, are located in the Asian states (Manchen et al., 2019) and among them, China is changed to the first country in mining and extracting REEs due to their most abundant REE deposits. As can be seen in **Table 1.7**, more than 90 % of mine production of rare earth occurs in China, although this country has less than 40 % of the identified deposits. While China's domestic demand has remarkably increased, it tightened its REEs export quota from 50145 tonnes to only 31130 tonnes from 2009 to 2012 which led to serious problems for REEs users that were outside of China (It was proved by the rare-earth crisis in 2011 with the record of the highest prices) (Binnemans et al., 2013).

Table 1.7. World rare earth element production and rare earth stores estimation, 2012 (Lucas et al., 2015).

Country	**Mine Production of REEs (Kilotonnes)**	**Deposits of Rare Earth Elements (Megatonnes)**
China	75	44
USA	1	13
Australia (mined and concentrated in Australia, extracted in Malaysia)	1	1
India	3	2
Other		33

In 2018, the total world REE deposits were estimated to be around 120 million tons (**Table 1.8**) (Manchen et al., 2019) which seems to be sufficient for global requirements over hundreds of years (Zhou et al., 2017). However, the REEs world demand was about 142 thousand tons in 2018 (Manchen et al., 2019).

Table 1.8. World mine production and reserves of REEs* (U.S. Geological Survey, 2019).

Country	Mine production		Reserves
	2017	2018	
United States	-	15000	1400000
Australia	19000	20000	3400000
Brazil	1700	1000	22000000
Burma (Myanmar)	Not available	5000	Not available
Burundi	-	1000	Not available
China	105000	120000	44000000
India	1800	1800	6900000
Malaysia	180	200	30000
Russia	2600	2600	12000000
Thailand	1300	1000	Not available
Vietnam	200	400	22000000
Other countries	-	-	4400000
World total (rounded)	132000	170000	120000000

*Data in metric tons of REEs oxide

It is worth mentioning that not only China has the most extensive deposits of REEs but also it has the most complicated processing technologies and facilities for producing the rare earth metals. Each year, China can produce around 120,000 tons of rare earth while the total world production is about 170,000 tons (Manchen et al., 2019, Zhou et al., 2016). Although mining in other countries (like the USA, India, and Australia) is growing, its process is very slow. The peak of all rare earths prices was in 2011 and after that their prices have fallen down which had a discouraging impact on new mining projects (Gambogi, 2013). This situation has also motivated other countries like Japan and most EU Member States that do not have any kind of main rare-earth reserves on their territory to search for secondary and alternative rare earth resources for developing their own rare-earth industry to acquire a source of both heavy and light rare earths (Binnemans et al., 2013). Using natural resources is essential in a sustainable and circular economy. This can only happen by recycling and reusing materials from end-of-life consumer goods.

REEs are considered as the most crucial raw materials group with the highest supply risk by the European Commission (European Commission Critical raw materials for the EU). To overcome the challenge of supplying the REEs, a threefold method can be suggested. The first strategy is to substitute crucial rare earths by less crucial metals. Secondly, the risk of supplying REEs can be reduced by investing in sustainable fundamental mining from new or old REEs

reserves. Nowadays, mining companies are now extensively looking for new usable rare earth reserves and old mines are being opened again (Humphries, 2012). Prior to the REEs mining boom in China, the global market was dominated by the US. The operations were started by Mountain Pass in California in 1965 (**Fig. 1.6**) and it was known as the main producer around the world for decades (Barakos, 2017). Notably, because of the contest in China as well as in response to environmental matters in the surrounding area of Mountain Pass, mining activities stopped in 1998 (Mancheri, 2015). The production was restarted in 2012 due to the REEs supply risk. Nonetheless, most of the countries have to invest in technospheric mining due to the absence of operational and/or economic primary reserves on their territory (Johansson et al., 2013).

Fig. 1.6. Molycorp Mountain Pass rare earth facility in California's Mojave Desert.

Generally, technospheric mining can have many forms. With consideration of crucial metal-having streams, such mining contains (1) direct recycling of pre-consumer manufacturing REEs residues/scrap; (2) urban mining of post-consumer (usually complicated multi-material) End-of-Life products; (3) landfill mining of historic (and future) urban and industrial waste residues having REEs. The focus of urban mining and direct recycling is on resources with very great content of rare earths. However, the total accessible volumes for recycling are relatively low. However, base metals like iron, copper, and aluminum along with valuable metals (silver, gold, and platinum-group metals) achieved high recycling rates. In spite of the fact that there is an extensive literature dealing with (mostly lab-scale) research attempts on recycling REEs, only

less than 1% of them were being recycled in 2011. This is generally because of ineffective collection, lack of incentives, and technological difficulties (Binnemans et al., 2013).

Generally, neodymium, dysprosium, europium, yttrium, and terbium (**Fig. 1.7**) are known as the five most critical REEs based on the medium-term criticality matrix of the U.S. Department of Energy (DOE), and their essential applications are in green energy as follows (Binnemans et al., 2013; US Department of Energy, 2011):

• Dysprosium and neodymium are utilized in the permanent magnets manufacturing which are employed in wind turbines and many other products like speakers, hard disk drives, and headphones.

• Yttrium, europium, and terbium are utilized besides cerium, lanthanum, and gadolinium in phosphors in low-energy fluorescent lamps.

• Yttrium, neodymium, lanthanum, cerium, and praseodymium are utilized in the manufacturing of nickel metal hydride (NiMH) batteries for hybrid vehicles.

In addition, their hazards are mentioned in **Table 1.9**. Consequently, recycling REEs from end-user products, such as fluorescent lamps and magnets that present over 70% of the rare-earth market in terms of value (32% for lamp phosphors; 38% for magnets), can provide the opportunity to maintain the supply of these crucial elements and decrease the dependency of UE from other countries. In this context, there is a necessity to develop advanced separation processes for recovery of Nd, Dy, and Tb which are three of the most critical elements.

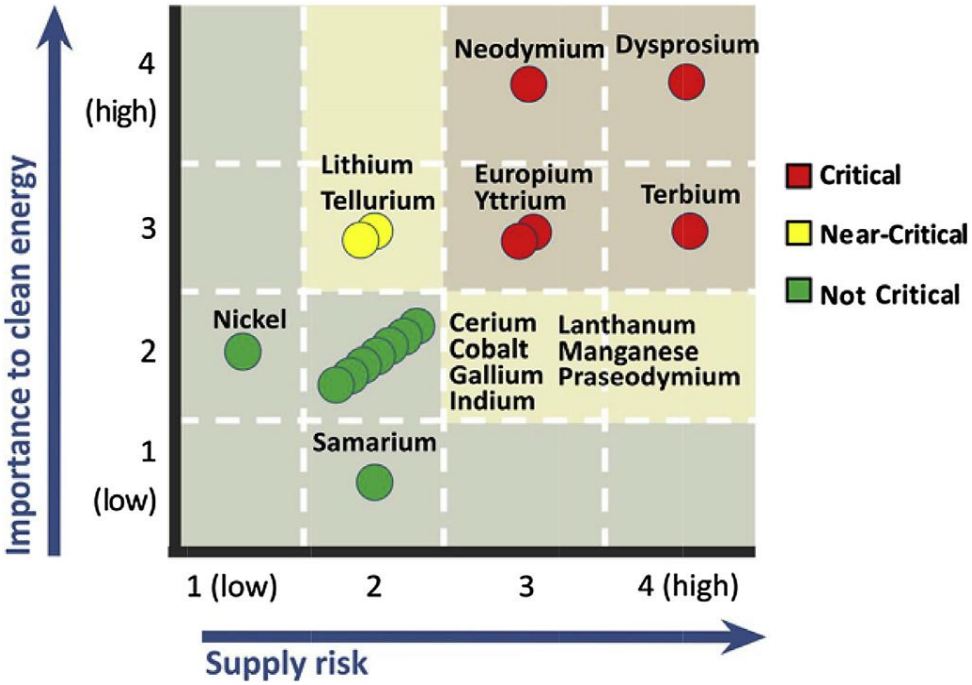

Fig. 1.7. DOE medium term (2015-2025) criticality matrix, representing the five most crucial rare-earth elements (Nd, Y, Tb, Eu, Dy).

Table 1.9. Significant uses of Dy, Nd, and Tb and their toxicological information (Rim et al., 2013).

Element	Toxicological information
Dy	Soluble Dy salts, like dysprosium nitrate and chloride, are mildly toxic when ingested. However, the insoluble salts are non-toxic. According to the toxicity of dysprosium chloride to mice, it is determined that the ingestion of 500 g or more might be fatal to a human.
Nd	Nd compounds are of low to moderate toxicity. Nonetheless, its toxicity has not been explored thoroughly. Neodymium salts are very irritating to the mucous membranes and eyes, and moderately irritating to the skin.
Tb	It may cause serious irritation to the skin and eyes.

1.7. Separation and recovery of REEs

Individual REEs purification has obtained remarkable attention in recent years due to the growing requirements for high-purity REEs and their compounds (Anastopoulos et al., 2016). Several techniques are used for the separation and recovery of metal ions from aqueous solution, like chemical precipitation, membrane technology, and extraction of solvent.

Among the different separation techniques, solvent extraction is extensively used for aqueous solutions treatment containing metal ions. However, it is costly on a large scale and yields to extensive environmental problems due to the toxic organic diluents and modifiers that are widely used (Yadav et al., 2015). The purification and separation of REEs using solvent extraction need the treatment of a large volume of dangerous volatile organic compound solvents (Florek et al., 2014). Since flammable volatile organic compound solvents are concerned, solvent extraction seems to be dangerous.

Chemical precipitation also needs an extensive amount of chemicals to decrease metals to a satisfactory discharge level. Extreme sludge production is known as its other drawbacks which needs more treatment, poor settling, slow precipitation of metal, metal precipitates aggregation, and the long-term environmental effects of sludge disposal (Aziz et al., 2008). High energy consumption related to the high operation pressures, the costs associated with fouling problems, and replacement of membranes can be considered as the main drawbacks of membrane technology.

1.8. Separation by adsorption

Adsorption can be considered highly effective, especially because of dilute solutions, cheap and easy techniques and being able to start environmentally without utilizing any organic solvents for recovery of metal ions from aqueous solution. Therefore, it can be considered as a competitive alternative to solvent extraction. Some adsorbents have been used for rare earth metals adsorption, such as *Sargassum sp* (Oliveira et al, 2011) activated carbon (Murty et al., 1996), titanium dioxide (Liang et al., 2001), cellulose (Zhu et al., 2015), b-cyclodextrin (Zhao et al., 2016), silica (Esser et al., 1994), aminocarboxylic adsorbents (Grebneva et al., 1996), and oxidized multiwalled carbon nanotubes (Koochaki-Mohammadpour et al., 2014), SiO_2/UF impregnated with organophosphorus extractant (Naser et al., 2015), activated biochars from cactus fibres (Hadjittofi, 2016), graphene oxide-corn zein composites (Xu et al., 2018) .

Due to some disadvantages that are available in the adsorbents which have been used for adsorption of REEs, such as low adsorption capacity, weak mechanical properties, poor chemical resistance, difficult adsorbent separation from the aqueous phase, and high-dose requirement of the adsorbent for complete metal ions removal, it is necessary to perform extensive investigations on the production of novel adsorbents to overcome such defects. The selection of adsorbent relies on the nature of the metal ion, as each type of metal may need a particular adsorbent. On the other hand, adsorption efficiency relies on physicochemical attributes, such as functional groups, porosity, particular surface area, and adsorbent particle size (Chen et al 2003).

1.8.1. Adsorption by metal oxides

Generally, the high surface area and high specific affinity of adsorbent are the two key factors to determine the efficiency of metal ion separation from polluted water. Metal oxides are attractive candidates as adsorbents for metal ion separation and recovery (Rittmann et al., 2011). The high surface area of metal oxides may provide rich sites for metal ion adsorption which is normally benefited from porous structures. The high specific affinity is mainly due to the abundant surface hydroxyls on metal oxides (Qu, 2008). Some metal oxides have been used as an adsorbent for adsorption of REEs, such as Al_2O_3 (Marmier et al., 1997), amorphous silica (Marmier et al., 1999), and α-TiO_2 (Ridley et al., 2005). The investigations showed that metal oxides are not only cheap and nontoxic but also chemically stable and environmentally friendly (Chu et al., 2009). Nonetheless, researchers all around the world have been trying to decrease the main disadvantage of metal oxides, such as not being easily dispersed in aqueous solution because of being microsized. Besides, by increasing particle size, the ratio of surface area to volume declines; therefore, the capacity of metal adsorption decreases.

1.8.2. Nanotechnology and nano metal oxides

Nanostructured materials with dimensions (grain size, layer shapes or thickness below 100 nm) have yielded to the growing interest in nanotechnology (Hornyak et al., 2009). The eccentric attributes of nanomaterials are related to their nano-dimensions. In fact, nanomaterials are the materials that have at least one dimension which is below 100 nm (Chattopadhyay et al., 2009).

During the last two decades, a lot of attempts have been done around the world in both the theory and the empirical research of the development, specification and applications of inorganic nanostructures containing metal oxides, composites and ceramics and they have yielded to a mature and multidisciplinary field. Nanostructured materials are generally known because of their green chemistry, stability, and various technical applications (Bhushan et al., 2010).

Amongst inorganic nanostructures, metal oxides nanostructures have received so much attention in recent years. They are applied in versatile applications, such as gas sensors, optical sensors, pressure sensors, electrochemical performance for energy storage, catalytic and photocatalytic, environmental application, etc. Separation of metal ions from polluted waters by the adsorption process is known as one of the most important environmental applications of metal oxides nanostructures that has been investigated by many researchers. Their major benefits include their ability to be simply dispersed in aqueous solution and the existence of a large number of their atoms, known as surface atoms, which not only have high adsorption capacities to many metal ion but also are unsaturated. In addition, the extremely small size of nanoparticles creates a large surface area in relation to their volume and makes them highly reactive in comparison to non-nanoforms of the same adsorbents (Srivastava et al., 2015). The adsorption behavior of nanometal oxides, such as nickel oxide (Saikrishna and Babu, 2015), aluminum oxide (Patra et al., 2012), titanium oxide (Jegadeesan et al., 2010), and zirconium oxide (Hristovski et al., 2008) have been proved by the researchers including the metals that were adsorbed by aluminum oxide, titanium oxide, and zirconium oxide from the papers mentioned above. The primary mechanisms for adsorption of REEs on nanostructured materials, like metal oxides, are surface complexation, precipitation, ion exchange, physical adsorption, and electrostatic attraction.

1.8.3. Biopolymers

Biopolymers are polymers produced from biobased materials that are also biodegradable. Biopolymeric materials contain alginates, cellulose, proteins, lignins, carrageenan, chitosan, and chitin derivatives. The salient attribute of biopolymers is that they own a great amount of various functional groups like amines and hydroxyls that can enable metal ions to bind either by chemisorption or physisorption (Saravanan and Sudha, 2014).

Amongst the biopolymers investigated for metal ions adsorption, alginate and chitosan as natural carbohydrate biopolymers are industrially and scientifically attractive and have received so much attention as adsorbent and complexing agent by their functional groups that have a strong affinity to heavy metal ions. Due to the fact that natural materials, which are accessible in great quantities, or particular wastes obtained from manufacturing operations, are extensively available, environmentally friendly and practically unexploited resources, they may have a great potential to be utilized as low-cost adsorbents (Spinelli et al., 2004).

Alginate

Alginate, a natural polysaccharide, is the binary copolymer of (1,4) glycosidically linked α-D-mannuronic acid (M) and β-L-guluronic acid (G) (**Fig. 1.8**). The abundance of carboxylic and hydroxyl groups gives alginate strong chelating properties for metal ions (Fiset et al., 2008). It is negatively charged in aqueous solution at pH > 3.4 owing to the carboxyl groups available in both M and G subunits, where the carboxyl groups are deprotonated excluding at very low pH (Yu et al., 2013). Polyvalent cations can interact with blocks of M and G residues cooperatively in the gelation process to create ionic cross-links between various polymer chains (**Fig. 1.9**) that is known as "egg-box" model (Braccini and Pérez, 2001). The polyvalent cations, like calcium cations, can be substituted by ionic adsorbates. Because of their ability to form stable structures, cross-linked alginate has been utilized for the adsorption of heavy metals, like lead (Yakup Arıca et al., 2003), mercury (Yakup Arıca et al., 2004), manganese (Gotoh et al., 2004), and chromium (Ibáñez and Umetsu, 2004). Alginate adsorbents have been also used for the REEs adsorption, such as sodium alginate hydrogel cross-linked with poly-γ-glutamate (Xu et al., 2015), calcium alginate beads (Nayak, 2005), and alginate–poly glutamic acid hybrid gels (Wang et al., 2014). The primary binding mechanism of metal ions to calcium-alginate gel beads contains ion exchange and adsorption. Additionally, new hypotheses of cation binding and alginate cross-linking (Siew et al., 2005) have been explored in recent studies. Based on them, only one or two M and G blocks are involved in creating a binding site. Moreover, Rodrigues and Lagoa proposed that the number of binding sites and binding mechanisms relied on the accessibility of cation in the solution (Rodrigues and Lagoa, 2006). Results showed the successful usability of alginate adsorbents to separate REEs from aqueous solution.

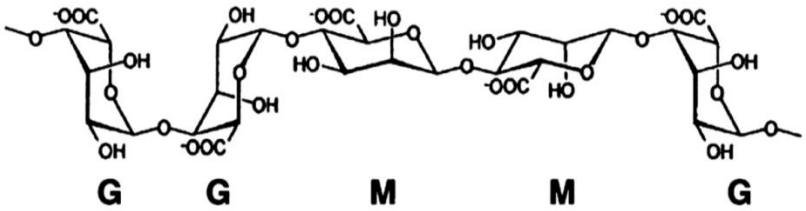

Fig. 1.8. Guluronic acid (G) and Mannuronic acid (M) subunits in the chemical structure of alginate at pH>3.4 (Yu et al., 2013).

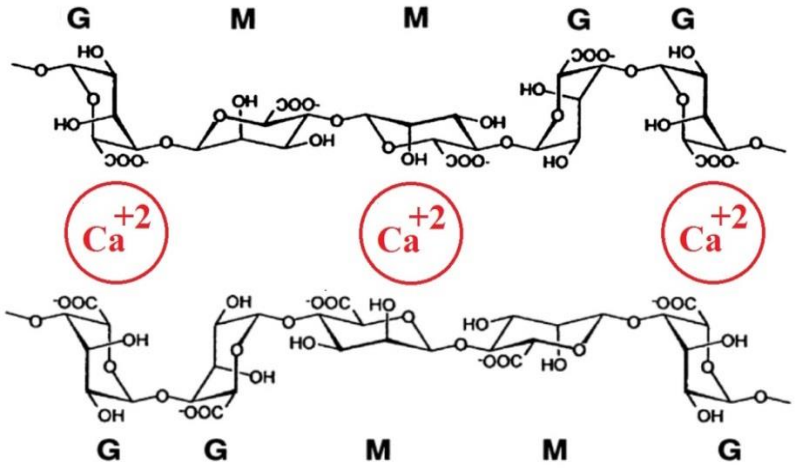

Fig. 1.9. Gelation process by a divalent cation (Braccini and Pérez, 2001).

Chitosan

Chitosan, a cationic polysaccharide composed of *N*-acetyl glucosamine and glucosamine subunits (**Fig. 1.10)**, is a potential biopolymer acquired cost-effectively by the derivation of chitin, which is a natural material extensively found in crustacean shells and is proved to have the best chelating properties among other natural polymers (Varma et al., 2004). It has also been extensively taken into consideration during the last decade for heavy metals adsorption from aqueous solution due to its unique properties, especially abundant amine (NH_2) and hydroxyl (OH) groups. The amine groups in the structure of chitosan are generally considered primary active sites for adsorption of the metal ion. In addition to amine groups, hydroxyl groups may contribute to adsorb metal ion. Chitosan is positively charged at pH < 6.5 owing to the abundant availability of amine groups that are protonated at low pH (Yu et al., 2013). Moreover, chitosan

has been presented to be able to efficiently adsorb metals, like chromium (Schmuhl et al., 2001), copper (Ng et al., 2002), and lead (Ng et al., 2003) from aqueous solutions.

Although the chitosan amine groups are commonly identified as the primary active sites for adsorption of metal ion, hydroxyl groups (especially in the C-3 position) may also contribute to adsorption (Guibal, 2004). Possible adsorption mechanisms for uptaking metal ion using chitosan contain ion electrostatic/exchange attraction and creation of ternary complexes. However, chelation is the most extensively specified binding mechanism to explain the adsorption of transition metal ion by chitosan. Along with chelation, dative covalent bonds with the copper ions can be created using the nitrogen atoms in amine groups of chitosan. Some hydroxyl groups might also be able to release protons and take part in the coordination. Consequently, association rings that involve the oxygen atoms of the hydroxyl groups of chitosan and the nitrogen atoms of non-protonated amine groups are formed (Guibal, 2004).

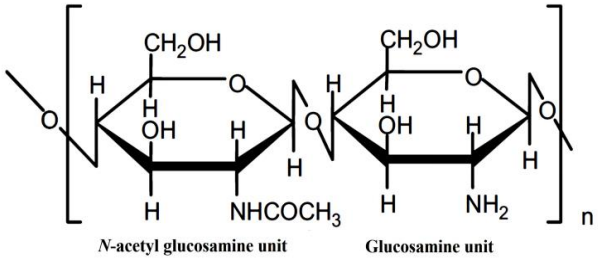

Fig. 1.10. *N*-acetyl glucosamine and glucosamine subunits in the chemical structure of chitosan (Lin and Lin, 2009).

Chitosan derivatives

In spite of the undeniable benefits of utilizing chitosan as biosorbent, it is reasonably solvable in acidic water solutions generally owing to the amino groups protonation ($R\text{-}NH_3^+$) with poor solvability higher than a pH of 6.5 (Guibal, 2004). The solvability of chitosan can be remarkably enhanced by presenting chemical groups due to the fact that it not only includes reactive amines but also primary and secondary hydroxyls as functional groups that are able to endure chemical modifications utilizing relatively mild reaction conditions (Wu et al., 2010).

Chitosan derivatives, like carboxymethylated chitosan (CMC), can be appropriate candidates as biosorbents for metal recovery while they are generally solvable under alkaline, acidic, and physiological conditions (Mansur et al., 2013). The water solvability of CMC relies

on several perspectives including the reagents and temperature that are utilized in the synthesis, chemical substitution degree and the media pH that is considerably affected by all parameters of the carboxymethylation process (Chen and Park, 2003). Carboxymethylation reaction can happen at various chemical functional groups, for example with hydroxyls (*O*-CMC), amines (*N*-CMC) or both (*N*,*O*-CMC) yielding to the creation of an extensive range of reactive functionalized polymers for numerous applications, such as adsorbent in wastewater treatment (Chen and Park, 2003; de Abreu and Campana-Filho, 2009). For instance, the structure of N,O-CMC as a derivative of chitosan containing carboxyl (COOH) groups is shown in **Fig. 1.11**. By introducing carboxyl groups in the backbone of chitosan, its adsorption behavior increases (Pestov and Bratskaya, 2016). Similar to chitosan, chelation by carboxyl, hydroxyl, and amine groups of CMC is the most binding mechanism for adsorption of the metal ion. Ion-imprinted O-CMC beads were utilized to selective adsorption of Ag^{+} from aqueous solution (Zhang et al., 2015).XPS and FT-IR analyses verified that the selective adsorption of Ag^{+} generally occurred on the beads surfaces by chelation via carboxyl, hydroxyl, and amine groups. N,O-CMC was used as a derivative of chitosan to chelate Zn^{2+} and Cu^{2+} ions (Tang and Hon, 2001; Sun and Wang, 2006).

Results showed that N,O-carboxymethyl-chitosan has favor adsorption capacity and it forms a chelate complex with metal ions. O-CMC, entrapped by silica, was used to adsorb Nd^{3+} from aqueous solution (Wang et al., 2013). The prepared adsorbent had a great ability of Nd^{3+}adsorption and could be utilized for Nd^{3+} adsorptive recovery from aqueous solutions.

The advantages of alginate and CMC are that both polymers are green, biodegradable, environmental-friendly, biocompatible, and non-toxic.

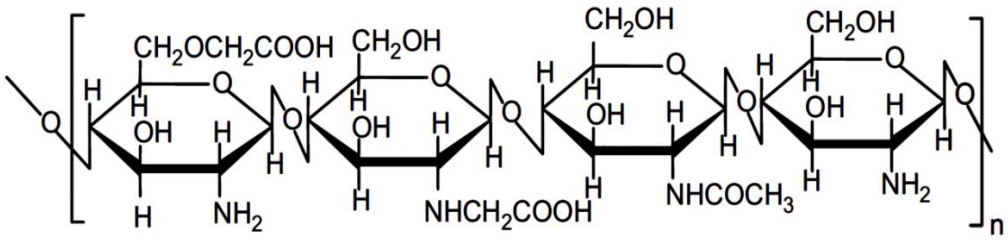

(b)

Fig. 1.11. Structure of N,O-CMC (Lin and Lin, 2009).

1.8.4. Synthetic metal chelating polymers

Metal chelating polymers have attracted attention in heavy metal ions separation from aqueous solutions and environmental remediation. In addition, they presented efficient physical, chemical and mechanical attributes, like high mechanical strength, adsorption capacity, selectivity, porosity, high surface area, and durability. Heavy metal ion selectivity of a chelating resin generally relies on the nature of the chelating group immobilized on the polymeric backbone (Tanco et al., 2002).

These chelating polymers are commonly synthesized by the active chelating groups' incorporation with O, N, and S into a polymeric matrix. This kind of chelating groups may be combined into the repetitive units of the polymer matrix or bound covalently to a polymer backbone as pendant groups by the polymerization of suitable monomers. The strong electrostatic exchange between metal ions and a chelating resin or the electrostatic exchange, obtained using a fast chemical reaction, lead to strong metal ligand bonds. The chelating interaction strength is controlled by the metal ion attributes, such as its electronic configuration, oxidation state, basicity, stereochemistry, and the ligand polarization on the resin (Zalloum and Mubarak, 2008).

Vasanthi and Ravikumar (2007) synthesized new polyesters containing phenylthiourea and azomethine groups in their polymer backbone using interfacial polycondensation procedure. The obtained polyesters were specified by viscosity, TGA, NMR, and IR analysis. Reddy and Reddy (2003) found that polymers containing azomethine group were most efficient in the elimination of metal ions, like Pb(II), Hg(II), Cr(VI) and Cd(II).

Zalloum and Mubarak (2008) synthesized poly(2-hydroxy-4- acryloyloxybenzophenone) (poly(2H4ABP)) and examined its chelation properties towards divalent heavy metal ions Zn(II), Cu(II), Pb(II) and Ni(II) in aqueous solution under different experimental conditions. Different amounts of crosslinked divinylbenzene were added to the poly(2H4ABP) and its adsorption capacity was compared with the uncross-linked one.

1.8.5. Synthetic biodegradable polyamide containing chelating groups

Polyamides (PAs) are generally known as the high-molecular-weight materials that contain amide units. The segments of hydrocarbon between the amide groups may be aliphatic, partially or wholly aromatic. The kind of the used hydrocarbon segment has an influence on the

structural regularity and chain flexibility that is significant for the crystalline phase formation. Nonetheless, their applications are restricted because of their great melting or softening temperatures and their insolvable character in most organic solvents. To fill these lacunas, PA structure modifications, like the flexible linkages introduction, bulky substituents into the polymer backbone or non-symmetrical structure, have been generally used.

PAs that contain heterocyclic units in the primary chain are generally well-known because of possessing superb thermal stabilities. In spite of the fact that PAs also include the identical amide linkage which is discovered in polypeptides, their biodegradation rate is so low compared to those that are introduced to be nondegradable. Moreover, it has been reported that microorganisms and enzymes have been used for the degradation of low molecular weight oligomers. The biodegradation has been greatly improved by introducing substituents, like hydroxyl, benzyl, and methyl (Hearle, 2001; Liou et al., 2002; García et al., 2010). In addition, introducing various functional groups in a polymer backbone which can efficiently bind with metal ions might make them as substitute adsorbents under the classification of chemically changed chelating polymers. Potential benefits of this type of adsorbent could be their chemical resistant and good binding capacity.

Ravikumar et al., (2014) synthesized novel aromatic poly(azomethine amide)s having thiourea groups. The prepared adsorbents were identified to be greatly efficient adsorbents for the elimination of Cd^{2+} and Cu^{2+}metal ions from aqueous solutions. Gomez-Valdemoro et al., (2010) used novel aromatic PAs for the extraction and removal of naturally deleterious cations from water environments. Considering the extraction of cation from aqueous media, the novel aromatic PAs yielded to the extraction of high percentages of Hg (II).

Mansoori and Mohsenzadeh (2015) investigated metal ion uptake from aqueous solutions using new designed PAs. The comparative study of Cu(II) and Co(II) adsorption showed the ability of the new synthesized PAs for metal ions adsorption from aqueous media.

1.8.6. Nanotechnology and nanocomposites

Although the metal oxides' size decreases from micrometer to nanometer levels, the enhanced energy of surface necessarily yields to their negligible stability. Therefore, nanometal oxides are prone to agglomeration owing to Van der Waals forces or further interactions (Pradeep and Anshup, 2009), and the great selectivity and capacity of nanometal oxides would

be considerably reduced or even missed. Moreover, due to the extreme pressure drops (or the difficulty of separation from aqueous systems) and negligible mechanical strength, nanometal oxides are not able to perform in fixed beds or any other flow-through systems. In order to enhance the applicability of nanometal oxides in real wastewater treatment, they can be mixed with other materials to obtain nanocomposites (Pan et al., 2009) that are multiphase solid materials where one of the phases is synthesized in one, two or three dimensions of less than 100 nanometers (nm) using nanotechnology.

1.8.6.1. Polymer/metal oxide nanocomposites

Researchers all around the world have been investigating how to reduce the drawbacks of using nanometal oxides. For this purpose, the metal oxides and polymers combination, utilized as adsorbents, has obtained considerable attention during the last decades. The proper selection of polymer with specific functional groups can even improve the properties of metal oxides.

Metal chelating synthetic polymers and biopolymers are extensively used for the preparation of polymer/metal oxide nanocomposites. Combining these polymers with metal oxides provides considerable advantages in comparison to blank forms. Various polymer/metal oxide nanocomposites have been successfully used to adsorb metal ions, such as polypyrrole/TiO_2 nanocomposite (Nobahar et al., 2014), Cu-chitosan/nano-Al_2O_3 (Zavareh et al., 2015), mixed metal oxide impregnated chitosan beads (Yamani et al., 2012), and Alginate/ titanate nanocomposite (Esmat et al., 2017).

1.8.6.2. Nanotechnology and usage of magnetic separation

Although rapid separation of adsorbents, especially nanocomposites, from large volumes of a solution is difficult, this problem can be solved by magnetic adsorbents due to the fact that they can be simply separated from the solution using an external magnetic field (Li et al., 2013; Ma et al., 2007).

Actually, by employing iron oxide in the structure of composites, two advantages can be obtained as follows: (1) easy separation of composite from aqueous solution and (2) overcoming the drawbacks of iron oxide, such as its easily oxidation in air, corroded in acidic medium, and its inclination to be aggregated with magnetic force. Therefore, combining nanotechnology of

nanocomposite adsorbents and magnetic separation methods could be used as adsorbents for metal separation or recovery.

Although adsorption of heavy metals with nanocomposites has been extensively studied, there have not been extensive investigations on the adsorption of rare earths by advanced nanocomposites. Some magnetic adsorbents have been utilized for adsorption of REEs, such as EDTA-functionalized magnetic nanoparticles (Dupont, et al., 2014a), acid-stable magnetic core-shell nanoparticles (Dupont, et al., 2014b), and magnetic alginate-chitosan gel beads (Wu et al., 2011).

CHAPTER II

SCOPE OF THE WORK

2.1. Scope of the work

The objective of this project is to investigate the separation/recovery of the Tb^{+3}, Dy^{+3}, and Nd^{+3} from aqueous solution by synthesizing novel magnetic nanocomposites using two biopolymers or a biopolymer mixed with a synthetic chelating polymer having different functional groups, and magnetic nanoparticles. For these purposes, calcium alginate (CA), caboxymethyl chitosan (CMC), and a novel synthetic biodegradable poly(pyrimidine-thiophene-amide) (P(PTA)) will be used to produce new nanocomposites that are green, environmental-friendly, and easy separable from aqueous media by an external magnetic field.

Such magnetic polymeric nanocomposites are expected to have some advantages, such as easy separation from aqueous solution, favourable adsorption capacity because of having different functional groups, favourable chemical resistance, and less agglomeration in aqueous solution. The new magnetic nanocomposites will be studied for the separation/recovery of Nd^{+3}, Tb^{+3}, and Dy^{+3} selected among the REEs that are critical metals with a high risk of supply.

2.2. Objectives

2.2.1. Syntheses and characterization of the magnetic nanocomposites

The magnetic nanoparticles ($Ni_{0.2}Zn_{0.2}Fe_{2.6}O_4$) nanocomposites will be synthesized by hydrothermal method to be used for the synthesis of the magnetic

P(PTA), a novel synthetic biodegradable polyamide, will be synthesized by polycondensation of a diamine-phenol in 1,3-dipropyl imidazolium bromide ionic liquid as a solvent to avoid the use of the toxic triphenyl phosphite/N-methylpyrolidone/pyridine/LiCl that is required in the conventional direct polycondensation.

The syntheses of the CA/CMC/$Ni_{0.2}Zn_{0.2}Fe_{2.6}O_4$, CA/P(PTA)/$Ni_{0.2}Zn_{0.2}Fe_{2.6}O_4$, and CMC/P(PTA)/$Ni_{0.2}Zn_{0.2}Fe_{2.6}O_4$ magnetic nanocomposites will be carried out by gelation technique, and the P(PTA)/$Ni_{0.2}Zn_{0.2}Fe_{2.6}O_4$ will be synthesized by hydrothermal technique.

To characterize the materials developed, various techniques will be used, including nuclear magnetic resonance (NMR), X-ray diffraction (XRD), field emission scanning electron

microscopy (FE-SEM), Energy-dispersive X-ray spectroscopy (EDX), thermogravimetric analysis (TGA), vibrating sample magnetometer (VSM), and Fourier transform infrared (FT-IR).

2.2.2. Adsorption studies of Nd^{+3}, Tb^{+3}, Dy^{+3} REEs from synthetic aqueous solutions

In the adsorption studies of Nd^{+3}, Tb^{+3}, and Dy^{+3} by the synthesized nanocomposites, the influence of different parameters such as pH, adsorbent dose, contact time, initial concentration of Nd^{+3}, Tb^{+3}, and Dy^{+3}, ionic strength on the adsorption efficiency will be investigated in single and ternary batch modes.

The adsorption kinetic and isotherm models will be applied for fitting the experimental adsorption data. The effect of temperature on the adsorption process of Nd^{+3}, Tb^{+3}, and Dy^{+3}, will be studied and thermodynamic parameters will be determined. In addition, to model the adsorption of the Nd^{+3}, Tb^{+3}, and Dy^{+3} in the ternary system, RSM-CCD will be applied. To evaluate the reusability of the synthesized nanocomposite, adsorption-desorption cycles will be performed. Finally, Nd^{+3}, Tb^{+3}, and Dy^{+3} adsorption in a fixed-bed column and fitting the experimental data by the models will be studied.

CHAPTER III

METHODOLOGY

3.1. Materials and reagents

Sodium alginate and CMC were respectively bought from China and PanReac AppliChem and Nantong Chem-Base Co. $Dy(NO_3)_3.5H_2O$ was purchased from Alfa Aesar. $Nd(NO_3)_3.6H_2O$, $Tb(NO_3)_3 \cdot 6H_2O$, $Zn(NO_3)_2.6H_2O$, $Fe(NO_3)_3.9H_2O$, $Ni(NO_3)_2 \cdot 6H_2O$, glutaraldehyde, cetyltrimethylammonium bromide (CTAB), 2-amino-4,6-dihydroxypyrimidine, 2-thiophenecarboxaldehyde, terephthalic acid, triphenyl phosphite (TPP), dimethyl sulfoxide (DMSO), and methanol were bought from Sigma-Aldrich. $CaCl_2$, HNO_3 and HCl were bought from PanReac AppliChem. Since the analytical grade of all chemicals was chosen, they were utilized without further purification.

3.2. Synthesis of the P(PTA)

The synthesis of the P(PTA) was performed in two steps. Firstly, a diamine-phenol monomer (TMAPD) was synthesized. Secondly, the polymer was obtained by polycondensation of TMAPD in 1,3-dipropyl imidazolium bromide ionic liquid as a solvent to avoid the use of the toxic triphenyl phosphite/N-methylpyrolidone/pyridine/LiCl that is required in the conventional direct polycondensation. Previously, the 1,3-dipropyl imidazolium bromide ionic liquid (IL) was prepared based on the procedure reported by Vygodskii et al. (2004).

The procedures of the syntheses of the TMAPD and P(PTA) were as follows:

3.2.1. Synthesis of the monomer (5,5'-(thiophene-2-ylmethylene)bis(2-aminopyrimidine-4,6-diol) (TMAPD))

TMAPD was synthesized according to the following procedure: A mixture of 2.54 g (0.02 mol) 2-amino-4,6-dihydroxypyrimidine, 1 mL (0.01 mol) 2-thiophenecarboxaldehyde, and 20 mL DMSO was stirred for 6 h at 110 $^{\circ}$C. While the reaction tested by thin-layer chromatography was completed, the solution temperature was decreased to the room temperature, and the violet powder obtained by pouring the solution into 400 mL of cold DW (-5 $^{\circ}$C) was filtered, rinsed many times using DW and then dried using vacuum oven at 100 $^{\circ}$C. The reaction yield was 92 % (3.20 g), and

the obtained compound did not show a sharp melting point and started to be decomposed at above 300 ˚C. TMAPD structure is shown in **Fig. 3.1**.

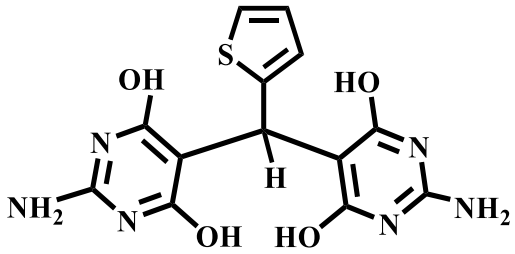

Fig. 3.1. Structure of TMAPD.

3.2.2. Synthesis of the biodegradable P(PTA) by the polycondensation reaction of TMAPD in TPP/IL

The P(PTA) was achieved by polycondensation of TMAPD using TPP-IL as catalyst and solvent by the following procedure: A flask of three-necked round-bottomed with the volume of 50 mL was fitted with a mechanical stirrer, a water cooled condenser, and argon gas and then, a mixture containing 1 mmol TMAPD, 1 mmol terephthalic acid, 0.7 g 1,3-dipropyl imidazolium bromide {[1,3-(pr)$_2$im]Br} as IL, and 1.29 mmol TPP was placed. The solution became sticky as the reaction continued at 110 ˚C for 2.5 h. In the following, the reaction mixture temperature was decreased to the temperature of the room and the precipitation of the obtained P(PTA) was performed using 100 mL of methanol. Then, after the precipitate filtration, the hot water was used for washing it. Afterward, the precipitate was further refined in a Soxhlet apparatus using methanol for 24 h to eliminate the oligomers with low molecular weight. The PA structure is shown in **Fig. 3.2**.

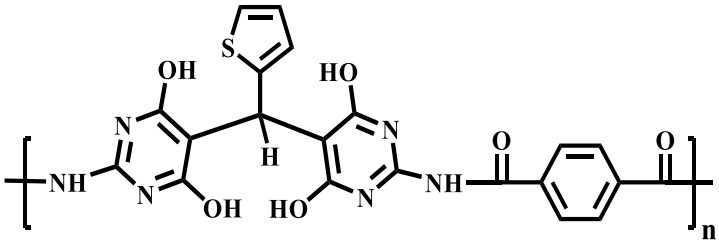

Fig. 3.2. Structure of the P(PTA).

3.3. Synthesis of the magnetic nanoparticles

Hydrothermal method was used to synthesize the $Ni_{0.2}Zn_{0.2}Fe_{2.6}O_4$ magnetic nanoparticles. A mixed solution of 2.6 M Fe^{3+}, 0.2 M Zn^{2+} and 0.2 M Ni^{2+} was made ready in HCl solution and in the following NaOH solution was added into mixed solution under nitrogen gas while the pH value of the mixture was set to 10.5. Thereafter, 0.3 g of CTAB was added to this mixture and it was then located into an autoclave (Teflon-lined stainless steel) for 8 h at 200 °C of an oven to perform hydrothermal treatment. Then, the autoclave temperature was reduced to the temperature of the room naturally, and the precipitate was collected and rinsed many times using deionized water to obtain neutral pH. Consequently, the obtained particles were dried at 50 °C.

3.4. Synthesis of the nanocomposites

Four different magnetic nanocomposites, namely CA/P(PTA)/$Ni_{0.2}Zn_{0.2}Fe_{2.6}O_4$, CMC/P(PTA)/$Ni_{0.2}Zn_{0.2}Fe_{2.6}O_4$, CA/CMC/$Ni_{0.2}Zn_{0.2}Fe_{2.6}O_4$, and P(PTA)/$Ni_{0.2}Zn_{0.2}Fe_{2.6}O_4$, were synthesized according to the procedures described below.

3.4.1. Synthesis of the magnetic CA/P(PTA)/$Ni_{0.2}Zn_{0.2}Fe_{2.6}O_4$ nanocomposite

Sodium alginate powder was dissolved in DW with a concentration of 1.5 % (w/v) to prepare a sodium alginate solution. 0.5 g of P (PTA) and 0.7 g of $Ni_{0.2}Zn_{0.2}Fe_{2.6}O_4$ were completely expanded in the sodium alginate solution with severe stirring for 24 h to achieve a homogeneous solution, A. Afterwards, the gelation process was performed by adding the solution A to a solution of $CaCl_2$ (0.05 M) and 2 % glutaraldehyde. Then, the mixture was stirred for 24 h. In the following, the desired product was accumulated by an external magnetic field and rinsed many times using DW until reaching the solution pH of 7 and then dried at 50 °C. Finally, it was powdered.

3.4.2. Synthesis of the magnetic CMC/P(PTA)/$Ni_{0.2}Zn_{0.2}Fe_{2.6}O_4$ nanocomposite

The magnetic nanocomposite was synthesized by the gelation method. CMC powder was dissolved in deionized water (DW) (3 % w/v) under stirring at 150 rpm for 3 h to prepare CMC solution. Then, 0.5 g of the P(PTA) and 0.7 g of $Ni_{0.2}Zn_{0.2}Fe_{2.6}O_4$ were added to CMC solution and fully dispersed with vigorous stirring within 24 h. The gelation process was then performed

by adding the mixture to a solution of $CaCl_2$ (0.05 M) and 2 % glutaraldehyde. The mixture was stirred for 24 h and the separation of the obtained nanocomposite was performed using an external magnet. It was also washed using deionized water many times to eliminate all impurities (unreacted GA) and reach the solution pH value of 7. Then, the CMC/P(PTA)/$Ni_{0.2}Zn_{0.2}Fe_{2.6}O_4$ bionanocomposite was dried at 50 °C. Ultimately, the obtained product was powdered.

3.4.3. Synthesis of the magnetic CA/CMC/$Ni_{0.2}Zn_{0.2}Fe_{2.6}O_4$ nanocomposite

The procedure of CA/CMC/$Ni_{0.2}Zn_{0.2}Fe_{2.6}O_4$ synthesis is mentioned in the following: 1 g of sodium alginate was dissolved in 80 mL of deionized water at room temperature using a laboratory stirrer. Thereafter, CMC powder (0.5 g) was added into the solution and mixed homogeneously. Then, the $Ni_{0.2}Zn_{0.2}Fe_{2.6}O_4$ (0.7 g) was added to the biopolymers mixture. In order to acquire a homogeneous blend solution, the magnetic and biopolymers particle solution was stirred at the temperature of the room for 24 h. Then, the gelation process was performed by adding the mixture to a solution of calcium chloride 0.05 M and 2 % glutaraldehyde. To separate the resulting bionanocomposite from solution, an external magnetic field was used and then it was washed several times with distilled water for removing any remaining glutaraldehyde and calcium chloride till the pH value of the solution was equal to 7. Finally, the CA/CMC/$Ni_{0.2}Zn_{0.2}Fe_{2.6}O_4$ bionanocomposite was dried at 50 °C. Ultimately, the obtained product was powdered.

3.4.4. Synthesis of the magnetic P(PTA)/$Ni_{0.2}Zn_{0.2}Fe_{2.6}O_4$ nanocomposite

The P(PTA)/$Ni_{0.2}Zn_{0.2}Fe_{2.6}O_4$ nanocomposite was synthesized by hydrothermal method as follows: 1.8 g of the P(PTA) was added to the solution of HCl and N,N-Dimethylformamide containing 0.2 M Ni^{2+}, 2.6 M $Fe^{3+,}$ and 0.2 M Zn^{2+}. Thereafter, NaOH solution was added into the mixed solution under nitrogen gas and the pH value of the mixture was set to 10.5. 0.3 g of CTAB and 4 mL glutaraldehyde were added to the mixture and thereafter it was located into an autoclave (Teflon-lined stainless steel) for 8 h at 200 °C of an oven. The autoclave temperature was then naturally reduced to the temperature of the room, and the product was collected and rinsed with DW several times to reach neutral pH. Consequently, the composite was dried at 50 °C.

3.5. Instrumentation and characterization

KBr pellet was used to record the FT-IR spectra on a PerkinElmer, USA. The GBC MMA tool with CuK_α radiation in the 2θ range of 10–70° was used to record the XRD pattern. FE-SEM (Zeiss Neon-40, Germany) was used for specifying the morphology of the products. The magnetic attributes of the products were investigated at the temperature of the room using a VSM (Daghigh Kavir Corporation, Iran). Moreover, TGA was performed on a Mettler TGA/SDTA 851e/LF/1100 thermobalance. The sample temperature was enhanced from the temperature of the room to 1000 °C (rate=10 °C/min) while nitrogen flow was constant. An Agilent 4100 MP-AES Spectrometer was employed to analyze Nd^{+3}, Dy^{+3}, and Tb^{+3} concentration.

3.6. Adsorption studies of Nd^{+3}, Tb^{+3}, and Dy^{+3}

The adsorption behavior of Nd^{+3}, Tb^{+3}, and Dy^{+3} by the magnetic nanocomposites was investigated in batch system to analyze the effects of different parameters on the process of adsorption and determaine the optimum conditions for maximum adsorption efficiency of the ions. In addition, the adsorption of the ions was studied in the packed-bed column.

3.6.1. Batch adsorption experiments

Batch adsorption tests were done in 125 mL flasks containing 50 mL solutions with the concentrations in the range of 30-300 mg/L that were made ready from the dilution of 1000 mg/L stock solutions of the metal ions at 180 rpm. The values of pH were regulated via adding a suitable amount of 0.1 M sodium hydroxide or nitric acid solutions and monitored by a pH meter. While the contact time was finished, a magnetic field was used to separate the adsorbent and the residual Nd^{+3}, Tb^{+3}, and Dy^{+3} in the solution were then analyzed using an Agilent 4100 MP-AES Spectrometer.

The adsorption efficiency (%) of Nd^{+3}, Tb^{+3}, and Dy^{+3} by the adsorbents was computed using the bellowing equation:

$$\text{Adsorption efficiency (\%)} = \left(\frac{C_0 - C_e}{C_0}\right) \times 100 \qquad (3.1)$$

Here C_i and C_f respectively refer to the initial and final concentration of Nd^{+3}, Tb^{+3}, and Dy^{+3} (mg/L).

The adsorption capacity (q_t (mg/g)) at time t is acquired as bellow:

$$q_t = \frac{(C_i - C_t) \times V}{M} \quad (3.2)$$

Here C_i and C_t (mg/L) respectively show Nd^{+3}, Tb^{+3}, and Dy^{+3} concentrations at primary and given time t. V (L) also refers to the solution volume and M (g) shows the adsorbent mass.

The equilibrium adsorption capacity (q_e (mg/g)) was computed using the equation in the following:

$$q_e = \frac{(C_i - C_e) \times V}{M} \quad (3.3)$$

Here C_e shows the concentration of Nd^{+3}, Tb^{+3}, and Dy^{+3} at equilibrium (mg/L).

3.6.1.1. pH effect

As mentioned in section **1.2**, the solution pH affects the solution chemistry of REEs. Therefore, the adsorption process is always pH-dependent and the capacity of adsorption is changed with the pH of the medium. The impact of pH on adsorption of Nd^{+3}, Tb^{+3}, and Dy^{+3} was explored at various levels of 1.5 to 5.5 by adding a given amount of the adsorbents into the Nd^{+3}, Tb^{+3}, and Dy^{+3} solutions at constant initial concentration and contact time at room temperature.

3.6.1.2. Contact time effect

The contact time is important as the possible rapidness of binding and adsorption processes of the metal ion by adsorbent needs to be identified to reach the optimum time for complete adsorption of the metal ion (Mehdinia et al., 2015). Any change in adsorption capacity by the consideration of contact time can be ascribed to the capacity of adsorbent sites and metal concentration gradient. The effect of contact time was performed at different contact times by adding a given quantity of the adsorbent into the Nd^{+3}, Tb^{+3}, and Dy^{+3} solutions under continuous stirring at constant initial concentration and pH at room temperature.

3.6.1.3. Adsorbent dosage effect

As the extent of adsorption is changed by increasing the amount of adsorbent due to the enhancement in the available number of active sites for adsorption of metal ion, the effect of the

adsorbent dosage on the adsorption of Nd^{+3}, Tb^{+3}, and Dy^{+3} from aqueous solutions was investigated by changing the dosage of the adsorbent at constant initial concentration, time and pH at room temperature.

3.6.1.4. Initial concentration effect

The metal ion mass transfer between the solid phase and aqueous is changed by the driving force that is varied at any initial concentration, resulting in adsorption capacity change. To investigate the influence of initial concentration on the adsorption of the metal ions from aqueous solution, the empirical tests were carried out in the solutions having a particular amount of the adsorbent with different concentrations of Nd^{+3}, Tb^{+3}, and Dy^{+3} ranging from 30 to 300 mg/L at constant pH value and time at room temperature.

3.6.1.5. Ionic strength effect

In general, industrial effluents contain various salts at higher levels that decrease the adsorption efficiency owing to the contest with target metal ions to involve adsorption sites. $NaNO_3$, KNO_3, and NaCl are the most important ones that have been applied to explore the ionic strength influence on the metal ions adsorption. Among all, $NaNO_3$ can be regarded as an efficient and widely-used salt that has been used by many researchers for this goal. Therefore, the ionic strength effect on the adsorption of Nd^{+3}, Tb^{+3}, and Dy^{+3} onto the adsorbents was studied by a series of experiments at various concentrations of $NaNO_3$ solutions.

3.6.1.6. Adsorption kinetic models

The solute uptake rate of a system is generally described using adsorption kinetics that governs the adsorbate uptake residence time at a solid-solution interface along the diffusion process. It is presumed that no mass transfer resistance (both internal and external) is observed along the whole process of the adsorption. Consequently, the adsorption kinetics can be investigated using the residual metal ion concentration in the solution.

Three kinetic models including pseudo-first-order, pseudo-second-order, and intra-particle diffusion were utilized to verify the validity of empirical data regarding Nd^{+3}, Tb^{+3}, and Dy^{+3} adsorption onto the adsorbents as following:

(1) Pseudo-first-order model (Janos et al., 2007):

$$q_t = q_e\,(1 - \exp^{-K_1 t}) \quad (3.4)$$

Where q_e (mg/g) refers to the capacity of adsorption at equilibrium, q_t is the adsorption capacity at time t, t is time, and K_1 (1/min) refers to the pseudo-first-order rate constant. The applicability of the model for adsorption of Nd^{+3}, Tb^{+3}, and Dy^{+3} onto the adsorbent is investigated by plotting q_t vs time 't'.

(2) Pseudo-second-order model (Smaranda et al., 2010):

$$q_t = K_2 q_e^2 t/1 + K_2 q_e t \quad (3.5)$$

The rate constant (K_2 (g/mg min)) and the coefficient of determination are calculated from the plot of q_t vs t.

(3) Intra-particle diffusion (Yousef et al., 2016):

$$q_t = K_i t^{0.5} + C \quad (3.6)$$

Here K_i (1/min) is the pseudo-first-order rate constant while C presents information about the thickness of the boundary layer. A higher value of C is related to the boundary layer diffusion effect. K_i and C are also computed using the plot of q_t vs t.

Error analysis was used to optimize the experimental data with the kinetic models. Chi-square (χ^2) was employed in this paper for comparing each model's validity using the equation in the following:

$$\chi^2 = \sum_{i=1}^{n} \frac{(q_{e,exp} - q_{e,cal})^2}{q_{e,cal}} \quad (3.7)$$

Here $q_{e,exp}$ and $q_{e,cal}$ respectively present the empirical and calculated adsorbent capacities while n represents the number of data points.

3.6.1.7. Adsorption isotherm models

Isotherm models are generally used to represent the relations between the amount of metal adsorbed onto the equivalent adsorption sites and metal concentration in solution while the temperature is constant (Papandreou et al., 2007).

In this work, the two most important isotherm models were applied to specify the maximum adsorption capacity of the adsorbent and its relationship with Nd^{+3}, Tb^{+3}, and Dy^{+3} adsorbed from the solution as follows:

(1) Langmuir model

This model is reliable for monolayer adsorption onto surfaces including the finite number of similar adsorption sites. The following equation is used to present this model (Wang et al., 2005):

$$q_e = \frac{q_m K_L C_e}{(1 + K_L C_e)} \quad (3.8)$$

Here q_e refers to the capacity of adsorption at equilibrium (mg/g) while q_m shows the maximum capacity of adsorption (mg/g). Moreover, C_e and K_L respectively refer to the Nd^{+3}, Tb^{+3}, and Dy^{+3} equilibrium concentrations in solution (mg/L) and Langmuir constant (L/mg). The isotherm constants values (q_m and K_L) are specified using the plot of q_e vs C_e.

(2) Freundlich model

Although it is assumed that the adsorption enthalpy is not dependent on the amount of adsorbed metal based on the Langmuir isotherm, Freundlich model principally presumes that the adsorption is performed on heterogeneous surfaces using a logarithmic reduce in adsorption enthalpy while the occupied sites fraction enhances. This can be computed using the equation in the following (Orha et al., 2007):

$$q_e = K\, C_e^{1/n} \quad (3.9)$$

Here K shows Freundlich constant ($mg^{1-1/n}\ L^{1/n}/g$) while n refers to the Freundlich exponent which is related to the intensity of adsorption (dimensionless). The isotherm constants values (K and n) are respectively specified using the plot of q_e vs C_e. Chi-square (χ^2) was also employed to compare each model's validity.

3.6.1.8. Temperature effect and the evaluation of thermodynamic parameters

The temperature can affect the adsorption efficiency. It is believed that the adsorbate molecules diffusion across the external boundary layer and in the internal pores of the adsorbent particle can be enhanced by enhancing the temperature which can be due to the reduction in the viscosity of the metal solution. Additionally, modifying temperature changes the adsorbent equilibrium capacity for a special adsorbate (Mondal and Kar, 2018). The temperature effect on the adsorption of Nd^{+3}, Tb^{+3}, and Dy^{+3} was determined by adding a certain amount of the adsorbent into the solutions containing REEs at different temperatures while other conditions were considered to be constant.

To realize the nature of Nd^{+3}, Tb^{+3}, and Dy^{+3} adsorption onto the adsorbents, parameters of thermodynamic, like and Gibbs free energy (ΔG°), entropy (ΔS°), and enthalpy (ΔH°) were computed as follows (Gabor et al., 2016):

$$\text{Ln } K_d = \frac{\Delta S^{\circ}}{R} - \frac{\Delta H^{\circ}}{RT} \quad (3.10)$$

$$K_d = \frac{q_e}{C_e} \quad (3.11)$$

$$\Delta G^{\circ} = - RT \text{ Ln } K_d \quad (3.12)$$

Where K_d demonstrates the distribution coefficient while R and T respectively present the gas constant (8.314 J/mol K) and the temperature (K). Moreover, ΔS° and ΔH° values are respectively calculated using the intercept and slope of the curves of Ln K_d versus 1/T.

3.6.1.9. Reusability studies

To investigate the re-usability of the developed adsorbents, the adsorption-elution-washing-adsorption cycle was repeated four times and the adsorption efficiency was determined. The metal ion desorption efficiency upon desorption from the adsorbent was calculated using the initial amounts of adsorbed Nd^{+3}, Tb^{+3}, and Dy^{+3} and the amounts found in the solution at the end of the desorption process, according to Eq. (3.13):

$$\text{Desorption efficiency (\%)} = \frac{M_{des}}{M_{ads}} \times 100 \quad (3.13)$$

Where M_{ads} is the amount of the adsorbed ions and M_{des} is the amount of the desorbed ions.

3.6.2. Column adsorption experiments

Column operations are necessary for practical uses and design of a fixed-bed system in the industry. Column system contains a vertical glass column of a given length and internal diameter. The column was filled with the composite between two layers of glass wool at the top and bottom to prevent the composite loss. The rare earth containing the solution of given concentration and pH was passed through a column in a down flow mode. In order to determine the residual rare earth ion concentration, the treated sample was periodically gathered from the column outlet. While no more metal ion adsorption happened and equilibrium between inlet and outlet rare earth, ion concentration was obtained and the column operation was therefore stopped. In the following,

Agilent 4100 MP-AES Spectrometer was used to analyze the samples obtained from the column for residual rare earth ion concentration.

The breakthrough curve is generally represented by C_t/C_0 as a time function. The amount of metal retained in the column (q_{total}, mg) is represented using the upper area in the breakthrough and can be computed using the equation in the following (Lim and Aris, 2014):

$$q_{total} = \frac{Q}{1000}\int_{t_0}^{t_{total}}(1 - \frac{C_t}{C_0}) \quad (3.14)$$

Where Q shows the flow rate (mL/min) which can be computed by dividing the effluent volume (V_{eff}, mL) by the total time (t_{total}, min):

$$Q = \frac{V_{eff}}{t_{total}} \quad (3.15)$$

The following equation can be also used to compute the total amount of the metal ions that is sent to the column (mg):

$$m_{total} = \frac{C_0 \times Q \times t_{total}}{1000} \quad (3.16)$$

The total adsorption efficiency (%) considering the flow volume can be computed from the ratio of the adsorbed metal mass (m_{total}) to the total amount of metal that is sent to the column (q_{total}) using the following equation:

$$Adsorption\ efficiency\ (\%) = \frac{q_{total}}{m_{total}} \times 100 \quad (3.17)$$

The following equations can be respectively used to compute the capacity of equilibrium adsorption (q_e (mg/g)) and the equilibrium metal concentration (C_e (mg/L)) :

$$q_e = \frac{q_{total}}{m} \quad (3.18)$$

$$C_e = \frac{m_{total} - q_{total}}{V_{eff}} \times 100 \quad (3.19)$$

Where m shows the adsorbent mass (g).

3.6.2.1. Adsorption modeling for breakthrough curve

The favored design of a column adsorption process depends on the proper prediction breakthrough curve for effluent parameters. The mathematical models, such as Thomas and Yan will be utilized to design the continuous fixed-bed column and predict the behavior of the breakthrough curve. The following equation presents the linear form of the Thomas model (Hanbali et al., 2014):

$$\frac{C_t}{C_0} = \frac{1}{1+\exp\left(\frac{K_{Th} q_e x}{Q} - K_{Th} C_0 t\right)} \quad (3.20)$$

Where K_{Th} and q_e respectively refer to the rate constant (mL/min.mg) and the maximum adsorption capacity (mg/g). Moreover, x refers to the mass of adsorbent (g) while C_0 and C_t respectively show the initial metal concentration (mg/L) and the effluent metal concentration (mg/L). t and Q also respectively show the contact time (min) and the flow rate (mL/min). The values of K_{Th} and q_e are achieved from the empirical data fitted by the plot of C_t/C_0 vs t.

Yan model is expressed as follows (Hanbali et al., 2014):

$$\frac{C_t}{C_0} = 1 - \frac{1}{1+\left(\frac{C_0 Q t}{q_e x}\right)^a} \quad (3.21)$$

Where a is a constant coefficient while C_0 and C_t respectively show the initial metal concentration (mg/L) and the effluent metal concentration (mg/L). t also shows the breakthrough time (min). The values of q_e and a can be obtained using the linear plot of C_t/C_0 vs t.

CHAPTER IV

GENERAL RESULTS AND DISCUSSION

4.1. Products characterization

4.1.1. Characterization of the TMAPD and P(PTA)

The successful synthesis of the TMAPD was confirmed by ^{13}C NMR and ^{1}H NMR spectra respectively recorded at 100 MHz and 400 MHz, by DMSO-d6 as a solvent according to the results as following: ^{1}H NMR (DMSO-d_6, δ in ppm) (**Fig. 4.1A**): 5.33 (s, 1H, CH), 6.61 (s, 4H, -NH_2), 6.78-6.80 (d, 1H, Ar-H, *J*= 5.6 Hz), 6.93-6.94 (d, 1H, Ar-H, *J*= 5.6 Hz), 7.42-7.44 (d, 1H, Ar-H, *J*= 5.2 Hz), 10.95-11.28 (m, 4H, broad, hydroxy pyrimidine). ^{13}C NMR (100 MHz, (DMSO-d_6, δ in ppm) (**Fig. 4.1B**): 30.98, 115.41, 128.27, 128.55, 137.86, 140.13, 143.76, 170.77. The result of the ^{1}H NMR of the P(PTA) in **Fig. 4.1C** is as follows: ^{1}H NMR (DMSO-d_6, δ in ppm): 5.37 (s, 1H, CH), 7.25-7.27 (m, 2H, Ar-H), 7.44 (s, 1H, Ar-H), 7.99-8.00 (d, 2H, Ar-H, *J*= 3.2 Hz), 8.06-8.08 (d, 2H, Ar-H, *J*= 5.2 Hz), 11.01 (s, 1H, OH amide), 11.32 (m, 4H, broad, hydroxy pyrimidine) that confirm the P(PTA) was synthesized successfully. Besides, the peaks at 3164-3337 cm^{-1} (O-H and NH_2 stretching), 3054 cm^{-1} (C-H aromatic stretching), 2958 cm^{-1} (stretching of C-H aliphatic), 1683 cm^{-1} (stretching of C=O amide), 1641 cm^{-1} (stretching of C=N), 1593 cm^{-1} (stretching of C=C), 1215 cm^{-1} (C-N), and 1167 cm^{-1} (C-O) in the FT-IR of the P(PTA) also confirmed its successful synthesis **Fig. 4.1D**. The results of the adsorption-desorption isotherm showed that the P(PTA) was nanoporous with a pore size of 22.5244 nm.

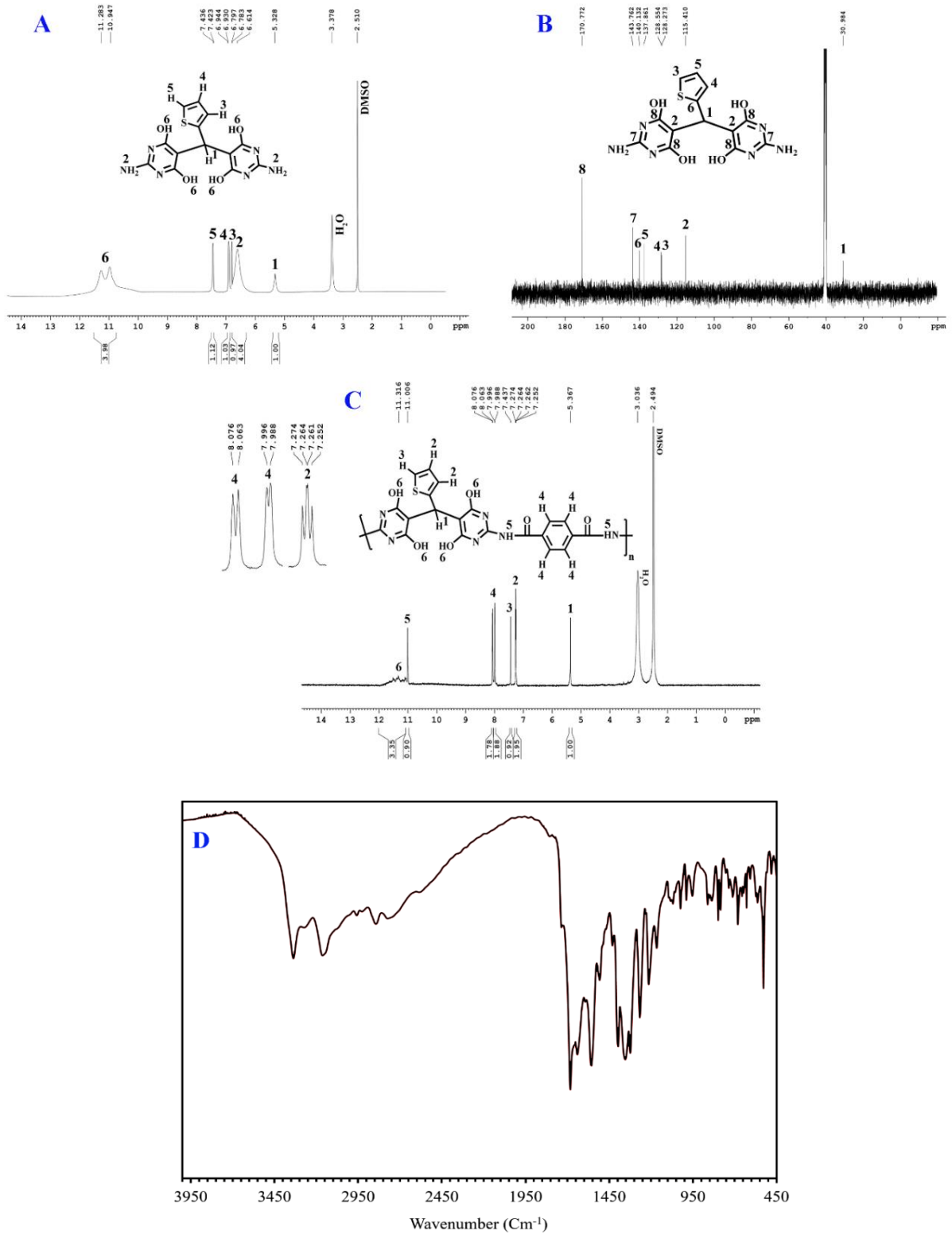

Fig. 4.1. (A) ^{1}H NMR of the TMAPD, (B) ^{13}C NMR of the TMAPD, (C) ^{1}H NMR of the P(PTA), and (D) FT-IR of the P(PTA).

4.1.2. Characterization of the $Ni_{0.2}Zn_{0.2}Fe_{2.6}O_4$

The results of FE-SEM showed that the size of nearly spherical $Ni_{0.2}Zn_{0.2}Fe_{2.6}O_4$ particles was less than 100 nm (**Fig. 4.2A**). In **Fig. 4.2B**, the peaks at 2θ = 18.13°, 30.07°, 35.50°, 37.08°, 43.07°, 53.95°, 56.96°, and 63.89° are in accordance with the standard pattern of nickel zinc ferrite (JCPDS 08-0234) (Ni et al., 2015; Babua and Tatarchuk, 2018, Albuquerque et al., 2000). The average size of the nanoparticles was 27.68 nm according to the Scherrer equation at the Full Width at Half Maximum (FWHM) of the strongest reflection of the XRD pattern of the $Ni_{0.2}Zn_{0.2}Fe_{2.6}O_4$. **Fig. 4.3** indicates that the nanoparticles are gathered and orientated vertically under a magnetic field.

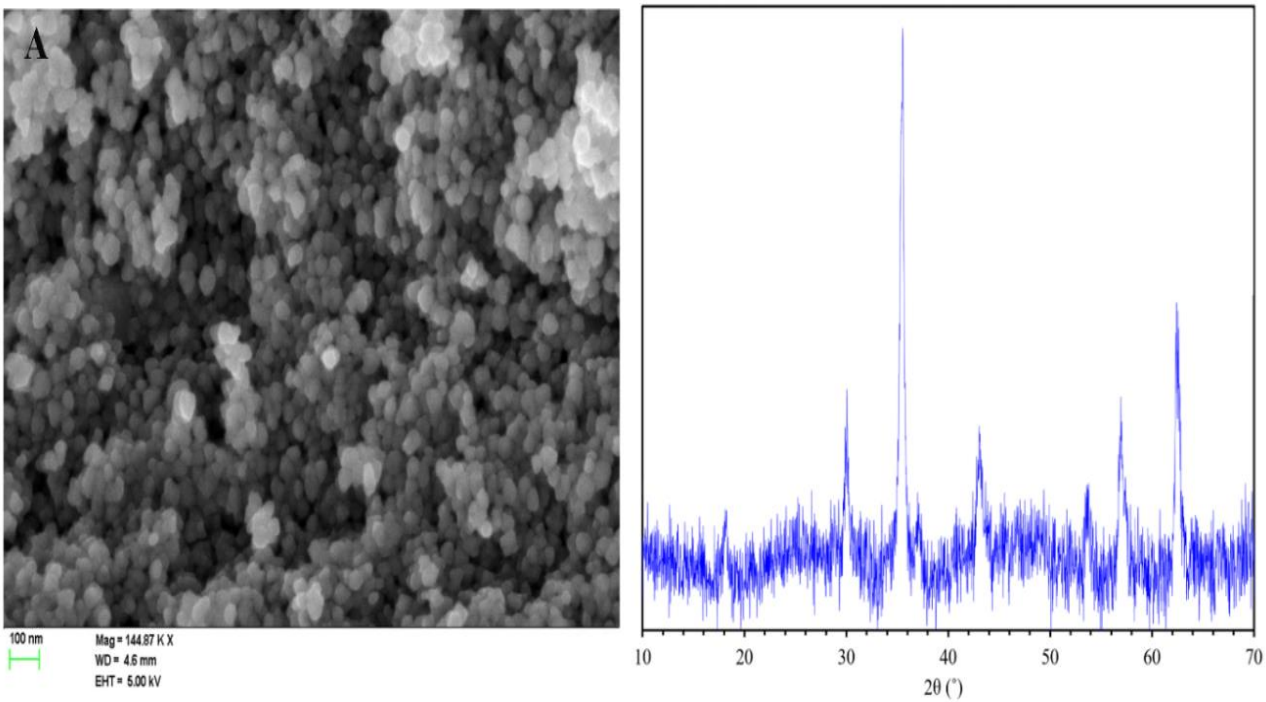

Fig. 4.2. (A) FE-SEM image and (B) XRD pattern of $Ni_{0.2}Zn_{0.2}Fe_{2.6}O_4$ nanopartciles.

Fig. 4.3. Orientation of the $Ni_{0.2}Zn_{0.2}Fe_{2.6}O_4$ under a magnetic field.

4.1.3. Characterization of the nanocomposites

The FE-SEM image of the CA/CMC/$Ni_{0.2}Zn_{0.2}Fe_{2.6}O_4$ in **Fig. 4.4** indicates that the $Ni_{0.2}Zn_{0.2}Fe_{2.6}O_4$ was distributed on the biopolymers' surface or embedded with the biopolymers that confirmed the effective synthesis of the magnetic nanocomposites. Such a result was obtained for the CA/P(PTA)/$Ni_{0.2}Zn_{0.2}Fe_{2.6}O_4$ and CMC/P(PTA)/$Ni_{0.2}Zn_{0.2}Fe_{2.6}O_4$. The FE-SEM image of the P(PTA)/$Ni_{0.2}Zn_{0.2}Fe_{2.6}O_4$ in **Fig. 4.5** shows that the $Ni_{0.2}Zn_{0.2}Fe_{2.6}O_4$ particles are also synthesized nearly spherically in the presence of the P(PTA) in the solution with the average particle size of 31.62 nm. Similar peaks were obtained in the XRD pattern of the P(PTA)/$Ni_{0.2}Zn_{0.2}Fe_{2.6}O_4$ in comparison to the XRD pattern of the $Ni_{0.2}Zn_{0.2}Fe_{2.6}O_4$. FT-IR results obtained for the nanocomposites confirmed their successful synthesis in comparison to the FT-IR results of the CA, CMC, $Ni_{0.2}Zn_{0.2}Fe_{2.6}O_4$, and P(PTA).

The EDX spectra of the biopolymer nanocomposites showed the successful crosslinking reaction of sodium alginate with calcium as the peak of Na^+ was not seen in the spectra, and the expected elements were seen in the EDX of the biopolymer nanocomposites. In the case of the P(PTA)/$Ni_{0.2}Zn_{0.2}Fe_{2.6}O_4$, the EDX spectrum showed N, C, O, Ni, Zn, Fe and S peaks that confirmed the creation of the P(PTA)/$Ni_{0.2}Zn_{0.2}Fe_{2.6}O_4$.

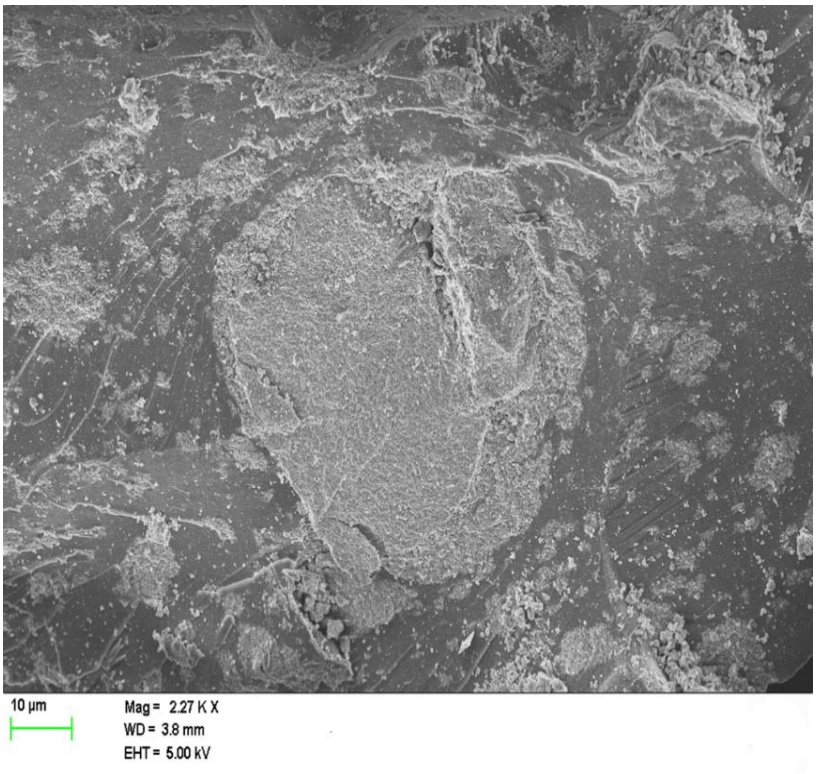

Fig. 4.4. FE-SEM image of the CA/CMC/ $Ni_{0.2}Zn_{0.2}Fe_{2.6}O_4$.

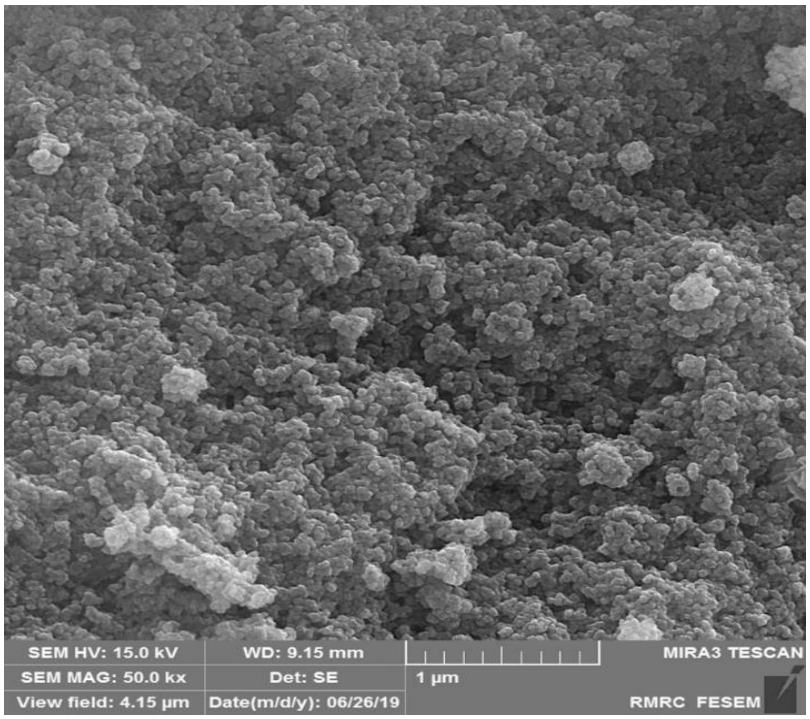

Fig. 4.5. FE-SEM image of the P(PTA)/$Ni_{0.2}Zn_{0.2}Fe_{2.6}O_4$.

According to the obtained results of VSM, the magnetic nanoparticles showed superparamagnetic behavior while the favorable magnetic saturation value was about 45.78 emu/g. Since the magnetic nanoparticles were combined with other materials, lower magnetic saturation (14.14 emu/g for the CA/CMC/$Ni_{0.2}Zn_{0.2}Fe_{2.6}O_4$, 15.28 emu/g for the CA/P(PTA)/$Ni_{0.2}Zn_{0.2}Fe_{2.6}O_4$, and 14.88 emu/g for the CMC/P(PTA)/$Ni_{0.2}Zn_{0.2}Fe_{2.6}O_4$) was obtained for all synthesized composites as expected. The obtained decrease did not affect the separation of the nanocomposites and they were easily separated by a magnetic field as shown in **Fig. 4.6**. In the case of the P(PTA)/$Ni_{0.2}Zn_{0.2}Fe_{2.6}O_4$, the magnetic saturation value (50.49 emu/g) was close to that obtained for the magnetic nanoparticles, indicating that the magnetic saturation was not affected under the condition of the solution and in the presence of the dissolved P(PTA) in the solution. Thus, the P(PTA)/$Ni_{0.2}Zn_{0.2}Fe_{2.6}O_4$ was the strongest magnetic adsorbent in comparison with others.

Fig. 4.6. Photo of magnetic separation.

According to the TGA analysis obtained for the P(PTA), favorable thermal stability as 17.53% weight loss was seen by increasing temperature from RT to 330 ˚C. The weight loss of the P(PTA) was 61.69 % by increasing temperature up to ~ 600 ˚C. Enhancing the temperature up to 1000 ˚C caused the complete decomposition of the P(PTA). By combining the P(PTA) with

the $Ni_{0.2}Zn_{0.2}Fe_{2.6}O_4$, CA, and CMC, degradation temperature was shifted to a higher temperature. The thermal stability of the synthesized products in the range of room temperature to 1000 ˚C was in the order of P(PTA)/$Ni_{0.2}Zn_{0.2}Fe_{2.6}O_4$ (43.21 % weight loss) > CA/P(PTA)/$Ni_{0.2}Zn_{0.2}Fe_{2.6}O_4$ (64.1 % weight loss) > CA/CMC/$Ni_{0.2}Zn_{0.2}Fe_{2.6}O_4$ (66.8 % weight loss) > CMC/P(PTA)/$Ni_{0.2}Zn_{0.2}Fe_{2.6}O_4$ (70.65 % weight loss).

4.2. Adsorption of Nd^{+3}, Tb^{+3}, and Dy^{+3} from aqueous solution

The adsorption of Nd^{+3}, Tb^{+3}, and Dy^{+3} from aqueous solution was studied in single, ternary, and column systems.

4.2.1. Investigation of general ability of the P(PTA) for Nd^{+3}, Tb^{+3}, and Dy^{+3} adsorption

The P(PTA) was used for the sorption of rare earth metals in primary tests. For this purpose, 0.1 g of the P(PTA) was added into 50 mL solution having 30 mg/L of Dy^{3+} at pH of 5.3, and in the following the solution was stirred for 14 h. The adsorption efficiency was approximately 100 %. Similar result of adsorption efficiency was achieved by adding 0.1 g of the P(PTA) into the multi-metal solution containing 10 mg/L of Dy^{+}, Tb^{+3}, and Nd^{+3}. The results confirmed the adsorption ability of the P(PTA) for adsorption of Nd^{+3}, Tb^{+3}, and Dy^{+3}. Moreover, the presence of pyrimidine and thiophene rings, hydroxyl groups and amide linkages in the backbones of the P(PTA) could act as hosts for the formation and adsorption of the complex with the metal ions. Mechanism of metal adsorption by the P(PTA) is offered (depicted) in **Fig. 4.7**.

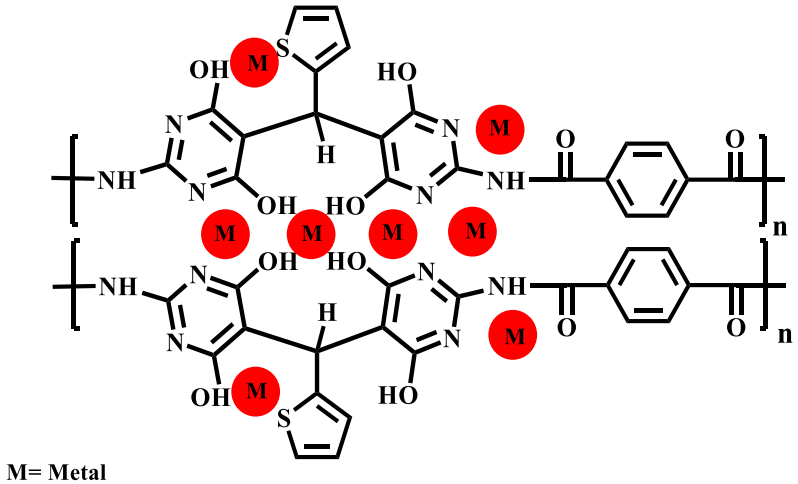

Fig. 4.7. Mechanism offered for the separation of metal ions.

4.2.2. Nd^{+3}, Tb^{+3}, and Dy^{+3} adsorption in the single system

The adsorption of Nd^{+3}, Tb^{+3}, and Dy^{+3} in the single system was studied as a function of different parameters including pH, contact time, adsorbent dosage, initial ion concentration, ionic strength, and temperature.

4.2.2.1. pH effect on Nd^{+3}, Tb^{+3}, and Dy^{+3} adsorption

pH is generally known as an essential controlling parameter along the adsorption process. In this regard, hydrogen ion concentration role was studied for the adsorption of Nd^{+3}, Tb^{+3}, and Dy^{+3} at various pH, particularly in the range of 1.5 to 5.5 (1.5, 2.5, 3.5, 4.5, and 5.5) with various prepared materials at room temperature of 25 $^{\circ}$C by batch mode adsorption studies at 30 mg/L of the ions with 0.03 g of the CA/CMC/$Ni_{0.2}Zn_{0.2}Fe_{2.6}O_4$, CMC/P(PTA)/$Ni_{0.2}Zn_{0.2}Fe_{2.6}O_4$, CMC/P(PTA)/$Ni_{0.2}Zn_{0.2}Fe_{2.6}O_4$ nanocomposites for 20 min. The experiments were not studied at a pH higher than 5.5 because the formation of the ions hydroxides may have taken place (Aghayan et al., 2013). The observed experimental results of the impact of pH on the ions adsorption from the aqueous solution using the adsorbents presented that the adsorption efficiency of the ions increased from 0 % to a maximum value for all the adsorbents, for a variation of pH from pH = 1.5 to pH = 5.5 within 20 min of adsorption study. Based on the obtained results, it was clear that there was practically no adsorption at pH = 1.5 due to the highly acidic solution, preventing the ions from further adsorption onto the surface of the adsorbents. The maximum adsorption efficiency was achieved at pH = 5.5 for all the adsorbents with initial ions concentration of 30 mg/L, which indicated their maximum adsorption efficiency at a higher pH value. However, while the pH value is low, electrostatic repulsion will be high along with the metal ions uptake which can be because of the high positive charge density and the protons on the surface active sites. Moreover, there is a competition between the metal ions and H^+ ions for occupying the same site which results in lower efficiency of elimination. On the other hand, by increasing the pH value, electrostatic repulsion will be reduced which can be due to the positive charge density reduction on the adsorption sites which results in an increase in the metal ions adsorption. Several earlier studies had also supported the mentioned fact about the influence of pH on adsorption (Koochaki-Mohammadpour et al., 2014, Akkaya, 2014). Therefore, the optimum value of the solution pH was 5.5. In the case of the

P(PTA)/$Ni_{0.2}Zn_{0.2}Fe_{2.6}O_4$ the influence of pH was not conducted and the solution pH for adsorption studies was 5.5.

4.2.2.2. Contact time effect on Nd^{+3}, Tb^{+3}, and Dy^{+3} adsorption

Nd^{+3}, Tb^{+3}, and Dy^{+3} adsorption efficiency also depends on their contact time with the adsorbents. The ions adsorption at various contact times was investigated for initial ions concentration of 30 mg/L at pH = 5.5 keeping all other parameters constant. Batch adsorption tests were carried out at 25 ˚C by changing the contact time from 2.5 to 70 minutes for the CA/CMC/$Ni_{0.2}Zn_{0.2}Fe_{2.6}O_4$ and CA/P(PTA)/$Ni_{0.2}Zn_{0.2}Fe_{2.6}O_4$, 2.5 to 120 min for the CMC/P(PTA)/$Ni_{0.2}Zn_{0.2}Fe_{2.6}O_4$, and 2.5 to 150 min for the P(PTA)/$Ni_{0.2}Zn_{0.2}Fe_{2.6}O_4$.

Based on the obtained results, more than 65% of adsorption efficiency took place within the first 5 min for the CA/CMC/$Ni_{0.2}Zn_{0.2}Fe_{2.6}O_4$ and CA/P(PTA)/$Ni_{0.2}Zn_{0.2}Fe_{2.6}O_4$ and equilibriums were respectively established after 40 min and 50 min. In the case of the CMC/P(PTA)/$Ni_{0.2}Zn_{0.2}Fe_{2.6}O_4$, the adsorption efficiency of more than 65% occurred at the contact time of 90 min. Similar result of adsorption efficiency was obtained at 50 mg/L of the ions with 0.13 g of the P(PTA)/$Ni_{0.2}Zn_{0.2}Fe_{2.6}O_4$ while a contact time of 30 min was applied. The value of adsorption efficiency was found to increase to more than 90% for the CA/CMC/$Ni_{0.2}Zn_{0.2}Fe_{2.6}O_4$ and CA/P(PTA)/$Ni_{0.2}Zn_{0.2}Fe_{2.6}O_4$ and 70% for the CMC/P(PTA)/$Ni_{0.2}Zn_{0.2}Fe_{2.6}O_4$ by enhancing the contact time to the equilibrium time.

For the P(PTA)/$Ni_{0.2}Zn_{0.2}Fe_{2.6}O_4$, the adsorption efficiency was found to increase to more than 80% with a contact time of 130 min as equilibrium for initial ions concentration of 50 mg/L. The change in the adsorption efficiency rate might refer to the fact that all adsorbent sites are initially empty and the solute concentration gradient is high. Therefore, the adsorption rate is high too. Thereafter, the ions uptake rate by adsorbent decreases owing to the reduction in adsorption sites besides the ions concentration. By passing the time, the number of sites on the adsorbent packed with the ions enhances too (Farghali et al., 2013). Notably, the adsorption rate is equal to the desorption rate at equilibrium while all the sites are packed. Therefore, it is observed that there is not any enhancement in adsorption efficiency by increasing the contact time after equilibrium. Decreased rate of removal, especially towards the end of experiments, indicates the feasible monolayer creation of the ions on the outer surface of the adsorbents. In the current study, steady growth in adsorption efficiency was seen up to a contact time of 40 min for the CA/CMC/$Ni_{0.2}Zn_{0.2}Fe_{2.6}O_4$, 50 min for the CA/P(PTA)/$Ni_{0.2}Zn_{0.2}Fe_{2.6}O_4$, 90 min for the

CMC/P(PTA)/$Ni_{0.2}Zn_{0.2}Fe_{2.6}O_4$, and 130 min for the P(PTA)/$Ni_{0.2}Zn_{0.2}Fe_{2.6}O_4$, while there was not any further enhancement in adsorption effectiveness with an enhancement in time.

4.2.2.3. Adsorbent dosage effect on Nd^{+3}, Tb^{+3}, and Dy^{+3} adsorption

Batch adsorption investigations were conducted at 25 °C at pH = 5.5 and the optimum time for each adsorbent. The influence of different adsorbent dosage on the adsorption efficiency of the ions from aqueous solution with adsorbents utilized in this work presented that the ions adsorption increased by enhancing the adsorbent dosage for all the adsorbents. It was seen that the adsorption efficiency of ions respectively increased from 53.08 to 97.75 %, 51.4 to 96.83 %, and 59.04 to 97.88 % for Nd^{+3}, Tb^{+3}, and Dy^{+3}, by using 0.01 to 0.04 g of the CA/CMC/$Ni_{0.2}Zn_{0.2}Fe_{2.6}O_4$ and initial ions concentration of 30 mg/L. Under the same conditions, the results were 51.14 to 96.73 %, 49.33 to 94.82 %, and 50.66 to 97.58 % for Nd^{+3}, Tb^{+3}, and Dy^{+3}, respectively, by using the CA/P(PTA)/$Ni_{0.2}Zn_{0.2}Fe_{2.6}O_4$. The adsorption efficiency increased from 26.63 to 88.24 %, 23.13 to 82.03 %, and 28.96 to 91.27 % for Nd^{+3}, Tb^{+3}, and Dy^{+3} respectively, using the CMC/P(PTA)/$Ni_{0.2}Zn_{0.2}Fe_{2.6}O_4$ in the range of 0.01 to 0.04 g that was lower than those of the CA/CMC/$Ni_{0.2}Zn_{0.2}Fe_{2.6}O_4$ and CA/P(PTA)/$Ni_{0.2}Zn_{0.2}Fe_{2.6}O_4$. By increasing the adsorbent dosage of the CMC/P(PTA)/$Ni_{0.2}Zn_{0.2}Fe_{2.6}O_4$ to 0.06 g, 98.15, 97.6, and 99.42 % adsorption efficiencies were respectively obtained for Nd^{+3}, Tb^{+3}, and Dy^{+3}. As for the P(PTA)/$Ni_{0.2}Zn_{0.2}Fe_{2.6}O_4$, the obtained results were 26.34 to 95.67 %, 31.21 to 97.48 %, and 32.08 to 98.41 % for Nd^{+3}, Tb^{+3}, and Dy^{+3}, respectively at 50 mg/L of the ions in the dosage range of 0.05 to 0.15 g. Such results were expected for a constant initial concentration of the ions because an increase in adsorbent dosage provides larger adsorption sites or surface area which results in a higher adsorption efficiency (Das and Das, 2013). However, it was seen that after upper value of the dosage for each adsorbent, there was not any considerable modification in the adsorption efficiency of the ions that might be owing to the active sites overlapping at a higher dosage. Therefore, there was not any considerable enhancement in the efficient surface area because of the adsorbent particles conglomeration (Pathania et al., 2017).

4.2.2.4. Initial concentration effect on Nd^{3+}, Tb^{+3}, and Dy^{+3} adsorption

The initial metal ions concentration plays a significant role in adsorption due to the fact that only a fixed amount of metal ions can be adsorbed by the given mass of adsorbent material. The initial concentration of the ions solution was ranging from 30 to 300 mg/L (except as for the

adsoption of the ions by the P(PTA)/$Ni_{0.2}Zn_{0.2}Fe_{2.6}O_4$ that the lower initial ions concentration value was 50 mg/L), and batch mode tests were carried out using the optimum dosage of the adsorbents at room temperature of 25 ˚C to explore the impact of initial concentration of the ions on their adsorption by the magnetic adsorbents. The experimental data presented that the ions adsorption efficiency reduced by enhancing the initial concentration. Adsorption efficiencies of the CA/CMC/$Ni_{0.2}Zn_{0.2}Fe_{2.6}O_4$ for Nd^{+3}, Tb^{+3}, and Dy^{+3} respectively decreased from 97.3 to 19.4 %, 96.83 to 27.53 %, and 97.85 to 31.51 % which indicated that increasing initial concentration had more effect on the adsorption of in comparison to Tb^{+3} and Dy^{+3}. The obtained values of the CA/P(PTA)/$Ni_{0.2}Zn_{0.2}Fe_{2.6}O_4$ were approximately similar to those of the CA/CMC/$Ni_{0.2}Zn_{0.2}Fe_{2.6}O_4$. At the optimum dosage of the CMC/P(PTA)/$Ni_{0.2}Zn_{0.2}Fe_{2.6}O_4$ (0.06 g), the obtained adsorption efficiencies at the initial concentration of 300 mg/L were 16.74, 21.45, and 21.76 % for Nd^{+3}, Tb^{+3}, and Dy^{+3}, respectively, that were lower than those of CA/CMC/$Ni_{0.2}Zn_{0.2}Fe_{2.6}O_4$ and CA/P(PTA)/$Ni_{0.2}Zn_{0.2}Fe_{2.6}O_4$ in the investigated range of initial concentration. The reason for the observed decrease by increasing initial concentration is due to the fact that the amount of ions that can be adsorbed for a given mass of adsorbent material is fixed. Therefore, the higher concentration of the ions leads to a smaller quantity of adsorption efficiency. While the concentration is low, there are large vacant active sites on the surface of the adsorbents and by increasing the initial ions concentration, the number of active sites that are required for adsorption is decreased. Nonetheless, the real amount of ions adsorbed per unit mass of adsorbent enhanced by increasing the ions concentration. Consequently, it can be due to the high driving force to overcome the mass transfer stability between the aqueous and solid phase at a high initial ions concentration. Actually, as the initial concentration of metal ions is increased, the interaction between adsorbent and adsorbate also enhances (Giese and Jordão, 2019). However, the adsorption efficiency of the ions is maximum at lower initial concentrations. Therefore, the process of the adsorption greatly relies on the initial concentration of the ions.

4.2.2.5. Adsorption kinetics

From fitting the data of kinetic of the adsorption of Nd^{+3}, Tb^{+3}, and Dy^{+3} by the adsorbents (**Tables 4.1-4.4**), it was found that the R^2 values of the ions for the pseudo-first-order model < 0.91 for the CA/CMC/$Ni_{0.2}Zn_{0.2}Fe_{2.6}O_4$, < 0.90 for the CA/P(PTA)/$Ni_{0.2}Zn_{0.2}Fe_{2.6}O_4$, < 0.89 for the CMC/P(PTA)/$Ni_{0.2}Zn_{0.2}Fe_{2.6}O_4$, and < 0.91 for the P(PTA)/$Ni_{0.2}Zn_{0.2}Fe_{2.6}O_4$ were

lower than those acquired by pseudo-second-order model (> 0.98 for the CA/CMC/$Ni_{0.2}Zn_{0.2}Fe_{2.6}O_4$ and CA/P(PTA)/$Ni_{0.2}Zn_{0.2}Fe_{2.6}O_4$, > 0.95 for the CMC/P(PTA)/$Ni_{0.2}Zn_{0.2}Fe_{2.6}O_4$, and > 0.97 for the P(PTA)/$Ni_{0.2}Zn_{0.2}Fe_{2.6}O_4$, implying that the adsorption of the ions was not described with pseudo–first–order model. Based on the obtained results, the calculated values of adsorption capacity ($q_{e,cal}$) of the metal ions onto the adsorbents at equilibrium by the pseudo–second–order were in good compromise with the experimental values ($q_{e,exp}$) of adsorption capacities of ions. The results were also confirmed by lower values of χ^2 obtained by pseudo–second–order fitting in comparison with those of the pseudo-first-order model. The stability of the empirical data with the pseudo–second–order kinetic model indicated that the ions adsorption onto the adsorbents was supervised by chemical adsorption (chemisorption). The pseudo–first–order and pseudo–second–order equations were not able to distinguish the diffusion method. The data were then fitted by the intra-particle diffusion technique. Based on the model, the curve of q_t vs. $t^{0.5}$ can be linear if intra-particle diffusion is related to the adsorption. If the plots go through the origin, then intra-particle diffusion is the rate-determining step (Iftekhar et al., 2018).

The data fitting by the intra-particle diffusion model showed a multi-steps adsorption process for each metal by the CA/CMC/$Ni_{0.2}Zn_{0.2}Fe_{2.6}O_4$, CA/P(PTA)/$Ni_{0.2}Zn_{0.2}Fe_{2.6}O_4$, and P(PTA)/$Ni_{0.2}Zn_{0.2}Fe_{2.6}O_4$. The first sharper portion was attributed to the diffusion of the ions through the solution to the external surface of the adsorbents (external diffusion). The second linear portion explained the gradual adsorption stage where the intra-particle diffusion is rate-limiting. Finally, the third linear portion denoted the establishment of the equilibrium step where the intra-particle diffusion started to decelerate owing to the remarkably low concentration of the ions in the solution (intraparticle diffusion) (Song et al., 2013). The curves did not go through the origin (intercept > 0) that might be indicative of some degree of effect and control by boundary layer. This might be representative of some degree of boundary layer control. Moreover, it also intimates that the intra-particle diffusion does not only contribute to the rate-determining step but also the adsorption rate may be simultaneously controlled by other processes (Das et al., 2017). In the case of the CMC/P(PTA)/$Ni_{0.2}Zn_{0.2}Fe_{2.6}O_4$, the R^2 values of 0.9737, 0.9782, and 0.9676 along with the χ^2 values of 1.63, 1.31, and 2.03 respectively obtained by fitting with the intra-particle diffusion for Nd^{+3}, Tb^{+3}, and Dy^{+3}, showed that this model can also explain the ions adsorption.

Table 4.1. Kinetic constants for adsorption of the ions by the CA/CMC/$Ni_{0.2}Zn_{0.2}Fe_{2.6}O_4$.

Model	Parameter	Nd^{+3}	Tb^{+3}	Dy^{+3}
Pseudo-first-order	K_1 (1/min)	0.279	0.271	0.269
	q_e (mg/g)	45.91	46.05	46.54
	R^2	0.8506	0.8712	0.9099
	χ^2	7.91	7.29	5.34
Pseudo-second-order	K_2 (g/mg min)	0.00967	0.00916	0.00899
	q_e (mg/g)	48.95	49.21	49.72
	h (mg/g min)	23.17	22.18	22.22
	R^2	0.9831	0.9893	0.9956
	χ^2	0.89	0.60	0.26
Intra-particle diffusion	K_i (1/min)	11.33	11.73	11.76
	R^2	0.9063	0.9091	0.8723
	χ^2	4.96	5.14	7.57

Table 4.2. Kinetic constants for adsorption of the ions by the CA/P(PTA)/$Ni_{0.2}Zn_{0.2}Fe_{2.6}O_4$.

Model	Parameter	Nd^{+3}	Tb^{+3}	Dy^{+3}
Pseudo-first-order	K_1 (1/min)	0.343	0.314	0.329
	q_e (mg/g)	45.38	44.69	45.37
	R^2	0.8249	0.8927	0.8794
	χ^2	6.67	4.58	5.03
Pseudo-second-order	K_2 (g/mg min)	0.01274	0.01158	0.01195
	q_e (mg/g)	48.05	47.43	48.13
	h (mg/g min)	29.41	26.05	27.68
	R^2	0.9878	0.9974	0.9964
	χ^2	0.46	0.11	0.15
Intra-particle diffusion	K_i (1/min)	9.58	9.98	9.88
	R^2	0.8999	0.8708	0.8745
	χ^2	3.81	5.52	5.24

Table 4.3. Kinetic constants for adsorption of the ions by the CMC/P(PTA)/$Ni_{0.2}Zn_{0.2}Fe_{2.6}O_4$.

Model	Parameter	Nd^{+3}	Tb^{+3}	Dy^{+3}
Pseudo-first-order	K_1 (1/min)	0.116	0.132	0.126
	q_e (mg/g)	31.15	32.29	32.71
	R^2	0.8831	0.8538	0.8803
	χ^2	7.24	8.77	7.52
Pseudo-second-order	K_2 (g/mg min)	0.0043	0.0049	0.0047
	q_e (mg/g)	34.85	35.80	36.27
	h (mg/g min)	5.22	6.28	6.18
	R^2	0.9629	0.9564	0.9686
	χ^2	2.3	2.61	1.97
Intra-particle diffusion	K_i (1/min)	11.16	11.02	11.20
	R^2	0.9737	0.9782	0.9676
	χ^2	1.63	1.31	2.03

Table 4.4. Kinetic constants for adsorption of the ions by the P(PTA)/$Ni_{0.2}Zn_{0.2}Fe_{2.6}O_4$.

Model	Parameter	Nd^{+3}	Tb^{+3}	Dy^{+3}
Pseudo-first-order	K (min^{-1})	0.121	0.1273	0.1349
	q_e ($mg.g^{-1}$)	14.69	15.13	15.31
	R^2	0.8954	0.9011	0.9023
	χ^2	1.30	1.24	1.18
Pseudo-second-order	k_2 ($g.mg^{-1}.min^{-1}$)	0.0100	0.0105	0.0112
	q_e ($mg.g^{-1}$)	16.15	16.55	16.68
	h ($mg.g^{-1}.min^{-1}$)	2.61	2.87	3.12
	R^2	0.9771	0.9787	0.9800
	χ^2	0.28	0.26	0.24
Intra-particle diffusion	K_{id} (min^{-1})	4.55	4.53	4.44
	R^2	0.9496	0.9376	0.9307
	χ^2	0.63	0.78	0.84

4.2.2.6. Adsorption isotherms

Adsorption capacity is generally considered as one of the most important attributes of an adsorbent with regard to a specific ion or molecule. The adsorption effectiveness of the magnetic adsorbents and their affinity towards the ions were determined by fitting the experimental data with equilibrium adsorption isotherms. The experimental adsorption data of the ions on the magnetic adsorbents were fitted with the nonlinear form of Langmuir and Freundlich isotherm models, and the results are presented in **Tables 4.5-4.8**. The results for the CA/CMC/$Ni_{0.2}Zn_{0.2}Fe_{2.6}O_4$ showed that the R^2 values of Freundlich isotherm were more than

0.975 for Tb^{+3} and Dy^{+3} while the values of R^2 by fitting with Langmuir were 0.7163 and 0.8212 for Tb^{+3} and Dy^{+3}, respectively, that were lower than those obtained by Freundlich model. The results indicated the multi-layer adsorption of Tb^{+3} and Dy^{+3}, and occurrence of the adsorption of the ions on a non-uniform surface. In contrast, higher value of R^2 (0.9703) was obtained by fitting the experimental data of Nd^{+3} by Langmuir in comparison with Freundlich with the value of 0.8364, revealing that adsorption was monolayer adsorption on the homogeneous surfaces. The results were confirmed by χ^2 values. Similar results of fitting were obtained by the CA/P(PTA)/$Ni_{0.2}Zn_{0.2}Fe_{2.6}O_4$, CMC/P(PTA)/$Ni_{0.2}Zn_{0.2}Fe_{2.6}O_4$ and P(PTA)/$Ni_{0.2}Zn_{0.2}Fe_{2.6}O_4$ for the ions except for adsorption of Nd^{+3} by the CMC/P(PTA)/$Ni_{0.2}Zn_{0.2}Fe_{2.6}O_4$ that showed the value of R^2 by Freundlich model (0.9709) was greater than that of Langmuir model (0.5679). The adsorption capacities estimated by Freundlich model for Tb^{+3} and Dy^{+3} by the CA/CMC/$Ni_{0.2}Zn_{0.2}Fe_{2.6}O_4$ were about 101.61 and 114.74 mg/g, while the calculated value from Langmuir model for Nd^{+3} was 73.37 mg/g. The calculated values of adsorption capacity for the ions obtained by the CA/P(PTA)/$Ni_{0.2}Zn_{0.2}Fe_{2.6}O_4$ were close to those of the CA/CMC/$Ni_{0.2}Zn_{0.2}Fe_{2.6}O_4$. As for the CMC/P(PTA)/$Ni_{0.2}Zn_{0.2}Fe_{2.6}O_4$, the obtained results from Freundlich model with the values of 39.82, 50.32, and 48.23 mg/g respectively for Nd^{+3}, Tb^{+3}, and Dy^{+3} were lower than those of the CA/P(PTA)/$Ni_{0.2}Zn_{0.2}Fe_{2.6}O_4$ and CA/CMC/$Ni_{0.2}Zn_{0.2}Fe_{2.6}O_4$. The P(PTA)/$Ni_{0.2}Zn_{0.2}Fe_{2.6}O_4$ presented the lowest values of adsorption capacity (18.68, 24.57, and 25.89 mg/g) among the synthesized adsorbents. Dimensionless constant (R_L) is generally considered as a factor of separation and defined as follows:

$$R_L = \frac{1}{1+bC_i} \qquad (4.1)$$

Here C_i (mg/L) presents the largest initial metal concentration.

R_L shows whether the adsorption is undesirable ($R_L > 1$), desirable ($0 < R_L < 1$), irreversible ($R_L = 0$) or linear ($R_L = 1$). The values of R_L were obtained to be $0 < R_L < 1$ that showed the desirability of the adsorption process of Nd^{+3}, Tb^{+3}, and Dy^{+3} (Zhang et al., 2011). The values of $0 < 1/n < 1$ or $n > 1$ indicated favorable adsorption condition (Zhang et al., 2011).

Table 4.5. Isotherm constants for the ions adsorption by the CA/CMC/$Ni_{0.2}Zn_{0.2}Fe_{2.6}O_4$.

Model	Parameter	Nd^{+3}	Tb^{+3}	Dy^{+3}
Langmuir	b (L/mg)	1.075	0.8	0.546
	q_m (mg/g)	73.37	88.61	100.20
	R_L	0.003	0.004	0.006
	R^2	0.9703	0.7163	0.8212
	χ^2	6.04	157.16	144.07
Freundlich	K ($mg^{1-1/n}$ $L^{1/n}$/g)	46.80	46.31	46.65
	n	10.31	6.83	5.93
	R^2	0.8364	0.9905	0.9751
	χ^2	33.32	5.23	20

Table 4.6. Isotherm constants for the ions adsorption by the CA/P(PTA)/$Ni_{0.2}Zn_{0.2}Fe_{2.6}O_4$.

Model	Parameter	Nd^{+3}	Tb^{+3}	Dy^{+3}
Langmuir	b (L/mg)	0.88	0.199	0.364
	q_m (mg/g)	71.44	98.34	99.91
	R_L	0.004	0.016	0.009
	R^2	0.9563	0.8428	0.7989
	χ^2	8.4	112.03	157.44
Freundlich	K ($mg^{1-1/n}$ $L^{1/n}$/g)	44.4	36.58	43.18
	n	8.45	4.91	5.54
	R^2	0.8534	0.9812	0.9877
	χ^2	28.24	13.37	9.64

Table 4.7. Isotherm constants for the ions adsorption by the CMC/P(PTA)/$Ni_{0.2}Zn_{0.2}Fe_{2.6}O_4$.

Model	Parameter	Nd^{+3}	Tb^{+3}	Dy^{+3}
Langmuir	b (L/mg)	3.28	1.51	6.391
	q_m (mg/g)	36.59	42.87	43.76
	R_L	0.001	0.0022	0.0005
	R^2	0.5679	0.5398	0.5771
	χ^2	16.7	43.21	47.31
Freundlich	K ($mg^{1-1/n}$ $L^{1/n}$/g)	24.23	23.7	26.13
	1/n	0.09	0.13	0.12
	R^2	0.9709	0.9482	0.9632
	χ^2	1.12	4.86	4.12

Table 4.8. Isotherm constants for the ions adsorption by the P(PTA)/$Ni_{0.2}Zn_{0.2}Fe_{2.6}O_4$.

Model	Parameter	Nd^{+3}	Tb^{+3}	Dy^{+3}
Langmuir	b ($mg.L^{-1}$)	3.07	1.75	2.47
	q_m ($mg.g^{-1}$)	18.30	22.81	24.00
	R_L	0.0011	0.0019	0.0014
	R^2	0.9859	0.7335	0.7885
	χ^2	0.01	2.76	2.7
Freundlich	K ((mg/g)(l/mg)1/n)	16.04	16.07	17.30
	n	36.10	12.74	13.38
	R^2	0.8571	0.9813	0.9625
	χ^2	0.13	0.19	0.48

Table 4.9 represents the adsorption capacity of the synthesized adsorbents in comparison to some adsorbents mentioned in the previous studies that showed the favorable applicability of the synthesized adsorbents for the adsorption of Nd^{+3}, Tb^{+3}, and Dy^{+3}. According to the isotherm results, it was noticed that the adsorption was in the order of $Dy^{+3} > Tb^{+3} > Nd^{+3}$. This result might be interpreted based on the parameters of atomic weight and ionic radius as mentioned by some researchers that metal ions go through adsorption sites easily when the ionic diameter becomes small and atomic weight becomes high (Ücer et al., 2006; Fagundes-Klen et al., 2007; Horsfall and Spiff, 2005). The researchers explained the differences by considering the diversity in the adsorption according to the ionic radius, a quick saturation of adsorption sites can be induced by the large ionic radius due to the steric overcrowding on the surface (Gao et al., 2009). Some researchers reported higher adsorption of metal ions with a large ionic radius in comparison with those having a smaller ionic radius (Jalali and Moradi, 2013; Zhang et al., 2016; Shaheen et al., 2012). It seems that the difference in adsorption capacity may be related not only to the properties of the metal ions but also to the of the adsorbents physical-chemical properties, implying that other factors might play important roles in the adsorption such as morphology, surface area, and functional groups. The mechanism of adsorption by the adsorbents might be as follows: The surface physical adsorption could occur quickly through weak Van Der Waals forces due to the great surface area of the adsorbents that have a great number of adsorption sites for the ions. Then, the presence of N-, O-, and S-containing groups (pyrimidine and thiophene rings, hydroxyl groups, and amide linkages in the backbones of the P(PTA), and amine, hydroxyl, and carboxylic groups of CA and CMC) could act as hosts active chelation groups for the adsorption and creation of a stable complex with the metal ions. Ion-exchange adsorption

also exists through ion exchange between the ions and active protons on the chains of the polymers.

Table 4.9. Adsorption capacity comparison of Nd^{+3}, Tb^{+3}, and Dy^{+3} onto different adsorbents.

Adsorbent	q_m (mg/g)			Reference
	Nd^{+3}	Tb^{+3}	Dy^{+3}	
Fe_3O_4-C_{18}-chitosan-DETA	27.1		28.3	(Liu et al., 2017)
EDTA functionalized chitosan	74			(Roosen and Binnemans, 2014)
Phosphonic acid functionalized silica	45			(Melnyk et al., 2012)
γ-Fe_2O_3-NH_4OH@SiO_2(APTMS)		46.5	23.2	(Kegl et al., 2019)
GA-g-PAM/SiO_2	12.24			(Iftekhar et al., 2018a)
Zr@XG-ZA	14.01[a]			(Iftekhar et al., 2018b)
EDASiDGA	16.15			(Ogata et al., 2015)
Oxidized multi-walled carbon nanotubes			78.12	Mohammadpour et al., 2014)
Carbon black derived from recycled tires	0.67			(Smith et al., 2016)
3D GO-CZ	9.68			(Xu et al., 2018)
Macroporous polymeric resin (TVEX-PHOR)		24.93		(Madbouly et al., 2019)
TA-MWCNTs		8.55		(Tong et al., 2011)
YZ		44.5		(Baybaş and Ulusoy, 2011)
Poly(acrylamide-expanded perlite)		118.3		(Akkaya, 2012)
P(HEMA-Hap)-phy		49.27		(Akkaya, 2014)
Supported biomass on zeolit		5.07		(Barros et al., 2019)
Acryloyl–phenyl thiourea		74.23		(Reddy et al., 2016)
Hybrid Lewis base ligands functionalized alumina-silica			125.4	(Awual et al., 2017)
MIL-101-PMIDA	70.9			(Lee et al., 2018)
CA@Fe_3O_4 NPs	41			(Ashour et al., 2017)
SBA-15-ZMVP			50	(Aghayan et al., 2013)
MPS (22 nm)-2NH-2COOH			44.8	(Kaneko et al., 2018)
o-CNCs-IIPs			28.97	(Zheng et al., 2020)
o-CNCs/o-MWCNTs-IIPs			38.7	(Zheng et al., 2020)
o-CNCs/GO-IIPs			41.79	(Zheng et al., 2020)
Imprinted mesoporous silica materials			22.33	(Zheng et al., 2016)
CA/CMC/$Ni_{0.2}Zn_{0.2}Fe_{2.6}O_4$	73.37	101.61[a]	114.74[a]	This study
CA/P(PTA)/$Ni_{0.2}Zn_{0.2}Fe_{2.6}O_4$	72.49	108.82[a]	113.08[a]	This study
CMC/P(PTA)/$Ni_{0.2}Zn_{0.2}Fe_{2.6}O_4$	39.82[a]	50.32[a]	48.23[a]	This study
P(PTA)/$Ni_{0.2}Zn_{0.2}Fe_{2.6}O_4$	18.68	24.57[a]	25.89[a]	This study
[a] Calculated from Freundlich isotherm				

4.2.2.7 Ionic strength effect

The presence of salts in the solution can cause a disturbance in the adsorption performance of target ions with competition for interaction with the active sites of the adsorbent. In the present study, the influence of $NaNO_3$ in the solution on the Nd^{+3}, Tb^{+3}, and Dy^{+3} adsorption was studied at pH = 5.5 with 30 mg/L concentration of the ions and $NaNO_3$ concentration in the range of 0.02 to 1 M at optimum conditions obtained for the dosage of the adsorbents and contact time. It was found that by increasing the concentration of $NaNO_3$, a negative influence on the adsorption efficiency of the adsorbents was obtained. The adsorption efficiency of the CA/CMC/$Ni_{0.2}Zn_{0.2}Fe_{2.6}O_4$ decreased from 97.75 to 85.7, 96.83 to 84.73, and 97.85 to 93.5 % for Nd^{+3}, Tb^{+3}, and Dy^{+3}, respectively. The negative effect of $NaNO_3$ on the adsorption the CMC/P(PTA)/$Ni_{0.2}Zn_{0.2}Fe_{2.6}O_4$ was approximately the same as the results obtained for the CA/CMC/$Ni_{0.2}Zn_{0.2}Fe_{2.6}O_4$ with the values of 98.15 to 88.39, 97.6 to 82.4, and 99.42 to 94.1 % that were respectively obtained for Nd^{+3}, Tb^{+3}, and Dy^{+3}. The values of adsorption efficiency obtained by the P(PTA)/$Ni_{0.2}Zn_{0.2}Fe_{2.6}O_4$ expressed reduction from 95.67 to 67.42 for Nd^{+3}, 97.48 to 81.7 for Tb^{+3}, and 98.41 to 87.41 % for Dy^{+3}, respectively. In the case of the CA/P(PTA)/$Ni_{0.2}Zn_{0.2}Fe_{2.6}O_4$, the presence of $NaNO_3$ in the solution had the highest negative effects on the adsorption of the ions with the values of 96.73 to 56.8, 94.82 to 63.23, and 97.58 to 63.96 % respectively obtained for Nd^{+3}, Tb^{+3}, and Dy^{+3}. The results might be due to the competition of Na^+ ions in the solution with the metal ions for interacting with the active sites of the adsorbents and reduction in the activity coefficient of the metal ions that causes the limitation of the ions transfer to the adsorbent surface. Similar effect of $NaNO_3$ for the adsorption of REEs using adsorbents has been reported by the researchers (Šolić et al., 2020).

4.2.2.8. Temperature effect and the evaluation of thermodynamic parameters

Investigating the effect of temperature on the ions adsorption efficiency using the synthesized nanocomposites was performed at different temperatures of 25, 35, and 45 $^{\circ}C$ with 90 mg/L of metal ion solutions at optimum conditions of adsorbent dosage and contact time. It was observed that the adsorption efficiency towards Nd^{+3}, Tb^{+3}, and Dy^{+3} was positively affected by increasing the temperature **(Tables 4.10-4.13)**.

As stated in section **3.6.1.8**, the viscosity of metal solution decreased at the higher temperature which resulted in an increase in the diffusion of adsorbate molecules across the external boundary layer and the internal pores of the adsorbent particle. The values of

thermodynamic parameters in **Tables 4.10-4.13** show that the values of ΔH° were positive, confirming the endothermic process of the ions adsorption. The positive values of ΔS° were a result of an increase in randomness on the liquid-solid interface. As for ΔG°, the obtained values for the CA/CMC/$Ni_{0.2}Zn_{0.2}Fe_{2.6}O_4$ and CA/P(PTA)/$Ni_{0.2}Zn_{0.2}Fe_{2.6}O_4$ were negative at all temperatures, indicating that the process was naturally spontaneous and feasible while the obtained values for the CMC/P(PTA)/$Ni_{0.2}Zn_{0.2}Fe_{2.6}O_4$ showed the spontaneity of the process at a higher temperature. In the case of P(PTA)/$Ni_{0.2}Zn_{0.2}Fe_{2.6}O_4$, the values of ΔG^0 were obtained to be positive at all temperatures in the case of Nd^{+3}, suggesting that the adsorption of Nd^{+3} onto the P(PTA)/$Ni_{0.2}Zn_{0.2}Fe_{2.6}O_4$ the was non-spontaneous, while the values obtained for Tb^{+3} and Dy^{+3} showed the spontaneity of the adsorption process at higher temperatures.

Table 4.10. Effect of temperature on the adsorption of the ions at 90 mg/L by the CA/CMC/$Ni_{0.2}Zn_{0.2}Fe_{2.6}O_4$ and thermodynamic parameters.

Temperature ($^{\circ}$C)	Adsorption efficiency (%)								
	Nd^{+3}			Tb^{+3}			Dy^{+3}		
25	61.72			68.51			71.95		
35	65.95			74.61			77.31		
45	71.81			80.59			83.84		
Thermodynamic parameters	Nd^{+3}			Tb^{+3}			Dy^{+3}		
ΔH° (kJ/mol)	19.00			26.86			29.27		
ΔS° (kJ/mol K)	0.068			0.097			0.106		
ΔG° (kJ/mol)	Temperature ($^{\circ}$C)								
	25			35			45		
	Nd^{+3}	Tb^{+3}	Dy^{+3}	Nd^{+3}	Tb^{+3}	Dy^{+3}	Nd^{+3}	Tb^{+3}	Dy^{+3}
	-1.737	-2.478	-2.887	-2.263	-3.331	-3.710	-3.062	-4.353	-4.943

Table 4.11. Effect of temperature on the adsorption of the ions at 90 mg/L by the CA/P(PTA)/$Ni_{0.2}Zn_{0.2}Fe_{2.6}O_4$ and thermodynamic parameters.

Temperature (°C)	Adsorption efficiency (%)								
	Nd^{+3}			Tb^{+3}			Dy^{+3}		
25	61.71			66.79			69.33		
35	65.10			71.78			73.90		
45	69.15			77.25			79.73		
Thermodynamic parameters	Nd^{+3}			Tb^{+3}			Dy^{+3}		
ΔH° (kJ/mol)	13.72			21.78			23.03		
ΔS° (kJ/mol K)	0.051			0.079			0.084		
ΔG° (kJ/mol)	Temperature (°C)								
	25			35			45		
	Nd^{+3}	Tb^{+3}	Dy^{+3}	Nd^{+3}	Tb^{+3}	Dy^{+3}	Nd^{+3}	Tb^{+3}	Dy^{+3}
	-1.736	-2.284	-2.574	-2.168	-2.961	-3.236	-2.725	-3.823	-4.211

Table 4.12. Effect of temperature on the adsorption of the ions at 90 mg/L by the CMC/P(PTA)/$Ni_{0.2}Zn_{0.2}Fe_{2.6}O_4$ and thermodynamic parameters.

Temperature (°C)	Adsorption efficiency (%)								
	Nd^{+3}			Tb^{+3}			Dy^{+3}		
25	45.72			50.58			52.61		
35	51.05			57.51			59.89		
45	58.08			64.8			67.5		
Thermodynamic parameters	Nd^{+3}			Tb^{+3}			Dy^{+3}		
ΔH° (kJ/mol)	20.66			24.40			25.97		
ΔS° (kJ/mol K)	0.065			0.079			0.085		
ΔG° (kJ/mol)	Temperature (°C)								
	25			35			45		
	Nd^{+3}	Tb^{+3}	Dy^{+3}	Nd^{+3}	Tb^{+3}	Dy^{+3}	Nd^{+3}	Tb^{+3}	Dy^{+3}
	0.877	0.394	0.193	0.359	-0.308	-0.559	-0.861	-1.131	-1.446

Table 4.13. Effect of temperature on the adsorption of the ions at 90 mg/L by the P(PTA)/$Ni_{0.2}Zn_{0.2}Fe_{2.6}O_4$ and thermodynamic parameters.

Temperature (°C)	Adsorption efficiency (%)								
	Nd^{+3}			Tb^{+3}			Dy^{+3}		
25	60.22			68.83			73.94		
35	63.53			71.54			77.32		
45	69.16			79.41			85.34		
Thermodynamic parameters	Nd^{+3}			Tb^{+3}			Dy^{+3}		
ΔH° (kJ/mol)	16.32			23.18			29.88		
ΔS° (kJ/mol K)	0.048			0.074			0.098		
ΔG° (kJ/mol)	Temperature (°C)								
	25			35			45		
	Nd^{+3}	Tb^{+3}	Dy^{+3}	Nd^{+3}	Tb^{+3}	Dy^{+3}	Nd^{+3}	Tb^{+3}	Dy^{+3}
	1.694	0.759	0.137	1.391	0.452	-0.328	0.770	-0.664	-1.753

4.2.2.9. Reusability studies

To study the reusability of the adsorbents, the optimum dosage of each adsorbent (0.04 g of the CA/CMC/$Ni_{0.2}Zn_{0.2}Fe_{2.6}O_4$ and CA/P(PTA)/$Ni_{0.2}Zn_{0.2}Fe_{2.6}O_4$, 0.06 g of the CMC/P(PTA)/$Ni_{0.2}Zn_{0.2}Fe_{2.6}O_4$, and 0.15 g of the P(PTA)/$Ni_{0.2}Zn_{0.2}Fe_{2.6}O_4$) was shaken with 50 mL solution of 30 mg/L of Nd^{+3}, Tb^{+3}, and Dy^{+3} (except for the P(PTA)/$Ni_{0.2}Zn_{0.2}Fe_{2.6}O_4$ with 50 mg/L of Nd^{+3}, Tb^{+3}, and Dy^{+3}) on a shaker at 180 rpm. The pH of the solution was adjusted to the desired value by adding HNO_3 or NaOH solutions. After reaching equilibrium at the optimum time, the magnetized adsorbents were separated by an external magnet and the concentrations of the Nd^{+3}, Tb^{+3}, and Dy^{+3} in the solutions were measured. Then, the adsorbents were washed with deionized water to remove the unadsorbed metal ions. For desorption of the ions from the adsorbents, 50 mL of 0.2 M HNO_3 was used. The desorption process was performed for 2 h. The regenerated adsorbent was employed for adsorption of the Nd^{+3}, Tb^{+3}, and Dy^{+3} at the optimized conditions. The desorption efficiency values of more than 95, 96, and 99 % were respectively obtained for Nd^{+3}, Tb^{+3}, and Dy^{+3} using the CA/CMC/$Ni_{0.2}Zn_{0.2}Fe_{2.6}O_4$. The desorption efficiencies of the Nd^{+3}, Tb^{+3}, and Dy^{+3} were respectively more than 89, 91, and 95 % for the CA/P(PTA)/$Ni_{0.2}Zn_{0.2}Fe_{2.6}O_4$, more than 82, 84, and 88 % for the CMC/P(PTA)/$Ni_{0.2}Zn_{0.2}Fe_{2.6}O_4$, and 82, 86, and 90 % for the P(PTA)/$Ni_{0.2}Zn_{0.2}Fe_{2.6}O_4$. It was observed that the adsorption efficiencies of the adsorbents were decreased after the fourth cycle. After the fourth cycle, the decreases in adsorption efficiency of Nd^{+3}, Tb^{+3}, and Dy^{+3} were

respectively more than 95, 94, and 95% using the CMC/P(PTA)/$Ni_{0.2}Zn_{0.2}Fe_{2.6}O_4$ that were lower than those of other adsorbents. After the fourth cycle of adsorption, adsorption efficiencies of Nd^{+3}, Tb^{+3}, and Dy^{+3} were reduced to 91.78, 90.36, and 93.56 % using the CA/P(PTA)/$Ni_{0.2}Zn_{0.2}Fe_{2.6}O_4$, 86.43, 84.61, and 87.52 % using the CMC/P(PTA)/$Ni_{0.2}Zn_{0.2}Fe_{2.6}O_4$, and 84.64, 86.37, and 88.75 % using the P(PTA)/$Ni_{0.2}Zn_{0.2}Fe_{2.6}O_4$, which showed higher efficiency of the CA/CMC/$Ni_{0.2}Zn_{0.2}Fe_{2.6}O_4$ in comparison with other adsorbents. The reduction in the efficiency of adsorption might be due to the chemically bonding of the ions with the functional groups that cannot be desorbed easily, decrease in the functional groups during acid treatment, and decrease in the weight of adsorbent during cycles. Nevertheless, the obtained results revealed that the adsorbents can be potentially used for the adsorption of the Nd^{+3}, Tb^{+3}, and Dy^{+3}.

4.2.2.10. Competitive adsorption

The optimum dosage of the adsorbents obtained in the single system was used to evaluate the adsorption of Nd^{+3}, Tb^{+3}, and Dy^{+3} ions competitively in the ternary system of 30 mg/L of the ions while the ratio of the ions was 1:1:1. The results showed that the adsorption efficiencies for Nd^{+3}, Tb^{+3}, and Dy^{+3} ions reduced to 28.25, 48.62, and 50.58 % using the CA/CMC/$Ni_{0.2}Zn_{0.2}Fe_{2.6}O_4$, 22.3, 48.05, and 50.28 % using the CA/P(PTA)/$Ni_{0.2}Zn_{0.2}Fe_{2.6}O_4$, 19.4, 37.6, and 40.9 % using the CMC/P(PTA)/$Ni_{0.2}Zn_{0.2}Fe_{2.6}O_4$, and 14.32, 32.46, and 34.64 % using the P(PTA)/$Ni_{0.2}Zn_{0.2}Fe_{2.6}O_4$. In a multi-component system, antagonism, synergism, and non-interaction effects can occur with values of $q_{mix}/q_0 < 1$, $q_{mix}/q_0 > 1$, and $q_{mix}/q_0 = 1$ (Wang et al., 2017), respectively, where q_{mix} and q_0 are respectively the adsorption capacities of each ion in the mixture and single systems. Results showed an antagonism effect of each ion on the adsorption of other ions in a multi-component system with the q_{mix}/q_0 values for Nd^{+3}, Tb^{+3} and Dy^{+3} that were respectively 0.27, 0.5, and 0.52 using CA/CMC/$Ni_{0.2}Zn_{0.2}Fe_{2.6}O_4$, 0.23, 0.51, and 0.51 using the CA/P(PTA)/$Ni_{0.2}Zn_{0.2}Fe_{2.6}O_4$, 0.2, 0.38, and 0.41 using the CMC/P(PTA)/$Ni_{0.2}Zn_{0.2}Fe_{2.6}O_4$. 0.15, 0.33, and 0.35 for Nd^{+3}, Tb^{+3}, and Dy^{+3} using the P(PTA)/$Ni_{0.2}Zn_{0.2}Fe_{2.6}O_4$. EDX spectrum was also recorded for each ions loaded-adsorbents after the adsorption process and the obtained results showed the existence of Nd^{+3}, Tb^{+3}, and Dy^{+3} peaks in the spectra.

4.2.3. Simultaneous adsorption of Nd^{3+}, Tb^{+3}, and Dy^{+3} in the ternary system

Although all the synthesized adsorbent showed their favorable efficacy for the adsorption of Nd^{3+}, Tb^{+3}, and Dy^{+3}, the CA/CMC/$Ni_{0.2}Zn_{0.2}Fe_{2.6}O_4$ was found to be more efficient than other adsorbents, according to the results obtained by the single adsorption studies. Therefore, it was applied for studying Nd^{+3}, Tb^{+3}, and Dy^{+3} adsorption in a multi-component system.

First, the effect of pH on the adsorption of Nd^{+3}, Tb^{+3}, and Dy^{+3} was investigated. The results were the same as those obtained in the single system as following: minimum adsorption efficiency at pH 1.5 due to the highly acidic solution and maximum adsorption efficiency at pH 5.5 because of reduction in H^+ ions. Then, to decrease the number of experiments, obtain useful information about the effect of independent parameters individually and/or interactively that leads to a decrease in experimental error, and model the process of Nd^{+3}, Tb^{+3}, and Dy^{+3} adsorption by the CA/CMC/$Ni_{0.2}Zn_{0.2}Fe_{2.6}O_4$, Response Surface Methodology (RSM) was applied. RSM approach usually includes three stages: design and experiments, response surface modeling by regression, and optimization. By considering adsorbent dosage, contact time, initial concentration, response (ions adsorption efficiency), and CCD at five levels of -α (-2), low (-1), central (0), high (+1) and +α (+2), 32 individual experimental runs were proposed by Design Expert 10.0. The quadratic polynomial model for response versus the independent variables was presented as follows (Srivastava, 2015):

$$Y = \beta_0 + \sum_{i=1}^{k} \beta_i x_i + \sum_{i=1}^{k} \sum_{j=1}^{k} \beta_{ij} x_i x_j + \sum_{i=1}^{k} \beta_{ii} x_i^2 + \varepsilon \qquad (4.2)$$

Where Y refers to the predicted response (adsorption efficiency), and β_0, β_i, β_{ii}, and β_{ij} respectively refer to the constant coefficient, linear coefficient, quadratic coefficient, and interaction coefficient. Notably, x_i and x_j are the independent variables, k shows the number of the independent variables, and ε is the residual error.

Analysis of variance (ANOVA) was used to obtain information about the adequacy of the models by evaluating coefficient of determination (R^2), lack of fit, and the Fisher test (F-value) values (Markandeya et al., 2017). By applying quadratic regression modeling between the response and independent variables for each metal, the equations obtained for adsorption efficiency (%) were as follows:

Nd (III) adsorption efficiency (%) = 45.421 + 1.866 X_1 + 514.024 X_2 – 0.571 X_3 – 1.322 X_4 + 0.175 X_5 – 0.0043 X_1X_3 + 0.00312 X_1X_4 – 0.00255 X_1X_5 – 2.27 X_2X_1 + 1.796 X_2X_3 + 1.351

X_2X_4 + 0.759 X_2X_5 + 0.00712 X_3X_4 -0.00258 X_3X_5 + 0.00469 X_4X_5 – 0.0126 $X1^2$ – 1237.07 X_2^2 – 0.000393 X_3^2 + 0.00122 X_4^2 – 0.00378 X_5^2 (4.3)

Tb (III) adsorption efficiency (%) = 51.793 + 1.663 X_1 + 410.645 X_2 – 0.502 X_3 – 0.603 X_4 + 0.24 X_5 – 7.549 X_1X_3 + 1.073 X_1X_4 – 1.132 X_1X_5 – 2.253 X_2X_1 + 1.651 X_2X_3 + 1.185 X_2X_4 + 1.283 X_2X_5 + 0.00328 X_3X_4 – 0.00178 X_3 X_5 + 0.00243 X_4X_5 -0.0124 $X1^2$ -1059.01 X_2^2 – 0.0001808 X_3^2 + 0.000553 X_4^2 – 0.00103X_5^2 (4.4)

Dy (III) adsorption efficiency (%) = 58.691 + 1.632 X_1 + 405.813 X_2 - 0.354 X_3 – 0.778 X_4 – 0.315 X_5 – 0.00156 X_1X_3 + 0.00241X_1X_4 – 0.000818 X_1X_5 – 2.405 X_2X_1 + 1.486 X_2X_3 + 1.371 X_2X_4 + 1.272 X_2X_5 + 0.00183 X_3X_4 – 0.00243 X_3X_5 + 0.00253 X_4X_5 – 0.0122 $X1^2$ – 1039.17 X_2^2 + 0.000237 X_3^2 + 0.000437 X_4^2 – 0.0000959 X_5^2 (4.5)

ANOVA results showed R^2 and R_{adj}^2 of 0.9951 and 0.9862 for Nd^{+3}, 0.9948 and 0.9853 for Tb^{+3}, and 0.9938 and 0.9826 for Dy^{+3}, indicating a good agreement between the predicted and experimental data. The F-values with a very low probability value of 0.0001 showed that the predicted models are statistically significant. The 'Adequate precision'' values for Nd^{+3}, Tb^{+3}, and Dy^{+3} obtained by ANOVA were favorable due to a value > 4 (Soltani et al., 2013). Additionally, the coefficient of variation values (C.V. %) were obtained to be 2.1, 1.87, and 1.97 for Nd^{+3}, Tb^{+3}, and Dy^{+3} respectively, that are low and show the reliability of the modeling. Under the conditions of pH = 5.5, the adsorbent dosage of 0.1 g, initial concentration of 30 mg/L, and contact time of 53 min were predicted by RSM while the adsorption efficiencies of Nd^{+3}, Tb^{+3}, and Dy^{+3} were respectively equal to 95.72, 96.17and 99.44 %.

4.2.3.1. Batch adsorption kinetic and isotherm studies

Using 50 mL of the solutions at 30 mg/L of Nd^{+3}, Tb^{+3}, and Dy^{+3} ions, kinetic studies were performed by contacting the ions with 0.09 g of the CA/CMC/$Ni_{0.2}Zn_{0.2}Fe_{2.6}O_4$ at different times. The CA/CMC/$Ni_{0.2}Zn_{0.2}Fe_{2.6}O_4$ was used at the dosage of 0.09 g contacting with 50 mL of Nd^{+3}, Tb^{+3}, and Dy^{+3} solutions at different concentrations in the range of 30-180 mg/L at pH = 5.5. The results of kinetic studies showed that the main mechanism for the adsorption of the ions is chemisorption due to the highest values of R^2 (0.9927 for Nd^{+3}, 0.9933 for Tb^{+3}, and 0.9929 for

Dy^{+3}) and lowest values of χ^2 (0.045 for Nd^{+3}, 0.043 for Tb^{+3}, and 0.048 for Dy^{+3}) obtained by PSO as compared with PFO (R^2 values of 0.9617, 0.9585, and 0.9587, and χ^2 values of 0.24, 0.268, and 0.279 respectively for Nd^{+3}, Tb^{+3}, and Dy^{+3}) and IPD (R^2 values of 0.8157, 0.8225, and 0.8222, and χ^2 values of 1.16, 1.15, and 1.20 respectively for Nd^{+3}, Tb^{+3}, and Dy^{+3}) models. From the fitting results obtained by the isotherm models, Freundlich isotherm showed to be more suitable for the description of the adsorption of Nd^{+3}, Tb^{+3}, and Dy^{+3} by the CA/CMC/$Ni_{0.2}Zn_{0.2}Fe_{2.6}O_4$ according to the higher values of R^2 (0.9879, 0.9654, and 0.9633 respectively for Nd^{+3}, Tb^{+3}, and Dy^{+3}) and lower values of χ^2 (0.159, 0.55, and 0.675 respectively for Nd^{+3}, Tb^{+3}, and Dy^{+3}) in comparison with the Langmuir model (R^2 values of 0.8773, 0.9238, and 0.9125, and χ^2 values of 1.62, 1.21, and 1.61 respectively for Nd^{+3}, Tb^{+3}, and Dy^{+3}). In addition, the values of R_L for Nd^{+3}, Tb^{+3}, and Dy^{+3} were between 0 and 1 (0.007, 0.006, and 0.004 respectively for Nd^{+3}, Tb^{+3}, and Dy^{+3}), suggesting favorable adsorption of Nd^{+3}, Tb^{+3}, and Dy^{+3} by the CA/CMC/$Ni_{0.2}Zn_{0.2}Fe_{2.6}O_4$. The values of 9, 9.26, and 9.71 that were obtained for n showed a strong interaction between the CA/CMC/$Ni_{0.2}Zn_{0.2}Fe_{2.6}O_4$ and the metal ions.

4.2.3.2. Ionic strength effect

The results of ionic strength presented a negative effect of $NaNO_3$ on the adsorption of Nd^{+3}, Tb^{+3}, and Dy^{+3}. As for Nd^{+3}, the negative effect was greater than those obtained for Tb^{+3} and Dy^{+3}. Greater negative effect of $NaNO_3$ on the adsorption efficiency of Nd (III) was found in comparison with Tb (III) and Dy (III). The adsorption efficiencies for Nd (III), Tb (III), and Dy (III) without the presence of $NaNO_3$ were 92.33, 93.91, and 96.25 %. In the presence of 0.1 M $NaNO_3$, adsorption efficiencies decreased to 77.12, 85.6, and 91.43 % respectively for Nd^{+3}, Tb^{+3}, and Dy^{+3} that might be due to the competition of sodium ions with Nd^{+3}, Tb^{+3}, and Dy^{+3} for interacting with the active adsorption sites of the adsorbent and a decrease in the adsorption sites of the adsorbent as a result of an increase in aggregation of the adsorbent by an enhancement in ionic strength.

4.2.3.3. Temperature effect and the evaluation of thermodynamic parameters

50 mL of the ions at the concentration of 90 mg/L was contacted with 0.09 g of the adsorbent to investigate the influence of various temperatures (25, 35, and 45 $^{\circ}$C) on the adsorption efficiency of the ions. A positive effect of temperature was seen for the process of

ions adsorption while adsorption efficiencies increased from 44.31, 47.14, and 49.21 to 52.64, 55.99, and 58.42 for Nd^{+3}, Tb^{+3}, and Dy^{+3}, respectively. The positive values of ΔH° (13.9, 14.76, and 15.45 respectively for Nd^{+3}, Tb^{+3}, and Dy^{+3}) showed an endothermic process. The positive values of ΔG° at all temperatures revealed a non-spontaneous process of the ions adsorption at the studied concentration. ΔS° values were also positive that indicated an increase in randomness at the interface of the solid–solution was obtained during the metal ions fixation on the adsorbent surface.

4.2.3.4. Reusability studies

Reusability test of the adsorbent was performed by the adsorbent loaded with the ions at the conditions of initial concentration = 30 mg/L and pH = 5.5 with 0.1 g of the adsorbent for 53 min. Desorption process by 0.2 M HNO_3 showed that desorption efficiencies were > 93, 96, and 97 % for Nd^{+3}, Tb^{+3}, and Dy^{+3}, respectively. Using the adsorbent in four cycles showed an insignificant decrease in the adsorption efficiency as the difference between the adsorption efficiency of the first cycle and the fourth cycle which were about 2.54, 1.63, and 1.16 % respectively for Nd^{+3}, Tb^{+3}, and Dy^{+3}. This result might be due to the reasons mentioned in section **4.2.2.9**. The reusability of the adsorbent was concluded according to the obtained results.

4.2.3.5. Column mode

The adsorption of Nd^{+3}, Tb^{+3}, and Dy^{+3} was studied using a glass column (D: 0.5 cm and L:12 cm) packed with 0.3 g of the adsorbent while mixed with 1.8 g acid-cleaned sand for decreasing pressure drop. First, a flow rate of 1 mL/min of DW provided by a peristaltic pump was passed upward for flushing the column for an hour. Then, a ternary solution of 30 mg/L of Nd^{+3}, Tb^{+3}, and Dy^{+3} was injected to the column for 520 min while a fraction collector was used to collect the effluent every 10 min. Finally, Agilent 4100 MP-AES Spectrometer was used to determine the concentration of the ions in the effluent. The times for breakthrough (C_e/C_0=0.05) and exhaustion (C_e/C_0=0.95) were obtained to be 95 and 410 min for Nd^{+3}, 105 and 430 min for Tb^{+3}, and 120 and 440 min for Dy^{+3}. Adsorption efficiencies of Nd^{+3}, Tb^{+3}, and Dy^{+3} were respectively 46.33, 47.07, and 49.11 % while the obtained adsorption capacities were equal to 22.70, 24.00, and 25.54 mg/g for Nd^{+3}, Tb^{+3}, and Dy^{+3}, respectively. Both Thomas and Yan

models were fitted well the experimental data of Nd^{+3}, Tb^{+3}, and Dy^{+3} column adsorption. The results of column adsorption indicated successful practical usage of the adsorbent.

CONCLUSIONS

The aim of this study was to synthesize novel magnetic nanocomposites and study their adsorption behavior towards Nd^{+3}, Tb^{+3}, and Dy^{+3}. For this purpose, the $Ni_{0.2}Zn_{0.2}Fe_{2.6}O_4$ as magnetic nanoparticles was firstly synthesized by hydrothermal method. The Poly(pyrimidine-thiophene-amide) (P(PTA)) was also synthesized in the first stage by polycondensation reaction of 5,5'-(thiophene-2-ylmethylene)bis(2-aminopyrimidine-4,6-diol) (TMAPD) with terephthalic acid in 1,3-dipropyl imidazolium bromide {[1,3-$(pr)_2$im]Br} ionic liquid as green media.
Then, the CA/CMC/$Ni_{0.2}Zn_{0.2}Fe_{2.6}O_4$, CA/P(PTA)/$Ni_{0.2}Zn_{0.2}Fe_{2.6}O_4$, and CMC/P(PTA)/$Ni_{0.2}Zn_{0.2}Fe_{2.6}O_4$ were synthesized by gelation method using Ca^{+2}.The P(PTA)/$Ni_{0.2}Zn_{0.2}Fe_{2.6}O_4$ was synthesized by hydrothermal method. The successful synthesis of the products was confirmed by FE-SEM, EDX, NMR, XRD, FT-IR, and VSM techniques. XRD result showed that the average particle size of the $Ni_{0.2}Zn_{0.2}Fe_{2.6}O_4$ was 27.68 nm. FE-SEM images of the $Ni_{0.2}Zn_{0.2}Fe_{2.6}O_4$ and P(PTA)/$Ni_{0.2}Zn_{0.2}Fe_{2.6}O_4$ showed that they were synthesized approximately spherical in shape with the size of particles < 100 nm. The FE-SEM images of the biopolymer nanocomposites showed that the particles of the $Ni_{0.2}Zn_{0.2}Fe_{2.6}O_4$ and/or P(PTA)/$Ni_{0.2}Zn_{0.2}Fe_{2.6}O_4$ were distributed on the surface of the biopolymers or embedded with the biopolymers. The results of VSM for the nanocomposites presented the values of 14.14, 15.28, and 14.88 emu/g respectively for the CA/CMC/$Ni_{0.2}Zn_{0.2}Fe_{2.6}O_4$, CA/P(PTA)/$Ni_{0.2}Zn_{0.2}Fe_{2.6}O_4$, and CMC/P(PTA)/$Ni_{0.2}Zn_{0.2}Fe_{2.6}O_4$ that were enough for their magnetic separation by an external magnetic field.

Batch adsorption experiments were used to study the adsorption capability of the adsorbents towards Nd^{+3}, Tb^{+3}, and Dy^{+3} in the single system by considering the main parameters including solution pH, contact time, adsorbent dosage, initial concentration of the ions, and ionic strength. The effect of pH on the adsorption efficiency of Nd^{+3}, Tb^{+3}, and Dy^{+3} showed that at pH = 1.5, the adsorption was almost zero due to highly acidic solution as a result of high concentration of H^+, meaning that the regeneration process predominated over the adsorption process at low pH. The optimum conditions for the maximum adsorption of Nd^{+3}, Tb^{+3}, and Dy^{+3} were obtained as follows: pH = 5.5, contact time = 40 min, and adsorbent dosage of 0.04 g at initial concentration of 30 mg/L for the CA/CMC/$Ni_{0.2}Zn_{0.2}Fe_{2.6}O_4$ with the adsorption efficiencies of 97.75, 96.83, and 97.85 % respectively for Nd^{+3}, Tb^{+3}, and Dy^{+3}, pH = 5.5,

contact time = 50 min, and adsorbent dosage of 0.04 g at initial concentration of 30 mg/L for the CA/P(PTA)/$Ni_{0.2}Zn_{0.2}Fe_{2.6}O_4$ with the adsorption efficiencies of 98.11, 95.62, and 98.15 % respectively for Nd^{+3}, Tb^{+3}, and Dy^{+3}, pH = 5.5, contact time = 90 min, and adsorbent dosage of 0.06 g at initial concentration of 30 mg/L for the CMC/P(PTA)/$Ni_{0.2}Zn_{0.2}Fe_{2.6}O_4$ with the adsorption efficiencies of 98.15, 97.6, and 99.42 % respectively for Nd^{+3}, Tb^{+3}, and Dy^{+3}, and pH = 5.5, contact time = 130 min, and adsorbent dosage of 0.15 g at initial concentration of 50 mg/L for the P(PTA)/$Ni_{0.2}Zn_{0.2}Fe_{2.6}O_4$ with the adsorption efficiencies of 95.67, 97.48, and 98.41 % respectively for Nd^{+3}, Tb^{+3}, and Dy^{+3}. By fitting the data of kinetic to pseudo-first-order, pseudo-second-order, and intra-particle diffusion models, it was obtained that the adsorption of Nd^{+3}, Tb^{+3}, and Dy^{+3} by all the nanocomposites followed pseudo-second-order model, showing the chemisorption process, except for the CMC/P(PTA)/$Ni_{0.2}Zn_{0.2}Fe_{2.6}O_4$ that the adsorption data followed both pseudo-second-order and intra-particle diffusion models.

The isotherm studies by fitting the data with Langmuir and Freundlich isotherm models showed that the adsorption of Tb^{+3} and Dy^{+3} by the nanocomposites followed Freundlich isotherm model, indicating non-uniform and multi-layer adsorption, while the adsorption isotherm data of Nd^{+3} by the nanocomposites followed Langmuir model, showing monolayer adsorption, except for the CMC/P(PTA)/$Ni_{0.2}Zn_{0.2}Fe_{2.6}O_4$ that followed Freundlich model.

The effect of ionic strength showed the negative effect of $NaNO_3$ on the adsorption of Nd^{+3}, Tb^{+3}, and Dy^{+3}. By increasing the molarity of $NaNO_3$, the adsorption efficiencies of the ions decreased from 97.75 to 85.7, 96.83 to 84.73, and 97.85 to 93.5 % for Nd^{+3}, Tb^{+3}, and Dy^{+3} by the CA/CMC/$Ni_{0.2}Zn_{0.2}Fe_{2.6}O_4$, 98.15 to 88.39, 97.6 to 82.4, and 99.42 to 94.1 % obtained respectively for Nd^{+3}, Tb^{+3}, and Dy^{+3} by the CMC/P(PTA)/$Ni_{0.2}Zn_{0.2}Fe_{2.6}O_4$, while increasing $NaNO_3$ concentration showed higher negative effect by the values of 56.8, 63.23, and 63.96 % at the $NaNO_3$ concentration of 1 M.

The effect of temperature on the adsorption of 90 mg/L of Nd^{+3}, Tb^{+3}, and Dy^{+3} showed that for all the nanocomposites, an increase in temperature of solution led to an increase in the adsorption efficiency of Nd^{+3}, Tb^{+3}, and Dy^{+3}. The thermodynamic parameters were calculated and the obtained values showed that the adsorption process by the adsorbents was endothermic ($\Delta H^o > 0$), and the randomness and disorder at the solid-solution interface increased during the adsorption of the ions ($\Delta S^o > 0$). At optimum conditions, the values of ΔG^o were negative at all temperatures for the CA/CMC/$Ni_{0.2}Zn_{0.2}Fe_{2.6}O_4$ and CA/P(PTA)/$Ni_{0.2}Zn_{0.2}Fe_{2.6}O_4$, showing

spontaneity of the process, while ΔG^o values were negative at higher temperature showing that the process was spontaneous at a higher temperature in the case of the CMC/P(PTA)/$Ni_{0.2}Zn_{0.2}Fe_{2.6}O_4$. The reusability test of the adsorbents showed that although all the adsorbents can be reused, CA/CMC/$Ni_{0.2}Zn_{0.2}Fe_{2.6}O_4$ was more efficient as the decrease in adsorption efficiency (1.36, 1.91, and 1.56 % respectively for Nd^{+3}, Tb^{+3}, and Dy^{+3}) that was lower than those of the CA/P(PTA)/$Ni_{0.2}Zn_{0.2}Fe_{2.6}O_4$, CMC/P(PTA)/$Ni_{0.2}Zn_{0.2}Fe_{2.6}O_4$, and P(PTA)/$Ni_{0.2}Zn_{0.2}Fe_{2.6}O_4$. The competitive adsorption of the ions showed antagonism effect ($q_{mix}/q_0 < 1$) of each ion on the adsorption efficiency of other ions in the ternary system.

The CA/CMC/$Ni_{0.2}Zn_{0.2}Fe_{2.6}O_4$ was used in the batch experiments to investigate the adsorption of Nd^{+3}, Tb^{+3}, and Dy^{+3} in a multi-component system. RSM-CCD was used to model the adsorption efficiency of the ions as a response, contact time, adsorbent dosage, and initial concentration of the ions as variables.

In summary, the results obtained in the multi-component system were as follows: the models proposed by RSM-CCD were statistically significant due to the favorable F-values with a very low probability value of < 0.0001. The adsorption efficiencies of Nd^{+3}, Tb^{+3}, and Dy^{+3} were respectively 95.72, 96.17, and 99.44 % at the conditions of pH = 5.5, the adsorbent dosage of 0.1 g, initial concentration of 30 mg/L, and contact time of 53 min predicted by RSM. The kinetic data of Nd^{+3}, Tb^{+3}, and Dy^{+3} adsorption were fitted well by the PSO model. Freundlich model fitted the data of isotherm study better than the Langmuir model. The presence of $NaNO_3$ in the solution had a negative effect on the adsorption of Nd^{+3}, Tb^{+3}, and Dy^{+3} and the adsorption efficiencies respectively decreased from 92.33 to 77.12, 93.91 to 85.6, and 96.25 to 91.43 % for Nd^{+3}, Tb^{+3}, and Dy^{+3} in the presence of 1 M $NaNO_3$.

The results for thermodynamic parameters studied at 90 mg/L of the ions were the same as those obtained for ΔH^o and ΔS^o in the single system while the values of ΔG^o were positive at all temperatures, showing non-spontaneous nature of the process. In addition, the CA/CMC/$Ni_{0.2}Zn_{0.2}Fe_{2.6}O_4$ (0.3 g mixed with 1.8 g acid-cleaned sand) was used in a column (D: 0.5 cm and L:12) cm for studying the adsorption of Nd^{+3}, Tb^{+3}, and Dy^{+3} for 520 min. The results of the column showed the adsorption efficiencies of 46.33, 47.07, and 49.11 % for Nd^{+3}, Tb^{+3}, and Dy^{+3} respectively. The experimental data of the column for Nd^{+3}, Tb^{+3}, and Dy^{+3} were fitted well with both Thomas and Yan models. In conclusion, the results of this research showed the

successful usage of the synthesized novel adsorbents for adsorption of Nd^{+3}, Tb^{+3}, and Dy^{+3} from aqueous media.

SCOPE FOR FUTURE WORK

Based on the findings of this research, the suggestions for the future studies may be as following:

1. Using CA and CMC in nanosize in the structure of the synthesized composites for investigating Nd^{+3}, Tb^{+3}, and Dy^{+3} adsorption.
2. Using a strong synthetic multifunctional polymer in the matrix of CA and CMC for investigating Nd^{+3}, Tb^{+3}, and Dy^{+3} adsorption.
3. Using the synthesized nanocomposites in the form of hydrogels instead of dried powder for investigating Nd^{+3}, Tb^{+3}, and Dy^{+3} adsorption.
4. Using the synthesized adsorbent for other REEs adsorption and the adsorption of metal ions such as Pb^{+2}, Ni^{+2}, Cd^{+2}, Cu^{+2}, etc.
5. The adsorption of Nd^{+3}, Tb^{+3}, and Dy^{+3} from real samples can be investigated.

REFERENCES

- Aghayan, H., Mahjoub, A.R., Khanchi, A.R., Samarium and dysprosium removal using 11-molybdo-vanadophosphoric acid supported on Zr modified mesoporous silica SBA-15, *Chemical Engineering Journal*, **225** (2013) 509–519.
- Akkaya, R., Synthesis and characterization of a new low-cost composite for the adsorption of rare earth ions from aqueous solutions, *Chemical Engineering Journal*, **200** (2012) 186–191.
- Akkaya, R., Terbium adsorption onto polyhydroxyethylmethacrylate–hydroxyapatite composite and its modified composition by phytic acid, *Desalination and Water Treatment*, **52** (2014) 1440-1447.
- Albuquerque, A.S., Ardisson, J.D., Macedo, W.A.A., Alves, M.C.M., Nanosized powders of NiZn ferrite: Synthesis, structure, and magnetism, *Journal of Applied Physics*, **87**, 4352 (2000).
- Anastopoulos, I., Bhatnagar, A., Lima, E.C. Adsorption of rare earth metals: A review of recent literature, *Journal of Molecular Liquids*, **221** (2016) 954-962.
- Anitha, A., Divya Rani, V.V., Krishna, R., Sreeja, V., Selvamurugan, N., Nair S.V., Tamura H., Jayakumar, R., Synthesis, characterization, cytotoxicity and antibacterial studies of chitosan, O-carboxymethyl and N,O-carboxymethyl chitosan nanoparticles, *Carbohydrate Polymers*, **78** (2009) 672–677 .
- Ashour, R.M., El-Sayed, R., Abdel-Magied, A.F., Abdel-Khalek, A.A., Ali, M.M., Forsberg, K., Uheida, A., Muhammed, M., Dutta, J., Selective separation of rare earth ions from aqueous solution using functionalized magnetite nanoparticles: kinetic and thermodynamic studies, *Chemical Engineering Journal*, **327** (2017) 286–296.
- Awual, M.R., Alharthi, N.H., Okamoto, Y., Karim, M.R., Halim, M.E., Hasan, M.M., Rahman, M.M., Islam, M.M., Khaleque, M.A., Sheikh, M.C., Ligand field effect for Dysprosium(III) and Lutetium(III) adsorption and EXAFS coordination with novel composite nanomaterials, *Chemical Engineering Journal*, **320** (2017) 427-435.
- Aziz H.A., Adlan M.N., Ariffin K.S., Heavy metals (Cd, Pb, Zn, Ni, Cu and Cr(III)) removal from water in Malaysia: post treatment by high quality limestone, *Bioresource Technology*, **99** (2008) 1578-1583.

- Babu, B.R., Tatarchuk, T., Elastic properties and antistructural modeling for Nickel-Zinc ferrite-aluminates, *Materials Chemistry and Physics*, **207** (2018) 534-541.
- Balaram, V., Rare earth elements: A review of applications, occurrence, exploration, analysis, recycling, and environmental impact, *Geoscience Frontiers*, **10** (2019) 1285-1303.
- Balaram, V., Recent advances in the determination of elemental impurities in pharmaceuticals - Status, challenges and moving frontiers, *Trends in Analytical Chemistry*, **80** (2016) 83-95.
- Barakos, G., An assessment tool for the mineability of rare earth element deposits. Ph.D. Diss. Technical University Bergakademie Freiberg, Germany, 2017.
- Barros, Ó., Costa, L., Costa, F., Lago, A., Rocha, V., Vipotnik, Z., Silva, B., Tavares, T., Recovery of rare earth elements from wastewater towards a circular economy, *Molecules*, **24** (2019) 1005.
- Baybaş, D., Ulusoy, U., Polyacrylamide–clinoptilolite/Y-zeolite composites: Characterization and adsorptive features for terbium, *Journal of Hazardous Materials*, **187** (2011) 241–249.
- Bhushan, B., Handbook of Nanotechnology, publisher Springer, (2010) 1-5.
- Binnemans, K., Tom Jones, P., Blanpain B., Van Gerven, T., Yang, Yongxiang., Walton Allan., Buchert, M., Recycling of rare earths: a critical review, *Journal of Cleaner Production*, **51** (2013) 1-22.
- Braccini, I., Pérez S., Molecular basis of Ca^{2+}-induced gelation in alginates and pectins: the egg-box model revisited, *Biomacromolecules*, **2** (2001) 1089-1096.
- Brookins, D.G., Aqueous geochemistry of rare earth elements. Geochemistry and Mineralogy of Rare Earth Elements, B.R. Lipin and G.A. McKay, eds. Washington, DC, *The Mineralogical Society of America*, **21** (1989) 201-212.
- Brzyska, W., Lanthanides and Actinides, Wydawnictwa Naukowo-Techniczne Poland, (1996) 40-41.
- Chakhmouradlan, A.R., Wall, F., Rare earth elements: Minerals, mines, magnets (and more), *Elements*, **8** (2012) 333–340.
- Chattopadhyay, K.K., Banerjee, A.N., Introduction to nanoscience and nanotechnology, Publisher PHI learnings pvt ltd, Chap 1 (2009) 1-5.

- Chen, W., Honghui, H., Bai, T., Jiang, S., Geochemistry of monazite within carbonatite related REE deposits, *Resources*, **6** (2017) 51.
- Chen, X.G., Park, H.J., Chemical characteristics of O-carboxymethyl chitosans related to the preparation conditions, *Carbohydrate Polymers*, **53** (2003) 355-359.
- Chu, L., Yan, S., Xing, X.H., Sun, X., Jurcik, B., Progress and perspectives of sludge ozonation as a powerful pretreatment method for minimization of excess sludge production, *Water Research*, **43** (2009) 1811-1822.
- Das, N., Das, D., Recovery of rare earth metals through biosorption: An overview, *Journal of Rare Earths*, **31** (2013) 933-943.
- Das, R., Giri, S., Muliwa, A.M., Maity, A., High-performance Hg(II) removal using thiol-functionalized polypyrrole (PPy/MAA) composite and effective catalytic activity of Hg(II)-adsorbed waste material, *ACS Sustainable Chemistry & Engineering*, **5** (2017) 7524-7536.
- de Abreu, F.R., Campana-Filho, S.P., Characteristics and properties of carboxymethyl chitosan, *Carbohydrate Polymers*, **75** (2009) 214-221.
- Dostal, J., Rare earth element deposits of alkaline igneous rocks, *Resources*, 6 (2017) 34.
- Dou, J., Liu, Z., A simple and efficient synthetic method for poly(ethylene terephthalate): phenylalkyl pyrrolidinium ionic liquid as polycondensation medium, *Green Chemistry*, **14** (2012) 2305-2313.
- Dupont, D., Brullot W., Bloemen, M., Verbiest, T., Binnemans, K., Selective uptake of rare earths from aqueous solutions by EDTA-functionalized magnetic and Nonmagnetic nanoparticles, *ACS Applied Materials & Interfaces*, **6** (2014a) 4980−4988.
- Dupont, David., Luyten, J., Bloemen, M., Verbiest, T., Binnemans, K., Acid-stable magnetic core−shell nanoparticles for the separation of rare earths, *Industrial & Engineering Chemistry Research*, **53** (2014b) 15222−15229.
- Esmat, M., Farghali, A.A., Khedr, M.H., El-Sherbiny I.M., Alginate-based nanocomposites for efficient removal of heavy metal ions, *International Journal of Biological Macromolecules*, **102** (2017) 272-283.
- Esser, B.K., Volpe, A., Kenneally, J.M., Smith, D.K., Preconcentration and purification of rare earth elements in natural waters using silica-immobilized 8-hydroxyquinoline and a supported organophosphorus extractant, *Analytical Chemistry*, **66** (1994) 1736-1742.

- European Commission Critical raw materials for the EU, Report of the Ad-hoc Working Group on defining critical raw materials, http://ec.europa.eu/enterprise/policies/raw-materials/critical/index_en.htm.
- Evans, E.1., Fellows, J., Coffer, A., Wood, R.D., Open complex formation around a lesion during nucleotide excision repair provides a structure for cleavage by human XPG protein, *The EMBO Journal*, **16** (1997) 625-638.
- Fagundes-Klen M.R., Ferri, P., Martins, T.D., Tavares, C.R.G., Silva, E.A., Equilibrium study of the binary mixture of cadmium–zinc ions biosorption by the Sargassum filipendula species using adsorption isotherms models and neural network, *Biochemical Engineering Journal*, 34 (2007) 136-146.
- Farghali, A.A., Bahgat, M., Allah, A.E., Khedr, M.H., Adsorption of Pb(II) ions from aqueous solutions using copper oxide nanostructures, *Beni-Suef University Journal of Basic and Applied Sciences*, **2** (2013) 61-71.
- Ferron, C.J., Bulatovic, S.M., Salter, R.S., Beneficiation of rare earth oxide minerals. Materials Science Forum. Trans Tech Publications, Switzerland, (1991).
- Fiset, J.F, Blais, J.F, Riveros, P.A., Review on the removal of metal ions from effluents using seaweeds, alginate derivatives and other sorbents, *Journal of Water Science*, **21** (2008) 283-308.
- Florek, J., Chalifour, F., Bilodeau, F., Larivière, D., Kleitz, F., Nanostructured hybrid materials for the selective recovery and enrichment of rare earth elements, *Advanced Functional Materials*, **24** (2014) 2668-2676.
- Gabor, A.E. Davidescu, C.M., Negrea, A., Ciopec, M., Butnariu, M., Ianasi, C., Muntean, C., Negrea, P., Lanthanum separation from aqueous solutions using magnesium silicate functionalized with tetrabutylammonium dihydrogen phosphate, *Journal of Chemical & Engineering Data*, **61** (2016) 535−542.
- Gambogi, J., 2016. Rare Earths. U.S. Geological Survey. Mineral Commodity Summaries.
- Gambogi, J., Rare Earths, United States Geological Survey, Mineral Commodity Summaries, (2017).
- Gambogi, J., Rare Earths, United States Geological Survey, Minerals Yearbook, (2011).
- Gambogi, J., Rare Earths. USGS Geological Survey, Mineral Commodity Summaries, USGS, Reston, VA, 2013.

- Ganguli, R., Cook, D.R., Rare earths: A review of the landscape, MRS Energy & Sustainability, (2018).
- Gao, Z., Bandosz, T.J., Zhao, Z., Han, M., Qiu, J., Investigation of factors affecting adsorption of transition metals on oxidized carbon nanotubes, *Journal of Hazardous Materials*, 167 (2009) 357–365.
- García, JM., García, F.C., Serna, F., de la Peña, J.L., High-performance aromatic polyamides, *Progress in Polymer Science*, **35** (2010) 623–686.
- Giese, E.C., Jordão, C.S., Biosorption of lanthanum and samarium by chemically modified free *Bacillus subtilis* cells, Applied Water Science, 9 (2019) 182.
- Gomez-Valdemoro, A., San-Jose, N., Clemente Garcia, F., De La Pena, J.L., Serna, F., Miguel Garcia, J., Novel aromatic polyamides with main chain and pendant 1,2,4-triazole moieties and their application to the extraction/elimination of mercury cations from aqueous media, *Polymer Chemistry*, **1** (2010) 1291–1301.
- Gotoh, T., Matsushima, K., Kikuchi, K.I., Adsorption of Cu and Mn on covalently cross-linked alginate gel beads, *Chemosphere*, **55** (2004) 57-64.
- Grebneva, O.N., Kuz'min, N.M., Tsysin, G.I., Zolotov, Y.A., On-line-sorption preconcentration and inductively coupled plasma atomic emission spectrometry determination of rare earth elements, *Spectrochimica Acta Part B: Atomic Spectroscopy*, **51** (1996) 1417-1423.
- Guibal, E., Interactions of metal ions with chitosan-based sorbents: a review, *Seperation and Purification Technology*, **38** (2004) 43-74.
- Gupta, C.K., Krishnamurthy, Extractive metallurgy of rare earths, CRC Press, (2004).
- Hadjittofi, L., Charalambous, S., Pashalidis, I., Removal of trivalent samarium from aqueous solutions by activated biochar derived from cactus fibres, *Journal of Rare Earths*, **34** (2016) 99–104.
- Hanbali, M., Holail, H., Hammud, H., Remediation of lead by pretreated red algae: adsorption isotherm, kinetic, column modeling and simulation studies, *Green Chemistry Letters and Reviews*, **7** (2014) 342–358.
- Hatch, G.P., Dynamics in the global market for rare earths. Elements, **8(5)** (2012) 341-346.
- Hearle, JW., High-performance fibres, Woodhead Publishing Ltd, Cambridge, England (2001).

- Hedrick, J.B., Rare earths, Us. geological survey minerals yearbook, (2004).
- Henderson, P., The rare earth elements: introduction and review. In: Jones, A.P., Wall, F., Williams, C.T. (Eds.) Rare earth minerals: Chemistry, origin and ore deposits. Chapman & Hall, London, (1996) 1–19.
- Hornyak, L., Tibbals, H.F., Dutta, J., Moore, J.J., Introduction to nanoscience and nanotechnology Taylor and Francis CRC Press ISBN: 978-1-4200-4779-0.
- Horsfall Jr, M., Spiff, A.I., Adsorption of transition metals in aqueous solutions by fluted pumpkin (Telfairia occidentalis Hook f) waste, *Chemistry & Biodiversity*, 2 (2005).
- Hristovski, K.D., Westerhoff, P.K., Crittenden, J.C., Olson, L.W., Arsenate removal by nanostructured ZrO_2 spheres, *Environmental Science & Technology*, **42** (2008) 3786-3790.
- Humphries, M., Rare Earth Elements: The Global Supply Chain, CRS Report for Congress, R41347 (www.crs.gov), 2012.
- Ibáñez, J.P., Umetsu, Y., Uptake of trivalent chromium from aqueous solutions using protonated dry alginate beads, *Hydrometallurgy*, **72** (2004) 327-334.
- Iftekhar, S., Srivastava, V., Casas, A., Sillanpää, M., Synthesis of novel GA-g-PAM/SiO_2 nanocomposite for the recovery of rare earth elements (REE) ions from aqueous solution, *Journal of Cleaner Production*, **170** (2018a) 251-259.
- Iftekhar, S., Srivastava, V., Hammouda, S.B., Sillanpää, M., Fabrication of novel metal ion imprinted xanthan gum-layered double hydroxide nanocomposite for adsorption of rare earth elements, *Carbohydrate Polymers*, **194** (2018b) 274-284.
- Jalali, M., Moradi, F., Competitive sorption of Cd, Cu, Mn, Ni, Pb and Zn in polluted and unpolluted calcareous soils, *Environmental Monitoring and Assessment*, 185 (2013) 8831–8846.
- Janos, P., Sypecka, J., Mlckovska, P., Kuran, P., Pilarova, V., Removal of metal ions from aqueous solutions by sorption onto untreated low-rank coal (oxihumolite), *Separation and Purification Technology*, **53** (2007) 322-329.
- Jegadeesan, G., Al-Abed, S.R., Sundaram, V., Choi, H., Scheckel, K.G., Dionysiou, D.D., Arsenic sorption on TiO_2 nanoparticles: size and crystallinity effects, *Water Research*, **44** (2010) 965-973.

- Johansson, N., Krook, J., Eklund, M., Berglund, B., An integrated review of concepts and initiatives for mining the technosphere: towards a new taxonomy, *Journal of Cleaner Production,* **55** (2013) 35-44.
- Kaneko, T., Nagata, F., Kugimiya, S., Kato, K., Optimization of carboxyl-functionalized mesoporous silica for the selective adsorption of dysprosium, *Journal of Environmental Chemical Engineering*, **6** (2018) 5990-5998.
- Kegl, T., Ban, I., Lobnik, A., Košak, A., Synthesis and characterization of novel γ-Fe_2O_3-NH_4OH@SiO_2(APTMS) nanoparticles for dysprosium adsorption, *Journal of Hazardous Materials*, **378** (2019) 120764.
- Koerth-Baker, M., 4 rare earth elements that will only get more important, (2012).
- Koochaki-Mohammadpour, S.M.A., Torab-Mostaedi, M., Talebizadeh-Rafsanjani, A., Naderi-Behdani, F., Adsorption isotherm, kinetic, thermodynamic, and desorption studies of lanthanum and dysprosium on oxidized multiwalled carbon nanotubes. J*ournal of Dispersion Science and Technology*, **35** (2014) 244−254.
- Lee, Y.R., Yu, K., Ravi, S., Ahn, W.S., Selective adsorption of rare earth elements over functionalized Cr-MIL-101, *ACS Applied Materials & Interfaces*, **10** (2018) 23918-23927.
- Li, H., XIAO, D., HE, H., Lin, R.; Zuo, P.; Adsorption behavior and adsorption mechanism of Cu(II) ions on amino-functionalized magnetic nanoparticles, *The Transactions of Nonferrous Metals Society of China*, **23** (2013) 2657−2665.
- Liang, P., Hu, B., Jiang, Z., Qin, Y., Peng, T., Nanometer-sized titanium dioxide micro-column on-line preconcentration of La, Y, Yb, Eu, Dy and their determination by inductively coupled plasma atomic emission spectrometry, *Journal of Analytical Atomic Spectrometry*, **16** (2001) 863-866.
- Lim, A.P., Aris A.Z., Continuous fixed-bed column study and adsorption modeling: Removal of cadmium (II) and lead (II) ions in aqueous solution by dead calcareous skeletons, *Biochemical Engineering Journal*, **87** (2014) 50-61.
- Lin C.C., Lin, C.W., Preparation of N,O-carboxymethyl chitosan nanoparticles as an insulin carrier, Drug Delivery, 16 (2009) 458–464.
- Liou, GS., Hsiao, SH., Ishida, M., Kakimoto, M., Imai, Y., Synthesis and characterization of novel soluble triphenylamine-containing aromatic polyamides based on N,N'-bis(4-

aminophenyl)-N,N'-diphenyl-1,4-phenylenediamine, *Journal of Polymer Science Part A: Polymer Chemistry*, **40** (2002) 2810−2818.

- Liu, E., Zheng, X., Xu, X., Zhang, F., Liu, E., Wang, Y., Li, C., Yan, Y., Preparation of diethylenetriamine-modified magnetic chitosan nanoparticles for adsorption of rare-earth metal ions, *New Journal of Chemistry*, **41** (2017) 7739-7750.
- Long, K.R., Van Gosen, B.S., Foley, N.K., Cordier, D., The principal rare earth elements deposits of the United States—A summary of domestic deposits and a global perspective: U.S. Geological Survey Scientific Investigations Report, 2010–5220, 96 p.
- Lucas, J., Lucas, P., Le Mercier, T., Rollat, A., Davenport, W., Rare earths: Science, technology, production and use, Elsevier Inc, (2014).
- Ma, Wei., Ya, F.Q., Han, M., Wang, R., Characteristics of equilibrium, kinetics studies for adsorption of fluoride on magnetic-chitosan particle, *Journal of Hazardous Materials*, **143** (2007) 296-302.
- Madbouly, H.A., El-Hefny, N.E., El-Nadi, Y.A., Adsorption and separation of terbium(III) and gadolinium(III) from aqueous nitrate medium using solid extractant, *Separation Science and Technology*, (2019) 1-13.
- Manchen, N.A., Sprecher, B., Bailey, G., Ge, J., Tukker, A., Effect of Chinese policies on rare earth supply chain resilience, *Resources, Conservation & Recycling*, **142** (2019) 101–112.
- Mancheri, N.A., World trade in rare earths, Chinese export restrictions, and implications, *Resource Policy*, **46** (2015) 262-271.
- Mansoori, Y., Mohsenzadeh, R., Designed polyamides based on 1,4-bis[(4-aminophenyl)-1,3,4-oxadiazolyl]phenylene (BAPO) for removal of Cu(II) and Co(II), *Designed Monomers and Polymers*, **18** (2015) 1-10.
- Mansur, H.S., Mansur, A.A.P., Curti, E., De Almeida, M.V., Functionalized chitosan/ quantum dots nano-hybrids for nanomedicine applications: towards biolabeling and biosorbing phosphate metabolites, *Journal of Materials Chemistry B*, **1** (2013) 1696-1711.
- Markandeya, Dhiman, N., Shukla, S.P., Kisku, G.C., Statistical optimization of process parameters for removal of dyes from wastewater on chitosan cenospheres nanocomposite using response surface methodology, *Journal of Cleaner Production*, **149** (2017) 597-606.

- Marmier, N., Delise´e, J.A., Fromage, F., Surface complexation modeling of Yb(III) and Cs(I) sorption on silica, *Journal of Colloid and Interface Science*, **212** (1999) 228–233.
- Marmier, N., Dumonceau, A.J., Fromage, F., Surface complexation modeling of Yb(III) sorption and desorption on hematite and alumina, *Journal of Contaminant Hydrology*, **26** (1997) 159–167.
- McLeod, C.L., Shaulis, B.J., Rare earth elements in planetary crusts: Insights from chemically evolved igneous suites on earth and the moon, *Minerals*, **8** (2018) 455.
- Mehdinia, A., Shegefti, S., Shemirani, F., Removal of Lead(II), Copper(II) and Zinc(II) ions from aqueous solutions using magnetic amine-functionalized mesoporous silica nanocomposites, *Journal of the Brazilian Chemical Society*, **26** (2015) 2249-2257.
- Melnyk, I.V., Goncharyk, V.P., Kozhara, L.I., Yurchenko, G.R., Matkovsky, A.K., Zub, Y.L., Alonso, B., Sorption properties of porous spray-dried microspheres functionalized by phosphonic acid groups, *Microporous and Mesoporous Materials*, **153** (2012) 171–177.
- MEP (Ministry of Environmental Protection). Pollutant discharge standards for the Rare Earth Industry (in Chinese), (2011a).
- Meyer, L., Bras, B., Rare earth metal recycling. Sustainable Systems and Technology, (2011) IEEE International Symposium, 16-18 May, Chicago Il.
- Mondal N.K., Kar, S., Potentiality of banana peel for removal of Congo red dye from aqueous solution: isotherm, kinetics and thermodynamics studies, *Applied Water Science*, **8** (2018) 157.
- Murty, D.S.R., Chakrapani, G., Preconcentration of rare earth elements on activated carbon and its application to groundwater and sea-water analysis, *Journal of Analytical Atomic Spectrometry*, **11** (1996) 815- 820.
- Naser, A., El-deen, G.S., Bhran, A.A., Metwally, S., El-Kamash, A., Elaboration of impregnated composite for sorption of europiumand neodymium ions from aqueous solutions, *Journal of Industrial and Engineering Chemistry*, **32** (2015) 264–272.
- Nayak, D., Lahiri, S., Biosorption of toxic, heavy, no-carrier-added radionuclides by calcium alginate beads, *Journal of Radioanalytical and Nuclear Chemistry*, **267** (2005) 59–65.
- Ng, J.C.Y., Cheung, W.H., McKay, G., Equilibrium studies for the sorption of lead from effluents using chitosan, *Chemosphere*, **52** (2003) 1021-1030.

- Ng, J.C.Y., Cheung, W.H., McKay, G., Equilibrium studies of the sorption of Cu(II) ions onto chitosan, *Journal of Colloid and Interface Science*, **255** (2002) 64-74.
- Ni, D., Lin, Z., Xiaoling, P., Xinqing, W., Hongliang, G., Preparation and characterization of nickel-zinc ferrites by a solvothermal method, *Rare Metal Materials and Engineering*, **44** (2015) 2126-2131.
- Ni, Y., Hughes, J.M., Mariano, A.N., Crystal chemistry of the monazite and xenotime structures, *American Mineralogist*, **80** (1995) 21-26.
- Nobahar, S., Parvini, M., Eisazadeh, H., Removal of copper ions from aqueous solutions using polypyrrole and its Nanocomposites, *Journal of Heat and Mass Transfer Research*, **1** (2014) 101-106.
- Ogata, T., Narita, H., Tanaka, M., Rapid and selective recovery of heavy rare earths by using an adsorbent with diglycol amic acid group, *Hydrometallurgy*, **155** (2015) 105-109.
- Oliveira, D., Inverno, C., Classification of rare earth deposit and occurrence types: what's new?, *Comunicações Geológicas*, **101** (2014) 821-823.
- Oliveira, R.C., Jouannin, C., Guibal, E., Garcia Jr, O., Samarium(III) and praseodymium(III) biosorption on *Sargassum* sp.: Batch study. *Process Biochemistry*, **46 (3)** (2011) 736–744.
- Orha, C., Manea, F., Ratiu, C., Burtica, G., Iovi, A., Obtaining and characterization of romanian zeolite supporting silver ions, *Environmental Engineering and Management Journal*, **6** (2007) 541-544.
- Pan, B.J., Pan, B.C., Zhang, W.M., Lv, L., Zhang, Q.X., Zheng, S.R., Development of polymeric and polymer-based hybrid adsorbents for pollutants removal from waters, *Chemical engineering Journal*, **151** (2009) 19–29.
- Papandreou, A., Stournaras, C., Panias, D., Copper and cadmium adsorption on pellets made from fired coal fly ash, *Journal of Hazardous Materials*, **148** (2007) 538-547.
- Pathania, D., Sharma S., Singh P., Removal of methylene blue by adsorption onto activated carbon developed from *Ficus carica* bast, *Arabian Journal of Chemistry*, **10** (2017) S1445-S1451.
- Patra, A.K., Dutta, A., Bhaumik, A., Self-assembled mesoporous g-Al_2O_3 spherical nanoparticles and their eficiency for the removal of arsenic from water. *Journal of Hazardous Materials*, **201-202** (2012) 170-177.

- Peiró, L.T., Méndez, G.V., Material and energy requirement for rare earth production, JOM, 65 (2013) 1327–1340.
- Pestov, A., Bratskaya, S., Chitosan and its derivatives as highly efficient polymer ligands, *Molecules*, **21** (2016) 330.
- Pradeep, T., Anshup, Noble metal nanoparticles for water purification: a critical review, *Thin Solid Films*, **517** (2009) 6441–6478.
- Puigdomenech, I., Windows software for the graphical presentation of chemical speciation, in: 219th ACS National Meeting. Abstracts of Papers, Vol.1. American Chemical Society, San Francisco, CA, March 26-30, 2000. Abstract I&EC-248.
- QU, J., Research progress of novel adsorption processes in water purification: a review, *Journal of Environmental Sciences*, **20** (2008) 1-13.
- Rare Earth Elements-Critical Resources for High Technology: United States Geological Survey, Fact Sheet 087-02.
- Ravikumar, L., Kalaivani, S., Vidhyadevi, T., Murugasen, A., Dinesh Kirupha, S., Sivanesan, S., Synthesis, characterization and metal ion adsorption studies on novel aromatic poly(azomethine amide)s containing thiourea groups, *Open Journal of Polymer Chemistry*, **4** (2014) 1-11.
- Reddy, A.R., Reddy, K.H., Heavy metal ion uptake properties of polystyrene-supported chelating polymer resins, *Journal of Chemical Sciences*, **115** (2003) 155–160.
- Reddy, N.S., Rao, K.M., Krishna, S.V., Ha, C.S., Synthesis of 1–acryloyl–3–phenyl thiourea based pH sensitive hydrogels for removal of samarium and terbium, Macromolecular Research, 24 (2016) 494–501.
- Ridley, M.K., Machesky M.L., Wesolowski, D.J., Palmer D.A., Surface complexation of neodymium at the rutile–water interface: a potentiometric and modeling study in NaCl media to 250 ^{o}C, *Geochimica et Cosmochimica Acta*, **69** (2005) 63–81.
- Rim, K.T., Koo, K.H., Park, J.S., Toxicological evaluations of rare earths and their health impacts to workers: A literature review, *Safety and Health at Work*, **4** (2013) 12–26.
- Rittmann, B.E., Mayer, B., Westerhoff, P., Edwards, M., Capturing the lost phosphorus. *Chemosphere*, **84(6)** (2011) 846–853.
- Rodrigues, J.R, Lagoa, R., Copper ions binding in Cu-alginate gelation, *Journal of Carbohydrate Chemistry*, **25** (2006) 219-232.

- Roosen, J., Binnemans, K., Adsorption and chromatographic separation of rare earths with EDTA- and DTPAfunctionalized chitosan biopolymers, *Journal of Materials Chemistry A*, **2** (2014) 1530–1540.
- Saikrishna, Y.V.S., Babu, R.R., Adsorption of Copper and Lead ions from aqueous solutions using nickel oxide nanostructure, *International Journal of Engineering Research and General Science*, **3** (2015) 77-84.
- Saravanan, D., Sudha, P.N., Batch adsorption studies for the removal of copper from wastewater using natural biopolymer, *Journal of ChemTech Research*, **6** (2014) 3496-3508.
- Schmuhl, R., Krieg, H., Keizer, K., Adsorption of Cu(II) and Cr(VI) ions by chitosan: Kinetics and equilibrium studies, *Water S.A*, **27** (2001) 1-7.
- Schüler, D., Buchert, M., Liu, R., Dittrich, S., Merz, C., Study on rare earths and their recycling, Öko-Institut eV Darmstadt, (2011).
- Shaheen, S.M., Derbalah, A.S., Moghanm, F.S., Removal of heavy metals from aqueous solution by zeolite in competitive sorption system, *International Journal of Environmental Science and Development*, **3** (2012).
- Siew, C.K., Williams, P.A., Young, N.W.G., New insights into the mechanism of gelation of alginate and pectin: charge annihilation and reversal mechanism, *Biomacromolecules*, **6** (2005) 963-969.
- Smaranda, C., Bulgariu, D., Gavrilescu, M., Equilibrium and kinetic studies of acid dye sorption onto soils from iasi area, *Environmental Engineering and Management Journal*, **9** (2010) 57-66.
- Smith, Y.R., Bhattacharyya, D., Willhard, T., Misra, M., Adsorption of aqueous rare earth elements using carbon black derived from recycled tires, *Chemical Engineering Journal*, **296** (2016) 102–111.
- Šolić, M., Maletić, S., Isakovski, M.K., Nikić, J., Watson, M., Kónya, Z., Tričković, J., Comparing the adsorption performance of multiwalled carbon nanotubes oxidized by varying degrees for removal of low levels of copper, nickel and chromium(VI) from aqueous solutions, *Water*, **12** (2020) 723.
- Soltani, R.D.C., Rezaee, A., Godini, H., Khataee, A.R., Hasanbeiki, A., Photoelectrochemical treatment of ammonium using seawater as a natural supporting electrolyte, *Chemistry and Ecology*, **29** (2013) 72-85.

- Song, S.T., Saman, N., Johari, K., Mat, H., Removal of Hg(II) from aqueous solution by adsorption using raw and chemically modified rice straw as novel adsorbents, *Industrial & Engineering Chemistry Research*, **52** (2013) 13092-13101.
- Spinelli, V.A., Laranjeira, M.C.M., Fávere, V.T., Preparation and characterization of quaternary chitosan salt: adsorption equilibrium of chromium(VI) ion, *Reactive and Functional Polymers*, **61** (2004) 347-352.
- Srivastava, V., Sharma, Y.C., Mika, Sillanpää., Application of response surface methodology for optimization of Co(II) removal from synthetic wastewater by adsorption on NiO nanoparticles, *Journal of Molecular Liquids*, **211** (2015) 613-620.
- Suli, L.M., Wan Ibrahim, W.H., Abdul Aziz, B., Deraman, M.R., Ismail, N.A., A review of rare earth mineral processing technology, *Chemical Engineering Research Bulletin*, **19** (2017) 20-35.
- Sun, S., Wang, A., Adsorption kinetics of Cu(II) ions using N,O-carboxymethyl-chitosan, *Journal of Hazardous Materials*, **131** (2006) 103-111.
- Tanco, M.A.L., Tanaka, D.A.P., Flores, V.C., Nagase, T., Suzuki, T.M., Preparation of porous chelating resin containing linear polymer ligand and the adsorption characteristics for harmful metal ions, *Reactive and Functional Polymers*, **53** (2002) 91-101.
- Tang, L.G., Hon, D.N.S., Chelation of Chitosan Derivatives with Zinc Ions. II. Association Complexes of Zn^{2+} onto O,N-Carboxymethyl Chitosan, *Journal of Applied Polymer Science*, **79** (2001) 1476–1485.
- Tiesman, J., Mining techniques, products, and shortages of rare earth elements, (2010).
- Tong, S., Zhao, S., Zhou, W., Li, R., Jia, Q., Modification of multi-walled carbon nanotubes with tannic acid for the adsorption of La, Tb and Lu ions, *Microchimica Acta*, **174** (2011) 257–264.
- Topp, N.E., The chemistry of the rare earth elements. Amsterdam, Elsevier. Ed. P.L. Robinson. Topics in Inorganic and General Chemistry, *Monograph*, **4** (1965) 53-56.
- U.S. Department of Energy 2011 Critical Materials Strategy, http://energy.gov/sites/prod/files/DOE_CMS2011_FINAL_Full.pdf.
- U.S. Geological Survey, Mineral Commodity Summaries 2019, 2019.

- Ücer, A., Uyaniak A., Ayün, S.F., Adsorption of Cu(II), Cd(II), Zn(II), Mn(II) and Fe(III) ions by tannic acid immobilized activated carbon, *Separation and Purification Technology*, 47 (2006) 113–118.
- US EPA (United States Environmental Protection Agency), Identification and description of mineral processing sectors and waste streams, (1991).
- US EPA (United States Environmental Protection Agency), Rare earth elements: A review of production, processing, recycling, and associated environmental issues, (2012).
- Varma, A.J., Deshpande S.V., Kennedy, J.F., Metal complexation by chitosan and its derivatives: a review, *Carbohydrate Polymers*, **55** (2004) 77–93.
- Vasanthi, B.J., Ravikumar, L., Synthesis and characterization of new poly(azomethine ester)s having phenylthiourea units, *European Polymer Journal*, **43** (2007) 4325-31.
- Velmurugan, K., Venkatachalapathy, V.S.K., Sendhilnathan, S., Synthesis of nickel zinc iron nanoparticles by coprecipitation technique, *Materials Research*, **13(3)** (2010) 299-303
- Vygodskii, Y.S., Lozinskaya, E.I., Shaplov, A.S., Lyssenko, K.A., Antipin, M.Y., Urman, Y.G., Implementation of ionic liquids as activating media for polycondensation processes, *Polymer*, **45** (2004) 5031–5045.
- Wang, F., Pan, Y., Cai, P., Guo, T., Xiao, H., Single and binary adsorption of heavy metal ions from aqueous solutions using sugarcane cellulose-based adsorbent, *Bioresource Technology*, **241** (2017) 482–490.
- Wang, F., Zhao, J., Wei, X., Huo, F., Li, W., Hu, Q., Liu, H., Adsorption of rare earths (III) by calcium alginate–poly glutamic acid hybrid gels, *Journal of Chemical Technology and Biotechnology*, **89** (2014) 969–977.
- Wang, F., Zhao, J., Zhou, H., Li, W., Sui, N., Liu, H., O-carboxymethyl chitosan entrapped by silica: preparation and adsorption behaviour toward neodymium (III) ions, *Journal of Chemical Technology and Biotechnology*, **88** (2013) 163–325.
- Wang, S., Zhu, Z., Sonochemical treatment of fly ash for dye removal from wastewater, *Journal of Hazardous Materials*, **126** (2005) 91-95.
- Wang, W., Zhang, H., Zhang, L., Wan, H., Zheng, S., Xu, Z., Adsorptive removal of phosphate by magnetic Fe_3O_4@C@ZrO_2, *Colloids and Surfaces A: Physicochemical and Engineering Aspects*, **469** (2015) 100-106.

- Wasserscheid, P., Welton, T., Ionic liquids in synthesis, Wiley-VCH Verlag GmbH & Co. KGaA, Weinheim, (2002).
- Wedephol, K.H., The composition of the continental crust, *Geochimica et Cosmochimica Acta*, **59** (1995) 1217-1232.
- Wu, D., Zhang, L., Wang, L., Zhu, B., Fan L., Adsorption of lanthanum by magnetic alginate-chitosan gel beads, *Journal of Chemical Technology and Biotechnology*, **86** (2011) 345–352.
- Wu, F.C., Tseng, R.L., Juang, R.S., A review and experimental verification of using chitosan and its derivatives as adsorbents for selected heavy metals, *Journal of Environmental Management*, **91** (2010) 798-806.
- Wübbeke, J., Rare earth elements in China: Policies and narratives of reinventing an industry, *Resources Policy*, **38** (2013) 384-394.
- Xu, S., Wang, Z., Gao, Y., Zhang, S., Wu, K., Adsorption of rare earths(III) using an efficient sodium alginate hydrogel cross-linked with poly-γ-glutamate, *PLoS One*, **10** (2015) 0124826.
- Xu, X., Jiang, X.Y., Jiao, F.P., Chen, X.Q., Yu, J.G., Tunable assembly of porous three-dimensional graphene oxide-corn zein composites with strong mechanical properties for adsorption of rare earth elements, *Journal of the Taiwan Institute of Chemical Engineers*, **85** (2018) 106-114.
- Xu, X., Jiang, X.Y., Jiao, F.P., Chen, X.Q., Yu, J.G., Tunable assembly of porous three-dimensional graphene oxide-corn zein composites with strong mechanical properties for adsorption of rare earth elements, *Journal of the Taiwan Institute of Chemical Engineers*, **85** (2018) 106-114.
- Yadav, K.K., Dasgupta, K., Singh, D.K., Anitha, M., Varshney, L., Singh, H., Solvent impregnated carbon nanotube embedded polymeric composite beads: An environment benign approach for the separation of rare earths, *Seperation and Purification Technology*, **143** (2015) 115-124.
- Yakup Arıca, M., Arpa, Ç., Ergene, A., Bayramoğlu, G., Genç Ö., Ca-alginate as a support for Pb(II) and Zn(II) biosorption with immobilized Phanerochaete chrysosporium, *Carbohydrate Polymers*, **52** (2003) 167-174.

- Yakup Arıca, M., Bayramoğlu, G., Yılmaz, M., Bektaş, S., Genç, Ö., Biosorption of Hg^{2+}, Cd^{2+}, and Zn^{2+} by Ca-alginate and immobilized wood-rotting fungus *Funalia trogii*, *Journal of Hazardous Materials*, **109** (2004) 191-199.
- Yamani, J.S., Miller, S.M., Spaulding, M.L., Zimmerman, J.B., Enhanced arsenic removal using mixed metal oxide impregnated chitosan beads, *Water Research*, **46** (2012) 4427-4434.
- Yan, H., Dai, J., Yang, Z., Yang, H., Cheng R., Enhanced and selective adsorption of copper(II) ions on surface carboxymethylated chitosan hydrogel beads, *Chemical Engineering Journal*, **174** (2011) 586–594.
- Yanfei, X., Zongyu, F., Xiaowei, H., Li, H., Yingying, C., Xiangsheng, L., Liangshi, W., Long, Z., Recovery of rare earth from the ion-adsorption type rare earths ore: II. Compound leaching, *Hydrometallurgy*, **163** (2016) 83-90.
- Yousef, N.S., Farouq, R., Hazzaa, R., Adsorption kinetics and isotherms for the removal of nickel ions from aqueous solutions by an ion-exchange resin: application of two and three parameter isotherm models, *Desalination and Water Treatment*, **57** (2016) 21925-21938.
- Yu, K., Ho, J., McCandlish, E., Buckley, B., Patel, R., Li, Z., Shapley, N.C., Copper ion adsorption by chitosan nanoparticles and alginate microparticles for water purification applications, *Colloids and Surfaces A: Physicochemical and Engineering Aspects*, **425** (2013) 31-41.
- Zalloum, R.M., Mubarak, M.S., Chelation properties of poly(2-hydroxy-4 acryloyloxybenzophenone) resins toward some divalent metal ions, *Journal of Applied Polymer Science*, **109** (2008) 3180-3184.
- Zavareh, S., Zarei, M., Darvishi, F., Azizi, H., As(III) adsorption and antimicrobial properties of Cu–chitosan/alumina nanocomposite, *Chemical Engineering Journal*, **273** (2015) 610–621.
- Zhang, C., Yu, Z., Zeng, G., Huang, B., Dong, H., Huang, J., Yang, Z., Wei, J., Hu, L., Zhang, Q., Phase transformation of crystalline iron oxides and their adsorption abilities for Pb and Cd, *Chemical Engineering Journal*, 284 (2016) 247–259.
- Zhang, L., Wu, D., Zhu, B., Yang, Y., Wang, L., Adsorption and selective separation of neodymium with magnetic alginate microcapsules containing the extractant 2-ethylhexyl phosphonic acid mono-2-ethylhexyl ester, *Journal of Chemical & Engineering Data*, **56** (2011) 2280–2289.

- Zhang, M., Zhang, Y., Helleur, Robert., Selective adsorption of Ag^{+} by ion-imprinted O-carboxymethyl chitosan beads grafted with thiourea–glutaraldehyde, *Chemical Engineering Journal*, **264** (2015) 56–65.
- Zhao, F., Repo E., Meng, Y., Wang, X., Yin, D., Sillanpää, M., An EDTA-β-cyclodextrin material for the adsorption of rare earth elements and its application in preconcentration of rare earth elements in seawater, *Journal of Colloid and Interface Science*, **465** (2016) 215–224.
- Zhao, Z., Sun, X., Dong, Y., Wang, Y., Synergistic effect of acid–base coupling bifunctional ionic liquids in impregnated resin for rare earth adsorption, *ACS Sustainable Chemistry & Engineering*, **4 (2)** (2016) 616–624.
- Zheng, X., Liu, E., Zhang, F., Yan, Y., Pan, J., Efficient adsorption and separation of dysprosium from NdFeB magnets in an acidic system by ion imprinted mesoporous silica sealed in a dialysis bag, *Green Chemistry*, **18** (2016) 5031–5040.
- Zheng, X., Zhang, Y., Bian, T., Zhang, Y., Li, Z., Pan, J., Oxidized carbon materials cooperative construct ionic imprinted cellulose nanocrystals films for efficient adsorption of Dy(III), *Chemical Engineering Journal*, **381** (2020) 122669.
- Zhou, B., Li, Z., Chen, C., Global potential of rare earth resources and rare earth demand from clean technologies, *Minerals*, **7** (2017) 203.
- Zhou, B., Li, Z., Zhao, Y., Zhang, C., Wei, Y., Rare earth elements supply vs. clean energy technologies: New problems to be solve, *Gospodarka Surowcami Mineralnymi*, **32** (2016) 29–44.
- Zhu Y., Zheng, Y., Wang, A., A simple approach to fabricate granular adsorbent for adsorption of rare elements, *International journal of biological macromolecules*, **72** (2015) 410-420.
- Zhu, Y., Zheng, Y., Wang, A., A simple approach to fabricate granular adsorbent for adsorption of rare elements, *International Journal of Biological Macromolecules*, **72** (2015) 410-420.

LIST OF PUBLICATIONS

- Hamedreza Javadian, Montserrat Ruiz, Tawfik A. Saleh, Ana Maria Sastre, Ca-alginate/carboxymethyl chitosan/$Ni_{0.2}Zn_{0.2}Fe_{2.6}O_4$ magnetic bionanocomposite: Synthesis, characterization and application for single adsorption of Nd^{+3}, Tb^{+3}, and Dy^{+3} rare earth elements from aqueous media, *Journal of Molecular Liquids*, 306 (2020) 112760. https://doi.org/10.1016/j.molliq.2020.112760
- Hamedreza Javadian, Montserrat Ruiz, Ana Maria Sastre, Response surface methodology based on central composite design for simultaneous adsorption of rare earth elements using nanoporous calcium alginate/carboxymethyl chitosan microbiocomposite powder containing $Ni_{0.2}Zn_{0.2}Fe_{2.6}O_4$ magnetic nanoparticles: Batch and column studies, *International Journal of Biological Macromolecules*, 154 (2020) 937-953. https://doi.org/10.1016/j.ijbiomac.2020.03.131
- Hamedreza Javadian, Montserrat Ruiz, Mehdi Taghavi, Ana Maria Sastre, Synthesis of magnetic CMC bionanocomposite containing a novel biodegradable nanoporous polyamide selectively synthesized in ionic liquid as green media: Investigation on Nd^{+3}, Tb^{+3}, and Dy^{+3} rare earths adsorption, *Journal of Molecular Liquids*, 308 (2020) 113017. https://doi.org/10.1016/j.molliq.2020.113017
- Hamedreza Javadian, Montserrat Ruiz, Mehdi Taghavi, Ana Maria Sastre, Synthesis of calcium alginate/novel selectively synthesized biodegradable poly(pyrimidine-thiophene-amide) with free hydroxyl groups in ionic liquid as green media /$Ni_{0.2}Zn_{0.2}Fe_{2.6}O_4$ magnetic bionanocomposite powder: Adsorption properties towards rare earth elements, Under Review in *Microchemical Journal*.
- Hamedreza Javadian, Montserrat Ruiz, Mehdi Taghavi, Ana Maria Sastre, One-step hydrothermal synthesis of green synthesized poly(pyrimidine-thiophene-amide) as novel polyamide in imidazolium based ionic liquid as green media/$Ni_{0.2}Zn_{0.2}Fe_{2.6}O_4$ nanocomposite: Investigation on Nd^{+3}, Tb^{+3}, and Dy^{+3} adsorption, Under Review in *Applied Organometallic Chemistry*.

ANNEX I

Ca-alginate/carboxymethyl chitosan/$Ni_{0.2}Zn_{0.2}Fe_{2.6}O_4$ magnetic bionanocomposite: Synthesis, characterization and application for single adsorption of Nd^{+3}, Tb^{+3}, and Dy^{+3} rare earth elements from aqueous media.

Hamedreza Javadian, Montserrat Ruiz, Tawfik A. Saleh, Ana Maria Sastre.

Journal of Molecular Liquids, 306 (2020) 112760.

https://doi.org/10.1016/j.molliq.2020.112760

Journal of Molecular Liquids 306 (2020) 112760

Contents lists available at ScienceDirect

Journal of Molecular Liquids

journal homepage: www.elsevier.com/locate/molliq

Ca-alginate/carboxymethyl chitosan/$Ni_{0.2}Zn_{0.2}Fe_{2.6}O_4$ magnetic bionanocomposite: Synthesis, characterization and application for single adsorption of Nd^{+3}, Tb^{+3}, and Dy^{+3} rare earth elements from aqueous media

Hamedreza Javadian [a,*], Montserrat Ruiz [b], Tawfik A. Saleh [c,*], Ana Maria Sastre [a]

[a] Department of Chemical Engineering, ETSEIB, Universitat Politècnica de Catalunya, Diagonal 647, 08028 Barcelona, Spain
[b] Department of Chemical Engineering, EPSEVG, Universitat Politècnica de Catalunya, Av. Víctor Balaguer, s/n, 08800 Vilanova i la Geltrú, Spain
[c] Chemistry Department, King Fahd University of Petroleum and Minerals, Dhahran 31261, Saudi Arabia

ARTICLE INFO

Article history:
Received 22 November 2019
Received in revised form 18 February 2020
Accepted 20 February 2020
Available online 21 February 2020

Keywords:
Carboxymethyl chitosan
Calcium alginate
$Ni_{0.2}Zn_{0.2}Fe_{2.6}O_4$
Adsorption
Rare earth elements

ABSTRACT

This study aims to research the adsorption of Nd^{+3}, Tb^{+3}, and Dy^{+3} from aqueous media onto the magnetic calcium alginate/carboxymethyl chitosan/$Ni_{0.2}Zn_{0.2}Fe_{2.6}O_4$ (CA/CMC/$Ni_{0.2}Zn_{0.2}Fe_{2.6}O_4$) bionanocomposite in a single system. FE-SEM, FT-IR, EDX, VSM, and TGA were applied to characterize the product. The VSM result showed the saturation magnetization values of 45.87 and 14.14 emu/g for the bare $Ni_{0.2}Zn_{0.2}Fe_{2.6}O_4$ nanoparticles and CA/CMC/$Ni_{0.2}Zn_{0.2}Fe_{2.6}O_4$, respectively. The adsorption results showed that at optimum conditions of contact time of 40 min, pH of 5.5, and 0.8 g/L, the adsorption efficiency of the adsorbent for Nd^{+3}, Tb^{+3}, and Dy^{+3} was 97.75, 96.83, and 97.85%, respectively. The ions adsorption kinetic onto the CA/CMC/$Ni_{0.2}Zn_{0.2}Fe_{2.6}O_4$ was in accordance with pseudo-second-order (PSO) model. The evaluation of equilibrium data was performed by the isotherm models of Langmuir and Freundlich. Fitting the experimental data of Tb^{+3} and Dy^{+3} was done better with Freunlich model than Langmuir model, while fitting tests for Nd^{+3} adsorption data showed better coverage using Langmuir model with a maximum adsorption capacity of 73.37 mg/g. The results of the parameters of thermodynamic showed the endothermic and spontaneous properties of the process. Additionally, the efficacy of the adsorbent was studied using 0.2 M HNO_3 in four adsorptions–desorption cycles. Overall, the obtained results demonstrated that the environmentally friendly magnetic bionanocomposite adsorbent can be applied effectively for Nd^{+3}, Tb^{+3}, and Dy^{+3} adsorption with favorable adsorption efficiency.

1. Introduction

Rare earth elements (REEs) are getting impressive considerations and progressively requested in innovative industries in view of their novel properties [1]. As of late, they have been discovered broad demands in batteries, electronics, and chemical engineering [2,3]. Because of enormous and expanding local requests, China reduced its amount of REEs send out from 50,145 tons in 2009 to just 31,130 tons in 2012. These fare quantities may create difficult issues for REE applicants outside of China, as proved by the crisis of REEs in 2011, recording high costs of these elements [4]. This circumstance has additionally animated many nations, for example, Japan and most EU Member States that don't have any sort of essential REEs stores on their region to search for option and auxiliary resources of REEs and to extend their own REEs industry so as to get a wellspring of REEs, especially heavy REEs [5]. In this manner, a productive method is expected to overcome all difficult issues with respect to REEs.

The conventional methodologies applied for REEs recovery are chemical precipitation, membrane separation, ion-exchange, reverse osmosis, extraction, and adsorption [6–8]. However, each method has its advantages and disadvantages. For instance, chemical precipitation has the advantage of low-cost and simple operation, but large amounts of chemical products are produced, resulting in landfill problems [9]. Membrane separation method has the advantages of high separation efficiency for heavy metal ions, yet low economic feasibility and high maintenance cost restrict its application on a large scale. Adsorption technology, which is easy to perform, highly effective, and low-cost, is considered as a fast and relatively inexpensive approach for metal ions adsorption [10]. Adsorption of REEs has been investigated by some materials such as biosorbents [11–13], carbon [14,15], silica other inorganic [16–18], and polymeric materials [19,20].

* Corresponding authors.
E-mail addresses: hamedreza.javadian@upc.edu, hamedreza.javadian@yahoo.com (H. Javadian), tawfik@kfupm.edu.sa (T.A. Saleh).

https://doi.org/10.1016/j.molliq.2020.112760
0167-7322/

Alginate, as a valuable natural polymer, has pulled in extreme consideration. It is an ordinary polysaccharide that is made up of the residues of mannuronic (M) and guluronic (G) acid (linear copolymer of β-D-mannuronic acid and α-L-guluronic acid units with (1–4) linkages) [21]. This environmentally friendly polymer has highlights of cheapness, plentiful sources, biocompatibility, and hydrophilicity. More often than not, industrially accessible alginates are extraction of brown algae cell wall [22]. It has been broadly utilized in immobilization studies owing to easy preparation, hydrophilicity and efficient adsorption of target contaminations.

Chitosan (CS) as a natural polysaccharide is generally made using the deacetylation of chitin. Its derivatives can be generated by the functional groups' modification, for instance, reactive hydroxyl, amino, and *N*-acetyl groups [23]. Carboxymethyl chitosan (CMC) is considered as the most significant derivatives amongst others. It is the result of the carboxylation of chitosan that has carboxymethyl substituents on amino and hydroxyl groups of the glucosamine units [24]. Because of having special characteristics such as nontoxicity, hydrophilicity, biodegradability, environmentally friendly, and metal-chelating capacity, it is viewed as a potential candidate for bioadsorption. Nevertheless, it couldn't be used for the recovery of ions because of being water-dissolvable and having weak chemical stability [25]. So as to defeat this issue, modification of CMC by other biopolymers such as alginate and inorganic nanoparticles can be regarded as one of the best techniques to increase its hydrolysis resistance.

The purpose of this study was to synthesize the $Ni_{0.2}Zn_{0.2}Fe_{2.6}O_4$ magnetic nanoparticles by the hydrothermal technique and using the synthesized nanoparticles for the synthesis of a bionanocomposite in gelation process of sodium alginate and carboxymethyl chitosan biopolymers in a medium of $CaCl_2$ and glutaraldehyde. After characterizing the product with various techniques including FE-SEM, EDX, XRD, FT-IR, and VSM, it was used as an adsorbent to investigate the adsorption efficiency of Nd^{+3}, Tb^{+3}, and Dy^{+3} depending on adsorbent dosage, pH, contact time, initial metal ion concentration by performing a series of batch experiments. Various kinetic and isotherm models were tested for fitting the experimental data. Thermodynamic parameters (ΔS°, ΔG°, and ΔH°) were also evaluated to find the property of adsorption process. To the best of our knowledge, the utilization of the CA/CMC/$Ni_{0.2}Zn_{0.2}Fe_{2.6}O_4$ has not been studied for Nd^{+3}, Tb^{+3}, and Dy^{+3} adsorption.

2. Materials and methods

2.1. Materials and reagents

Carboxymethyl chitosan and sodium alginate were purchased from Nantong Chem-Base Co, China, and PanReac AppliChem, respectively. $Nd(NO_3)_3.6H_2O$, $Tb(NO_3)_3\cdot 6H_2O$, $Dy(NO_3).5H_2O$, $Zn(NO_3)_2$, $Fe(NO_3)_3.6H_2O$, $Ni(NO_3)_2\cdot 6H_2O$, and glutaraldehyde were bought from Sigma-Aldrich. Since the analytical grade of all chemicals was chosen, they were utilized without further purification. The experiment solutions of Nd^{+3}, Tb^{+3}, and Dy^{+3} were prepared by dilution of 1000 mg/L of ions. The values of pH were regulated via adding a suitable amount of 0.1 M sodium hydroxide or nitric acid solutions and monitored by a pH meter.

2.2. Instrumentation and characterization

FT-IR spectra were recorded on a PerkinElmer, USA, by KBr pellet. XRD pattern was recorded by a GBC MMA instrument with CuK_α radiation in the 2θ range of 10–70^0. A FE-SEM (Zeiss Neon-40, Germany) was also utilized for characterizing the products morphology. The magnetic properties of the products were explored at the room temperature (RT) by employing a VSM (Daghigh Kavir Corporation, Iran). TGA was done on a Mettler TGA/SDTA 851e/LF/1100 thermobalance. The temperature of the sample was increased from RT to 1000 °C (rate = 10 °C/min) under constant nitrogen flow. For analyzing Nd^{+3}, Tb^{+3}, and Dy^{+3} concentration, an Agilent 4100 MP-AES Spectrometer was used.

2.3. Synthesis of the $Ni_{0.2}Zn_{0.2}Fe_{2.6}O_4$ magnetic nanoparticles

The $Ni_{0.2}Zn_{0.2}Fe_{2.6}O_4$ magnetic nanoparticles were synthesized by the hydrothermal method. A mixed solution of 0.2 M Ni^{2+}, 0.2 M Zn^{2+} and 2.6 M Fe^{3+} was prepared in HCl solution, and then NaOH solution was introduced under nitrogen gas and the value of the pH of the mixture was regulated to 10.5. To this mixture, 0.3 g of CTAB was added, and then it was placed into an autoclave (Teflon-lined stainless steel) at 200 °C of an oven for 8 h for hydrothermal treatment. In the following, the temperature of the autoclave was naturally decreased to RT. The precipitate was then collected and washed with deionized water (DW) several times to reach pH = 7. Finally, the obtained particles were dried at 50 °C.

2.4. Synthesis of the CA/CMC/$Ni_{0.2}Zn_{0.2}Fe_{2.6}O_4$ magnetic bionanocomposite

The synthesis procedure of the CA/CMC/$Ni_{0.2}Zn_{0.2}Fe_{2.6}O_4$ was as follows: Sodium alginate (1 g) was dissolved in 80 mL of DW at RT by a laboratory stirrer. 0.50 g of the carboxymethyl chitosan was introduced into the solution and homogeneously mixed. 0.7 g of the $Ni_{0.2}Zn_{0.2}Fe_{2.6}O_4$ was added to the mixture of the biopolymers. To obtain a homogeneous blend solution, the mixture of biopolymers and magnetic particles was stirred at the RT for 24 h. In the following, it was added into the solution of calcium chloride 0.05 M and 2% glutaraldehyde for gelation process. After the completion of gelation process, an external magnetic field was utilized for the separation of the resulting bionanocomposite, and then it was washed using DW several times to eliminate any remaining calcium chloride and glutaraldehyde until the pH of the solution reached 7. The washed CA/CMC/$Ni_{0.2}Zn_{0.2}Fe_{2.6}O_4$ bionanocomposite was dried at 50 °C. Finally, it was powdered.

2.5. Batch adsorption and reusability studies

The stock solutions of metal ions were prepared by dissolving Tb$(NO_3)_3\cdot 6H_2O$, $Nd(NO_3)_3.6H_2O$, and $Dy(NO_3).5H_2O$ separately in DW to achieve 1000 mg/L of each ion, and all the experiment solutions containing 50 mL of single ion prepared by dilution of each stock solution to the required concentration were agitated at 180 rpm by a laboratory shaker. Equal concentration of the ions was applied in single batch adsorption studies. For studying the influences of pH and adsorbent dosage on the ions adsorption efficiency, batch adsorption experiments were performed in the pH range of 1.5–5.5 and dosage range of 0.01–0.06 g, respectively. For the kinetic evaluation, the adsorbent was added into the solutions with 30 mg/L initial concentration, and the tests were performed at different contact time (2.5–70 min). Initial metal concentration in the range of 30–300 mg/L at the optimum time was used to investigate the isotherm of the adsorption. The effect of ionic strength was studied with $NaNO_3$ solution at various concentrations of 0.02, 0.04, 0.06, 0.08, and 0.1 M. To evaluate thermodynamic parameters, the experiments were carried out at three various temperatures of 25, 35 and 45 °C at a constant initial concentration of 90 mg/L. The ions concentration in the solution was measured by an Agilent 4100 MP-AES Spectrometer. The adsorption efficiency (%) and capacity of metal adsorption by the CA/CMC/$Ni_{0.2}Zn_{0.2}Fe_{2.6}O_4$ were computed using the equations in the following:

$$\text{Adsorption efficiency}\ (\%) = (C_0 - C_e)/C_o \times 100 \quad (1)$$

$$q_e = (C_0 - C_e) \times V/m \quad (2)$$

$$q_t = (C_0 - C_t) \times V/m \quad (3)$$

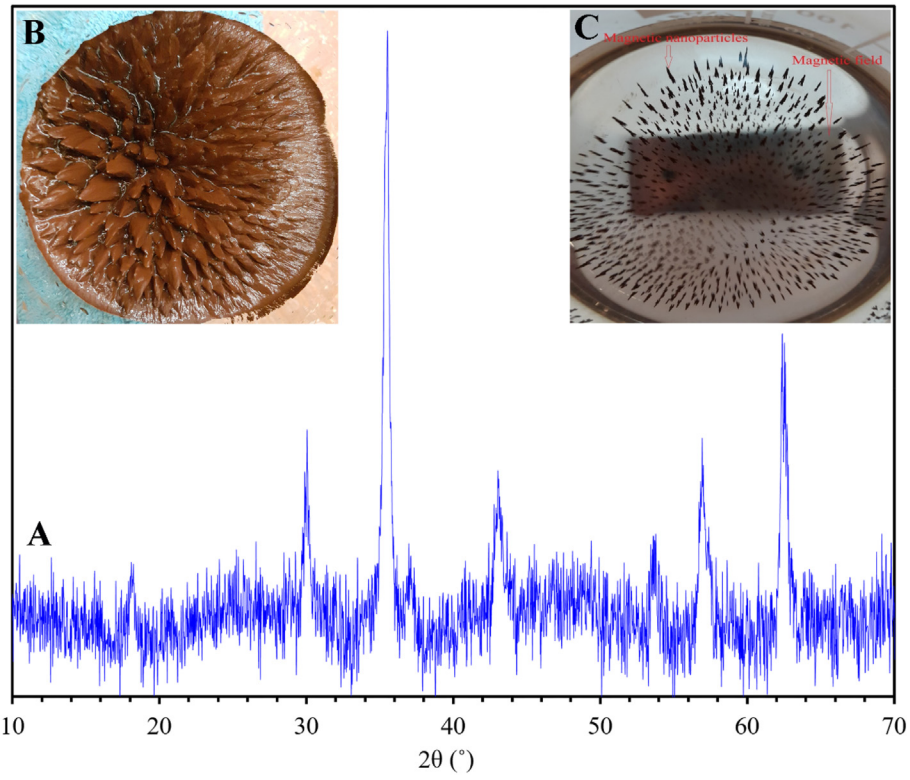

Fig. 1. (A) XRD pattern of $Ni_{0.2}Zn_{0.2}Fe_{2.6}O_4$ nanopartciles; Photo of $Ni_{0.2}Zn_{0.2}Fe_{2.6}O_4$ nanoparticles (B) before drying and (C) in the solution under magnetic field after drying.

where the q_e and q_t (mg/g) refer to the quantities of metal ion adsorbed at equilibrium and adsorption time t in min, respectively. C_0 and C_e show the initial and equilibrium concentrations of metal ion in mg/L, respectively. C_t refers to the concentration of a metal ion in solution at time t (min). Moreover, m refers to the adsorbent weight (g), and V refers to the solution volume in L.

To investigate the reusability of the CA/CMC/$Ni_{0.2}Zn_{0.2}Fe_{2.6}O_4$, a given amount of the adsorbent was treated with 50 mL of 30 mg/L metal solution at pH of 5.5 by a shaker at speed of 180 rpm to obtain the exhausted adsorbent. The ions-loaded adsorbent was separated with an external magnetic field, washed by DW to eliminate the unadsorbed ions and then agitated for 2 h by 50 mL HNO_3 (0.2 M) eluent solution. Subsequently, the regenerated CA/CMC/$Ni_{0.2}Zn_{0.2}Fe_{2.6}O_4$ was separated and washed several times with DW until the solution pH reached 7. The regenerated adsorbent was applied in four cycles of adsorption with the same regeneration procedure.

3. Results and discussion

3.1. Analyses of the products

Fig. 1 indicates the XRD pattern of the $Ni_{0.2}Zn_{0.2}Fe_{2.6}O_4$. The peaks at $2\theta = 18.13°, 30.07°, 35.50°, 37.08°, 43.07°, 53.95°, 56.96°$, and $63.89°$ are in agreement with the standard pattern of nickel zinc ferrite (JCPDS 08-0234) [26]. Full Width at Half Maximum (FWHM) of the strongest reflection of the XRD pattern was utilized to estimate the average crystal size based on the Scherrer equation as following [27]:

$$D = k\lambda/\beta \cos\theta \quad (4)$$

Where k shows the shape function, 0.89, λ refers to the X-ray radiation wavelength, β refers to the FWHM at $2\theta = 35.50°$, and θ shows the diffraction angle. Based on the equation of Scherrer, the calculated value of D was 27.68 nm.

The $Ni_{0.2}Zn_{0.2}Fe_{2.6}O_4$ FE-SEM image in Fig. 2A indicates that the synthesized particles are nearly spherical in shape and homogenous in distribution with a diameter of <100 nm. Fig. 2B shows the distribution of the magnetic nanoparticles on the surface of the CA/CMC or embedding with the CA/CMC that confirms the successful synthesis of the CA/CMC/$Ni_{0.2}Zn_{0.2}Fe_{2.6}O_4$ magnetic bionanocomposite.

Fig. 3 indicates the FT-IR spectra of CA, CMC, $Ni_{0.2}Zn_{0.2}Fe_{2.6}O_4$, and CA/CMC/$Ni_{0.2}Zn_{0.2}Fe_{2.6}O_4$. The FT-IR spectra of CA and CMC respectively in Fig. 3A and B show O—H stretching vibration at 3389 (CA) and 3436 (CMC) cm^{-1}, carboxylic groups asymmetrical stretching at 1622 (CA) and 1631 (CMC) cm^{-1}, carboxylic groups symmetrical stretching at 1423 (CA) and 1411 (CMC) cm^{-1} and C-O-C stretching at 1052 (CA) and 1061 (CMC) cm^{-1} [28,29]. The FT-IR spectrum of the $Ni_{0.2}Zn_{0.2}Fe_{2.6}O_4$ in Fig. 3C shows a broad absorption band with a value of 3424 cm^{-1} and less intensive band at 1633 cm^{-1} related to the O—H groups stretching vibration [30]. The bands at 2925 and 2853 cm^{-1} respectively correspond to the anti-symmetric and symmetric C—H vibrations of CTAB [31]. The band at 567 cm^{-1} relates to the inherent metal stretching vibrations at the tetrahedral site (Fe—O), and the value of 478 cm^{-1} is related to the octahedral metal (M-O) stretching [30]. The comparison of the spectrum in Fig. 3D with other spectra expresses the successful synthesis of the CA/CMC/$Ni_{0.2}Zn_{0.2}Fe_{2.6}O_4$.

EDX was recorded to analyze the elements of the products (Fig. 4). Fig. 4A shows Ni, Zn, Fe, and O peaks that confirm the formation of the $Ni_{0.2}Zn_{0.2}Fe_{2.6}O_4$. The elemental analysis of the nanocomposite in Fig. 4B represents similar peaks available in Fig. 4A along with the new peaks for N and Ca because of combining the nanoparticles with CA and CMC. Sodium peak is not seen in the spectrum of the CA/CMC/$Ni_{0.2}Zn_{0.2}Fe_{2.6}O_4$, suggesting that sodium ions were released completely from the matrix of sodium alginate into the solution during the crosslinking reaction process of sodium alginate with calcium.

The CA/CMC/$Ni_{0.2}Zn_{0.2}Fe_{2.6}O_4$ weight loss curve recorded in the range of RT to 1000 °C is demonstrated in Fig. 5A. As it is seen, there are three different weight-loss steps in the TGA curve of the CA/CMC/

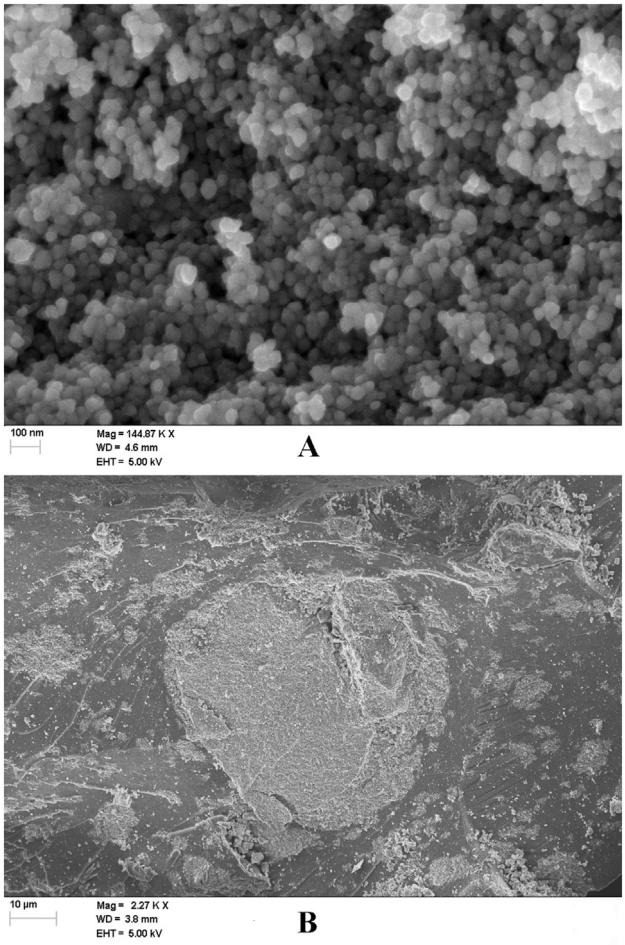

Fig. 2. FE-SEM images of (A) $Ni_{0.2}Zn_{0.2}Fe_{2.6}O_4$ and (B) CA/CMC/$Ni_{0.2}Zn_{0.2}Fe_{2.6}O_4$.

$Ni_{0.2}Zn_{0.2}Fe_{2.6}O_4$. Obviously, the first step (around 190 °C) with a weight loss of 8.77% can be attributed to trapped and physisorbed water evaporation. The second step between around 190 and 550 °C is the largest weight loss with the amount of 35.08% that could be due to the sorption and degradation of CA and CMC. The last step with 22.95% weight loss at a temperature beyond 550 °C could be related to the further decomposition of CA and CMC and their conversion to CO_2 and H_2O. At the end of the process, the residue percentage is about 33.2% that is principally assigned to the presence of the $Ni_{0.2}Zn_{0.2}Fe_{2.6}O_4$.

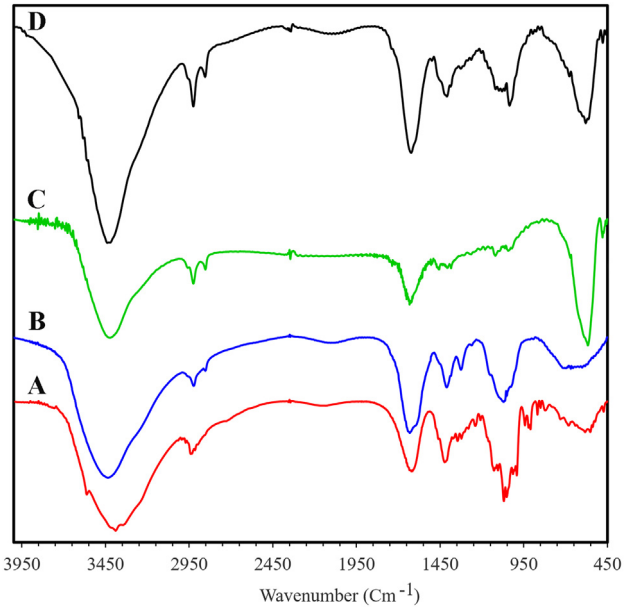

Fig. 3. FT-IR spectra of (A) CA, (B) CMC, (C) $Ni_{0.2}Zn_{0.2}Fe_{2.6}O_4$, and (D) CA/CMC/$Ni_{0.2}Zn_{0.2}Fe_{2.6}O_4$.

An important issue related to the magnetic bionanocomposite is that it should possess sufficient magnetic properties for its practical application. According to the magnetic hysteresis loops in Fig. 5B, the saturation magnetization value for $Ni_{0.2}Zn_{0.2}Fe_{2.6}O_4$ is about 45.87 emu/g that indicates superparamagnetic behavior of the synthesized product. It is obvious from Fig. 5C that the process of the synthesis of the CA/CMC/$Ni_{0.2}Zn_{0.2}Fe_{2.6}O_4$ results in a decrease of saturation magnetization to the value of 14.14 emu/g. This decline is due to the combination of the magnetic nanoparticles with CA and CMC. Despite this difference, the ions-loaded CA/CMC/$Ni_{0.2}Zn_{0.2}Fe_{2.6}O_4$ could be easily separated by applying an external magnetic field from aqueous solution to avoid secondary pollution as indicated in Fig. 5D.

3.2. pH effect

pH of the solution as a key parameter of the adsorption process affects solution chemistry, metal speciation, adsorption capacity, the activity of adsorbent functional groups, and mechanism of adsorption. It is associated directly with H^+ competition with ions for the occupation of the surface active sites of the adsorbent. Adsorption efficiency values of Nd^{+3}, Tb^{+3}, and Dy^{+3} onto the CA/CMC/$Ni_{0.2}Zn_{0.2}Fe_{2.6}O_4$ as a pH function are demonstrated in Fig. 6A. Electrostatic interaction could have a key role on Nd^{+3}, Tb^{+3}, and Dy^{+3} adsorption onto the CA/CMC/$Ni_{0.2}Zn_{0.2}Fe_{2.6}O_4$ at different pH values. It can be interpreted that at lower pH values, the adsorption efficiency of the adsorbent is low and increase with increasing solution pH. At pH = 1.5 that is highly acidic, the protonation of the adsorbent functional groups blocks the metal ions approach to the binding sites of the adsorbent. The metal ions and H^+ ions compete for the same binding sites of the adsorbent, leading to decrease in adsorption efficiency [32]. At pH = 1.5, adsorption efficiency value is zero for all ions. When pH values are adjusted between 2.5 and 5.5, adsorption efficiency for Nd^{+3}, Tb^{+3}, and Dy^{+3} onto the CA/CMC/$Ni_{0.2}Zn_{0.2}Fe_{2.6}O_4$ increases with pH increase owing to the reduction in competition between H^+ ions and metal ions. The maximum adsorption efficiency for all metal ions occurs at pH = 5.5. pH increase beyond 5.5 was not investigated to prohibit the precipitation of the ions in the form of hydroxide. Further experiments were carried out at pH = 5.5 as optimum pH.

3.3. Contact time effect

It is essential to consider the adsorption rate in designing the batch experiments. The influence of contact time on Nd^{+3}, Tb^{+3}, and Dy^{+3} adsorption onto the CA/CMC/$Ni_{0.2}Zn_{0.2}Fe_{2.6}O_4$ bionanocomposite is shown in Fig. 6B. As can be observed, adsorption efficiency of the adsorbent increases rapidly during the first period and then increases slowly until reaching equilibrium state. The experimental outcomes indicate that Nd^{+3}, Tb^{+3}, and Dy^{+3} adsorption can be split into two definite parts: an extremely rapid initial adsorption occurs in the first 10 min, and then much slower adsorption is seen for higher contact time. In general, approximately 80% of the metal ions contact quickly in the first 10 min because of the presence of largely accessible active sites of the adsorbent and then slowly increase owing to a gradual decrease in the active sites and weakness of the driving force and finally adsorption reaches equilibrium [33]. The contact time of 40 min was taken as an optimum time for adsorption of Nd^{+3}, Tb^{+3}, and Dy^{+3}.

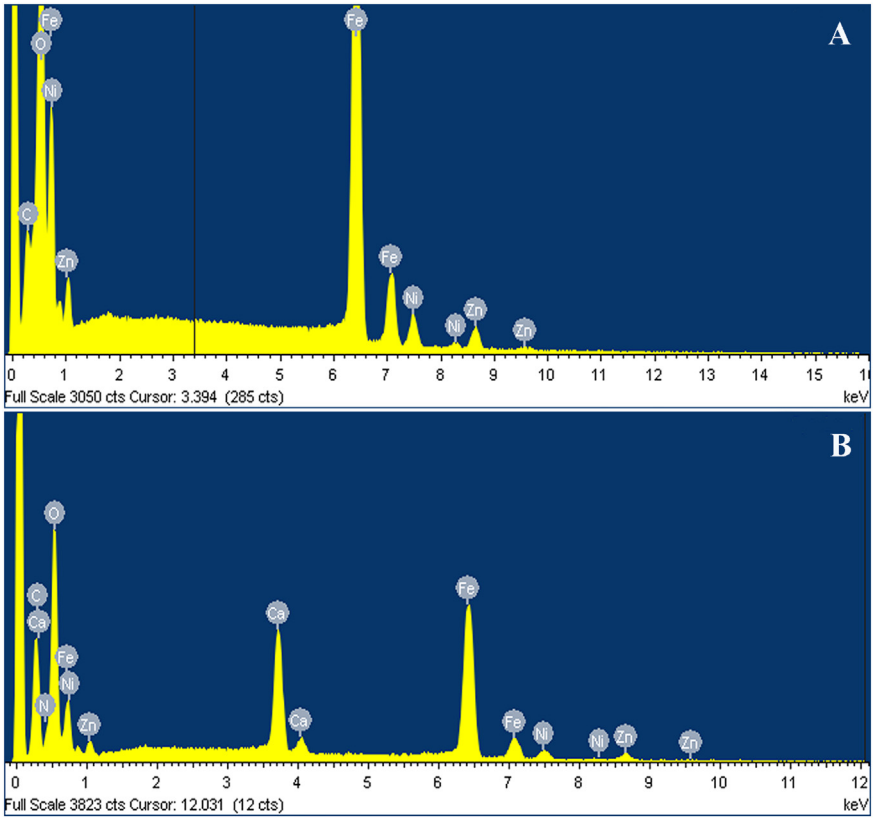

Fig. 4. EDX spectra of (A) $Ni_{0.2}Zn_{0.2}Fe_{2.6}O_4$ and (B) CA/CMC/$Ni_{0.2}Zn_{0.2}Fe_{2.6}O_4$.

3.4. Adsorbent dosage effect

The adsorbent dosage is considered as an important factor that affects the adsorption process and determines adsorbent capacity by the quantity of binding sites accessible for the adsorption of a specified initial concentration. Fig. 6C depicts the dependency of Nd^{+3}, Tb^{+3}, and Dy^{+3} adsorption efficiency to the adsorbent dosage. It expresses that Nd^{+3}, Tb^{+3}, and Dy^{+3} adsorption efficiency onto the adsorbent increase steeply (53.08–95.29, 51.4–94.43, and 59.04–96.1%, respectively) by increasing adsorbent dosage in the range of 0.01 to 0.03 g. Although increasing the adsorbent dosage indicates an increase in number of binding sites available for ions adsorption, adsorption efficiency for all ions remains unchanged at a dosage higher than 0.04 g since the adsorption reaches equilibrium. Therefore, the optimum dosage of 0.04 g in 50 mL solution (0.8 g/L) was used for studying other adsorption parameters.

3.5. Initial concentration effect

Fig. 6D shows the adsorption efficiency values of the CA/CMC/$Ni_{0.2}Zn_{0.2}Fe_{2.6}O_4$ at different metal ions concentrations of 30 to 300 mg/L. It is demonstrated that the adsorption efficiency decreases by increasing the initial concentration because a given amount of the adsorbent has constant binding sites that are not enough at higher concentration to adsorb the ions, while calculating the capacity of the adsorbent showed that it respectively increased from 36.49 to 74.4, 36.31 to 103.23, and 36.68 to 118.17 mg/g for Nd^{+3}, Tb^{+3}, and Dy^{+3}. These results are due to a larger driving force at higher initial ion concentration that overcomes the whole mass transfer resistance available between the solid and liquid phases, causing more collisions between Nd^{+3}, Tb^{+3}, and Dy^{+3} and the active sites of the CA/CMC/$Ni_{0.2}Zn_{0.2}Fe_{2.6}O_4$ bionanocomposite that result in higher adsorption of the ions [34].

3.6. Adsorption kinetics and isotherms

Adsorption efficiency can be evaluated by adsorption kinetics as a key characteristic of adsorption process. Three kinetic methods namely pseudo-first-order (PFO), PSO, and intra-particle diffusion (IPD) were employed to fit the experimental data for the prediction of the kinetic parameters as following:

The PFO equation is written as follows [35]:

$$q_t = q_e\left(1 - \exp.^{-K_1^t}\right) \tag{5}$$

where K_1 shows the PFO rate constant (1/min).

The PSO kinetic equation [36] is presented as follows:

$$q_t = K_2 {q_e}^2 t/1 + K_2 q_e t \tag{6}$$

where K_2 (g/mg min) shows PSO rate constant.

The initial adsorption rate (h) can be computed using the values of K_2 and q_e by the following equation:

$$h = K_2 {q_e}^2 \tag{7}$$

The IPD equation [37] is written as follows:

$$q_t = K_i t^{0.5} + C \tag{8}$$

where K_i (1/min) refers to IPD rate constant, and C provides data about the boundary layer thickness: the greater value of C corresponds to the boundary layer diffusion influence.

For understanding the mechanism of the adsorption process, adsorption isotherms are applied. Langmuir and Freundlich isotherms were chosen as two important isotherm models in this study. Regarding Langmuir adsorption isotherm, monolayer adsorption occurs within the

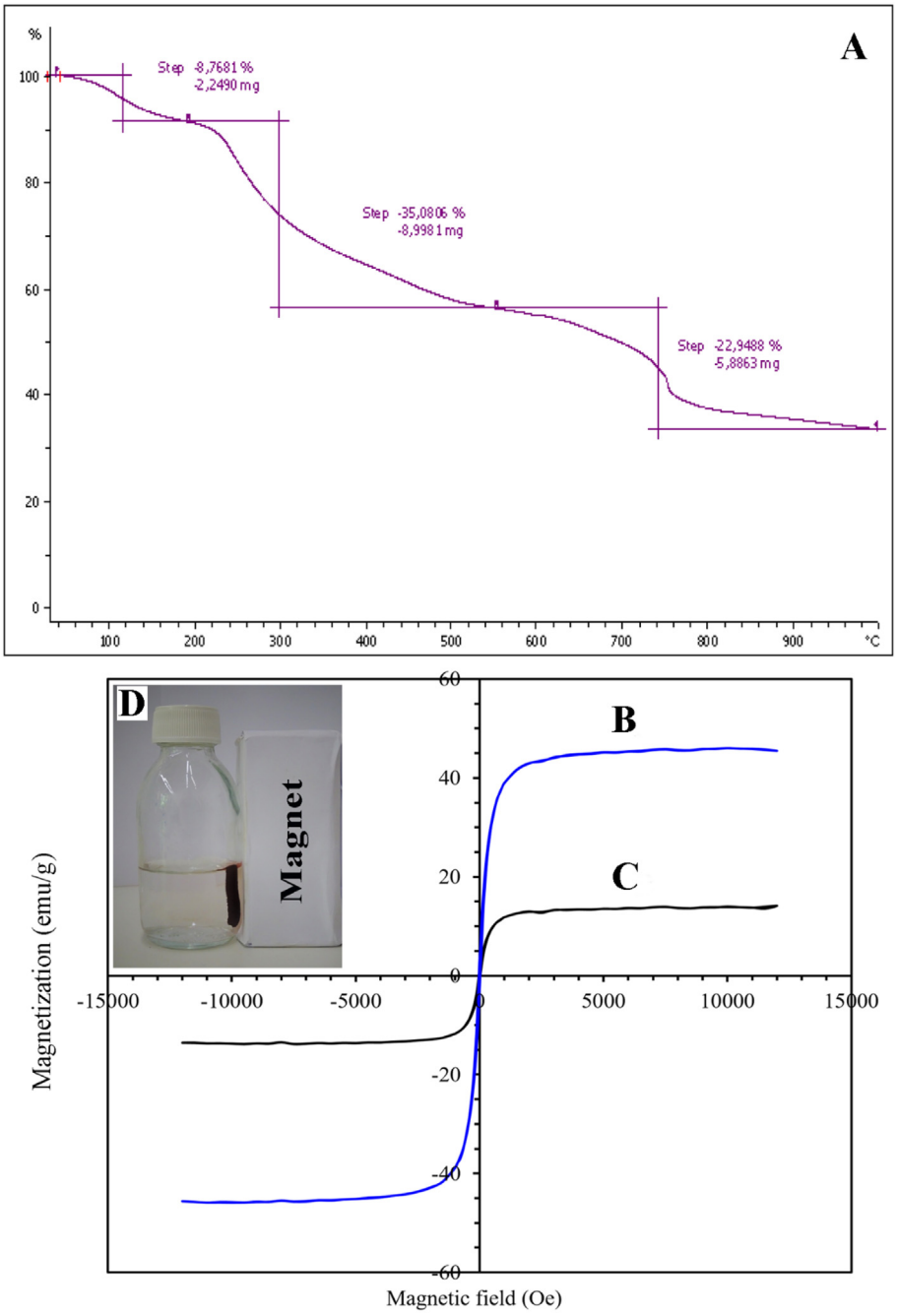

Fig. 5. (A) TGA curve of CA/CMC/$Ni_{0.2}Zn_{0.2}Fe_{2.6}O_4$; Magnetization curves of (B) $Ni_{0.2}Zn_{0.2}Fe_{2.6}O_4$ and (C) CA/CMC/$Ni_{0.2}Zn_{0.2}Fe_{2.6}O_4$; (D) Magnetic separation of the ions-loaded adsorbent.

adsorbent at specific homogeneous sites. The nonlinear form of Langmuir isotherm is expressed using the following equation [38]:

$$q_e = \frac{b\ qm\ Ce}{(1 + bCe)} \tag{9}$$

where q_e and q_m (mg/g) respectively show the equilibrium capacity of adsorption and the maximum adsorption capacity. C_e (mg/L) is ion equilibrium concentration, and b (L/mg) shows the constant of Langmuir model.

The main characteristic of Langmuir model is indicated by 'R_L', which is a dimensionless constant that is generally known as separation factor or equilibrium parameter. It is indicated by the bellowing equation:

$$RL = \frac{1}{1 + bC_i} \tag{10}$$

where C_i (mg/L) shows the greatest initial metal concentration.

Freundlich isotherm is performed to explain heterogeneous systems. The nonlinear form of Freundlich isotherm is presented as follows [39]:

$$q_e = K\ C_e^{1/n} \tag{11}$$

where K ($mg^{1-1/n}\ L^{1/n}/g$) refers to the constant of Freundlich isotherm,

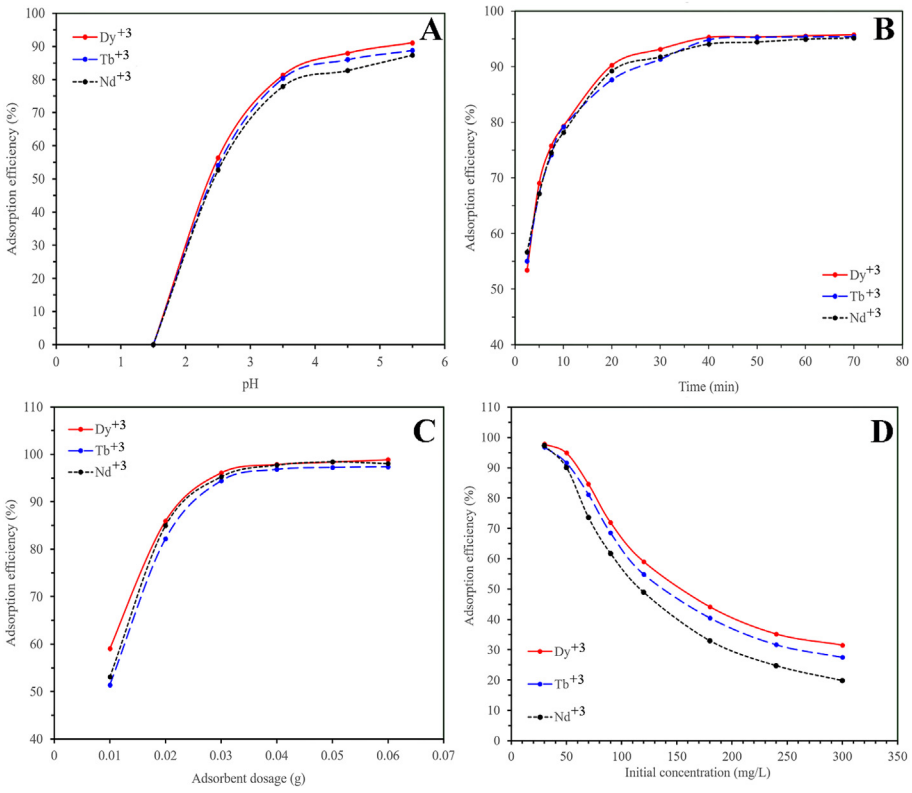

Fig. 6. Effects of (A) pH, (B) contact time, (C) adsorbent dosage, and (D) initial concentration on the adsorption of the ions.

and n shows adsorption intensity. A value of $n > 1$ expresses that adsorption is desirable.

Fitting the experimental data with the kinetic and isotherm models was optimized by error analysis. In this study, Chi-square (χ^2) was used to compare the validity of each model by the following equation:

$$\chi^2 = \sum_{i=1}^{n} \frac{\left(q_{e,\,exp} - q_{e,cal}\right)^2}{q_{e,cal}} \tag{12}$$

where $q_{e,exp}$ and $q_{e,cal}$ respectively refer to the experimental and computed adsorbent capacities, and n shows data point numbers.

Table 1 indicates essential parameters computed from the kinetic models. The theoretical values of q_e obtained from PFO kinetic model in Nd^{+3}, Tb^{+3}, and Dy^{+3} adsorption are not in agreement with the experimental values, while the experimental values of q_e ($q_{e,exp}$) are close to theoretical q_e ($q_{e,cal}$) values calculated by PSO model. The coefficient of determination values obtained by fitting the data with PFO model is lower than those of PSO model. Consequently, PSO model can be chosen to fit the data more efficiently compared to PFO model. According to IPD model, involving IPD in adsorption process creates a linear plot of uptake, q_t versus $t^{0.5}$. Furthermore, the rate controlling step is shown by IPD model if the lines pass through the origin. The values of R^2 show that IPD model is not appropriate for explaining the adsorption kinetic. The values of R^2 and error analyses obtained by PSO kinetic model are respectively the highest and lowest values. Therefore, Nd^{+3}, Tb^{+3}, and Dy^{+3} adsorption onto the CA/CMC/$Ni_{0.2}Zn_{0.2}Fe_{2.6}O_4$ are well described by PSO model. The results express that the rate-limiting step in Nd^{+3}, Tb^{+3}, and Dy^{+3} adsorption is chemisorption that involves valence forces by exchanging or sharing electrons between the adsorbent and the ions. The K_2 value from the PSO model for Dy^{+3} is greater than the values obtained for Nd^{+3} and Tb^{+3} ions, suggesting that Dy^{+3} adsorption onto the adsorbent is faster than those of Nd^{+3} and Tb^{+3} ions. From the results of isotherm fitting shown in Table 2, Tb^{+3} and Dy^{+3} adsorption data for the CA/CMC/$Ni_{0.2}Zn_{0.2}Fe_{2.6}O_4$ were fitted well with Freundlich isotherm model with the R^2 values of 0.9905 and 0.9751, respectively, suggesting the adsorption of the ions on heterogeneous sites. In the case of Nd^{+3}, the data

Table 1
Kinetic constants for adsorption of Nd^{+3}, Tb^{+3}, and Dy^{+3} by the CA/CMC/$Ni_{0.2}Zn_{0.2}Fe_{2.6}O_4$.

		Nd^{+3}	Tb^{+3}	Dy^{+3}
PFO	K_1 (1/min)	0.279	0.271	0.269
	q_e (mg/g)	45.91	46.05	46.54
	R^2	0.8506	0.8712	0.9099
	χ^2	7.91	7.29	5.34
PSO	K_2 (g/mg min)	0.00967	0.00916	0.00899
	q_e (mg/g)	48.95	49.21	49.72
	h (mg/g min)	23.17	22.18	22.22
	R^2	0.9831	0.9893	0.9956
	χ^2	0.89	0.60	0.26
IPD	K_i (1/min)	11.33	11.73	11.76
	R^2	0.9063	0.9091	0.8723
	χ^2	4.96	5.14	7.57

Table 2
Isotherm constants for adsorption of Nd^{+3}, Tb^{+3}, and Dy^{+3} by the CA/CMC/$Ni_{0.2}Zn_{0.2}Fe_{2.6}O_4$.

		Nd^{+3}	Tb^{+3}	Dy^{+3}
Langmuir	b (L/mg)	1.075	0.8	0.546
	q_m (mg/g)	73.37	88.61	100.20
	R_L	0.003	0.004	0.006
	R^2	0.9703	0.7163	0.8212
	χ^2	6.04	157.16	144.07
Freundlich	K ($mg^{1-1/n}\,L^{1/n}/g$)	46.80	46.31	46.65
	n	10.31	6.83	5.93
	R^2	0.8364	0.9905	0.9751
	χ^2	33.32	5.23	20

of adsorption were efficiently fitted with Langmuir isotherm with the R^2 value of 0.9703, suggesting that the Langmuir surface adsorption mechanism controls the adsorption of Nd^{+3} onto the CA/CMC/$Ni_{0.2}Zn_{0.2}Fe_{2.6}O_4$. Therefore, it can be mentioned that the number of adsorption sites of the adsorbent is limited that leads to the monolayer adsorption of Nd^{+3}, and no further adsorption occurs when covering the active sites with the ions takes place. R_L exhibits favorable isotherm if $0 < R_L < 1$, unfavorable if $R_L > 1$, irreversible if $R_L = 0$ or linear if $R_L = 1$ [40]. R_L value in Table 2 is between 0 and 1 for Nd^{+3}, Tb^{+3}, and Dy^{+3} adsorption onto the CA/CMC/$Ni_{0.2}Zn_{0.2}Fe_{2.6}O_4$, indicating that the adsorption process is favorable. The values of n for adsorption of the ions are higher than 1, representing a favorable adsorption condition. A comparison of the adsorption capacity of different adsorbents is represented in Table 3.

3.7. Ionic strength effect

It has been confirmed that salts presence in the solution can affect adsorption efficiency. The adsorption efficiency of Nd^{+3}, Tb^{+3}, and Dy^{+3} was studied in the existence of $NaNO_3$ in the range of 0.02 to 0.1 M at the constant concentration of the ions (30 mg/L). The obtained results are indicated in Fig. 7A. The adsorption efficiency of the adsorbent decreases for Nd^{+3}, Tb^{+3}, and Dy^{+3} from 97.75 to 85.7, 96.83 to 84.73, and 97.85 to 93.5%, respectively, that shows the ionic strength slightly affects on the adsorption of Dy^{+3} in comparison with the decrease obtained for Nd^{+3} and Tb^{+3}. The decrease in the adsorption efficiency could be associated with Na^+ ions competition with the metal ions for the CA/CMC/$Ni_{0.2}Zn_{0.2}Fe_{2.6}O_4$ active adsorption sites [64]. Enhancing Na^+ ion concentration may also lead to a reduction in the activity coefficient of the metal ions that cause the limitation of the ions transfer to the adsorbent surface [65].

Table 3
Comparison of the adsorption capacity of Nd^{+3}, Tb^{+3}, and Dy^{+3} onto various adsorbents.

Adsorbent	q_m (mg/g)			Reference
	Nd^{+3}	Tb^{+3}	Dy^{+3}	
Fe3O4-C18-chitosan-DETA	27.1		28.3	[41]
EDTA functionalized chitosan	74			[42]
Phosphonic acid functionalized silica microspheres	45			[43]
γ-Fe_2O_3-NH_4OH@SiO_2 (APTMS)			23.2	[44]
Cellulose functionalized with thiourea	73			[45]
MIL-101-PMIDA	70.9			[46]
A layered thiostannate, $(Me_2NH_2)_{1.33}(Me_3NH)_{0.67}Sn_3S_7 \cdot 1.25H_2O$ (FJSM-SnS)	126			[47]
Oxidized multi-walled carbon nanotubes			78.12	[48]
Lanthanide-ion imprinted polymers	126.5			[49]
Macroporous polymeric resin (TVEX-PHOR)		24.93		[50]
TA-MWCNTs		8.55		[51]
PAAm–YZ		42.9		[52]
Poly(acrylamide-expanded perlite) [P(AAm-EP)]		118.3		[53]
P(HEMA–Hap)		109.66		[54]
Poly(amidoxime-hydroxamic acid) resins		125		[55]
CaHAP/NF		130.43		[56]
Acryloyl–phenyl thiourea		74.23		[57]
Hybrid Lewis base ligands functionalized alumina-silica			125.4	[58]
CA@Fe_3O_4 NPs	41			[59]
11-Molybdo-vanadophosphoric acid supported on Zr modified mesoporous silica SBA-15			50	[60]
MPS (22 nm)-2NH-2COOH			44.8	[61]
o-CNCs/GO-IIPs			48.14	[62]
Imprinted mesoporous silica materials			22.33	[63]
CA/CMC/$Ni_{0.2}Zn_{0.2}Fe_{2.6}O_4$	73.37	101.61[a]	114.74[a]	This study

[a] Calculated from Freundlich isotherm.

3.8. Temperature effect

The temperature influence on the adsorption efficiency of Nd^{+3}, Tb^{+3}, and Dy^{+3} onto the CA/CMC/$Ni_{0.2}Zn_{0.2}Fe_{2.6}O_4$ bionanocomposite was studied by performing the experiments at various temperatures (25, 35, and 45 °C), and the results are demonstrated in Table 4. As can be observed, the adsorption efficiency increases for all metal ions with temperature increase that may be owing to the increase in metal ions mobility and their tendency to be adsorbed onto the adsorbent surface, and due to higher activity of the binding sites with an increase in temperature as well.

3.9. Thermodynamic parameters evaluation

The ΔH° and ΔS° thermodynamic parameters were computed as follows [66]:

$$\mathrm{Ln}\ K_d = \frac{\Delta S^\circ}{R} - \frac{\Delta H^\circ}{RT} \tag{13}$$

where R shows the gas constant (8.314 J/mol K), and T refers to the temperature (K). The intercept and slope of the curves of Ln K_d versus 1/T are used to calculate the values of ΔS° and ΔH°, respectively (Fig. 7B).

K_d demonstrates the distribution coefficient that was obtained by the following equation [67]:

$$K_d = \frac{q_e}{C_e} \tag{14}$$

The ΔG° quantities were also computed at different temperatures utilizing the bellowing equation [68]:

$$\Delta G^\circ = -RT\ \mathrm{Ln}\ K_d \tag{15}$$

The obtained thermodynamic parameters at different temperatures in Table 4 indicate that Nd^{+3}, Tb^{+3}, and Dy^{+3} adsorption onto the CA/CMC/$Ni_{0.2}Zn_{0.2}Fe_{2.6}O_4$ is naturally feasible and spontaneous due the negative quantities of Gibbs free energy changes. In addition, by increasing temperature from 25 °C to 35 and 45 °C, the value of Gibbs free energy change for Nd^{+3}, Tb^{+3}, and Dy^{+3} adsorption onto the adsorbent becomes more negative, indicating more feasibility of the adsorption of the metal ions onto the adsorbent at higher temperature [67]. The ΔH° positive values suggest the endothermic adsorption process of Nd^{+3}, Tb^{+3}, and Dy^{+3} onto the adsorbent [66]. Furthermore, the ΔS° positive values indicate that the randomness and disorder at the solid-solution interface increases during the adsorption of the ions [68].

3.10. Reusability studies

The desorption process resulted in the desorption efficiency values of > 95, 96, and 99 % for Nd^{+3}, Tb^{+3}, and Dy^{+3} ions, respectively. The results of the ions adsorption efficiency of the adsorbent regarding the cycle number by 0.04 g of the adsorbent are displayed in Fig. 7C. As can be seen, the highest adsorption efficiency of Nd^{+3}, Tb^{+3}, and Dy^{+3} adsorption is related to the first cycle because the number of fresh active sites existing on the adsorbent surface for Nd^{+3}, Tb^{+3}, and Dy^{+3} adsorption is abundant; therefore, adsorption occurs through the stronger bonds. It is seen that the first cycle respectively results in adsorption efficiencies of 96.72, 96.32, and 97.12% for Nd^{+3}, Tb^{+3}, and Dy^{+3} by the CA/CMC/$Ni_{0.2}Zn_{0.2}Fe_{2.6}O_4$. The adsorption efficiency for the metal ions is found to be decreased during the four adsorption-desorption cycles; nevertheless, the reduction is not so significant. The obtained results at the end of the fourth cycle signify that the adsorption efficiency of the CA/CMC/$Ni_{0.2}Zn_{0.2}Fe_{2.6}O_4$ remains >95, 94, and 95% for Nd^{+3}, Tb^{+3}, and Dy^{+3}, respectively, and the slight decrease in adsorption efficiency could be related to the fact that Nd^{+3}, Tb^{+3}, and Dy^{+3} are not released from adsorption sites during the cycles, leading to the

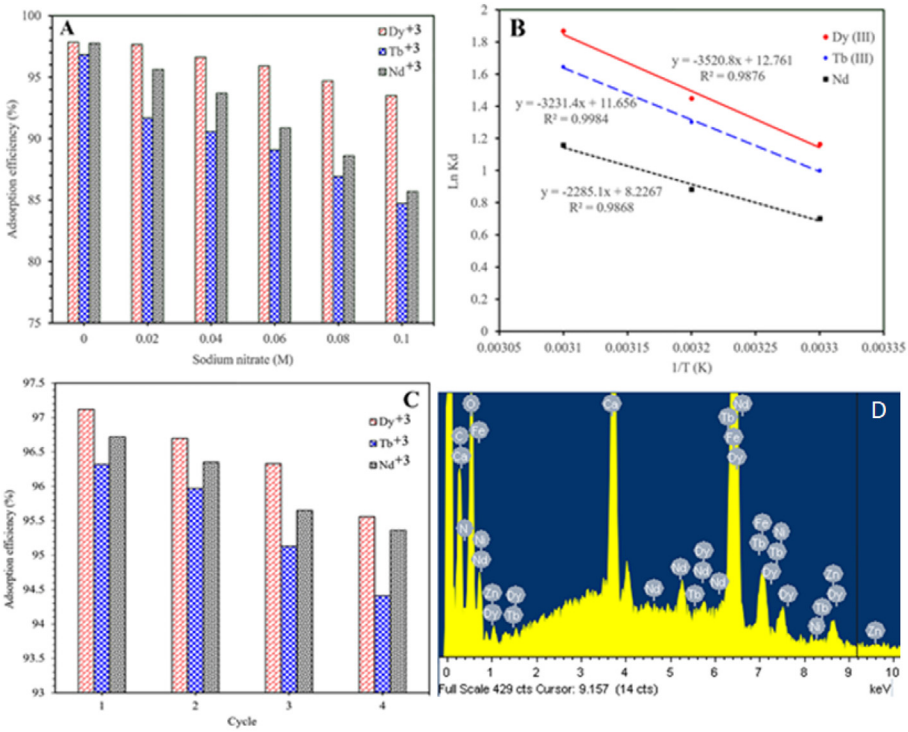

Fig. 7. (A) Effect of ionic strength on the adsorption of Nd^{+3}, Tb^{+3}, and Dy^{+3}, (B) Ln K_d versus 1/T for calculation of enthalpy and entropy changes, (C) Reusability of CA/CMC/$Ni_{0.2}Zn_{0.2}Fe_{2.6}O_4$ for adsorption of the ions, and (D) EDX spectrum of CA/CMC/$Ni_{0.2}Zn_{0.2}Fe_{2.6}O_4$ after adsorption of the ions.

inactivation of a portion of the surface sites. The obtained results suggest the CA/CMC/$Ni_{0.2}Zn_{0.2}Fe_{2.6}O_4$ as a recyclable adsorbent for Nd^{+3}, Tb^{+3}, and Dy^{+3} adsorption.

3.11. Competitive adsorption

To evaluate competitive adsorption of Nd^{+3}, Tb^{+3}, and Dy^{+3} in the ternary system of 30 mg/L (1:1:1), 0.04 g of the CA/CMC/$Ni_{0.2}Zn_{0.2}Fe_{2.6}O_4$ (the same as a single system) was used. According to the value of q_{mix}/q_0, three kinds of influences including antagonism, synergism, and non-interaction can occur in a multicomponent system as following:

- Antagonism ($q_{mix}/q_0 < 1$): the influence of component mixture in solution is lower than its influence in single mode.
- Synergism ($q_{mix}/q_0 > 1$): the influence of component mixture in solution is higher than its influence in single mode.
- Non-interaction ($q_{mix}/q_0 = 1$): the influence of the component mixture in solution is neither less nor more compared with its influence in single mode.

Table 4
Effect of temperature on the adsorption of Nd^{+3}, Tb^{+3}, and Dy^{+3} at 90 mg/L and thermodynamic parameters.

Temperature (°C)	Adsorption efficiency (%)		
	Nd^{+3}	Tb^{+3}	Dy^{+3}
25	61.72	68.51	71.95
35	65.95	74.61	77.31
45	71.81	80.59	83.84

		Thermodynamic parameters		
		Nd^{+3}	Tb^{+3}	Dy^{+3}
ΔH° (kJ/mol)		19.00	26.86	29.27
ΔS° (kJ/mol K)		0.068	0.097	0.106
	Temperature (°C)			
ΔG° (kJ/mol)	25	−1.737	−2.478	−2.887
	35	−2.263	−3.331	−3.71
	45	−3.062	−4.353	−4.943

Where q_{mix} and q_0 are the adsorption capacities of each ion in the mixture and single systems, respectively.

The value of q_{mix}/q_0 for each ion was respectively calculated to be 0.27, 0.5, and 0.52 for Nd^{+3}, Tb^{+3} and Dy^{+3}. The obtained results state that the q_{mix}/q_0 value for all ions is <1 in a ternary mixture; therefore, the existence of each ion shows an antagonism influence on the adsorption of other ions in the process. The adsorption efficiency of the adsorbent for Nd^{+3}, Tb^{+3}, and Dy^{+3} decreased to 28.25, 48.62, and 50.58%, respectively. EDX spectrum was also recorded after the ions adsorption process, and the result is illustrated in Fig. 7D. The existence of Nd^{+3}, Tb^{+3}, and Dy^{+3} in the spectrum strongly confirms the successful adsorption of these ions from a ternary mixture by the CA/CMC/$Ni_{0.2}Zn_{0.2}Fe_{2.6}O_4$.

4. Conclusion

The goal of this research work was to synthesize the CA/CMC/$Ni_{0.2}Zn_{0.2}Fe_{2.6}O_4$ as a novel magnetic bionanocomposite adsorbent for adsorption of Nd^{+3}, Tb^{+3}, and Dy^{+3} from aqueous media. The adsorbent was characterized by FE-SEM, EDX, XRD, FT-IR, EDX, and VSM techniques, and the influence of different factors such as pH, contact time, adsorbent dosage, initial concentration, ionic strength, and temperature was considered by batch adsorption tests. The maximum adsorption capacity of the CA/CMC/$Ni_{0.2}Zn_{0.2}Fe_{2.6}O_4$ for Nd^{+3} acquired by Langmuir isotherm model was 73.37 mg/g at pH = 5.5, while Freundlich model fitted the Tb^{+3} and Dy^{+3} adsorption data at the same conditions. Kinetic studies indicated that PSO with the highest R^2 and lowest error can describe the adsorption mechanism of the metal ions. The results obtained

from affecting $NaNO_3$ as ionic strength showed a slight reduction in the values of adsorption efficiency. The values of the parameters of thermodynamic (ΔG°, ΔS°, and ΔH°) demonstrated that the metal ions adsorption was endothermic and spontaneous in nature. 0.2 M HNO_3 easily desorbed the ions, and the adsorbent was utilized four times with the adsorption efficiency values of >95, 94, and 95% for Nd^{+3}, Tb^{+3}, and Dy^{+3}, respectively, at the end of the fourth cycle. The results of this study showed the CA/CMC/$Ni_{0.2}Zn_{0.2}Fe_{2.6}O_4$ as a promising novel adsorbent for Nd^{+3}, Tb^{+3}, and Dy^{+3} adsorption.

CRediT authorship contribution statement

Hamedreza Javadian: Investigation, Data curation, Formal analysis, Writing - original draft, Writing - review & editing. **Montserrat Ruiz:** Data curation, Supervision. **Tawfik A. Saleh:** Writing - review & editing. **Ana Maria Sastre:** Conceptualization, Supervision.

Declaration of competing interest

There is not conflict of interest.

Acknowledgments

This work has been supported by the Spanish Ministry of Economy and Competitiveness (Ref. CTM2017-83581-R). Hamedreza Javadian acknowledges the financial support received (Ref. BES-2015-072506).

References

[1] J. Ponou, L.P. Wang, S. Matsuo, G. Dodbiba, T. Fujita, Recovery of dysprosium ions by biosorption-desorption onto organic plants wastes, Int. J. Soc. Mater. 20 (2014) 141–146.
[2] K. Vidal, L. Ortega-San-Martin, A. Larranaga, R.I. Merino, A. Orera, M.I. Arriortua, Effects of synthesis conditions on the structural, stability and ion conducting properties of $Li_{0.30}(La_{0.50}Ln_{0.50})_{0.567}TiO_3$ (Ln = La, Pr, Nd) solid electrolytes for rechargeable lithium batteries, Ceram. Int. 40 (2014) 8761–8768.
[3] X. Xu, J. Zou, X.R. Zhao, X.Y. Jiang, F.P. Jiao, J.G. Yu, Q. Liu, J. Teng, Facile assembly of three-dimensional cylindrical egg white embedded graphene oxide composite with good reusability for aqueous adsorption of rare earth elements, Colloids Surf. A Physicochem. Eng. Asp. 570 (2019) 127–140.
[4] K. Binnemans, P. Tom Jones, B. Blanpain, T. Van Gerven, Y. Yang, A. Walton, M. Buchert, Recycling of rare earths: a critical review, J. Clean. Prod. 51 (2013) 1–22.
[5] A.H. King, R.G. Eggert, K.A. Gschneidner Jr, The rare earths as critical materials, Handbook on the Physics and Chemistry of Rare Earths, 50 (2016) 19–46.
[6] Z.V.P. Murthy, A. Choudhary, Separation and estimation of nanofiltration membrane transport parameters for cerium and neodymium, Rare Metals 31 (2012) 500–506.
[7] S.J. Nejad, H. Abolghasemi, M.A. Moosavian, M.G. Maragheh, Fractional factorial design for the optimization of supercritical carbon dioxide extraction of La^{3+}, Ce^{3+} and Sm^{3+} ions from a solid matrix using Bis(2,4,4-Trimethylpentyl) Dithiophosphinic acid plus tributylphosphate, Chem. Eng. Res. Des. 89 (2011) 827–835.
[8] R. Kala, T.P. Rao, Ion imprinted polymer particles for separation of yttrium from selected lanthanides, J. Sep. Sci. 29 (2006) 1281–1287.
[9] X. Wang, L. Chen, L. Wang, Q. Fan, D. Pan, J. Li, F. Chi, Y. Xie, S. Yu, C. Xiao, F. Luo, J. Wang, X. Wang, C. Chen, W. Wu, W. Shi, S. Wang, X. Wang, Synthesis of novel nanomaterials and their application in efficient removal of radionuclides, Sci. China Chem. 62 (2019) 933–967.
[10] X. Liu, R. Ma, X. Wang, Y. Ma, Y. Yang, L. Zhuang, S. Zhang, R. Jehan, J. Chen, X. Wang, Graphene oxide-based materials for efficient removal of heavy metal ions from aqueous solution: a review, Environ. Pollut. 252 (2019) 62–73.
[11] D.B. Wu, J. Zhao, L. Zhang, Q.S. Wu, Y.H. Yang, Lanthanum adsorption using iron oxide loaded calcium alginate beads, Hydrometallurgy 101 (2010) 76–83.
[12] D.B. Wu, L. Zhang, L. Wang, B.H. Zhu, L.Y. Fan, Adsorption of lanthanum by magnetic alginate-chitosan gel beads, J. Chem. Technol. Biotechnol. 86 (2011) 345–352.
[13] L. Zhang, D.B. Wu, B.H. Zhu, Y.H. Yang, L. Wang, Adsorption and selective separation of neodymium with magnetic alginate microcapsules containing the extractant 2-ethylhexyl phosphonic acid mono-2-ethylhexyl ester, J. Chem. Eng. Data 56 (2011) 2280–2289.
[14] N.S. Awwad, H.M.H. Gad, M.I. Ahmad, H.F. Aly, Sorption of lanthanum and erbium from aqueous solution by activated carbon prepared from rice husk, Colloids Surf., B. 81 (2010) 593–599.
[15] S.M.A. Koochaki-Mohammadpour, M. Torab-Mostaedi, A. Talebizadeh-Rafsanjani, F. Naderi-Behdani, Adsorption isotherm, kinetic, thermodynamic, and desorption studies of lanthanum and dysprosium on oxidized multiwalled carbon nanotubes, J. Dispers. Sci. Technol. 35 (2014) 244–254.
[16] T.A. Saleh, Nanocomposite of carbon nanotubes/silica nanoparticles and their use for adsorption of Pb (II): from surface properties to sorption mechanism, Desalin. Water Treat. 57 (23) (2016) 10730–10744.
[17] F. Granados-Correa, J. Vilchis-Granados, M. Jimenez-Reyes, L.A. Quiroz-Granados, Adsorption behaviour of La(III) and Eu(III) ions from aqueous solutions by hydroxyapatite: kinetic, isotherm, and thermodynamic studies, J. Chem. 2013 (2013) 1–9.
[18] D.B. Wu, C.M. Zhu, Y.G. Chen, B.H. Zhu, Y.H. Yang, Q.G. Wang, W.M. Ye, Preparation, characterization and adsorptive study of rare earth ions using magnetic GMZ bentonite. Appl. Clay Sci. 62–63 (2012) 87–93.
[19] G.S. Hong, L.D. Shen, M. Wang, Y. Yang, X.F. Wang, M.F. Zhu, B.S. Hsiao, Nanofibrous polydopamine complex membranes for adsorption of lanthanum (III) ions, Chem. Eng. J. 244 (2014) 307–316.
[20] M.A. Maheswari, M.S. Subramanian, Extraction chromatographic method for the separation of actinides and lanthanides using EDHBA grafted AXAD-16 polymer, Talanta 65 (2005) 735–742.
[21] W.M. Algothmi, N.M. Bandaru, Y. Yu, J.G. Shapter, A.V. Ellis, Alginate-graphene oxide hybrid gel beads: an efficient copper adsorbent material, J. Colloid Interface Sci. 397 (2013) 32–38.
[22] H. Hecht, S. Srebnik, Structural characterization of sodium alginate and calcium alginate, Biomacromolecules 17 (2016) 2160–2167.
[23] M. Rinaudo, Chitin and chitosan: properties and applications, Prog. Polym. Sci. 31 (2006) 603–632.
[24] S. Zinadini, A.A. Zinatizadeh, M. Rahimi, V. Vatanpour, H. Zangeneh, M. Beygzadeh, Novel high flux antifouling nanofiltration membranes for dye removal containing carboxymethyl chitosan coated Fe_3O_4 nanoparticles, Desalination 349 (2014) 145–154.
[25] F.C. Wang, J.M. Zhao, H.C. Zhou, W. Li, N. Sui, H. Liu, O-carboxymethyl chitosan entrapped by silica: preparation and adsorption behaviour toward neodymium (III) ions, J. Chem. Technol. Biot. 88 (2013) 317–325.
[26] D. Ni, Z. Lin, P. Xiaoling, W. Xinqing, G. Hongliang, Preparation and characterization of nickel-zinc ferrites by a solvothermal method, Rare Metal Mat Eng 44 (9) (2015) 2126–2131.
[27] M. Sundararajan, P. Sakthivel, A. Christina Fernandez, Structural, optical and electrical properties of ZnO-ZnS nanocomposites prepared by simple hydrothermal method, J. Alloy Compd. 768 (2018) 553–562.
[28] C. Larosa, M. Salerno, J. Silva de Lima, R. Merijs Meri, M. Fernandes da Silva, L. Bezerra de Carvalho, A. Converti, Characterisation of bare and tannase-loaded calcium alginate beads by microscopic, thermogravimetric, FTIR and XRD analyses, Int. J. Biol. Macromol. 115 (2018) 900–906.
[29] T.A. Saleh, Isotherm, kinetic, and thermodynamic studies on hg (II) adsorption from aqueous solution by silica-multiwall carbon nanotubes, Environ. Sci. Pollut. Res. 22 (21) (2015) 16721–16731.
[30] G. Fadillah, T.A. Saleh, S. Wahyuningsih, S.F. ENK Putri, Electrochemical removal of methylene blue using alginate-modified graphene adsorbents, Chem. Eng. J. 378 (2019), 122140.
[31] S.A. Elfeky, S. Ebrahim Mahmoud, A. Fahmy Youssef, Applications of CTAB modified magnetic nanoparticles for removal of chromium (VI) from contaminated water, J. Adv. Res. 8 (4) (2017) 435–443.
[32] H. Abdolmohammad-Zadeh, Z. Ayazi, Z. Naghdi, Nickel oxide/chitosan nanocomposite as a magnetic adsorbent for preconcentration of Zn(II) ions, J. Magn. Magn. Mater. 488 (2019), 165311.
[33] X. Huang, D. Wei, X. Zhang, D. Fan, X. Sun, B. Du, Q. Wei, Synthesis of amino-functionalized magnetic aerobic granular sludge-biochar for Pb(II) removal: adsorption performance and mechanism studies, Sci. Total Environ. 685 (2019) 681–689.
[34] H. Lu, Y. Li, Y. Wang, X. Li, Preparation of $CoFe_2O_4$@vacancy@$mSiO_2$ core-shell composites for removal of organic pollutant in aqueous solution, J. Saudi Chem. Soc. 23 (2019) 536–545.
[35] N.H. Kera, M. Bhaumik, K. Pillay, S. Sinha Ray, A. Maity, Selective removal of toxic Cr (VI) from aqueous solution by adsorption combined with reduction at a magnetic nanocomposite surface, J. Colloid Interface Sci. 503 (2017) 214–228.
[36] H. Javadian, F. Ghorbani, H. Tayebi, S.M. Hosseini Asl, Study of the adsorption of Cd (II) from aqueous solution using zeolite-based geopolymer, synthesized from coal fly ash; kinetic, isotherm and thermodynamic studies, Arab. J. Chem. 8 (2015) 837–849.
[37] H. Javadian, F. Zamani Sorkhrodi, B. Babzadeh Koutenaei, Experimental investigation on enhancing aqueous cadmium removal via nanostructure composite of modified hexagonal type mesoporous silica with polyaniline/polypyrrole nanoparticles, J. Ind. Eng. Chem. 20 (2014) 3678–3688.
[38] M.A. Espinade Franco, C. Bonfantede Carvalho, M. Marques Bonetto, R. de Pelegrini Soares, L. Amaral Féris, Diclofenac removal from water by adsorption using activated carbon in batch mode and fixed-bed column: isotherms, thermodynamic study and breakthrough curves modeling, J. Clean. Prod. 181 (2018) 145–154.
[39] A. Cristiana Fröhlich, E. Luiz Foletto, G. Luiz Dotto, Preparation and characterization of $NiFe_2O_4$/activated carbon composite as potential magnetic adsorbent for removal of ibuprofen and ketoprofen pharmaceuticals from aqueous solutions, J. Clean. Prod. 229 (2019) 828–837.
[40] H. Javadian, Adsorption performance of suitable nanostructured novel composite adsorbent of poly(N-methylaniline) for removal of heavy metal from aqueous solutions, J. Ind. Eng. Chem. 20 (2014) 4344–4352.
[41] E. Liu, X. Zheng, X. Xu, F. Zhang, E. Liu, Y. Wang, C. Li, Y. Yan, Preparation of diethylenetriamine-modified magnetic chitosan nanoparticles for adsorption of rare-earth metal ions, New J. Chem. 41 (2017) 7739–7750.
[42] J. Roosen, K. Binnemans, Adsorption and chromatographic separation of rare earths with EDTA- and DTPAfunctionalized chitosan biopolymers, J. Mater. Chem. A 2 (2014) 1530–1540.

[43] I.V. Melnyk, V.P. Goncharyk, L.I. Kozhara, G.R. Yurchenko, A.K. Matkovsky, Y.L. Zub, B. Alonso, Sorption properties of porous spray-dried microspheres functionalized by phosphonic acid groups, Microporous Mesoporous Mater. 153 (2012) 171–177.
[44] T. Kegl, I. Ban, A. Lobnik, A. Košak, Synthesis and characterization of novel γ-Fe_2O_3-NH_4OH@SiO_2(APTMS) nanoparticles for dysprosium adsorption, J. Hazard. Mater. 378 (2019), 120764.
[45] A. Negrea, A. Gabor, C.M. Davidescu, M. Ciopec, P. Negrea, N. Duteanu, A. Barbulescu, Rare earth elements removal from water using natural polymers, Sci. Rep. 8 (2018) 316.
[46] Y.R. Lee, K. Yu, S. Ravi, W.S. Ahn, Selective adsorption of rare earth elements over functionalized Cr-MIL-101, Appl. Mater. Interfaces 10 (2018) 23918–23927.
[47] X.-H. Qi, K.-Z. Du, M.-L. Feng, Y.-J. Gao, X.-Y. Huang, M.G. Kanatzidis, Layered $A_2Sn_3S_7 \cdot 1.25H_2O$ (A = organic cation) as efficient ion-exchanger for rare earth element recovery, J. Am. Chem. Soc. 139 (12) (2017) 4314–4317.
[48] S.M.A. Koochaki-Mohammadpour, M. Torab-Mostaedi, A. Talebizadeh-Rafsanjani, F. Naderi-Behdani, Adsorption isotherm, kinetic, thermodynamic, and desorption studies of lanthanum and dysprosium on oxidized multiwalled carbon nanotubes, J. Dispers. Sci. Technol. 35 (2014) 244–254.
[49] M.M. Yusoff, N.R. Nik Mostapa, Md. Shaheen Sarkar, T.K. Biswas, Md. Lutfor Rahman, S.E. Arshad, M.S. Sarjadi, A.D. Kulkarni, Synthesis of ion imprinted polymers for selective recognition and separation of rare earth metals, J. Rare Earth 35 (2017) 177–186.
[50] H.A. Madbouly, N.E. El-Hefny, Y.A. El-Nadi, Adsorption and separation of terbium (III) and gadolinium(III) from aqueous nitrate medium using solid extractant, Sep. Sci. Technol. (2019) 1–13.
[51] S. Tong, S. Zhao, W. Zhou, R. Li, Q. Jia, Modification of multi-walled carbon nanotubes with tannic acid for the adsorption of La, Tb and Lu ions, Microchim. Acta 174 (2011) 257–264.
[52] D. Baybaş, U. Ulusoy, Polyacrylamide–clinoptilolite/Y-zeolite composites: characterization and adsorptive features for terbium, J. Hazard. Mater. 187 (1) (2011) 241–249.
[53] R. Akkaya, Synthesis and characterization of a new low-cost composite for the adsorption of rare earth ions from aqueous solutions, Chem. Eng. J. 200 (2012) 186–191.
[54] R. Akkaya, Terbium adsorption onto polyhydroxyethylmethacrylate–hydroxyapatite composite and its modified composition by phytic acid, Desalin. Water Treat. 52 (2014) 1440–1447.
[55] F.A. Alakhras, K.A. Dari, M.S. Mubarak, Synthesis and chelating properties of some poly (Amidoxime-hydroxamic acid) resins toward some trivalent lanthanide metal ions, J. Appl. Polym. Sci. 97 (2) (2005) 691–696.
[56] M.A. Attia, S.I. Moussa, R.R. Sheha, H.H. Someda, E.A. Saad, Hydroxyapatite/$NiFe_2O_4$ superparamagnetic composite: facile synthesis and adsorption of rare elements, Appl. Radiat. Isot. 145 (2019) 85–94.
[57] N.S. Reddy, K.M. Rao, S.V. Krishna, C.S. Ha, Synthesis of 1–acryloyl–3–phenyl thiourea based pH sensitive hydrogels for removal of samarium and terbium, Macromol. Res. 24 (2016) 494–501.
[58] M.R. Awual, N.H. Alharthi, Y. Okamoto, M.R. Karim, M.E. Halim, M.M. Hasan, M.M. Rahman, M.M. Islam, M.A. Khaleque, M.C. Sheikh, Ligand field effect for Dysprosium(III) and lutetium(III) adsorption and EXAFS coordination with novel composite nanomaterials, Chem. Eng. J. 320 (2017) 427–435.
[59] R.M. Ashour, R. El-Sayed, A.F. Abdel-Magied, A.A. Abdel-Khalek, M.M. Ali, K. Forsberg, A. Uheida, M. Muhammed, J. Dutta, Selective separation of rare earth ions from aqueous solution using functionalized magnetite nanoparticles: kinetic and thermodynamic studies, Chem. Eng. J. 327 (2017) 286–296.
[60] H. Aghayan, A. Mahjoub, A. Khanchi, Samarium and dysprosium removal using 11-molybdo-vanadophosphoric acid supported on Zr modified mesoporous silica SBA-15, Chem. Eng. J. 225 (2013) 509–519.
[61] T. Kaneko, F. Nagata, S. Kugimiya, K. Katob, Optimization of carboxyl-functionalized mesoporous silica for the selective adsorption of dysprosium, J Environmen Chem Eng 6 (2018) 5990–5998.
[62] X. Zheng, Y. Zhang, T. Bian, Y. Zhang, Z. Li, J. Pan, Oxidized carbon materials cooperative construct ionic imprinted cellulose nanocrystals films for efficient adsorption of Dy(III), Chem. Eng. J. 381 (2020), 122669.
[63] X. Zheng, E. Liu, F. Zhang, Y. Yan, J. Pan, Efficient adsorption and separation of dysprosium from NdFeB magnets in an acidic system by ion imprinted mesoporous silica sealed in a dialysis bag, Green Chem. 18 (2016) 5031–5040.
[64] İ. Kara, D. Yilmazer, S. Tunali Akar, Metakaolin based geopolymer as an effective adsorbent for adsorption of zinc(II) and nickel(II) ions from aqueous solutions, Appl. Clay Sci. 139 (2017) 54–63.
[65] D. Alipour, A.R. Keshtkar, M.A. Moosavian, Adsorption of thorium (IV) from simulated radioactive solutions using a novel electrospun PVA/TiO_2/ZnO nanofiber adsorbent functionalized with mercapto groups: study in single and multi-component systems, Appl. Surf. Sci. 366 (2016) 19–29.
[66] M. Rajabi, K. Mahanpoor, O. Moradi, Preparation of PMMA/GO and PMMA/GO-Fe_3O_4 nanocomposites for malachite green dye adsorption: kinetic and thermodynamic studies, Compos Part B Eng 167 (2019) 544–555.
[67] H. Javadian, P. Vahedian, M. Toosi, Adsorption characteristics of Ni(II) from aqueous solution and industrial wastewater onto Polyaniline/HMS nanocomposite powder, Appl. Surf. Sci. 284 (2013) 13–22.
[68] N. Subedi, A. Lähde, E. Abu-Danso, J. Iqbal, A. Bhatnagar, A comparative study of magnetic chitosan (Chi@Fe_3O_4) and graphene oxide modified magnetic chitosan (Chi@Fe_3O_4GO) nanocomposites for efficient removal of Cr(VI) from water, Int. J. Biol. Macromol. 137 (2019) 948–959.

ANNEX II

Response surface methodology based on central composite design for simultaneous adsorption of rare earth elements using nanoporous calcium alginate/carboxymethyl chitosan microbiocomposite powder containing $Ni_{0.2}Zn_{0.2}Fe_{2.6}O_4$ magnetic nanoparticles: Batch and column studies.

Hamedreza Javadian, Montserrat Ruiz, Ana Maria Sastre,

International Journal of Biological Macromolecules, 154 (2020) 937-953.

https://doi.org/10.1016/j.ijbiomac.2020.03.131

International Journal of Biological Macromolecules 154 (2020) 937–953

Contents lists available at ScienceDirect

International Journal of Biological Macromolecules

journal homepage: http://www.elsevier.com/locate/ijbiomac

Response surface methodology based on central composite design for simultaneous adsorption of rare earth elements using nanoporous calcium alginate/carboxymethyl chitosan microbiocomposite powder containing $Ni_{0.2}Zn_{0.2}Fe_{2.6}O_4$ magnetic nanoparticles: Batch and column studies

Hamedreza Javadian [a,*], Montserrat Ruiz [b], Ana Maria Sastre [a]

[a] Department of Chemical Engineering, ETSEIB, Universitat Politècnica de Catalunya, Diagonal 647, 08028 Barcelona, Spain
[b] Department of Chemical Engineering, EPSEVG, Universitat Politècnica de Catalunya, Av. Víctor Balaguer, s/n, 08800 Vilanova i la Geltrú, Spain

ARTICLE INFO

Article history:
Received 22 November 2019
Received in revised form 20 February 2020
Accepted 14 March 2020
Available online xxxx

Keywords:
Calcium alginate
Carboxymethyl chitosan
$Ni_{0.2}Zn_{0.2}Fe_{2.6}O_4$
Adsorption
Rare earth elements
RSM

ABSTRACT

In this research paper, the utilization of the magnetic calcium alginate/carboxymethyl chitosan/$Ni_{0.2}Zn_{0.2}Fe_{2.6}O_4$ (CA/CMC/$Ni_{0.2}Zn_{0.2}Fe_{2.6}O_4$) was investigated for the simultaneous aqueous adsorption of Nd (III), Tb (III), and Dy (III). The magnetic products were characterized by FE-SEM, EDX, XRD, FT-IR, TGA, and VSM techniques. The saturation magnetization value for $Ni_{0.2}Zn_{0.2}Fe_{2.6}O_4$ and CA/CMC/$Ni_{0.2}Zn_{0.2}Fe_{2.6}O_4$ was found to be 45.87 and 14.14 emu/g, respectively. Using RSM, a quadratic polynomial equation was obtained to predict the adsorption efficiency of each ion. Under the conditions of pH = 5.5, adsorbent dosage of 0.1 g, initial concentration of 30 mg/L, and contact time of 53 min predicted by RSM, the adsorption efficiencies of Nd (III), Tb (III), and Dy (III) were respectively 95.72, 96.17, and 99.44%. The isotherm and kinetic data were respectively fitted well with Freundlich and pseudo-second-order (PSO) models. The desorption of the loaded ions was effectively carried out by 0.2 M HNO_3, and the adsorbent was consecutively utilized with 2.54, 1.63, and 1.16% decrease in adsorption efficiency for Nd (III), Tb (III), and Dy (III), respectively, after the forth cycle. Additionally, the adsorption behavior of the CA/CMC/$Ni_{0.2}Zn_{0.2}Fe_{2.6}O_4$ towards Nd (III), Tb (III), and Dy (III) was studied by using a fixed-bed column technique.

1. Introduction

Rare earth elements (REEs) are regularly alluded in terms of "seeds of technology" due to their utilization in electronic devices, high strength lasting magnets, green energy sectors, lasers, automotive catalytic converters, fiber superconductors/optics, etc. [1,2]. Because of the progressing advancement in new trend-setting innovations, there is an over-expanding interest for REEs in the universal markets, with an accentuation on distinguishing new origins to guarantee satisfactory supply for utilizing in the present and future. This issue becomes more important since >90% of mine production of rare earth occurs in China, and its REEs export was decreased 19,015 tons from 2009 to 2012, leading to serious problems for REE users outside of China. Therefore, REEs recovery from wastes has been one of the most incredible worries in the ongoing years [3].

A few techniques, such as solvent extraction, chemical precipitation, ion exchange, membrane separation, adsorption and so on, have been applied for the REEs recovery [4,5]. Investigators have noted adsorption as a standout technique because of being easy, cost-effective, and environmentally friendly for REEs recovery in comparison with the regular techniques [6].

Alginate, as a natural biopolymer, is extracted from brown algae. Some of its benefits, such as biodegradability, biocompatibility, being cheap and nontoxic, make it a great potential material to be broadly and effectively utilized in water treatment [7–10]. It tends to be utilized to produce hydrogels under conditions of moderate pH and temperatures. Alginate can likewise be altered via physicochemical procedures to enhance its chemical and mechanical strength [11]. In this manner, its adsorption behavior can be increased by raising its adsorption capacity [12]. The utilization of alginate in the form of hydrogel beads is a typical technique to enhance its adsorption capacity [13].

* Corresponding author at: Department of Chemical Engineering, ETSEIB, Universitat Politècnica de Catalunya, Diagonal 647, 08028 Barcelona, Spain
E-mail address: hamedreza.javadian@upc.edu (H. Javadian).

https://doi.org/10.1016/j.ijbiomac.2020.03.131
0141-8130/

Chitosan-based adsorbent materials are broadly applied for the adsorption removal of contaminations aqueous solution [14]. Chitosan possesses valuable characteristics, for example, biodegradability, hydrophilicity, nontoxicity, biocompatibility, high mechanical strength, film preparation, and antibacterial characteristics [15]. Its chemical structure contains amino (-NH_2) and hydroxyl (-OH) groups as major active functional groups for adsorption of metal ions from aqueous media [16,17]. The dissolvability of chitosan can be enhanced by modifying its structure with –COOH groups without influencing on the mentioned characteristics [18]. Besides, the carboxyl gathering presented in carboxymethyl chitosan (CMC) is additionally useful for the adsorption of metal ions.

It is necessary to easily separate adsorbents that are applied in the form of ultrafine powder for the separation of metal ions from aqueous media. For this purpose, centrifugation and filtration methods are not efficient to completely separate such a powder from aqueous media, while adsorbents having magnetic properties can be easily separated using an external magnetic field [19]. The active surface and small size of nanoparticles lead to their easy aggregation in aqueous media [20]. To solve this issue, amending the stability, increasing the application of magnetic nanoparticles, and their combining with biopolymers such as alginate and carboxymethyl chitosan could be considered as effective methods.

The goal of this study was to synthesize the CA/CMC/$Ni_{0.2}Zn_{0.2}Fe_{2.6}O_4$ as a magnetic adsorbent for simultaneous adsorption of Nd (III), Tb (III), and Dy (III) ions from aqueous solution. The adsorbent was analyzed by FE-SEM, EDX, XRD, FT-IR, TGA, and VSM techniques. The influences of adsorbent dosage, contact time, and initial concentration as main parameters were studied, and RSM-CCD was used to optimize them. The kinetic and isotherm models were applied for fitting the experimental data. The performance of the CA/CMC/$Ni_{0.2}Zn_{0.2}Fe_{2.6}O_4$ was also evaluated in a fixed-bed column.

2. Materials and methods

2.1. Materials and reagents

Carboxymethyl chitosan and sodium alginate were purchased from Nantong Chem-Base Co, China, and PanReac AppliChem, respectively. $Dy(NO_3)_3.5H_2O$ was purchased from Alfa Aesar. $Nd(NO_3)_3.6H_2O$, $Tb(NO_3)_3\cdot 6H_2O$, $Zn(NO_3)_2.6H_2O$, $Fe(NO_3)_3.9H_2O$, $Ni(NO_3)_2\cdot 6H_2O$, $CaCl_2$, and glutaraldehyde were bought from Sigma-Aldrich. Analytical grade materials were used without further purification. The experiment solutions of Nd (III), Tb (III), and Dy (III) ions were made by dilution of 1000 mg/L of ions. HNO_3 or NaOH solution with the molarity of 0.1 was utilized to carefully adjust the pH of the solutions.

Table 1
CCD levels, experimental design and the responses.

Symbol	—	Unit	Levels				
	—		−α (−2)	Low (−1)	Central (0)	High (1)	+α (+2)
X_1	Contact time	min	2	19	36	53	70
X_2	Adsorbent dosage	g	0.05	0.125	0.2	0.275	0.35
X_3	Nd (III) concentration	mg/L	30	45	60	75	90
X_4	Tb (III) concentration	mg/L	30	45	60	75	90
X_5	Dy (III) concentration	mg/L	30	45	60	75	90

Run	Factors					Nd adsorption efficiency (%)		Tb adsorption efficiency (%)		Dy adsorption efficiency (%)	
	X1	X2	X3	X4	X5	Observed	Predicated	Observed	Predicated	Observed	Predicated
1	36	0.2	60	60	30	90.76	90.92	95.85	96.19	97.53	98.38
2	53	0.275	75	75	75	94.56	95.81	96.87	97.99	98.11	99.49
3	36	0.2	90	60	60	87.96	86.97	90.53	89.74	92.89	92.17
4(C)	36	0.2	60	60	60	91.45	91.56	94.03	93.83	95.75	95.59
5	19	0.125	45	45	75	67.08	65.91	70.16	68.76	73.17	71.86
6	36	0.2	60	90	60	89.7	90.18	91.64	91.83	92.85	92.90
7	19	0.125	75	75	75	54.56	53.65	57.87	57.07	59.06	58.32
8	19	0.125	75	45	45	62.65	61.90	67.59	66.71	72.45	71.31
9	70	0.2	60	60	60	88.12	86.43	90.56	88.55	92.92	90.59
10	53	0.125	75	75	45	71.98	71.84	77.64	77.97	79.51	79.74
11(C[a])	36	0.2	60	60	60	91.97	91.56	94.46	93.83	96.01	95.59
12	2	0.2	60	60	60	65.78	67.47	67.73	70.34	69.45	72.25
13	53	0.275	75	45	45	92.56	93.97	95.54	96.59	97.98	98.96
14	19	0.275	75	45	75	89.1	89.74	91.94	91.86	95.7	95.71
15	53	0.125	45	45	45	87.6	87.20	90.19	89.92	92.85	92.51
16	36	0.2	30	60	60	94.46	95.45	96.21	97.60	98.25	99.45
17(C)	36	0.2	60	60	60	91.72	91.56	94.09	93.83	95.71	95.59
18(C)	36	0.2	60	60	60	90.96	91.56	93.52	93.83	95.35	95.59
19(C)	36	0.2	60	60	60	91.58	91.56	93.85	93.83	95.32	95.59
20	36	0.2	60	30	60	95.64	95.16	94.43	94.84	98.65	99.07
21	19	0.275	45	45	45	92.75	92.82	94.74	94.09	97.54	96.76
22	53	0.275	45	75	45	94.56	95.23	96.44	97.00	98.45	99.05
23	19	0.275	75	75	45	92.49	92.81	94.63	94.58	96.2	95.99
24	53	0.125	45	75	75	76.01	75.45	79.06	78.86	81.63	81.69
25	19	0.125	45	75	45	59.07	57.58	68.72	67.35	69.38	67.85
26(C)	36	0.2	60	60	60	91.7	91.56	93.65	93.83	95.9	95.59
27	53	0.125	75	45	75	65.46	65.63	72.26	72.55	76.16	76.61
28	19	0.275	45	75	75	90.07	89.98	94.78	94.21	96.59	96.21
29	53	0.275	45	45	75	94.11	95.10	96.07	96.59	98.5	99.31
30	36	0.05	60	60	60	35.32	37.94	45.19	47.04	47.59	49.51
31	36	0.35	60	60	60	92.14	89.52	94.22	92.97	96.36	94.91
32	36	0.2	60	60	90	85.56	85.40	89.35	89.61	93.01	92.63

[a] Central point.

2.2. Instrumentation and characterization

The record of FT-IR spectra were performed from 4000 to 450 cm^{-1} on a PerkinElmer, USA, by the KBr disk method. To identify the crystalline structure of the product, XRD pattern was taken down on a GBC MMA instrument with CuK_α radiation (wavelength $\lambda = 0.154$ nm) in the 2θ range of 10–70^0. The morphological structure and particle size of the products were determined by FE-SEM (Zeiss Neon-40, Germany). The magnetic characteristics of the products were studied using VSM (Daghigh Kavir Corporation, Iran) at room temperature (RT). Thermal analyses were done on a Mettler TGA/SDTA 851e/LF/1100 thermobalance. The temperature of the samples was increased from RT to 1000 °C at rate = 10 °C/min under a constant flow of N_2. For analyzing the concentration of Nd (III), Tb (III), and Dy (III), an Agilent 4100 MP-AES Spectrometer was used. The Design Expert software, version 10, was utilized to define the experimental design by CCD and analyze the regression of the experimental data.

2.3. Synthesis of the $Ni_{0.2}Zn_{0.2}Fe_{2.6}O_4$ magnetic nanoparticles

The $Ni_{0.2}Zn_{0.2}Fe_{2.6}O_4$ magnetic nanoparticles were synthesized using hydrothermal method. A mixture of 0.2 M Ni^{2+}, 0.2 M Zn^{2+} and 2.6 M Fe^{3+} was prepared in HCl solution, and then NaOH solution was added into mixed solution under nitrogen gas and the mixture pH value was adjusted to 10.5. 0.3 g of CTAB was added to the mixture, and then it was placed into an autoclave (Teflon-lined stainless steel) and maintained at 200 °C of an oven for 8 h for hydrothermal treatment. The temperature of the autoclave was naturally decreased to RT, and the precipitate was collected and rinsed several times with deionized water to reach neutral pH. Finally, the obtained particles were dried at 50 °C.

2.4. Synthesis of the CA/CMC/$Ni_{0.2}Zn_{0.2}Fe_{2.6}O_4$ magnetic bionanocomposite

The synthesis procedure of the CA/CMC/$Ni_{0.2}Zn_{0.2}Fe_{2.6}O_4$ was as follows: Sodium alginate (1 g) was dissolved in 80 mL of deionized water at RT using a laboratory stirrer. 0.5 g of the carboxymethyl chitosan powder was added into the solution and homogeneously mixed. 0.7 g of the $Ni_{0.2}Zn_{0.2}Fe_{2.6}O_4$ was added to the mixture of the biopolymers. To obtain a homogeneous blend solution, the mixture of biopolymers and magnetic particles was stirred at RT for 24 h. Then, it was added to the solution of calcium chloride 0.05 M and 2% glutaraldehyde for the gelation process. An external magnetic field was used to separate the resulting bionanocomposite from solution, and then it was washed several times with deionized water for removing remaining calcium chloride and glutaraldehyde until the pH value the solution was reached 7. The CA/CMC/$Ni_{0.2}Zn_{0.2}Fe_{2.6}O_4$ bionanocomposite was dried at 50 °C. Finally, it was powdered.

2.5. Batch adsorption

The adsorption experiments of Nd (III), Tb (III), and Dy (III) by the CA/CMC/$Ni_{0.2}Zn_{0.2}Fe_{2.6}O_4$ bionanocomposite were done in 125 mL flasks containing 50 mL solutions prepared from the dilution of 1000 mg/L stock solutions at different pHs, adsorbent dosages, contact times, and initial concentrations with the ratio of 1:1:1. The agitation of the flasks was carried out on a laboratory shaker (rpm = 180).

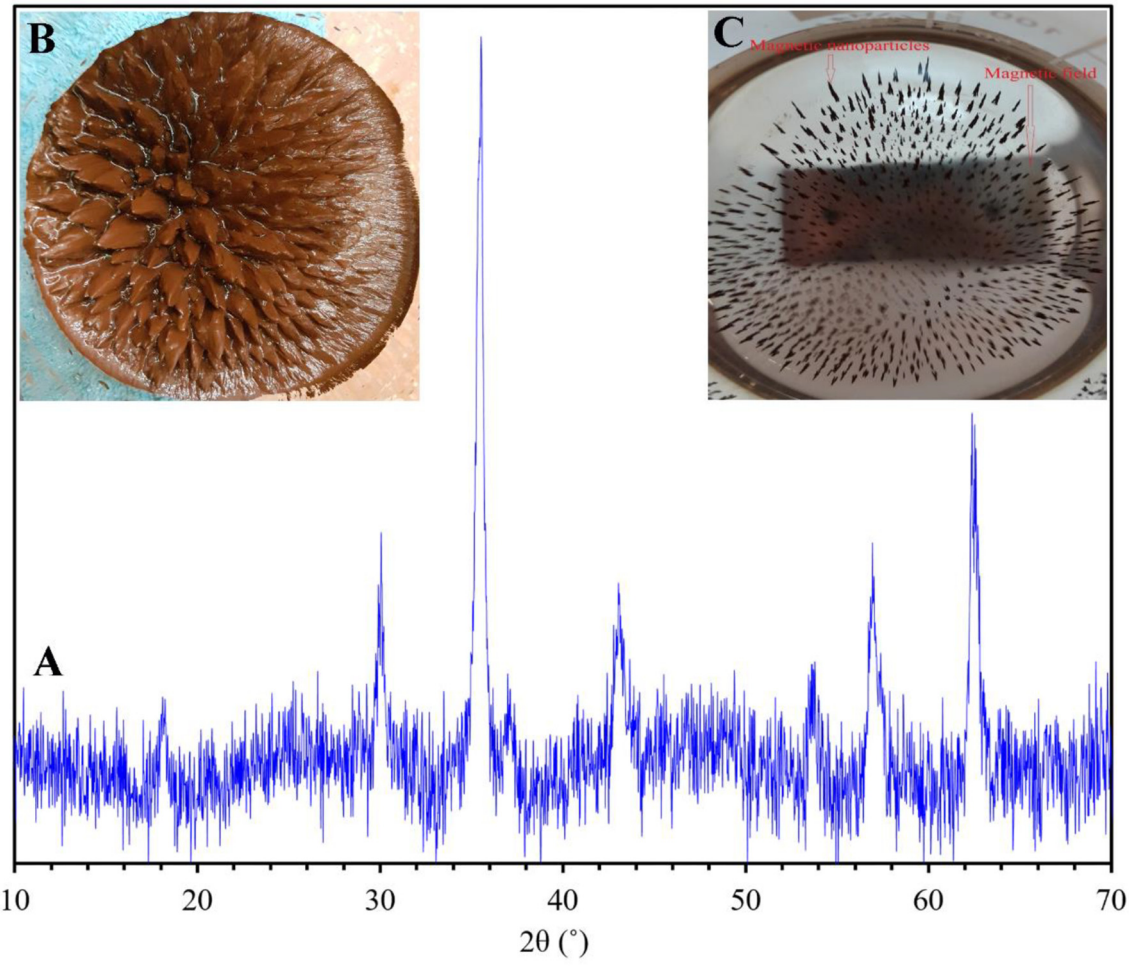

Fig. 1. (A) XRD pattern of $Ni_{0.2}Zn_{0.2}Fe_{2.6}O_4$ nanoparticles; photo of $Ni_{0.2}Zn_{0.2}Fe_{2.6}O_4$ nanoparticles (B) before drying and (C) in the solution under magnetic field after drying.

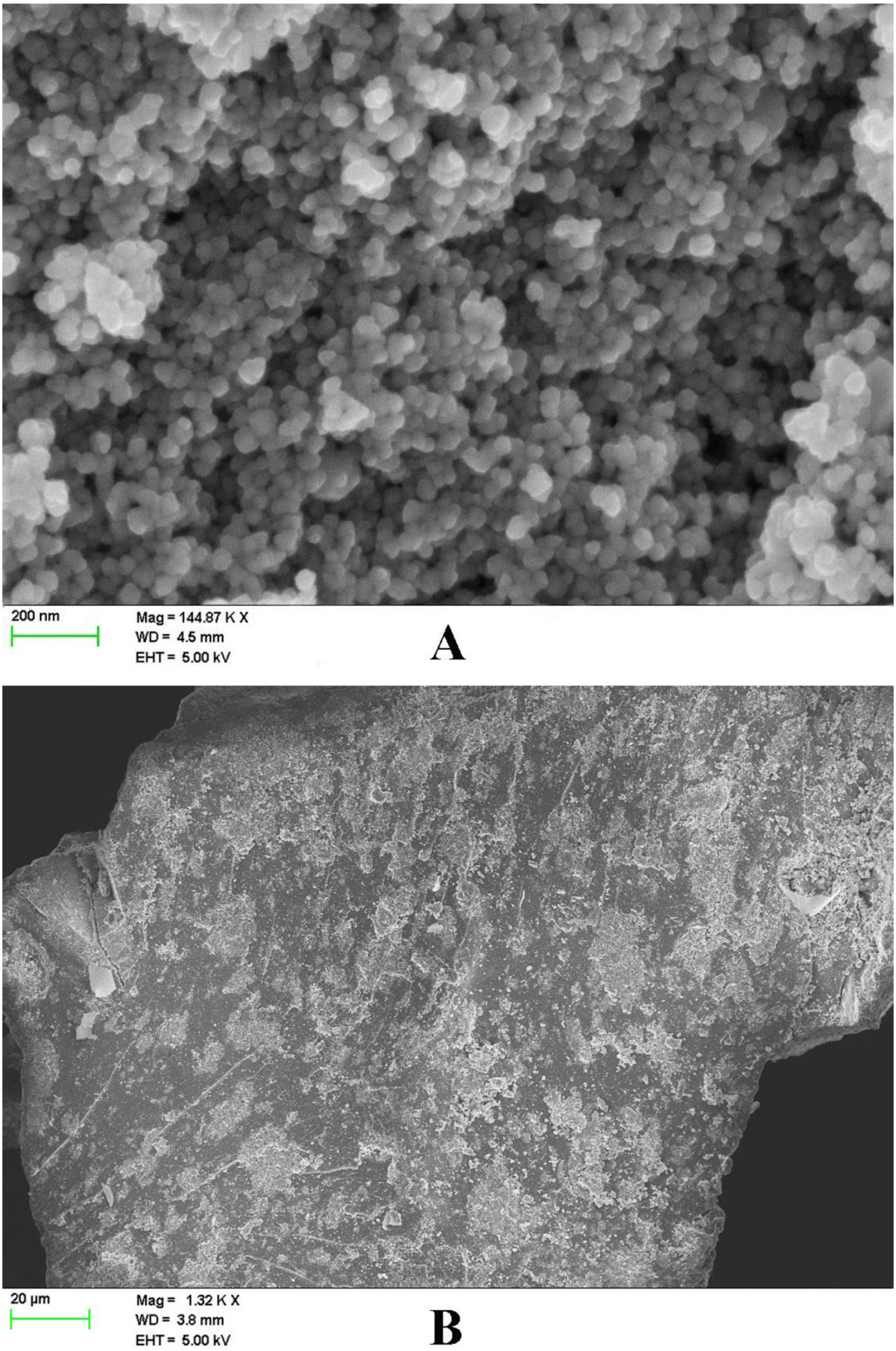

Fig. 2. FE-SEM images of (A) $Ni_{0.2}Zn_{0.2}Fe_{2.6}O_4$ and (B) CA/CMC/$Ni_{0.2}Zn_{0.2}Fe_{2.6}O_4$.

After adsorption process for a predefined time, the adsorbent was externally separated by a magnetic field, and the adsorption efficiency and adsorption capacity of the metal ions by the CA/CMC/$Ni_{0.2}Zn_{0.2}Fe_{2.6}O_4$ were computed using the equations as following:

$$\text{Adsorption efficiency}\ (\%) = \frac{C_0 - C_e}{C_0} \times 100 \quad (1)$$

$$q_e = \frac{(C_0 - C_e) \times V}{m} \quad (2)$$

$$q_t = \frac{(C_0 - C_t) \times V}{m} \quad (3)$$

where q_e and q_t (mg/g) respectively refer to the quantities of metal ion adsorbed on the adsorbent at equilibrium and adsorption time t (min), C_0 (mg/L) is the initial concentration of metal ion, and C_e (mg/L) is the equilibrium concentration of metal ion. Moreover, C_t refers to the concentration of metal ion in solution at time t, V is the volume (L) of solution, and m refers to the weight (g) of the adsorbent.

2.6. Central composite design

Experimental design is applied by investigators to decrease the number of experiments in the adsorption process. It also presents helpful information about the effect of independent parameters individually and/or interactively that leads to a decrease in experimental error [21]. RSM was utilized to model the adsorption process of the ions by investigating the independent variables including adsorbent dosage, contact time, initial concentration, and response (ions adsorption efficiency). For simultaneous adsorption of Nd (III), Tb (III), and Dy (III) ions by the CA/CMC/$Ni_{0.2}Zn_{0.2}Fe_{2.6}O_4$ by using batch mode, CCD was utilized at five levels ($-\alpha$ (-2), low (-1), central (0), high ($+1$) and $+\alpha$ ($+2$)) (Table 1).

Analysis of variance (ANOVA) was used to obtain information about the adequacy of the models by evaluating coefficient of determination (R [2]), lack of fit, and the Fisher test (F-value) values [22]. The quadratic polynomial model for response versus the independent variables was presented as follows [23]:

$$Y = \beta_0 + \sum_{i=1}^{k} \beta_i x_i + \sum_{i=1}^{k} \sum_{j=1}^{k} \beta_{ij} x_i x_j + \sum_{i=1}^{k} \beta_{ii} x_i^2 + \varepsilon \quad (4)$$

where Y refers to the predicted response (adsorption efficiency), and β_0, β_i, β_{ii}, and β_{ij}, respectively refer to the constant coefficient, linear coefficient, quadratic coefficient, and interaction coefficient. Notably, x_i and x_j are the independent variables, k shows the number of the independent variables, and ε is the residual error.

2.7. Column mode

Fixed-bed column investigation is necessary to successfully design a process and study the behavior of adsorbent in a large-scale utilization. To investigate the fixed-bed column, a column made of glass with an internal diameter of 0.5 cm and a length of 12 cm was used. 0.3 g of the adsorbent was mixed with 1.8 g of acid-cleaned sand, and the mixture was packed in the column between two layers of glass wool. Sand was applied to decrease the pressure drop. The final height of the mixture in the column was about 6.5 cm. An upward flow rate (1 mL/min) was provided by a peristaltic pump to flush the column with deionized water for 1 h. Then, the column was fed with a ternary solution of the ions at 30 mg/L initial concentration as an influent for 520 min. The collection of the effluent was performed every 10 min by a fraction collector, and the concentration of the ions was determined by Agilent 4100 MP-AES Spectrometer.

The breakthrough curve is usually shown by C_t/C_0 versus time. The amount of ion adsorbed (q_{total}, mg) was obtained by calculating the curve of breakthrough (upper area) by using the following equation:

$$q_{total} = \frac{Q}{1000} \int_{t_0}^{t_{total}} \left(1 - \frac{C_t}{C_0}\right) \quad (5)$$

where Q is the flow rate (mL/min) that was determined via division of the effluent volume (V_{eff}, mL) to the total time (t_{total}, min):

$$Q = \frac{V_{eff}}{t_{total}} \quad (6)$$

The entire quantity of the metals passed through the column (mg) was obtained by the following equation:

$$m_{total} = \frac{C_0 \times Q \times t_{total}}{1000} \quad (7)$$

The total metal adsorption efficiency was calculated from the ratio of the entire quantity of the metals sent to the column (q_{total}) to the metal mass adsorbed (m_{total}) by the following equation:

$$\text{Adsorption efficiency} = \frac{q_{total}}{m_{total}} \times 100 \quad (8)$$

The capacity of equilibrium adsorption (q_e (mg/g)) and the equilibrium metal concentration (C_e (mg/L)) were respectively computed using Eqs. (9) and (10) as following:

$$q_e = \frac{q_{total}}{m} \quad (9)$$

$$C_e = \frac{m_{total} - q_{total}}{V_{eff}} \times 100 \quad (10)$$

where m shows the adsorbent mass (g).

2.8. Error analysis

Error analysis was used to optimize the fitness of the experimental data obtained from the non-linear approach. In this study, Chi-square (χ^2) was employed to compare the validity of each model by the following equation:

$$\chi 2 = \sum_{i=1}^{n} \frac{\left(q_{e,\,exp} - q_{e,cal}\right)^2}{q_{e,cal}} \quad (11)$$

where n shows the number of data points, $q_{e,exp}$ is the experimental capacity of the adsorbent, and $q_{e,cal}$ refers to the computed capacity of the adsorbent.

3. Results and discussion

3.1. Products characterization

Fig. 1 indicates the XRD pattern of the $Ni_{0.2}Zn_{0.2}Fe_{2.6}O_4$. The peaks at $2\theta = 18.13°, 30.07°, 35.50°, 37.08°, 43.07°, 53.95°, 56.96°$ and $63.89°$ are in agreement with the standard pattern of nickel zinc ferrite (JCPDS 08-0234) [24]. Full Width at Half Maximum (FWHM) of the strongest reflection of the XRD pattern was used to estimate the average crystal size based on the Scherrer equation as following [25]:

$$D = k\,\lambda/\beta\ \cos\theta \quad (12)$$

where k refers to the function of shape (k = 0.89), and λ refers to the radiation X-ray wavelength. Moreover, β and θ respectively refer to the Full Width at Half Maximum (FWHM) at 2θ = 35.50°, and the diffraction angle. Based on the Scherrer equation, the calculated value of D was 27.68 nm.

The FE-SEM image of the $Ni_{0.2}Zn_{0.2}Fe_{2.6}O_4$ in Fig. 2A indicates that the synthesized particles are nearly spherical in shape and homogenous in distribution with a diameter <100 nm. Fig. 2B shows the distribution of the magnetic nanoparticles on the surface of the CA/CMC or embedding with the CA/CMC that confirms the successful synthesis of the CA/CMC/$Ni_{0.2}Zn_{0.2}Fe_{2.6}O_4$ magnetic bionanocomposite.

Fig. 3 indicates the FT-IR spectrum for CA, CMC, $Ni_{0.2}Zn_{0.2}Fe_{2.6}O_4$ and CA/CMC/$Ni_{0.2}Zn_{0.2}Fe_{2.6}O_4$. The FT-IR spectrum for CA and CMC in Fig. 3A and B, respectively, shows O—H stretching vibration at 3389 (CA) and 3436 (CMC) cm^{-1}, carboxyl groups asymmetrical stretching at 1622 (CA) and 1631 (CMC) cm^{-1}, carboxyl groups symmetrical stretching at 1423 (CA) and 1411 (CMC) cm^{-1} and C-O-C stretching at 1052 (CA) and 1061 (CMC) cm^{-1} [26,27]. The FT-IR spectrum of the $Ni_{0.2}Zn_{0.2}Fe_{2.6}O_4$ in Fig. 3C shows a broad band at around 3424 cm^{-1} and less intensive band at 1633 cm^{-1} that are related to the O—H groups stretching vibration [28]. The bands at 2925 and 2853 cm^{-1} are assigned to the anti-symmetric and symmetric C—H vibrations of CTAB [29]. The band at 567 cm^{-1} attributes to intrinsic metal stretching vibrations at the tetrahedral site (Fe—O), and octahedral metal stretching (M-O) is seen at around 478 cm^{-1} [28]. The successful synthesis of the CA/CMC/$Ni_{0.2}Zn_{0.2}Fe_{2.6}O_4$ can be confirmed by comparing its spectrum shown in Fig. 3D with other spectra.

N_2 adsorption–desorption isotherm and the corresponding Barrett-Joyner-Halenda (BJH) pore size distribution of the CA/CMC/$Ni_{0.2}Zn_{0.2}Fe_{2.6}O_4$ are shown in Fig. 4. The nitrogen adsorption-desorption isotherm for the sample in Fig. 4A is assigned to type IV indicating the presence of mesoporous structure. The Brunauer–Emmett–Teller (BET) surface area, pore volume, and pore size (obtained by the BJH method (Fig. 4B)) were calculated to be 7.1143 m^2/g, 0.034971 cm^3/g, and 19.0379 nm, respectively. The results clearly demonstrate the formation of the CA/CMC/$Ni_{0.2}Zn_{0.2}Fe_{2.6}O_4$ with nano size pores.

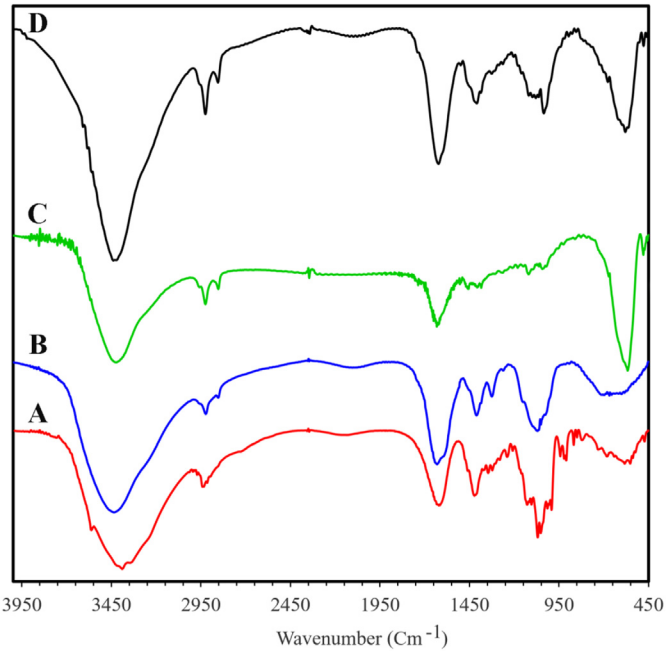

Fig. 3. FT-IR spectra of (A) CA, (B) CMC, (C) $Ni_{0.2}Zn_{0.2}Fe_{2.6}O_4$, and (D) CA/CMC/$Ni_{0.2}Zn_{0.2}Fe_{2.6}O_4$.

EDX was recorded to analyze the elements of the products, and the results are presented in Fig. 5. Fig. 5A shows Ni, Zn, Fe, and O peaks that confirm the formation of the $Ni_{0.2}Zn_{0.2}Fe_{2.6}O_4$. The elemental analysis of the nanocomposite in Fig. 5B represents similar peaks available in Fig. 5A along with the new peaks for N and Ca because of combining the nanoparticles with CA and CMC. Sodium peak is not seen in the spectrum of the CA/CMC/$Ni_{0.2}Zn_{0.2}Fe_{2.6}O_4$, suggesting that sodium ions were released completely from the matrix of sodium alginate into the solution during the crosslinking reaction process of sodium alginate with calcium. EDX spectrum was also recorded after the adsorption process and the result is presented in Fig. 5C. The existence of Nd (III), Tb (III), and Dy (III) in the spectrum strongly confirms the successful adsorption of these ions by the CA/CMC/$Ni_{0.2}Zn_{0.2}Fe_{2.6}O_4$.

The CA/CMC/$Ni_{0.2}Zn_{0.2}Fe_{2.6}O_4$ weight loss curve recorded in the range of RT to 1000 °C is demonstrated in Fig. 6. As it is seen, there are three different weight-loss steps in the TGA curve of the CA/CMC/$Ni_{0.2}Zn_{0.2}Fe_{2.6}O_4$. Obviously, the first step (around 190 °C) with a weight loss of 8.77% can be attributed to trapped and physisorbed water evaporation. The second step between around 190 and 550 °C is the largest weight loss with the amount of 35.08% that could be due to sorption and degradation of CA and CMC. The last step with 22.95% weight loss at temperature beyond 550 °C could be related to the further decomposition of CA and CMC and their conversion to CO_2 and H_2O. At the end of the process, the residue percentage is about 33.2% that is principally assigned to the presence of the $Ni_{0.2}Zn_{0.2}Fe_{2.6}O_4$.

According to the magnetic hysteresis loops in Fig. 7A, the magnetic saturation value for $Ni_{0.2}Zn_{0.2}Fe_{2.6}O_4$ is about 45.87 emu/g that indicates the superparamagnetic behavior of the synthesized product. Based on Fig. 7B, it is obvious that the process of the synthesis of the CA/CMC/$Ni_{0.2}Zn_{0.2}Fe_{2.6}O_4$ results in a decrease of saturation magnetization to the value of 14.14 emu/g. This decline is due to combining the magnetic nanoparticles by CA and CMC. Despite this difference, the CA/CMC/$Ni_{0.2}Zn_{0.2}Fe_{2.6}O_4$ can be easily separated from aqueous solution using an external magnetic field to avoid secondary pollution. Fig. 7C shows the easy separation of the metal ions-loaded adsorbent from the solution by applying an external magnetic field.

3.2. Effect of pH

Solution pH is considered as an essential parameter in the process of adsorption owing to its effect on metal ions solubility, counter ions concentration on the adsorbent functional groups, and the adsorbate ionization degree. In this study, the influence of pH value on the process of adsorption was considered from 1.5 to 5.5. The pH_{ZPC} of the CA/CMC/$Ni_{0.2}Zn_{0.2}Fe_{2.6}O_4$ was found to be 6. Since the precipitation of the ions may occur at pH values higher than 5.5, the experiments were carried out near to pH_{ZPC}; therefore, adsorption of the ions were not studied at pH > 5.5. As it is indicated in Fig. 8, the adsorption efficiency for the ions at pH = 1.5 is zero that indicates a highly acidic solution strongly affects the ions adsorption. At acidic solution, H^+ concentration and its mobility are high that lead to strong competition with the ions to occupy the active sites. Actually, the protonation of the active sites occurs in a low value of pH, leading to electrostatic repulsion between positively charged cations and positively charged active sites; therefore, the value of adsorption efficiency is low. As the pH of solution increases, the amount of H^+ being available in the solution decreases; hence, more negatively charged sites are available that facilitate higher uptake of the ions by electrostatic attraction [30]. According to the obtained results, further adsorption studies were performed at pH = 5.5 as an optimum value.

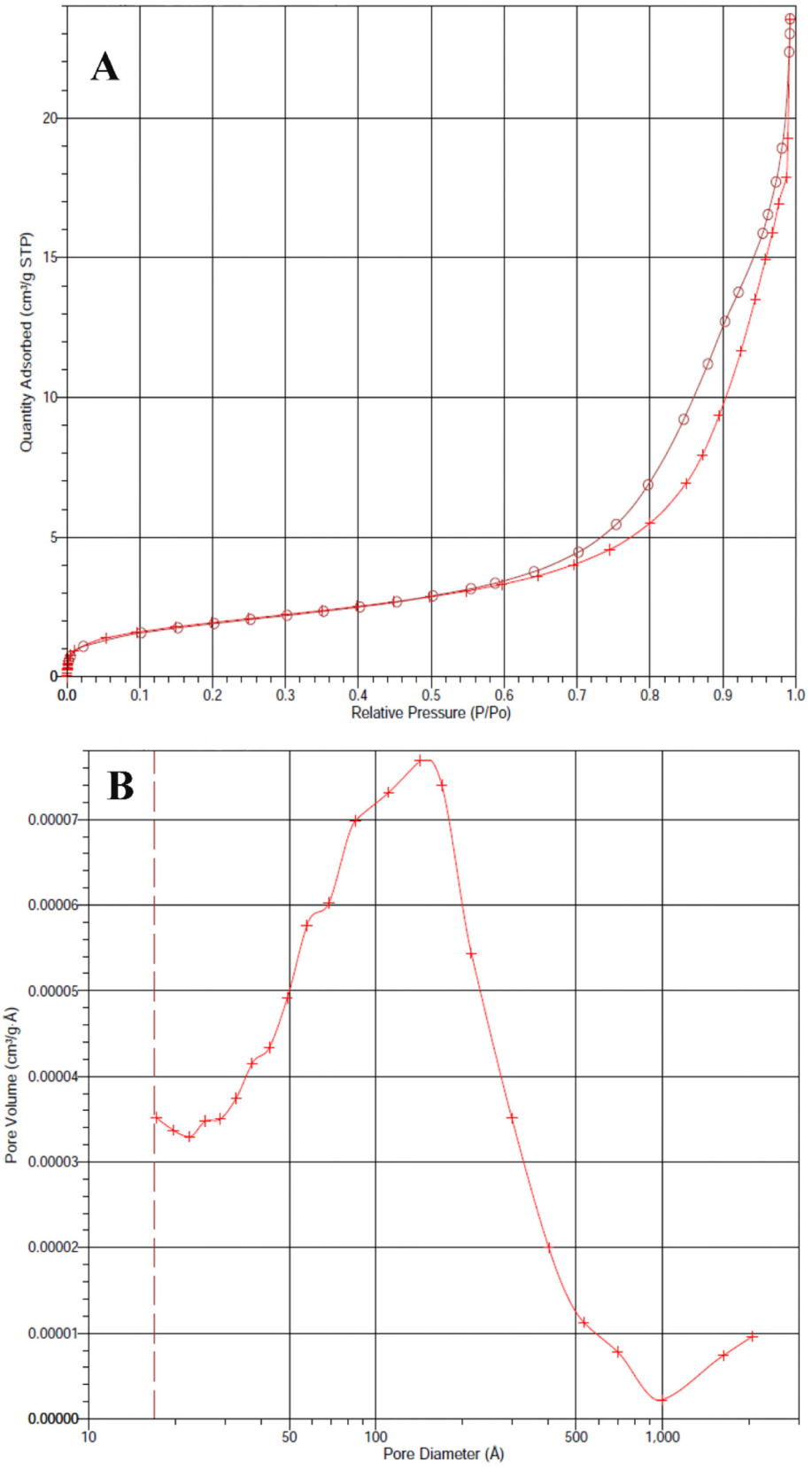

Fig. 4. (A) N_2 adsorption−desorption isotherm and (B) pore size distributions of the synthesized CA/CMC/$Ni_{0.2}Zn_{0.2}Fe_{2.6}O_4$.

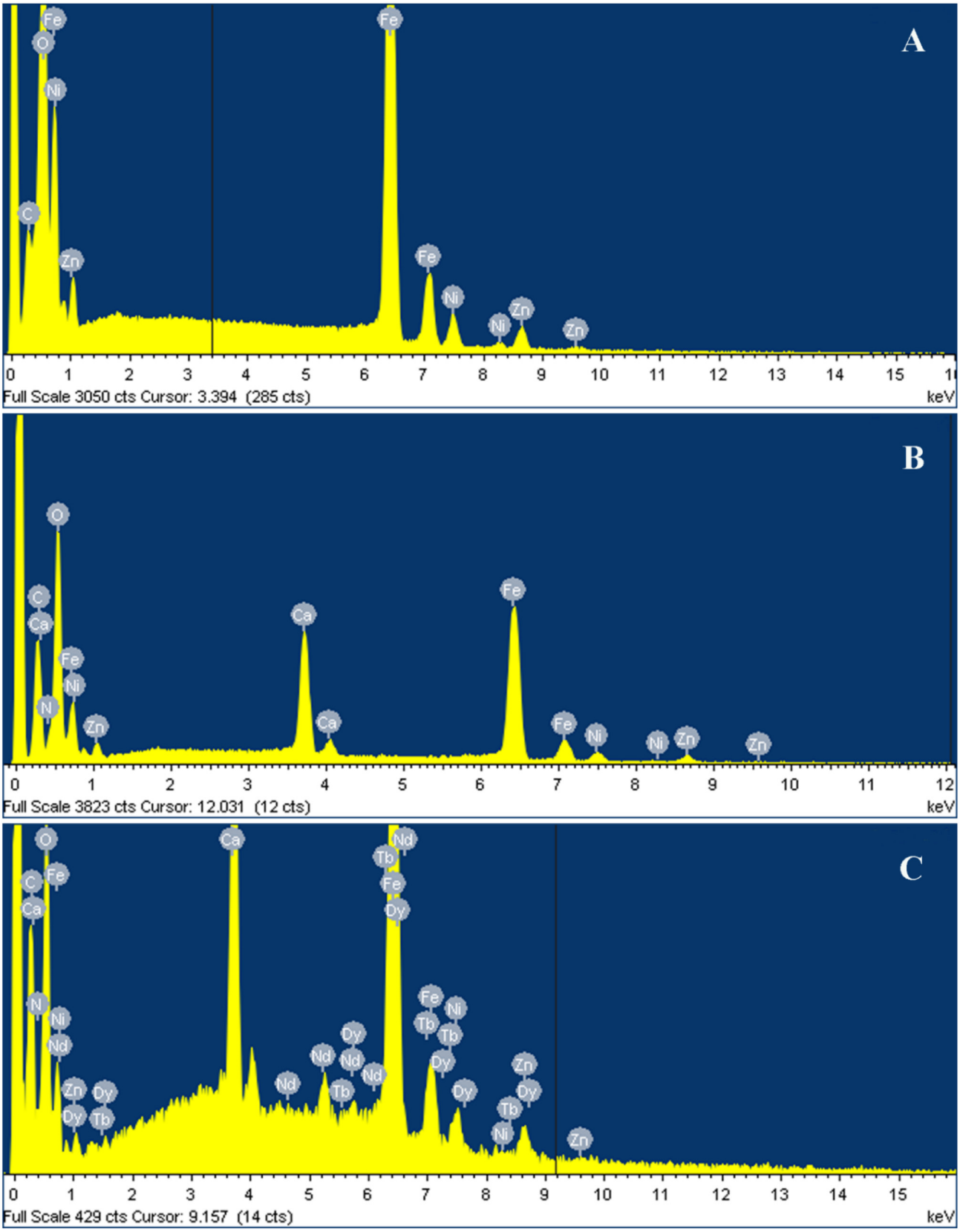

Fig. 5. EDX spectra of (A) $Ni_{0.2}Zn_{0.2}Fe_{2.6}O_4$ and (B) CA/CMC/$Ni_{0.2}Zn_{0.2}Fe_{2.6}O_4$, and (C) CA/CMC/$Ni_{0.2}Zn_{0.2}Fe_{2.6}O_4$ after adsorption of the ions.

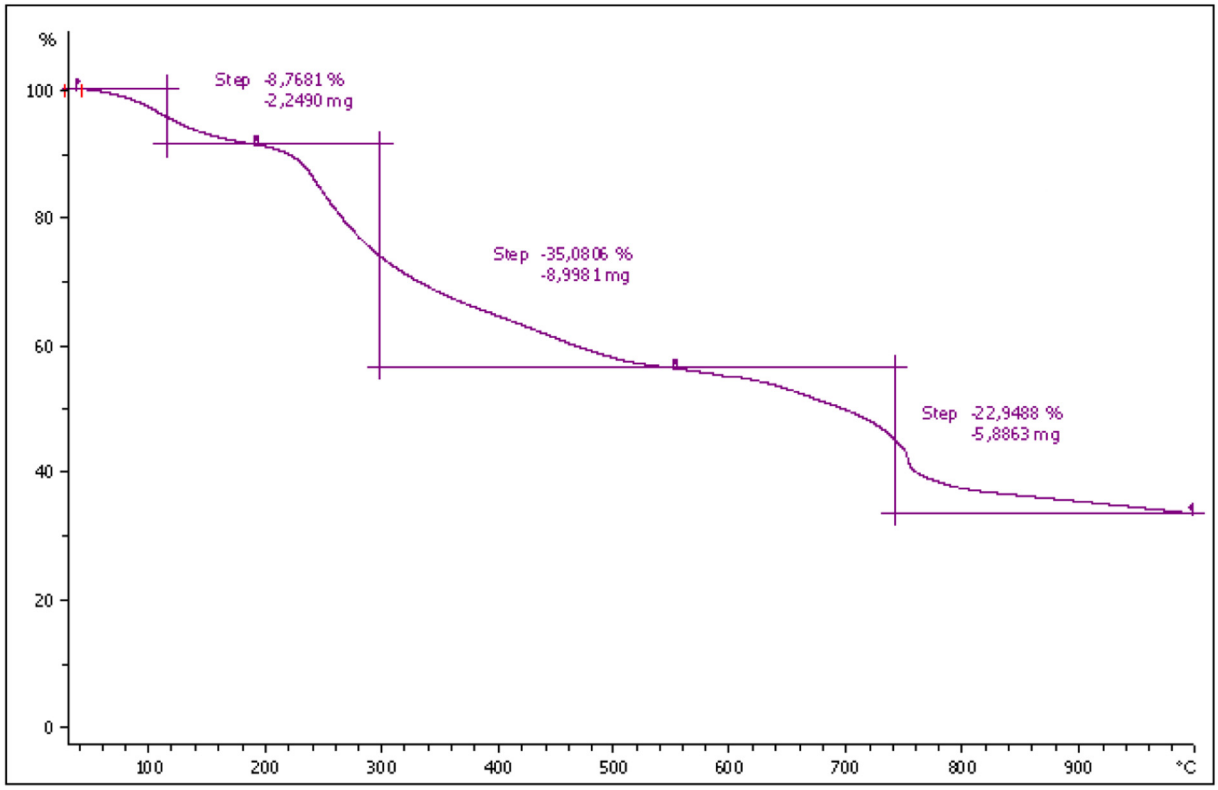

Fig. 6. TGA curve of CA/CMC/$Ni_{0.2}Zn_{0.2}Fe_{2.6}O_4$.

3.3. Central composite design

A total number of 32 experiments suggested by Design Expert 10.0 was performed to investigate the interaction of contact time (X_1), adsorbent dosage (X_2), Nd (III) concentration (X_3), Tb (III) concentration (X_4), and Dy (III) concentration (X_5). Table 1 indicates the design of experiments plus the predicted and actual values (adsorption efficiency (%)). Quadratic regression modeling was applied between the

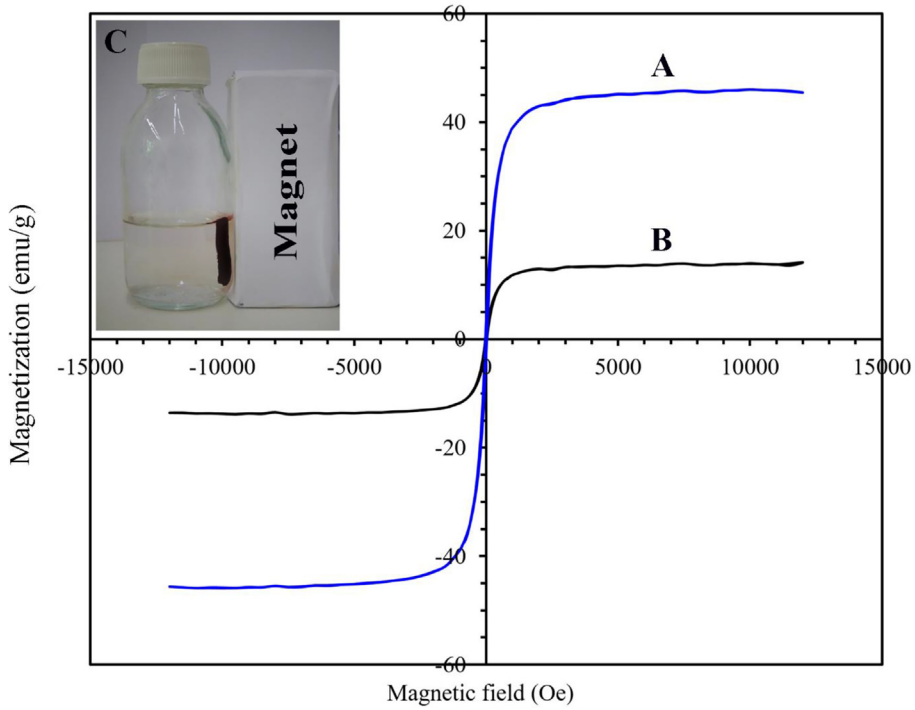

Fig. 7. Magnetization curves of (A) $Ni_{0.2}Zn_{0.2}Fe_{2.6}O_4$ and (B) CA/CMC/$Ni_{0.2}Zn_{0.2}Fe_{2.6}O_4$; (C) Magnetic separation of the ions-loaded adsorbent.

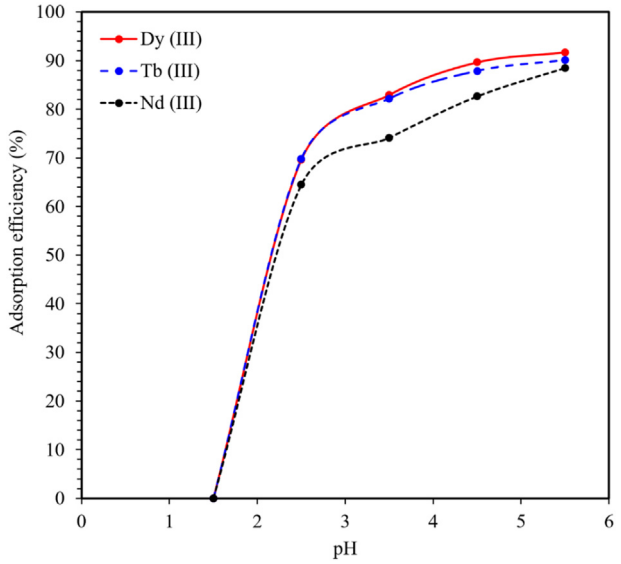

Fig. 8. Effects of pH on the adsorption of the ions.

response and independent variables for each metal, and the obtained equations were as follows:

$$\text{Nd (III) adsorption efficiency } (\%) = 45.421 + 1.866\,X_1 + 514.024\,X_2 - 0.571\,X_3 - 1.322\,X_4 + 0.175\,X_5 - 0.0043\,X_1X_3 + 0.00312\,X_1X_4 - 0.00255\,X_1X_5 - 2.27\,X_2X_1 + 1.796\,X_2X_3 + 1.351\,X_2X_4 + 0.759\,X_2X_5 + 0.00712\,X_3X_4 - 0.00258\,X_3X_5 + 0.00469\,X_4X_5 - 0.0126\,X1^2 - 1237.07\,X_2{}^2 - 0.000393\,X_3{}^2 + 0.00122\,X_4{}^2 - 0.00378\,X_5{}^2 \quad (13)$$

$$\text{Tb (III) adsorption efficiency } (\%) = 51.793 + 1.663\,X_1 + 410.645\,X_2 - 0.502\,X_3 - 0.603\,X_4 + 0.24\,X_5 - 7.549\,X_1X_3 + 1.073\,X_1X_4 - 1.132\,X_1X_5 - 2.253\,X_2X_1 + 1.651\,X_2X_3 + 1.185\,X_2X_4 + 1.283\,X_2X_5 + 0.00328\,X_3X_4 - 0.00178\,X_3\,X_5 + 0.00243\,X_4X_5 - 0.0124\,X1^2 - 1059.01\,X_2{}^2 - 0.0001808\,X_3{}^2 + 0.000553\,X_4{}^2 - 0.00103X_5{}^2 \quad (14)$$

$$\text{Dy (III) adsorption efficiency } (\%) = 58.691 + 1.632\,X_1 + 405.813\,X_2 - 0.354\,X_3 - 0.778\,X_4 - 0.315\,X_5 - 0.00156\,X_1X_3 + 0.00241X_1X_4 - 0.000818\,X_1X_5 - 2.405\,X_2X_1 + 1.486\,X_2X_3 + 1.371\,X_2X_4 + 1.272\,X_2X_5 + 0.00183\,X_3X_4 - 0.00243\,X_3X_5 + 0.00253\,X_4X_5 - 0.0122\,X1^2 - 1039.17\,X_2{}^2 + 0.000237\,X_3{}^2 + 0.000437\,X_4{}^2 - 0.0000959\,X_5{}^2 \quad (15)$$

The reliability of the models was examined by ANOVA. ANOVA represents the significance of variations associated with the models in comparison with the variations related to the experimental data [22]. The values of R^2 and R_{adj} [2] in Table 2 indicate a good agreement between the predicted and experimental data. In Table 2, the F-values with a very low probability value of < 0.0001 show that the predicted models are statistically significant. The 'Adequate precision" value for Nd (III), Tb (III), and Dy (III) obtained by ANOVA is favorable as a value >4 is preferable [31]. Additionally, the coefficient of variation value (C.V. %) is low, showing the reliability of the modeling. As can be observed from Fig. 9, the dispersal of the data points is not evident. A relatively straight line of normal probability plot should follow a nearly straight line to be favorable. In addition, the residuals are dispersed randomly in Figs. 10 and 11, indicating a favorable fitness between the predicted and experimental data.

Table 2
ANOVA results for adsorption of the ions by the CA/CMC/$Ni_{0.2}Zn_{0.2}Fe_{2.6}O_4$.

Source	DF[a]	Nd (III)				Tb (III)				Dy (III)			
		SS[b]	MS[c]	F-Value	P-value	SS[b]	MS[c]	F-Value	P-value	SS[b]	MS[c]	F-Value	P-value
Model	20	6816.27	340.81	111.8	<0.0001	5455.58	272.78	104.63	<0.0001	5394.59	269.73	88.64	<0.0001
X_1	1	539.13	539.13	176.86	<0.0001	497.77	497.77	190.92	<0.0001	504.53	504.53	165.81	<0.0001
X_1^2	1	391.55	391.55	128.45	<0.0001	379.51	379.51	145.56	<0.0001	368.18	368.18	121	<0.0001
X_2	1	3989.46	3989.46	1308.75	<0.0001	3164.35	3164.35	1213.69	<0.0001	3091.74	3091.74	1016.05	<0.0001
X_2^2	1	1420.35	1420.35	465.95	<0.0001	1040.89	1040.89	399.24	<0.0001	1002.26	1002.26	329.38	<0.0001
X_3	1	107.91	107.91	35.40	<0.0001	92.75	92.75	35.57	<0.0001	79.42	79.42	26.10	0.0003
X_3^2	1	0.23	0.23	0.075	0.7887	0.049	0.049	0.019	0.8939	0.084	0.084	0.027	0.8713
X_4	1	37.23	37.23	12.21	0.0050	13.59	13.59	5.21	0.0433	57.10	57.10	18.77	0.0012
X_4^2	1	2.24	2.24	0.74	0.4094	0.45	0.45	0.17	0.6844	0.28	0.28	0.093	0.7657
X_5	1	45.68	45.68	14.98	0.0026	64.94	64.94	24.91	0.0004	49.54	49.54	16.28	0.0020
X_5^2	1	21.24	21.24	6.97	0.0230	1.59	1.59	0.61	0.4506	0.014	0.014	0.00449	0.9478
X_1X_2	1	134.04	134.04	43.97	<0.0001	132.14	132.14	50.68	<0.0001	150.55	150.55	49.48	<0.0001
X_1X_3	1	19.25	19.25	6.32	0.0288	0.59	0.59	0.23	0.6428	2.56	2.56	0.84	0.3787
X_1X_4	1	10.19	10.19	3.34	0.0947	1.2	1.2	0.46	0.5117	6.05	6.05	1.99	0.1861
X_1X_5	1	6.77	6.77	2.22	0.1642	1.33	1.33	0.51	0.4893	0.7	0.7	0.23	0.6415
X_2X_3	1	65.33	65.33	21.43	0.0007	55.2	55.2	21.17	0.0008	44.76	44.76	14.71	0.0028
X_2X_4	1	37.00	37.00	12.14	0.0051	28.46	28.46	10.92	0.0070	38.07	38.07	12.51	0.0047
X_2X_5	1	11.68	11.68	3.83	0.0762	33.35	33.35	12.79	0.0043	32.78	32.78	10.77	0.0073
X_3X_4	1	41.12	41.12	13.49	0.0037	8.76	8.76	3.36	0.0940	2.72	2.72	0.89	0.3645
X_3X_5	1	5.39	5.39	1.77	0.2104	2.59	2.59	0.99	0.3401	4.82	4.82	1.58	0.2343
X_4X_5	1	17.87	17.87	5.86	0.0339	4.82	4.82	1.85	0.2012	5.22	5.22	1.72	0.2169
Residual	11	33.53	3.05			28.68	2.61			33.47	3.04		
Lack of Fit	6	32.95	5.49	46.87	0.0003	28.11	4.68	41.14	0.0004	33.07	5.51	68.67	0.0001
Pure Error	5	0.59	0.12			0.57	0.11			0.4	0.08		
Cor. Total	31	6849.80				5484.26				5428.06			
		R^2=0.9951		R_{adj} [2]=0.9862		R^2 = 0.9948		R_{adj} [2]=0.9853		R^2 = 0.9938		R_{adj} [2]=0.9826	
		AP[d]=40.91		C.V. % = 2.10		AP[d]=38.95		C.V. % = 1.87		AP[d]=35.37		C.V. % = 1.97	

[a] Degree of Freedom.
[b] Sum of Square.
[c] Mean Square.
[d] Adequate precision.

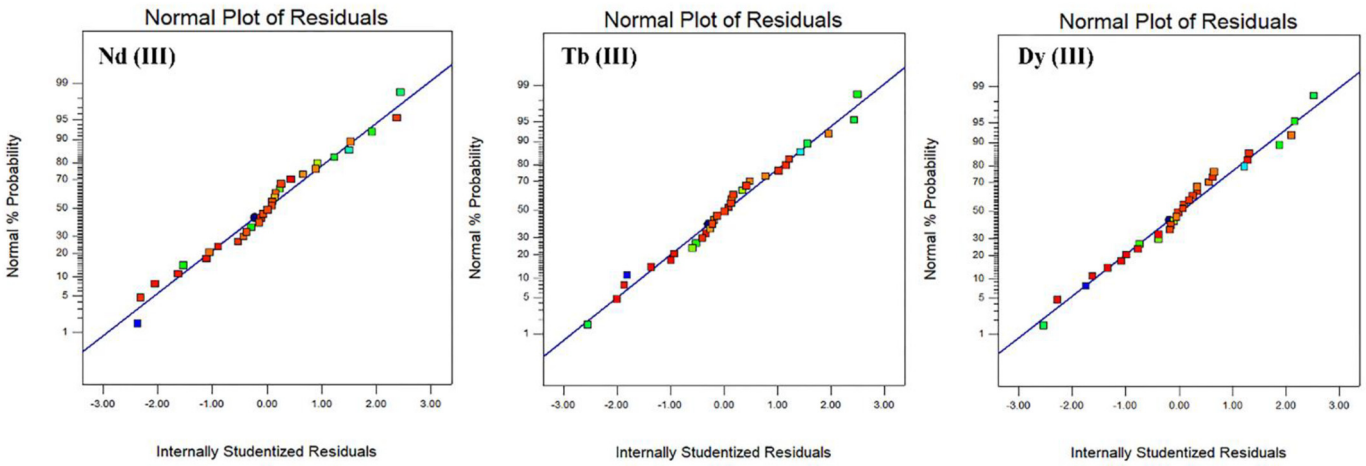

Fig. 9. Normal probability plots of residuals for the ions adsorption.

3.4. Three-dimensional response surface plot

To understand the main and interaction influences of two parameters in the adsorption process, 3D response surface plots are applied by considering them as function of adsorption efficiency while other factors are kept at constant values. The interactive effects of contact time, adsorbent dosage, and initial concentration of the ions are presented in Figs. 12A-I.

The effect of contact time and adsorbent dosage simultaneously on the ions adsorption is seen in Figs. 12A-C. It is evident that adsorption efficiency increases by enhancing contact time and adsorbent dosage. An increase in adsorption efficiency by an enhancement in the dosage of the adsorbent can be interpreted that increasing adsorbent dosage supplies more surface area and active binding sites for the ions adsorption onto the adsorbent [32]. According to the results of affecting time on the adsorption efficiency, two phases for the adsorption of the metal ions are seen as follows: the first phase that is sharper is related to the large number of the active sites that are empty on the adsorbent surface and high metal ions concentration. The second phase is assigned to the gradual decrease in the active sites, the decrease in intra-particle diffusion with the contact time, and the decrease in driving force that lead to an equilibrium state.

The concurrent influence of contact time and initial concentration in Figs. 12D-F shows higher adsorption efficiency of the ions at lower initial concentration since the adsorbent surface area is larger for the adsorption of the metal ions. An enhancement in the concentration of ions causes a decrease in adsorption efficiency because of decreasing available active sites for the ions adsorption as a result of the adsorption sites saturation [33]. Due to the higher ratio of initial number of the ions to the available adsorption sites at a higher ions concentration, lower adsorption efficiency is expected. It can be seen that increasing contact time beyond the optimum value leads to a decrease in adsorption efficiency for all the ions that could be due to the release or desorption of some ions from the substrate surfaces [34].

Figs. 12G-I are related to the simultaneous influence of adsorbent dosage and initial concentration. An increase in adsorbent dosage causes that adsorption efficiency increases due to the reason mentioned above. However, increasing adsorbent dosage at more than the optimum value leads to a decrease in adsorption efficiency due to the agglomeration of the adsorbent particles and screening effect. The total surface area of the adsorbent declines by such agglomeration, resulting in a reduction in the ions adsorption efficiency [35].

3.5. Confirmation experiments

The validity of the RSM model was investigated by performing four experiments for Nd (III), Tb (III), and Dy (III) ions adsorption onto the adsorbent. The adsorption efficiency acquired for each ion under the

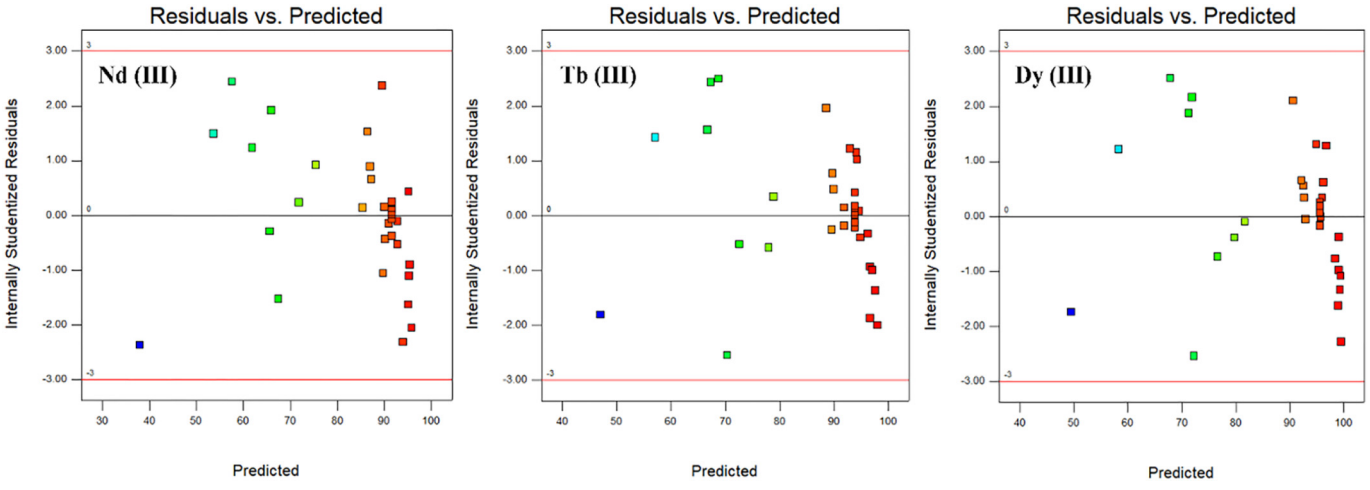

Fig. 10. Plots of studentized residuals versus predicted for the ions adsorption.

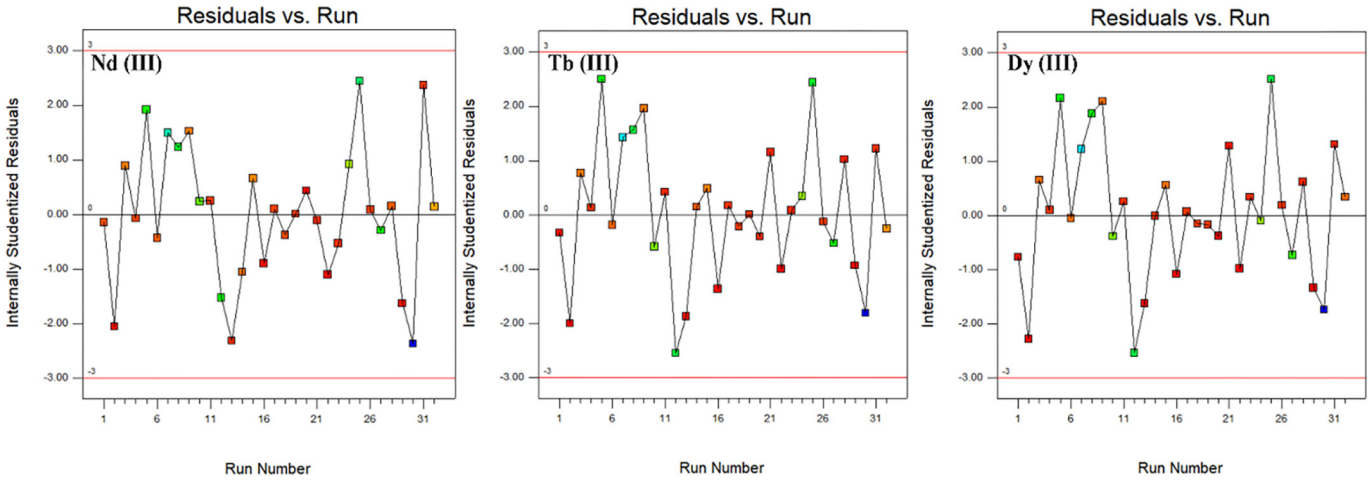

Fig. 11. Plots of studentized residuals versus experimental run number for the ions.

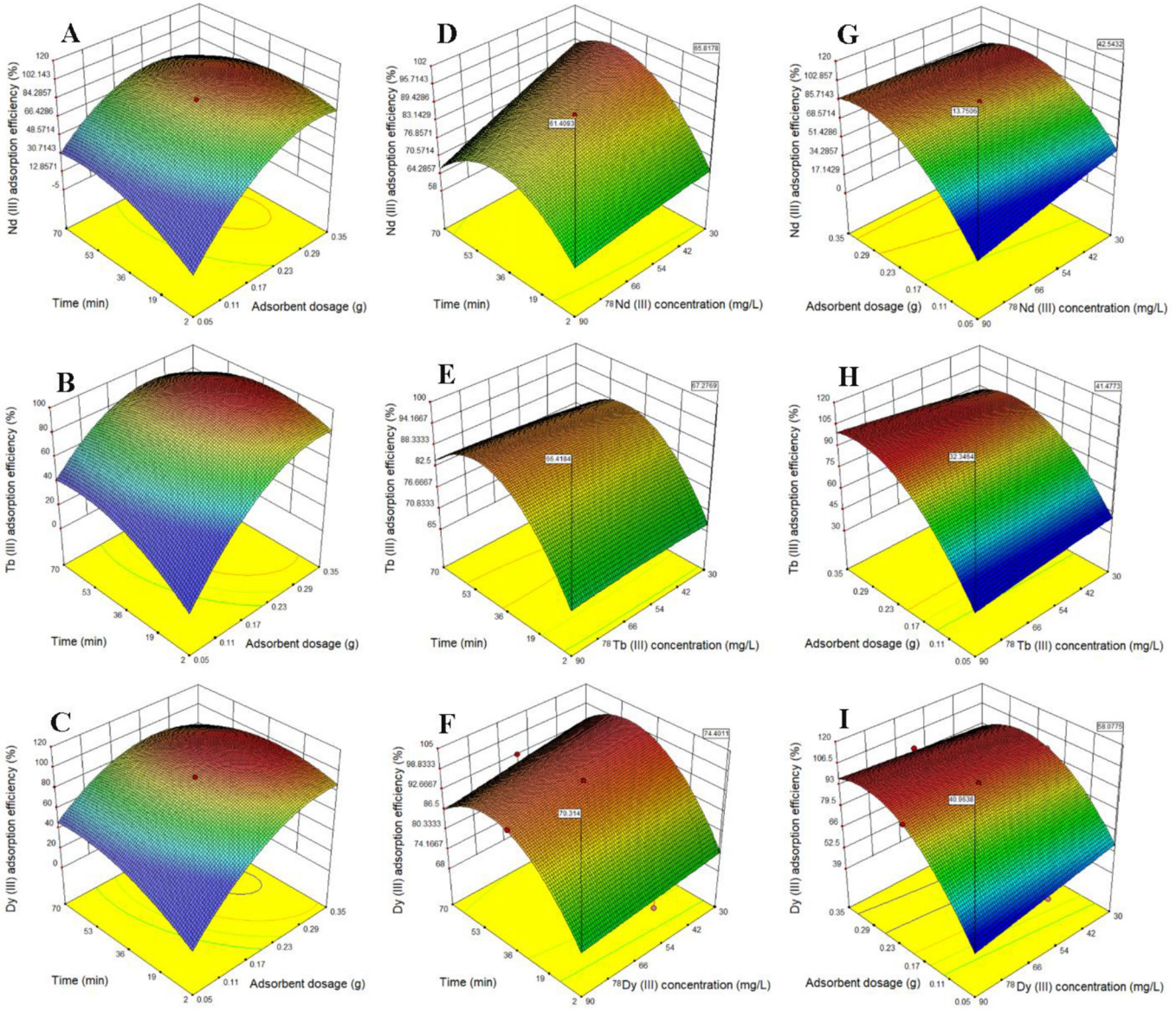

Fig. 12. 3D response surface plots of the ions adsorption onto CA/CMC/$Ni_{0.2}Zn_{0.2}Fe_{2.6}O_4$.

conditions given by CCD was compared with the value predicted by RSM. As can be observed from the obtained results presented in Table 3, difference between the values obtained from the experiments and predicted by the model results in error percentage in the range of 0.54–1.87, 0.58–2.28, and 0.61–2.11% for Nd (III), Tb (III), and Dy (III), respectively. At pH = 5.5, the adsorption efficiency under the conditions given by the model (adsorbent dosage = 0.1 g, contact time = 53 min, and initial concentration = 30 mg/L) was calculated to be 95.72, 96.17, and 99.44% with 1.17, 0.58, and 0.61% error for Nd (III), Tb (III), and Dy (III), respectively, indicating its agreement with the experimental value. The errors show the capability of the RSM model for the prediction of values that are favorably in accordance with the experimental data.

3.6. Batch adsorption kinetic studies

Kinetic investigations were carried out using the solutions with the volume of 50 mL prepared at 30 mg/L of Nd (III), Tb (III), and Dy (III) ions that were contacted with 0.09 g of the adsorbent at various times. Non-linear pseudo-first-order (PFO), PSO, and intra-particle diffusion (IPD) models were applied to model the kinetic data of Nd (III), Tb (III), and Dy (III) ions adsorption. The equations are as follows [36,37]:

$$q_t = q_e\ (1 - \exp.^{-K_1 t})\ \text{PFO} \tag{16}$$

$$q_t = K_2 q_e{}^2 t / 1 + K_2 q_e t\ \text{PSO} \tag{17}$$

$$q_t = K_i t^{0.5} + C\ \text{IPD} \tag{18}$$

where K_1 (1/min), K_2 (g/mg min), and K_i (1/min) respectively refer to the PFO rate constant, PSO rate constant, and the rate constant of IPD. Moreover, C provides information about the thickness of the boundary layer: higher value of C is related to the boundary layer diffusion influence.

The initial rate of adsorption (h) can be computed using K_2 and q_e values by the following equation:

$$h = K_2 q_e{}^2 \tag{19}$$

The values of kinetic parameters are shown in Table 4. As it is obvious from the results, the highest values of R^2 and the lowest values of χ^2 obtained by PSO shows that the main mechanism for controlling the adsorption of Nd (III), Tb (III), and Dy (III) ions onto the CA/CMC/$Ni_{0.2}Zn_{0.2}Fe_{2.6}O_4$ is chemisorption. The values of R^2 obtained by IPD model show that the adsorption of the ions is a multi-stage process. The stages were related to the strong electrostatic forces of attractions between the ions and the functional groups of the adsorbent, and gradual adsorption by the ions diffusion into the pores of the adsorbent until the occupation of most or all of the active sites. In addition, IPD model was not the sole rate-limiting step (the related plots do not pass through the origin).

Table 4
Kinetic constants for adsorption of Nd (III), Tb (III), and Dy (III) by the CA/CMC/$Ni_{0.2}Zn_{0.2}Fe_{2.6}O_4$.

		Nd (III)	Tb (III)	Dy (III)
PFO	K_1 (1/min)	0.2905	0.290	0.289
	q_e (mg/g)	15.07	15.30	15.61
	R^2	0.9617	0.9585	0.9587
	χ^2	0.240	0.268	0.279
PSO	K_2 (g/mg min) × 10^2	2.99	2.93	2.86
	q_e (mg/g)	16.15	16.40	16.74
	h (mg/g min) × 10^{-2s}	7.79	7.88	8.01
	R^2	0.9927	0.9933	0.9929
	χ^2	0.045	0.043	0.048
IPD	K_i (1/min)	3.88	3.96	4.05
	R^2	0.8157	0.8225	0.8222
	χ^2	1.16	1.15	1.20

3.7. Batch adsorption isotherm studies

Batch isotherm experiments were performed using 50 mL of metal ions solutions at different concentrations in the range of 30–180 mg/L contacting with 0.09 g of the CA/CMC/$Ni_{0.2}Zn_{0.2}Fe_{2.6}O_4$ at pH = 5.5. The data obtained at equilibrium were modeled by Langmuir and Freundlich models that are respectively related to monolayer and multilayer adsorption. The nonlinear Langmuir and Freundlich models were used according to following equations [38,39]:

$$qe = \frac{b\ qm\ Ce}{(1 + bCe)}\ \text{Langmuir} \tag{20}$$

$$q_{e=}\ K\ C_e{}^{1/n}\ \text{Freundlich} \tag{21}$$

where q_e and q_m (mg/g) respectively refer to the equilibrium adsorption and maximum adsorption capacities, and C_e (mg/L) shows the adsorbate equilibrium concentration. Moreover, b (L/mg) and K ($mg^{1-1/n}\ L^{1/n}/g$) respectively refer to Langmuir and Freundlich constants, and n shows adsorption intensity. Adsorption is favorable if $n > 1$.

The coefficient of determination (R [2]) values and the corresponding parameters obtained by the models are presented in Table 5. The n values are 9, 9.26, and 9.71 for Nd (III), Tb (III), and Dy (III), respectively, showing a strong interaction between the CA/CMC/$Ni_{0.2}Zn_{0.2}Fe_{2.6}O_4$ and the metal ions. According to the values of R^2 and χ^2, it is obvious that Freundlich model better fits the experimental data than Langmuir model for Nd (III), Tb (III), and Dy (III) ions adsorption. Consequently, the adsorption of the ions is multilayer adsorption, and the adsorption takes place on a non-uniform surface.

3.8. Ionic strength effect

The ions adsorption can be affected by the co-ions that are available in the solution. The influence of salt concentration, known as ionic strength, on the adsorption efficiency of the ions by the CA/

Table 3
Confirmation experiments for the ions adsorption onto the CA/CMC/$Ni_{0.2}Zn_{0.2}Fe_{2.6}O_4$.

No.	Condition					Nd (III)		Tb (III)		Dy (III)		Error (%)		
	Time (min)	Adsorbent dosage (g)	Initial concentration (mg/L)			Observed	Predicted	Observed	Predicted	Observed	Predicted			
			Nd (III)	Tb (III)	Dy (III)							Nd (III)	Tb (III)	Dy (III)
1	53	0.1	30	30	30	94.61	95.72	96.73	96.17	98.83	99.44	1.17	0.58	0.61
2	19	0.125	75	45	45	63.12	61.9	68.27	66.71	72.85	71.31	1.93	2.28	2.11
3	36	0.2	90	60	60	87.44	86.97	90.86	89.74	93.73	92.17	0.54	1.23	1.66
4	53	0.275	45	75	45	93.48	95.23	96.18	97	97.54	99.05	1.87	0.85	1.54

Table 5
Isotherm constants for adsorption of Nd (III), Tb (III), and Dy (III) by the CA/CMC/$Ni_{0.2}Zn_{0.2}Fe_{2.6}O_4$.

		Nd (III)	Tb (III)	Dy (III)
Langmuir	b (L/mg)	0.78	0.89	1.27
	q_m (mg/g)	23.15	24.41	25.24
	R^2	0.8773	0.9238	0.9125
	χ^2	1.62	1.21	1.61
Freundlich	K ($mg^{1-1/n}$ $L^{1/n}$/g)	14.40	15.46	16.49
	n	9	9.26	9.71
	R^2	0.9879	0.9654	0.9633
	χ^2	0.159	0.55	0.675

CMC/$Ni_{0.2}Zn_{0.2}Fe_{2.6}O_4$ was evaluated using $NaNO_3$ at various concentrations ranging from 0.02 to 0.1 M, and the results are presented in Fig. 13A. As it is illustrated in Fig. 13A, the presence of $NaNO_3$ has a greater negative effect on the adsorption efficiency of Nd (III) in comparison with Tb (III) and Dy (III). The adsorption efficiency for Nd (III), Tb (III), and Dy (III) respectively decreases from 92.33 to 77.12, 93.91 to 85.6, and 96.25 to 91.43% by an increase in $NaNO_3$ concentration. This phenomenon can be related to the competition between the metal ions and sodium ions for the available active adsorption sites of the adsorbent [40]. In addition, the aggregation of adsorbent could be heightened by enhancing ionic strength that results in a decrease in adsorption sites of adsorbent [41].

3.9. Thermodynamic parameters

Thermodynamic parameters are considered as key factors to realize the optimal condition and give further information regarding changes in inherent energetic related to adsorption process. The adsorption process was conducted at various temperatures (25, 35, and 45 °C) to obtain ΔS° and ΔH° values based on the following equation:

$$\mathrm{Ln}K_d = \frac{\Delta S^\circ}{R} - \frac{\Delta H^\circ}{RT} \quad (22)$$

where R, T, and K_d respectively refer to the gas constant (8.314 J/mol K), temperature (K), and distribution coefficient that was obtained by the equation as following:

$$K_d = \frac{q_e}{C_e} \quad (23)$$

where C_e refer to the equilibrium concentration in the solution (mg/L). ΔH° value for each metal is calculated from the slope of Ln K_d versus 1/T plot, and ΔS° value is computed from its intercept (Fig. 13B). The ΔG° values were also calculated at different temperatures by using the following equation:

$$\Delta G^\circ = -RT \ln K_d \quad (24)$$

Table 6 shows the values of thermodynamic parameters. The ΔG° values for the ions are positive at all temperatures that show the process is non-spontaneous, and the adsorption of the ions onto the adsorbent requires additional energy from an external source. The lower values of ΔG° at higher temperatures mean that an increase in temperature leads to an increase in the tendency of spontaneous reaction. The ΔH° value > zero shows the endothermic adsorption of the metal ions, and the ΔS° value > zero expresses the increase in randomness at the interface of solid–solution during the metal ions fixation on the CA/CMC/$Ni_{0.2}Zn_{0.2}Fe_{2.6}O_4$ surface [39].

3.10. Reusability studies

The synthesized CA/CMC/$Ni_{0.2}Zn_{0.2}Fe_{2.6}O_4$ was utilized in four consecutive adsorption-desorption cycles to investigate its reusability. For this purpose, the adsorption of the ions by the CA/CMC/$Ni_{0.2}Zn_{0.2}Fe_{2.6}O_4$ was performed at initial concentration = 30 mg/L and pH = 5.5 with 0.1 g of the adsorbent for 53 min. The batch flask containing the CA/CMC/$Ni_{0.2}Zn_{0.2}Fe_{2.6}O_4$ and 50 mL of 0.2 M HNO_3 as eluent was shaken for 2 h for desorption of the ions loaded onto the adsorbents. Then, the adsorbent was separated by an external magnetic field from the HNO_3 solution, and the functional groups were neutralized by NaOH solution. The neutralized CA/CMC/$Ni_{0.2}Zn_{0.2}Fe_{2.6}O_4$ was then used for the adsorption of 30 mg/L of the ions in the next cycle. Nd+3, Tb+3, and Dy+3 ions were desorbed from the adsorbent > 93, 96, and 97 %, respectively.

The results of adsorption efficiency in 4 cycles are shown in Fig. 13C. Due to the decrease in the release of the ions and number of active sites by acid treatment during the cycles, the adsorption efficiency for Nd (III), Tb (III), and Dy (III) respectively decreases from 94.18 to 91.64, 96.45 to 94.82, and 98.33 to 97.17%. After the last cycle, the adsorption efficiency of the CA/CMC/$Ni_{0.2}Zn_{0.2}Fe_{2.6}O_4$ indicates 2.54, 1.63, and 1.16% lose for Nd (III), Tb (III), and Dy, respectively, in comparison with the first cycle. The results also indicated that the CA/CMC/$Ni_{0.2}Zn_{0.2}Fe_{2.6}O_4$ remained magnetic during the process of adsorption-desorption. According to the results, the adsorbent suitability for a practical application can be concluded.

3.11. Column mode

Fig. 14A presents the Nd (III), Tb (III), and Dy (III) ions adsorption breakthrough curves obtained from the fixed-bed column packed with

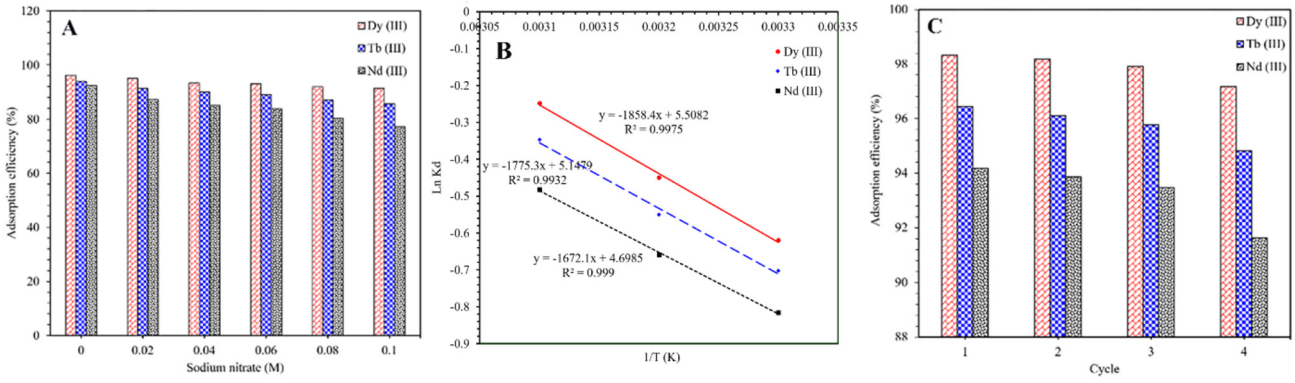

Fig. 13. (A) Effect of ionic strength on the adsorption of Nd (III), Tb (III), and Dy (III), (B) Ln K_d versus 1/T for calculation of enthalpy and entropy changes, and (C) Reusability of CA/CMC/$Ni_{0.2}Zn_{0.2}Fe_{2.6}O_4$ for adsorption of the ions.

Table 6
Effect of temperature on the adsorption of Nd (III), Tb (III), and Dy (III) at 90 mg/L and thermodynamic parameters.

Adsorption efficiency (%)				
Temperature (°C)		Nd (III)	Tb (III)	Dy (III)
25		44.31	47.14	49.21
35		48.23	50.48	53.45
45		52.64	55.99	58.42
	Thermodynamic parameters			
		Nd (III)	Tb (III)	Dy (III)
ΔH° (kJ/mol)		13.9	14.76	15.45
ΔS° (kJ/mol K)		0.039	0.043	0.046
	Temperature (°C)			
ΔG° (kJ/mol)	25	2.022	1.739	1.534
	35	1.686	1.408	1.151
	45	1.274	0.918	0.655

the CA/CMC/$Ni_{0.2}Zn_{0.2}Fe_{2.6}O_4$. According to the obtained results, the breakthrough and exhaustion times that respectively correspond to $C_e/C_0 = 0.05$ and 0.95 are about 95 and 410 min for Nd (III), 105 and 430 min for Tb (III), and 120 and 440 min for Dy (III). Exhaust volume (V_{eff}) for Nd (III), Tb (III), and Dy (III) is respectively 410, 430, and 440 mL.

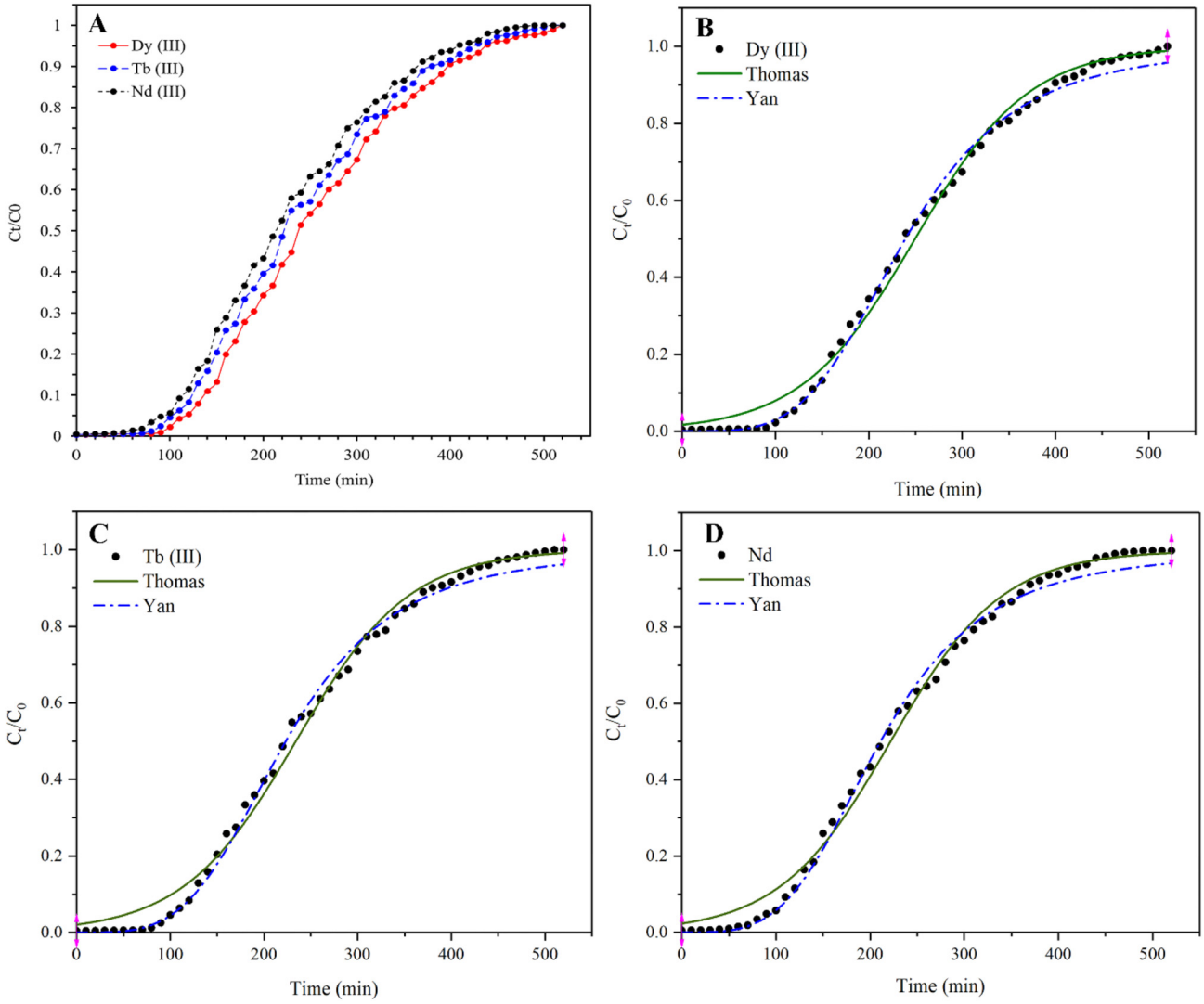

Fig. 14. (A) Experimental data of the column adsorption and (B–D) Modeling of the experimental data with Thomas and Yan models.

Table 7
Parameters of breakthrough and the values predicted by Thomas and Yan models.

Metal	Breakthrough analysis			Thomas model			Yan model		
	q_e	Adsorption efficiency (%)	C_e	$K_{Th} \times 10^4$	q_e	R^2	q_e	a	R^2
Nd (III)	22.70	46.33	16.10	5.65	22.18	0.9945	21.10	3.74	0.9957
Tb (III)	22.70	47.07	15.88	5.52	23.44	0.9937	22.32	3.83	0.9962
Dy (III)	25.54	49.11	15.26	5.46	24.96	0.9940	23.92	4.01	0.9970

Nonlinear Thomas and Yan models were utilized to fit the experimental data of the fixed-bed column by Eq. (25) and Eq. (26), respectively.

$$\frac{C_t}{C_0} = \frac{1}{1 + \exp\left(\frac{K_{Th} q_e x}{Q} - K_{Th} C_0 t\right)} \tag{25}$$

$$\frac{C_t}{C_0} = 1 - \frac{1}{1 + \left(\frac{C_0 Q t}{q_e x}\right)^a} \tag{26}$$

where K_{Th} shows the rate constant (mL/min mg), a is a constant coefficient and q_e is the maximum adsorption capacity (mg/g), x is the mass of adsorbent (g), C_0 is the initial concentration (mg/L) of the ions, C_t is outlet ions concentration (mg/L), t is the contact time (min), and Q is the flow rate (mL/min). K_{Th}, a, and q_e values are computed using the slope and intercept of the plot of $\frac{C_t}{C_0}$ against t.

The parameters obtained by the models (Figs. 14B-D) are indicated in Table 7. The adsorption capacity (q_e) for Nd (III), Tb (III), and Dy (III), calculated by Eq. (9), is respectively 22.70, 24.00, and 25.54 mg/g under the studied conditions. According to the values of R [2], both models can fit the experimental data well but Yan model presents higher values of R^2 in comparison with Thomas model. The rate constant value of Thomas (K_{Th}) for Nd (III) is higher than those of Tb (III), and Dy (III), showing higher intensity of Nd (III) adsorption onto the CA/CMC/$Ni_{0.2}Zn_{0.2}Fe_{2.6}O_4$, while the amount of maximum adsorption capacity (q_e) for Dy (III) is greater than the value obtained for Nd (III) and Tb (III). This is in conformity with the results achieved from experiments of batch adsorption.

4. Conclusion

In this paper, the CA/CMC/$Ni_{0.2}Zn_{0.2}Fe_{2.6}O_4$ was synthesized successfully by the gelation process of CA/CMC in the presence of the $Ni_{0.2}Zn_{0.2}Fe_{2.6}O_4$. RSM-CCD was applied to explore the influences of experimental parameters on Nd (III), Tb (III), and Dy (III) ions adsorption. The conditions predicted by RSM for optimum adsorption of 30 mg/L of the ions were 0.1 g of the adsorbent and 53 min contact time at pH = 5.5. The experimental data were fitted by isotherm and kinetic models. PSO kinetic model fitted the data better compared with IPD and PFO models. The data of equilibrium were fitted well with Freundlich model. The values of ΔH° revealed the endothermic adsorption process of the metal ions. 0.2 M HNO_3 was used for regeneration of the ion-loaded adsorbent, and the adsorbent was repeatedly used in four cycles with >91, 94, and 97% adsorption efficiency for Nd (III), Tb (III), and Dy (III), respectively, after the fourth cycle. Besides, the ions were successfully adsorbed in a continuous process by applying a packed-bed column, and the data were found to be fitted well by Thomas and Yan models. The results showed that the CA/CMC/$Ni_{0.2}Zn_{0.2}Fe_{2.6}O_4$ can be applied as a potential adsorbent in both adsorption modes (batch and column) for Nd (III), Tb (III), and Dy (III) ions adsorption.

CRediT authorship contribution statement

Hamedreza Javadian: Investigation, Data curation, Formal analysis, Writing - original draft, Writing - review & editing. **Montserrat Ruiz:** Data curation, Supervision. **Ana Maria Sastre:** Conceptualization, Supervision.

Acknowledgments

This work has been supported by the Spanish Ministry of Economy and Competitiveness (Ref. CTM2017-83581-R). Hamedreza Javadian acknowledges the financial support received (Ref. BES-2015-072506).

References

[1] G.A. Moldoveanu, V.G. Papangelakis, Recovery of rare earth elements adsorbed on clay minerals. I. Desorption mechanism, Hydrometallurgy 117–118 (2012) 71–78.
[2] J. Ponou, L.P. Wang, G. Dodbiba, K. Okaya, T. Fujita, K. Mitsuhashi, T. Atarashi, G. Satoh, M. Noda, Recovery of rare earth elements from aqueous solution obtained from Vietnamese clay minerals using dried and carbonized parachlorella, J. Environ. Chem. Eng. 2 (2014) 1070–1081.
[3] W. Franus, M.M. Wiatros-Motyka, M. Wdowin, Coal fly ash as a resource for rare earth elements, Environ. Sci. Pollut. Res. 22 (12) (2015) 9464–9474.
[4] D. Sadovsky, A. Brenner, B. Astrachan, B. Asaf, R. Gonen, Biosorption potential of cerium ions using *Spirulina* biomass, J. Rare Earths 34 (2016) 644–652.
[5] F. Zhao, E. Repo, Y. Meng, X. Wang, D. Yin, M. Sillanpää, An EDTA-β-cyclodextrin material for the adsorption of rare earth elements and its application in preconcentration of rare earth elements in seawater, J. Colloid Interface Sci. 465 (2016) 215–224.
[6] K. Vijayaraghavan, R. Balasubramanian, Single and binary biosorption of cerium and europium onto crab shell particles, Chem. Eng. J. 163 (2010) 337–343.
[7] J.L. Wang, C. Chen, Biosorbents for heavy metals removal and their future, Biotechnol. Adv. 27 (2) (2009) 195–226.
[8] H.A. Shawky, Improvement of water quality using alginate/montmorillonite composite beads, J. Appl. Polym. Sci. 119 (4) (2010) 2371–2378.
[9] Y. Ma, P. Qi, J. Ju, Q. Wang, L. Hao, R. Wang, K. Sui, Y. Tan, Gelatin/alginate composite nanofiber membranes for effective and even adsorption of cationic dyes, Compos Part B Eng 162 (2019) 671–677.
[10] F. Ahmadpoor, S.A. Shojaosadati, S.Z. Mousavi, Magnetic silica coated iron carbide/alginate beads: synthesis and application for adsorption of cu (II) from aqueous solutions, Int. J. Biol. Macromol. 128 (2019) 941–947.
[11] T. Guo, Y. Pei, K. Tang, X. He, J. Huang, F. Wang, Mechanical and drug release properties of alginate beads reinforced with cellulose, J. Appl. Polym. Sci. 134 (8) (2016) 44495.
[12] Z.H. Hu, A.M. Omer, X.K. Ouyang, D. Yu, Fabrication of carboxylated cellulose nanocrystal/sodium alginate hydrogel beads for adsorption of Pb(II) from aqueous solution, Int. J. Biol. Macromol. 108 (2018) 149–157.
[13] R. Ahmad, A. Mirza, Adsorption of Pb (II) and cu (II) by alginate-au-mica bionanocomposite: kinetic, isotherm and thermodynamic studies, Process Saf Environ 109 (2017) 1–10.
[14] L. Zhang, Y. Zeng, Z. Cheng, Removal of heavy metal ions using chitosan and modified chitosan: a review, J. Mol. Liq. 214 (2016) 175–191.
[15] M. Li, J. Xu, R. Li, D. Wang, T. Li, M. Yuan, J. Wang, Simple preparation of aminothiourea-modified chitosan as corrosion inhibitor and heavy metal ion adsorbent, J. Colloid Interface Sci. 417 (3) (2014) 131–136.
[16] D.W. Cho, B.H. Jeon, C.M. Chon, Y. Kim, F.W. Schwartz, E.S. Lee, H. Song, A novel chitosan/clay/magnetite composite for adsorption of cu(II) and as(V), Chem. Eng. J. 200–202 (34) (2012) 654–662.
[17] L. Fan, C. Luo, Z. Lv, F. Lu, H. Qiu, Removal of Ag^+ from water environment using a novel magnetic thiourea-chitosan imprinted Ag^+, J. Hazard. Mater. 194 (11) (2011) 193–201.
[18] P.O. Boamah, Y. Huang, M. Hua, Q. Zhang, J. Wu, J. Onumah, L.K. Sam-Amoah, P.O. Boamah, Sorption of heavy metal ions onto carboxylate chitosan derivatives—a mini-review, Ecotoxicol. Environ. Saf. 116 (2015) 113–120.
[19] H. Yang, H. Li, J. Zhai, L. Sun, Y. Zhao, H. Yu, Magnetic prussian blue/graphene oxide nanocomposites caged in calcium alginate microbeads for elimination of cesium ions from water and soil, Chem. Eng. J. 246 (2014) 10–19.
[20] G. Reiss, A. Hütten, Magnetic nanoparticles: applications beyond data storage, Nat. Mater. 4 (2005) 725–726.

[21] D. Gusain, F. Bux, Y. Chandra Sharma, Abatement of chromium by adsorption on nanocrystalline zirconia using response surface methodology, J. Mol. Liq. 197 (2014) 131–141.
[22] N. Markandeya, S. Dhiman, P. Shukla, G.C. Kisku, Statistical optimization of process parameters for removal of dyes from wastewater on chitosan cenospheres nanocomposite using response surface methodology, J. Clean. Prod. 149 (2017) 597–606.
[23] V. Srivastava, Y.C. Sharma, M. Sillanpää, Application of response surface methodology for optimization of co(II) removal from synthetic wastewater by adsorption on NiO nanoparticles, J. Mol. Liq. 211 (2015) 613–620.
[24] D. Ni, Z. Lin, P. Xiaoling, W. Xinqing, G. Hongliang, Preparation and characterization of nickel-zinc ferrites by a solvothermal method, Rare Metal Mat Eng 44 (9) (2015) 2126–2131.
[25] C. Tamez, R. Hernandez, J.G. Parsons, Removal of cu (II) and Pb (II) from aqueous solution using engineered iron oxide nanoparticles, Microchem. J. 125 (2016) 97–104.
[26] R. Fabryanty, C. Valencia, F. Edi Soetaredjo, J. Nyoo Putro, S. Permatasari Santoso, A. Kurniawan, Y.H. Ju, S. Ismadji, Removal of crystal violet dye by adsorption using bentonite-alginate composite, J. Environ. Chem. Eng. 5 (2017) 5677–5687.
[27] S.P. Wu, X.Z. Dai, J.R. Kan, F.D. Shilong, M.Y. Zhu, Fabrication of carboxymethyl chitosan–hemicellulose resin for adsorptive removal of heavy metals from wastewater, Chin. Chem. Lett. 28 (2017) 625–632.
[28] A.S.A. Bakr, Y.M. Moustafa, E.A. Motawea, M.M. Yehia, M.M.H. Khalil, Removal of ferrous ions from their aqueous solutions onto $NiFe_2O_4$–alginate composite beads, J. Environ. Chem. Eng. 3 (2015) 1486–1496.
[29] S.A. Elfeky, S. Ebrahim Mahmoud, A. Fahmy Youssef, Applications of CTAB modified magnetic nanoparticles for removal of chromium (VI) from contaminated water, J. Adv. Res. 8 (4) (2017) 435–443.
[30] R. Darvishi Cheshmeh Soltani, G. Shams Khorramabadi, A.R. Khataee, S. Jorfi, Silica nanopowders/alginate composite for adsorption of lead (II) ions in aqueous solutions, J. Taiwan Inst. Chem. Eng. 45 (2014) 973–980.
[31] R.D.C. Soltani, A. Rezaee, H. Godini, A.R. Khataee, A. Hasanbeiki, Photoelectrochemical treatment of ammonium using seawater as a natural supporting electrolyte, Chem. Ecol. 29 (2013) 72–85.
[32] M. El kady, H. Shokry, H. Hamad, Effect of superparamagnetic nanoparticles on the physicochemical properties of nano hydroxyapatite for groundwater treatment: adsorption mechanism of Fe(II) and Mn (II), RSC Adv. 6 (2016) 82244–82259.
[33] A. Mohseni-Bandpi, B. Kakavandi, R.R. Kalantary, A. Azari, A. Keramati, Development of a novel magnetite-chitosan composite for the removal of fluoride from drinking water: adsorption modeling and optimization, RSC Adv. 5 (2015) 73279–73289.
[34] H. Shekari, M.H. Sayadi, M.R. Rezaei, A. Allahresani, Synthesis of nickel ferrite/titanium oxide magnetic nanocomposite and its use to remove hexavalent chromium from aqueous solutions, Surf. Interface. 8 (2017) 199–205.
[35] K.S. Padmavathy, G. Madhu, P.V. Haseena, A study on effects of pH, adsorbent dosage, time, initial concentration and adsorption isotherm study for the removal of hexavalent chromium (Cr (VI)) from wastewater by magnetite nanoparticles, Procedia Technol 24 (2016) 585–594.
[36] S.C.W. Sakti, Y. Narita, T. Sasaki, S. Tanaka Nuryono, A novel pyridinium functionalized magnetic chitosan with pH-independent and rapid adsorption kinetics for magnetic separation of Cr(VI), J. Environ. Chem. Eng. 3 (2015) 1953–1961.
[37] H. Javadian, P. Vahedian, M. Toosi, Adsorption characteristics of Ni(II) from aqueous solution and industrial wastewater onto Polyaniline/HMS nanocomposite powder, Appl. Surf. Sci. 284 (2013) 13–22.
[38] V.S. Munagapati, D.S. Kim, Equilibrium isotherms, kinetics, and thermodynamics studies for Congo red adsorption using calcium alginate beads impregnated with nano-goethite, Ecotoxicol. Environ. Saf. 141 (2017) 226–234.
[39] H. Javadian, M. Torabi Angaji, M. Naushad, Synthesis and characterization of polyaniline/γ-alumina nanocomposite: a comparative study for the adsorption of three different anionic dyes, J. Ind. Eng. Chem. 20 (2014) 3890–3900.
[40] S. Malamis, E. Katsou, A review on zinc and nickel adsorption on natural and modified zeolite, bentonite and vermiculite: examination of process parameters, kinetics and isotherms, J. Hazard. Mater. 252 (2013) 428–461.
[41] F.F. Zeng, Y. He, Z.H. Lian, J.M. Xu, The impact of solution chemistry of electrolyte on the sorption of pentachlorophenol and phenanthrene by natural hematite nanoparticles, Sci. Total Environ. 466 (2014) 577–585.

ANNEX III

Synthesis of magnetic CMC bionanocomposite containing a novel biodegradable nanoporous polyamide selectively synthesized in ionic liquid as green media: Investigation on Nd^{+3}, Tb^{+3}, and Dy^{+3} rare earths adsorption.

Hamedreza Javadian, Montserrat Ruiz, Mehdi Taghavi, Ana Maria Sastre,

Journal of Molecular Liquids, 308 (2020) 113017.

https://doi.org/10.1016/j.molliq.2020.113017

Journal of Molecular Liquids 308 (2020) 113017

Contents lists available at ScienceDirect

Journal of Molecular Liquids

journal homepage: www.elsevier.com/locate/molliq

Synthesis of magnetic CMC bionanocomposite containing a novel biodegradable nanoporous polyamide selectively synthesized in ionic liquid as green media: Investigation on Nd^{+3}, Tb^{+3}, and Dy^{+3} rare earth elements adsorption

Hamedreza Javadian [a,*], Montserrat Ruiz [b], Mehdi Taghavi [c], Ana Maria Sastre [a]

[a] Department of Chemical Engineering, ETSEIB, Universitat Politècnica de Catalunya, Diagonal 647, 08028 Barcelona, Spain
[b] Department of Chemical Engineering, EPSEVG, Universitat Politècnica de Catalunya, Av. Víctor Balaguer, s/n, 08800 Vilanova i la Geltrú, Spain
[c] Department of Chemistry, Faculty of Science, Shahid Chamran University of Ahvaz, 61357-43337, Iran

ARTICLE INFO

Article history:
Received 27 October 2019
Received in revised form 20 March 2020
Accepted 28 March 2020
Available online 31 March 2020

Keywords:
Carboxymethyl chitosan
Poly(pyrimidine-thiophene-amide)
Magnetic
Bionanocomposite
Adsorption
Rare earth elements

ABSTRACT

In this research study, the carboxymethyl chitosan/poly(pyrimidine-thiophene-amide)/$Ni_{0.2}Zn_{0.2}Fe_{2.6}O_4$ (CMC/P(PTA)/$Ni_{0.2}Zn_{0.2}Fe_{2.6}O_4$) was prepared as a novel magnetic bionanocomposite adsorbent. FE-SEM, EDX, NMR, XRD, FT-IR, and VSM techniques were applied for the analyses of the products. The adsorption behavior of the prepared bionanocomposite was investigated towards Nd^{+3}, Tb^{+3}, and Dy^{+3} as adsorbates. The adsorption process was evaluated considering the influence of independent parameters including pH of the solution, contact time, adsorbent dosage, initial metal ions concentration, and ionic strength. The adsorption efficiency values of 98.15, 97.6, and 99.42% were respectively obtained for Nd^{+3}, Tb^{+3}, and Dy^{+3} at optimum conditions of pH = 5.5, 30 mg/L of the ions, adsorbent dosage of 0.06 g, and contact time of 90 min. The data of the adsorption equilibrium of the ions were fitted well by Freundlich model. Kinetic studies showed that Nd^{+3}, Tb^{+3}, and Dy^{+3} adsorption followed both pseudo-second-order (PSO) and intra-particle diffusion (IPD) kinetic models. The values of ΔH° indicated that the ions adsorption process onto the bionanocomposite was endothermic, and the ΔG° values revealed that it was spontaneous at higher temperature. The CMC/P(PTA)/$Ni_{0.2}Zn_{0.2}Fe_{2.6}O_4$ could be regenerated by 0.2 M HNO_3 and its separation was viable utilizing a magnetic field with the saturation magnetization value of 14.88 emu/g.

1. Introduction

Rare earth elements (REEs) contain 17 components of the periodic table that include 15 lanthanides together with yttrium and scandium [1–3]. Light and heavy REEs are the additional subdivision of REEs based on atomic number. They possess exceptional properties and are regularly named as "seeds of technology" [4]. They are extensively utilized in various fields, for example, electronics, metallurgy, catalysis, alloys, superconductors, lasers, fertilizers, chemical reagents, nuclear energy, and magnets [5,6]. The total demand for REEs was reported 128,000 tons in 2011, and this amount was raised up to 170,000 tons in 2015. It is also anticipated that it would increase up to 255,000 tons in 2020 with around 6–10%/year growth rate [7]. This anticipated large demand for REEs is as a result of their broad usage in numerous fields of human life. According to this matter, their recovery from wastes seems to be necessary. Different techniques, such as precipitation, ion exchange, solvent extraction, and adsorption have been utilized for REEs recovery from aqueous media [8–11]. Numerous investigations have shown adsorption as a high-efficient, cost-effective and simple technique for REEs recovery from aqueous media amongst the physicochemical treatment techniques.

Chitosan is a derivation of chitin, a natural polysaccharide that comprises β(1–4)-2-amino-2-deoxy-D-glucan units and possesses superb adsorption performance for metal ions, chiefly owing to containing a large amount of amino and hydroxyl groups [12]. Its structure is like a crystal with hydrogen bonds. Nonetheless, the protonation of the amino groups in the acidic medium leads to losing structural strength by the formation of a gel-like solution that results in significant restrictions of its applications [13]. So as to solve this issue, the modification of chitosan has been carried out by sulfonation, nitration, hydroxyalkylation, quarternarization, hydroxylation, polyethyleneglycol-grafting, carboxymethylation, and so on [14,15]. Amongst the derivatives of chitosan, carboxymethyl chitosan

* Corresponding author.
E-mail address: Hamedreza.javadian@upc.edu (H. Javadian).

https://doi.org/10.1016/j.molliq.2020.113017
0167-7322/

(CMC) is an amphoteric ether derivative that each molecule comprises the active groups of —COOH, —OH, and —NH_2. The carboxymethylation of chitosan causes it to be dissolved in water. Thus, the problem related to losing the structural stability that takes place by —NH_2 protonation in the acidic medium can be solved [16]. In addition, carboxyl groups are able to increase metal ions adsorption [17]. Whereas chitosan is a natural polymer, its derivatives like CMC also have some advantages such as being biocompatible and low toxic.

Recently, numerous polycondensation reactions have been conducted in ionic liquids (ILs) at room temperature (RT) as a substitute to several volatile toxic solvents [18]. In industry, it is necessary to substitute a great number of organic solvents with environmentally, nonvolatile and green solvents for preparing high molecular weight polymers. The attraction of ambient temperature imidazolium based ILs for substantial commercial productions and applications as solvents and catalysts in polymerization, extraction, and as alternatives for ordinary volatile organic solvents has been confirmed. Reviewing the ILs application in polymer fabrication verifies their performance. Consequently, different processes of polycondensation in the ionic medium have been effectively conducted [19].

In recent years, increasing attention in the studies of synthetic polymer-polymer composites owing to the unique combination of beneficial properties and construction of multifunctional structures of each component has been reported. These composites display potentially greater thermal, mechanical, and electrical properties than the unique polymer [20]. Synthetic PAs are generally known as the first engineering plastics and are still considered as one of the best and most prominent classes of these types of materials. Hence, these polymers introduction in the natural polymers chemical structures is able to supply enhanced properties for individual usages, for which polymer having these sequences have shown incredibly excellent properties [21].

In this study, CMC, a novel biodegradable nanoporous polyamide (poly(pyrimidine-thiophene-amide)) synthesized by polycondensation reaction of 5,5′-(thiophen-2-ylmethylene)bis(2-aminopyrimidine-4,6-diol) (TMAPD) with terephthalic acid in 1,3-dipropyl imidazolium bromide {[1,3-$(pr)_2$im]Br} ionic liquid as green media, and the hydrothermally synthesized $Ni_{0.2}Zn_{0.2}Fe_{2.6}O_4$ were applied to produce a novel bionanocomposite (CMC/P(PTA)/$Ni_{0.2}Zn_{0.2}Fe_{2.6}O_4$) by the gelation process. FE-SEM, EDX, NMR, XRD, FT-IR, and VSM were utilized to confirm the fabrication of the products. In the following, it was used as an adsorbent to investigate its effectiveness for Nd^{+3}, Tb^{+3}, and Dy^{+3} ions adsorption. The influences of different factors including solution pH, contact time, adsorbent dosage, initial metal ions concentration, and ionic strength on the adsorption efficiency were considered. The models of adsorption kinetic and isotherm were employed to reach the best fitting of the experimental data. The reusability of the adsorbent was also investigated.

2. Materials and methods

2.1. Materials and reagents

Carboxymethyl chitosan was purchased from Nantong Chem-Base Co, China. $Dy(NO_3)\cdot 5H_2O$ was purchased from Alfa Aesar. $Nd(NO_3)_3\cdot 6H_2O$, $Tb(NO_3)_3\cdot 6H_2O$, $Zn(NO_3)_2\cdot 6H_2O$, $Fe(NO_3)_3\cdot 9H_2O$, $Ni(NO_3)_2\cdot 6H_2O$, glutaraldehyde, 2-amino-4,6-dihydroxypyrimidine, 2-thiophenecarboxaldehyde, terephthalic acid, triphenyl phosphite (TPP), dimethyl sulfoxide (DMSO), and methanol were bought from Sigma-Aldrich. All chemicals chosen in this study were at analytical grade and were utilized as received without further purification. The experiment solutions of Nd^{+3}, Tb^{+3}, and Dy^{+3} ions were made by the dilution of 1000 mg/L of ions. To adjust the initial value of pH in the test solutions to the desired value, appropriate molarity of HNO_3 or NaOH was used.

2.2. Instrumentation and characterization

The XRD pattern was recorded by an X-ray diffractometer (GBC MMA), and the samples were scanned from $2\theta = 10°$ to 70°. A spectrophotometer (PerkinElmer, USA) was also used to record FT-IR spectra. Bruker Advance DRX was employed to record ^{1}H NMR and ^{13}C NMR spectra at 400 MHz and 100 MHz, respectively, by DMSO-d_6 as a solvent. The nitrogen adsorption-desorption isotherm was measured at −196 °C using a Micromeritics Tristar 3000 apparatus. The morphology of the products was explored by a FE-SEM (Zeiss Neon-40, Germany). TGA measurements were performed by Mettler TGA/SDTA 851e/LF/1100 thermobalance under the atmosphere of N_2 from RT to 1000 °C with a rate of 10 °C/min. Magnetic measurements were done using a vibrating sample magnetometer (VSM, Daghigh Kavir Corporation, Iran). For analyzing the concentration of Nd^{+3}, Tb^{+3}, and Dy^{+3}, an Agilent 4100 MP-AES Spectrometer was used.

2.3. Synthesis of the $Ni_{0.2}Zn_{0.2}Fe_{2.6}O_4$ magnetic nanoparticles

The $Ni_{0.2}Zn_{0.2}Fe_{2.6}O_4$ magnetic nanoparticles were synthesized by the hydrothermal method. A mixed solution of 0.2 M Ni^{2+}, 0.2 M Zn^{2+}, and 2.6 M Fe^{3+} was prepared in HCl solution, and then NaOH solution was added into the mixed solution under nitrogen gas, and the mixture pH value was set to 10.5. 0.3 g of CTAB was added to this mixture, and then it was placed into an autoclave (Teflon-lined stainless steel) at 200 °C of an oven. After 8 h of hydrothermal treatment, the temperature of the autoclave was naturally decreased to RT, and the precipitate was collected and washed several times with deionized water (DW) to reach neutral pH. Finally, the obtained particles were dried at 50 °C.

2.4. Synthesis of the ionic liquid (1,3-dipropyl imidazolium bromide) and the monomer (5,5′-(thiophen-2-ylmethylene)bis(2-aminopyrimidine-4,6-diol (TMAPD))

The RT ionic liquid (IL) was synthesized based on the process presented in the literature [22]. TMAPD was synthesized according to the following procedure: A mixture of 2.54 g (0.02 mol) 2-amino-4,6-dihydroxypyrimidine, 1 mL (0.01 mol) 2-thiophenecarboxaldehyde, and 20 mL DMSO was stirred for 6 h at 110 °C. After completion of the reaction tested by thin-layer chromatography, the temperature of the solution was decreased to RT, and the violet powder obtained by pouring the solution into 400 mL of cold DW (−5 °C) was filtered, rinsed several times using DW and then dried using vacuum oven at 100 °C. The reaction yield was 92% (3.20 g), and the obtained compound has not shown sharp melting point and started to be decomposed above 300 °C. FT-IR (KBr, cm^{-1}): 3153–3477 (stretching of O—H and NH_2), 3049 (stretching of C—H aromatic), 2944 (stretching of C—H aliphatic), 1651 (stretching of C═N), 1586 (stretching of C═C), 1232 (C—N) and 1163 (C—O). ^{1}H NMR (DMSO-d_6, δ in ppm) (Fig. 1): 5.33 (s, 1H, CH), 6.61 (s, 4H, —NH_2), 6.78–6.80 (d, 1H, Ar—H, $J = 5.6$ Hz), 6.93–6.94 (d, 1H, Ar—H, $J = 5.6$ Hz), 7.42–7.44 (d, 1H, Ar—H, $J = 5.2$ Hz), 10.95–11.28 (m, 4H, broad, hydroxy pyrimidine). ^{13}C NMR (100 MHz, DMSO-d_6, δ in ppm) (Fig. 2): 30.98, 115.41, 128.27, 128.55, 137.86, 140.13, 143.76, 170.77.

2.5. Synthesis of the biodegradable nanoporous P(PTA) by polycondensation reaction of TMAPD in TPP/IL

The synthesis of the biodegradable nanoporous P(PTA) was carried out from a compound containing multi polar thiophene, amine, and free hydroxyl chelating groups. It was particularly synthesized from the diamine-phenol compound in 1,3-dipropyl imidazolium bromide as an ionic liquid without using toxic triphenyl phosphite/*N*-methylpyrolidone/pyridine/LiCl that is needed in the ordinary direct polycondensation. The P(PTA) was achieved by polycondensation of

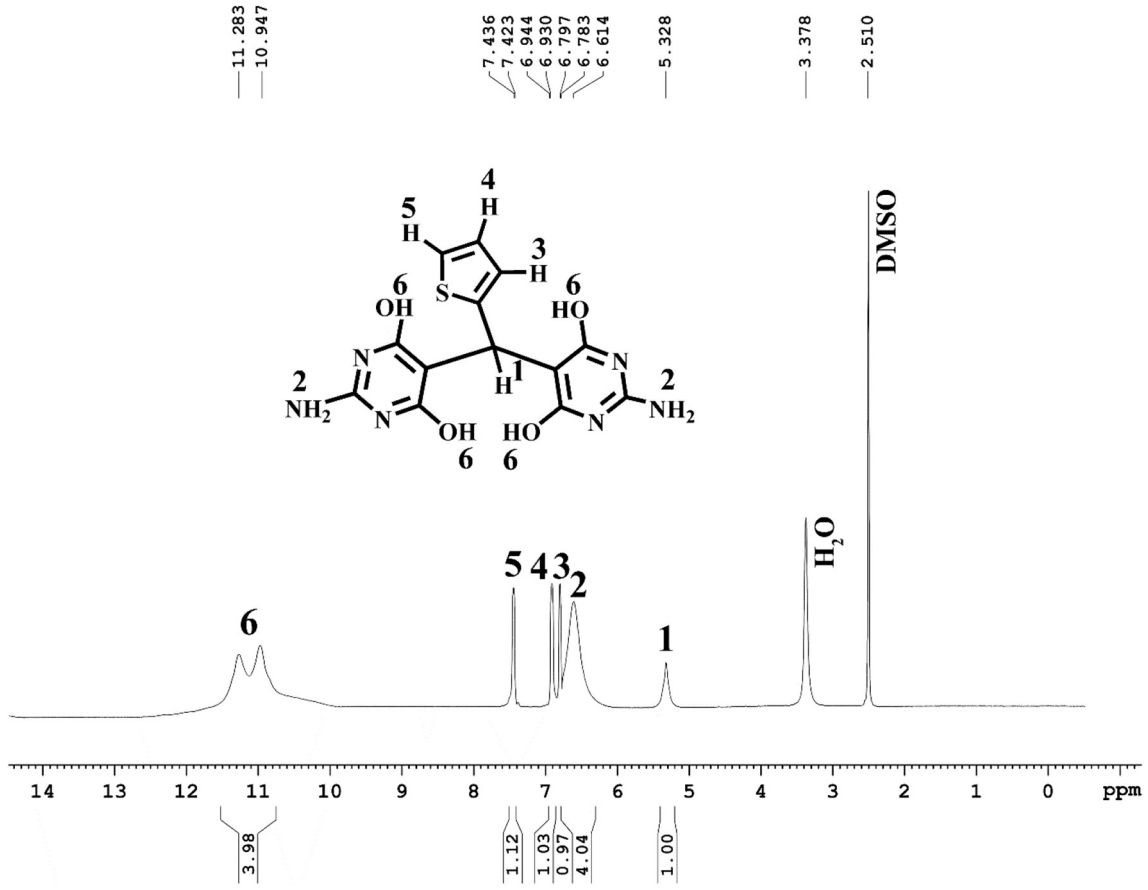

Fig. 1. ^{1}H NMR of the monomer.

TMAPD using TPP-IL as catalyst and solvent by the following procedure: A flask of three-necked round-bottomed with the volume of 50 mL was fitted with a mechanical stirrer, a water cooled condenser, and argon gas, and then a mixture containing 1 mmol TMAPD, 1 mmol terephthalic acid, 0.7 g 1,3-dipropyl imidazolium bromide {[1,3-(pr)$_2$im]Br} as IL, and 1.29 mmol TPP was placed. The solution became sticky as the reaction continued at 110 °C for 2.5 h. In the following, the reaction mixture temperature was decreased to RT and the precipitation of the obtained P(PTA) was performed using 100 mL of methanol. After the precipitate filtration, the hot water was used for washing it. Afterward, the precipitate was further refined in a Soxhlet apparatus using methanol for 24 h to eliminate the oligomers with low molecular weight. FT-IR (KBr, cm^{-1}): 3164–3337 (stretching of O—H and NH_2), 3054 (stretching of C—H aromatic), 2958 (stretching of C—H aliphatic), 1683 (stretching of C═O amide), 1641 (stretching of C═N), 1593 (stretching of C═C), 1215 (C—N) and 1167 (C—O). ^{1}H NMR (DMSO-d_6, δ in ppm) (Fig. 3): 5.37 (s, 1H, CH), 7.25–7.27 (m, 2H, Ar—H), 7.44 (s, 1H, Ar—H), 7.99–8.00 (d, 2H, Ar—H, J = 3.2 Hz), 8.06–8.08 (d, 2H, Ar—H, J = 5.2 Hz), 11.01 (s, 1H, OH amide), 11.32 (m, 4H, broad, hydroxy pyrimidine).

2.6. Synthesis of the CMC/P(PTA)/$Ni_{0.2}Zn_{0.2}Fe_{2.6}O_4$ magnetic bionanocomposite

The magnetic bionanocomposite was synthesized by the gelation method. Carboxymethyl chitosan powder was dissolved in dionized water (DW) (3% w/v) under stirring at 150 rpm for 3 h to prepare carboxymethyl chitosan solution. Then, 0.5 g of the P(PTA) and 0.7 g of the $Ni_{0.2}Zn_{0.2}Fe_{2.6}O_4$ were added to carboxymethyl chitosan solution and fully dispersed with vigorous stirring within 24 h. The gelation process was then performed by adding the mixture to a solution of $CaCl_2$ (0.05 M) and 2% glutaraldehyde. The mixture was stirred for 24 h, and the separation of the obtained bionanocomposite was performed using an external magnet. It was washed using deionized water several times to eliminate all impurities (unreacted GA) and remaining calcium chloride and reach the solution pH value of 7. The washed CMC/P(PTA)/$Ni_{0.2}Zn_{0.2}Fe_{2.6}O_4$ bionanocomposite was dried at 50 °C. Finally, it was powdered.

2.7. Adsorption experiments

Nd^{+3}, Tb^{+3}, and Dy^{+3} metal ions adsorption onto the CMC/P(PTA)/$Ni_{0.2}Zn_{0.2}Fe_{2.6}O_4$ was done by batch equilibrium method in aqueous solution at 25 °C. The standard stock solutions of 1000 mg/L of $Nd(NO_3)_3\cdot 6H_2O$, $Tb(NO_3)_3\cdot 6H_2O$, $Dy(NO_3)\cdot 5H_2O$ ions were prepared. The adsorption experiments were carried out by mixing 0.03 g of the adsorbent with 50 mL of metal ions solutions at 180 rpm and 25 °C. The influence of pH on the adsorption efficiency of the adsorbent was tested between 1.5 and 5.5. The ions adsorption onto the adsorbent was carried out at various time intervals (2.5–120 min) to evaluate adsorption kinetics. The influence of the adsorbent dosage on the adsorption of the ions was carried out from 0.01 to 0.07 g. To study the adsorption isotherms, different initial concentrations of the metal ions (30, 50, 70, 90, 120, 180, 240, and 300 mg/L) were utilized. The ionic strength influence on the adsorption efficiency was also taken into consideration by preparing the solutions with the ionic strengths of 0.02, 0.04, 0.06, 0.08, and 0.1 M using $NaNO_3$. The magnetic adsorbent was separated at the end of each experiment, and the metal ions concentration in the solutions was measured by Agilent 4100 MP-AES Spectrometer. The adsorption efficiency (%) and capacity of adsorption of the metal ions by the CMC/P(PTA)/$Ni_{0.2}Zn_{0.2}Fe_{2.6}O_4$ were calculated based on the

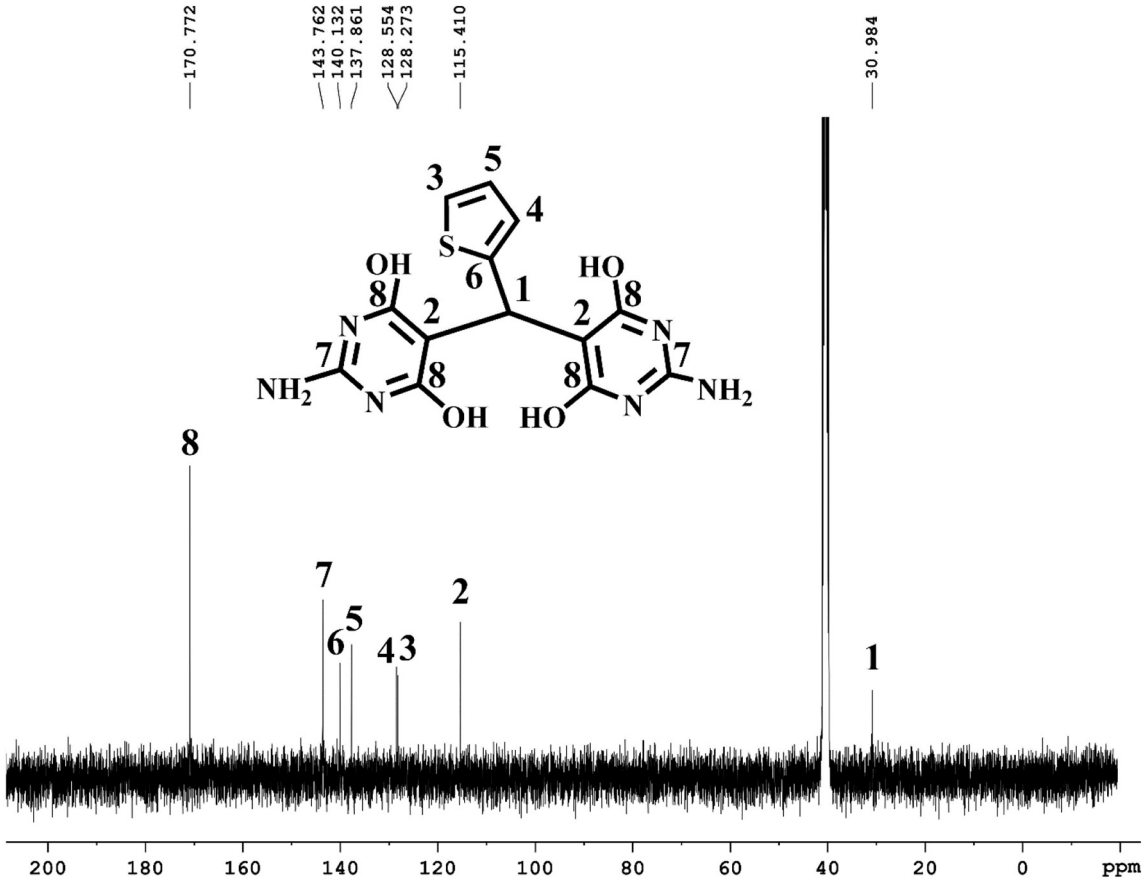

Fig. 2. ^{13}C NMR of the monomer.

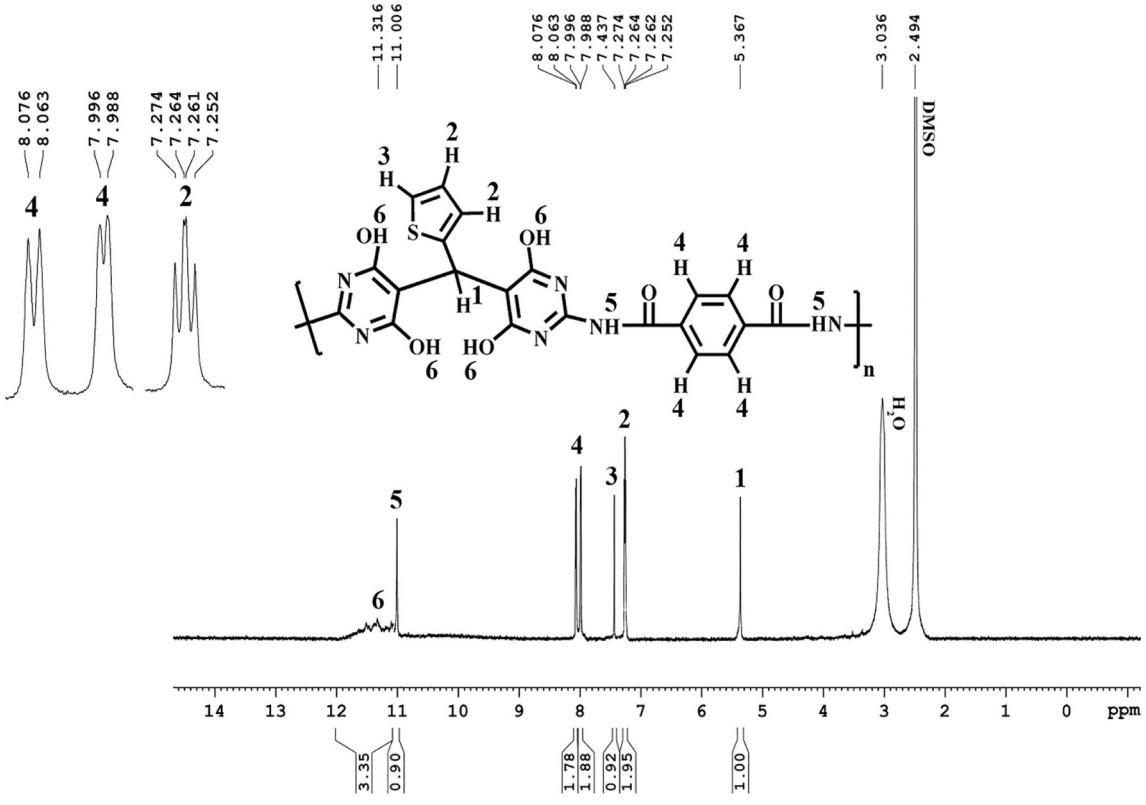

Fig. 3. ^{1}H NMR of the polymer.

bellowing equations:

$$\text{Adsorption efficiency}\ (\%) = (C_0 - C_e)/C_o \times 100 \quad (1)$$

$$q_e = (C_0 - C_e) \times V/m \quad (2)$$

$$q_t = (C_0 - C_t) \times V/m \quad (3)$$

where q_e and q_t (mg/g) show the amounts of adsorbed ion at equilibrium and adsorption time t (min), respectively. C_0 and C_e refer to the initial and equilibrium concentrations of metal ion (mg/L), respectively. C_t shows the concentration of metal ion in the solution at time t, V shows the volume of solution (L), and m refers to the weight of the adsorbent (g).

2.8. Reusability studies

The reusability experiments were performed on the CMC/P(PTA)/$Ni_{0.2}Zn_{0.2}Fe_{2.6}O_4$ using adsorption-desorption cycles. A given amount of the bionanocomposite was added into 50 mL solutions of 30 mg/L of each metal ion at an optimum time. After the adsorption process, the obtained metal ions-loaded bionanocomposite was washed several

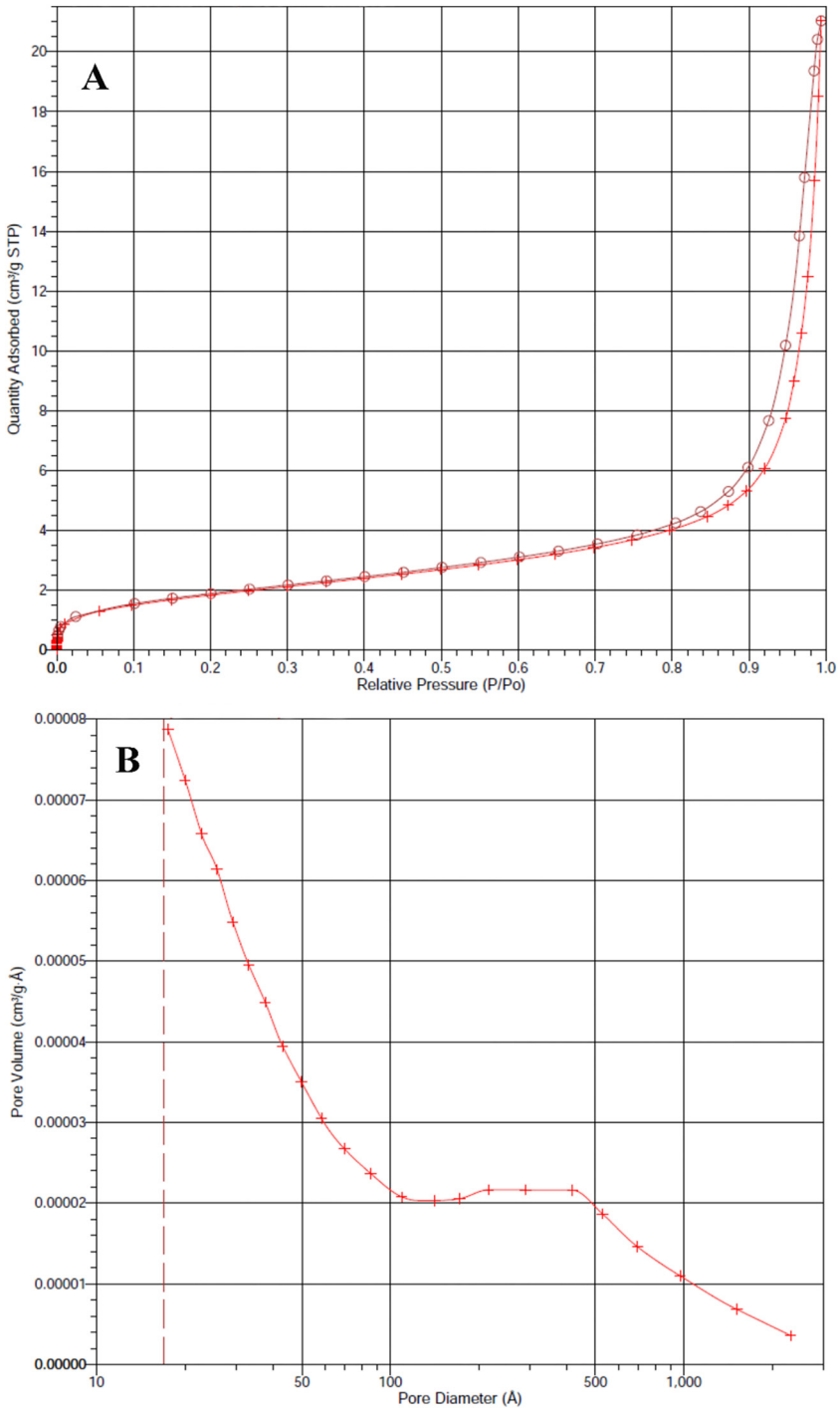

Fig. 4. (A) N_2 adsorption–desorption isotherm and (B) pore size distributions of the synthesized P(PTA).

times with DW to eliminate the unreacted metal ions, and then it was added to 0.2 M HNO_3 solution for desorption process at shaking speed = 180 rpm and temperature of 25 °C for 2 h. After ending the process and collecting the adsorbent, the concentration of the ions was measured by Agilent 4100 MP-AES Spectrometer. The adsorption-desorption process was occurred four times using the identical adsorbent.

3. Results and discussion

3.1. Analyses of the products

N_2 adsorption–desorption isotherm and the corresponding Barrett-Joyner-Halenda (BJH) pore size distribution of the P(PTA) are shown in Fig. 4. The nitrogen adsorption-desorption isotherm for the sample in Fig. 4A is assigned to type IV indicating the presence of mesoporous structure. The Brunauer–Emmett–Teller (BET) surface area, pore volume, and pore size (obtained by the BJH method (Fig. 4B)) were calculated to be 6.7420 m^2/g, 0.030884 cm^3/g, and 22.5244 nm, respectively. The results clearly demonstrate the formation of the P(PTA) with nano size pores.

The XRD pattern of the $Ni_{0.2}Zn_{0.2}Fe_{2.6}O_4$ is indicated in Fig. 5. The peaks at 2θ = 18.13°, 30.07°, 35.50°, 37.08°, 43.07°, 53.95°, 56.96°, and 63.89° are in agreement with the standard pattern of nickel zinc ferrite (JCPDS 08-0234) [23]. Full Width at Half Maximum (FWHM) of the XRD pattern strongest reflection was used to estimate the average crystal size via the Scherrer equation as following [24]:

$$D = k\lambda/\beta \cos\theta \quad (4)$$

where k shows the function of shape (k = 0.89), λ refers to the X-ray wavelength of the radiation, and β presents the Full Width at Half Maximum (FWHM) at 2θ = 35.50° and θ shows the diffraction angle. Based on the Scherrer equation, the calculated value of D was 27.68 nm.

The FE-SEM image of the $Ni_{0.2}Zn_{0.2}Fe_{2.6}O_4$ in Fig. 6A indicates that the synthesized particles are almost spherical in shape and homogenous in distribution with a diameter < 100 nm. Fig. 6B shows the distribution of the magnetic nanoparticles and P(PTA) on the surface of the CMC or embedding with the CMC that confirms the successful synthesis of the CMC/P(PTA)/$Ni_{0.2}Zn_{0.2}Fe_{2.6}O_4$ magnetic bionanocomposite.

Fig. 7 indicates the FT-IR spectrum for CMC, $Ni_{0.2}Zn_{0.2}Fe_{2.6}O_4$, P(PTA), and CMC/P(PTA)/$Ni_{0.2}Zn_{0.2}Fe_{2.6}O_4$. The FT-IR spectrum of the $Ni_{0.2}Zn_{0.2}Fe_{2.6}O_4$ in Fig. 7A shows a broad band at 3424 cm^{-1}, and less intensive band at 1633 cm^{-1} related to the O—H groups stretching vibration [25]. The bands at 2925 and 2853 cm^{-1} are respectively assigned to the anti-symmetric and symmetric C—H vibrations of CTAB [26]. The band at 567 cm^{-1} attributes to the inherent metal stretching vibrations at the tetrahedral site (Fe—O), and the value of 478 cm^{-1} corresponds to the octahedral metal stretching (M-O) [25]. In Fig. 7B, the peaks related to the P(PTA) are as follows: 3164–3337 cm^{-1} (O—H and NH_2 stretching), 3054 cm^{-1} (C—H aromatic stretching), 2958 cm^{-1} (stretching of C—H aliphatic), 1683 cm^{-1} (stretching of C═O amide), 1641 cm^{-1} (stretching of C═N), 1593 cm^{-1} (stretching of C═C), 1215 cm^{-1} (C—N), and 1167 cm^{-1} (C—O). The peaks in the FT-IR spectrum of CMC (Fig. 7C) shown at 3436, 1631, 1411, and 1061 cm^{-1} are respectively attributed to the stretching vibration of O—H, the carboxyl groups asymmetrical and symmetrical stretching, and stretching of C—O—C [27]. The comparison of the spectrum obtained for the CMC/P(PTA)/$Ni_{0.2}Zn_{0.2}Fe_{2.6}O_4$ (Fig. 7D) with other spectra expresses the successful synthesis of the bionanocomposite.

EDX was recorded to analyze the elements of the products, and the results are presented in Fig. 8. Fig. 8A shows Ni, Zn, Fe, and O peaks that confirm the formation of the $Ni_{0.2}Zn_{0.2}Fe_{2.6}O_4$. The elemental analysis of the nanocomposite in Fig. 8B represents similar peaks that are available in Fig. 8A along with the new peaks of N, S, and Ca due to the presence of the P(PTA) and CMC. Sodium peak is not seen in the spectrum of the CMC/P(PTA)/$Ni_{0.2}Zn_{0.2}Fe_{2.6}O_4$, suggesting that sodium ions were released completely from the matrix of sodium alginate into the solution during the crosslinking reaction process of sodium alginate with calcium.

The thermo-stability of the obtained P(PTA) and nanocomposite, analyzed using TGA/DTGA under N_2 atmosphere with the heating rate of 10 °C/min, is presented in Fig. 9. As it is clear in Fig. 9A, there are five different weight-loss steps in the TGA curve of the P(PTA). Obviously, the first step (around 100 °C) with a weight loss of 1.17% can be attributed to water evaporation. The second step (from around 100 to 290 °C) with the amount of 9.6% weight loss can be attributed to the preliminary degradation of aliphatic groups of P(PTA). At the third step, ranging between 300 and 330 °C, the aromatic groups of the P(PTA) are degrading gradually, and the forth step with the weight loss of 44.16% corresponds to their further decomposition. The final step can be related to the complete degradation of the polymer residue and its conversion to CO_2 and H_2O. Fig. 9B shows the TGA curve of the CMC/P(PTA)/$Ni_{0.2}Zn_{0.2}Fe_{2.6}O_4$. The thermal stability of the bionanocomposite compared to the pure P(PTA) has increased. It is obvious that the temperature of decomposition is shifted to higher temperatures due to the inorganic material existence in the matrix of the polymer, indicating that the thermal stability of the composite increases with the $Ni_{0.2}Zn_{0.2}Fe_{2.6}O_4$ loading.

According to the magnetic hysteresis loops in Fig. 10A, the $Ni_{0.2}Zn_{0.2}Fe_{2.6}O_4$ magnetic saturation value is about 45.87 emu/g that indicates superparamagnetic behavior of the synthesized product. Based on Fig. 10B, it is obvious that the synthesis process of the CMC/P(PTA)/$Ni_{0.2}Zn_{0.2}Fe_{2.6}O_4$ results in saturation magnetization reduction from 45.87 to 14.88 emu/g. This decrease is due to the combination of the magnetic nanoparticles with the P(PTA) and CMC. Despite this difference, the CMC/P(PTA)/$Ni_{0.2}Zn_{0.2}Fe_{2.6}O_4$ could be easily separated from aqueous solution by an external magnetic field to avoid secondary pollution. As indicated in Fig. 10C, the metal ions-loaded adsorbent is separated easily by applying an external magnetic field from the solution due to its high magnetization value.

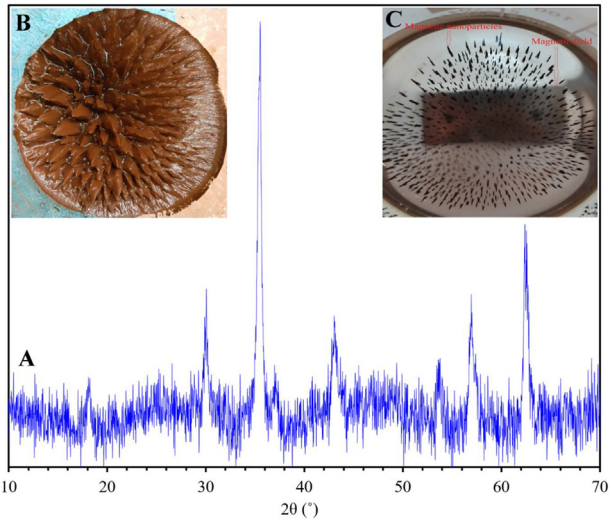

Fig. 5. (A) XRD pattern of $Ni_{0.2}Zn_{0.2}Fe_{2.6}O_4$ nanoparticles; Photo of $Ni_{0.2}Zn_{0.2}Fe_{2.6}O_4$ nanoparticles (B) before drying and (C) in the solution under magnetic field after drying.

3.2. pH effect

The influence of initial solution pH is considered as a major factor to obtain high adsorption efficiency during adsorption process. To analyze the influence of the pH of the solution on the adsorption efficiency of Nd^{+3}, Tb^{+3}, and Dy^{+3} by the CMC/P(PTA)/$Ni_{0.2}Zn_{0.2}Fe_{2.6}O_4$, the pH

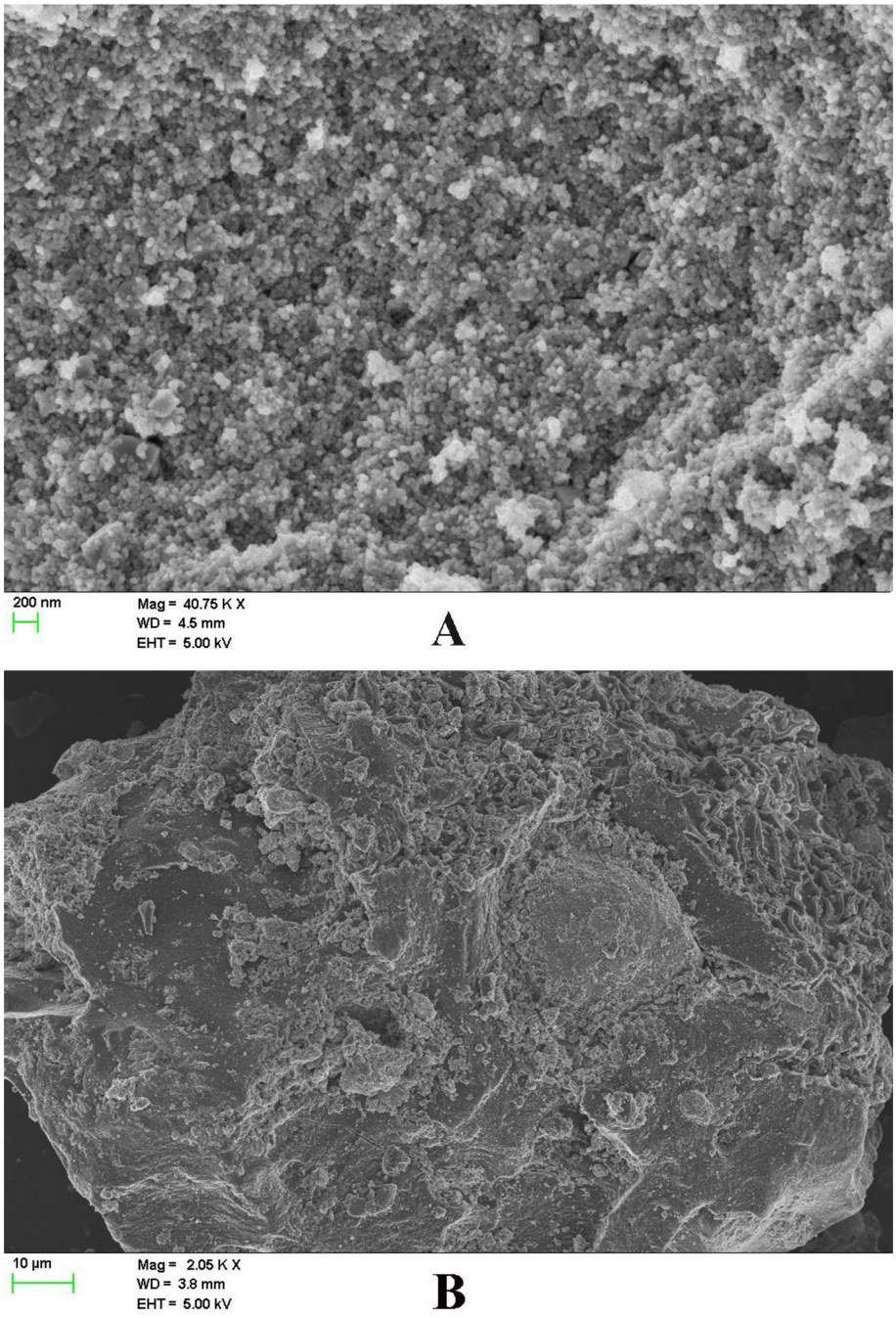

Fig. 6. FE-SEM images of (A) $Ni_{0.2}Zn_{0.2}Fe_{2.6}O_4$ and (B) CMC/P(PTA)/$Ni_{0.2}Zn_{0.2}Fe_{2.6}O_4$.

value was considered between 1.5 and 5.5. As it is clear in Fig. 11A, the adsorption of the metal ions is significantly associated with the value of pH since it influences the metal ions solubility and the ionization status of the groups available on the CMC/P(PTA)/$Ni_{0.2}Zn_{0.2}Fe_{2.6}O_4$. The obtained results state that the metal ions adsorption efficiency on the adsorbent surface increases remarkably with pH value increase from 1.5 to 5.5 because the interaction between hydrogen and metal cations for binding the active sites reduces. The little protonation of the functional groups also inhibits the relation between the adsorbent and the metal ions that could be the major cause for a low value of adsorption efficiency at lower pH values [28]. The influence of solution pH on the metal ions adsorption was not studied for a pH > 5.5 in order to prevent the metal ions precipitation formation as the hydroxides. Therefore, solution pH = 5.5 was applied as an optimum value for further adsorption studies.

3.3. Contact time effect

One of the key factors in treatment of a sample is the contact time of solution and adsorbent as it can present the interaction kinetics of an adsorbent with an adsorbate. Therefore, the influence of contact time on Nd^{+3}, Tb^{+3}, and Dy^{+3} ions adsorption onto the CMC/P(PTA)/$Ni_{0.2}Zn_{0.2}Fe_{2.6}O_4$ was studied at 25 °C and 30 mg/L of each metal ion. The obtained results in Fig. 11B indicate that the quantities of Nd^{+3}, Tb^{+3}, and Dy^{+3} adsorbed per unit mass of the adsorbent increase by an enhancement in contact time, and adsorption efficiencies of 60.07,

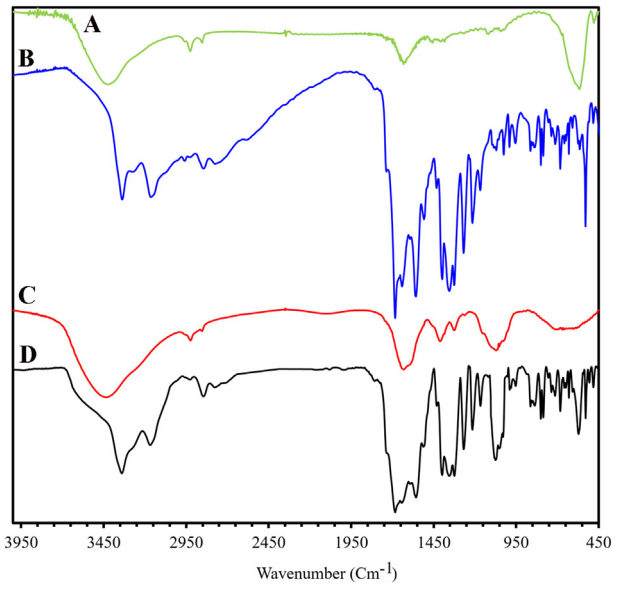

Fig. 7. FT-IR spectra of (A) $Ni_{0.2}Zn_{0.2}Fe_{2.6}O_4$, (B) P(PTA), (C) CMC, and (D) CMC/P(PTA)/$Ni_{0.2}Zn_{0.2}Fe_{2.6}O_4$.

63.56, and 63.96% are respectively obtained for Nd^{+3}, Tb^{+3}, and Dy^{+3} within 50 min. The plots in Fig. 11B indicate two phases for the metal ions adsorption. The sharper portion at the first phase is related to a great number of empty active sites on the surface of the adsorbent and high concentration of the ions. The second step is assigned to the decrease in IPD with contact time that leads to an equilibrium state. The reason for this condition is the external active sites saturation and low ions concentration [29]. As can be seen, the required time to achieve an equilibrium state is 90 min for all ions, and a further increase in contact time does not have any significant influence on the metal ions adsorption. Therefore, further experiments were performed by considering the optimum contact time of 90 min.

3.4. Kinetics of adsorption

The parameters of adsorption kinetics are extremely useful in the application of adsorbents since they control adsorbate uptake residence time at the interface of solid and solution and can augment the realization of designing a water treatment process. Kinetic data analysis provides significant data about the mechanism of adsorption that is helpful for designing and modeling the process of adsorption. Hence, three different kinetic models as pseudo-first order (PFO), PSO, and IPD models were employed to fit the experimental data. The nonlinear regression forms of the models were applied as follows [30,31]:

$$q_t = q_e\left(1 - \exp^{-K_1 t}\right) \text{ (PFO)} \quad (5)$$

$$q_t = K_2 q_e{}^2 t/1 + K_2 q_e t \text{ (PSO)} \quad (6)$$

$$q_t = K_i t^{0.5} + C \text{ (IPD)} \quad (7)$$

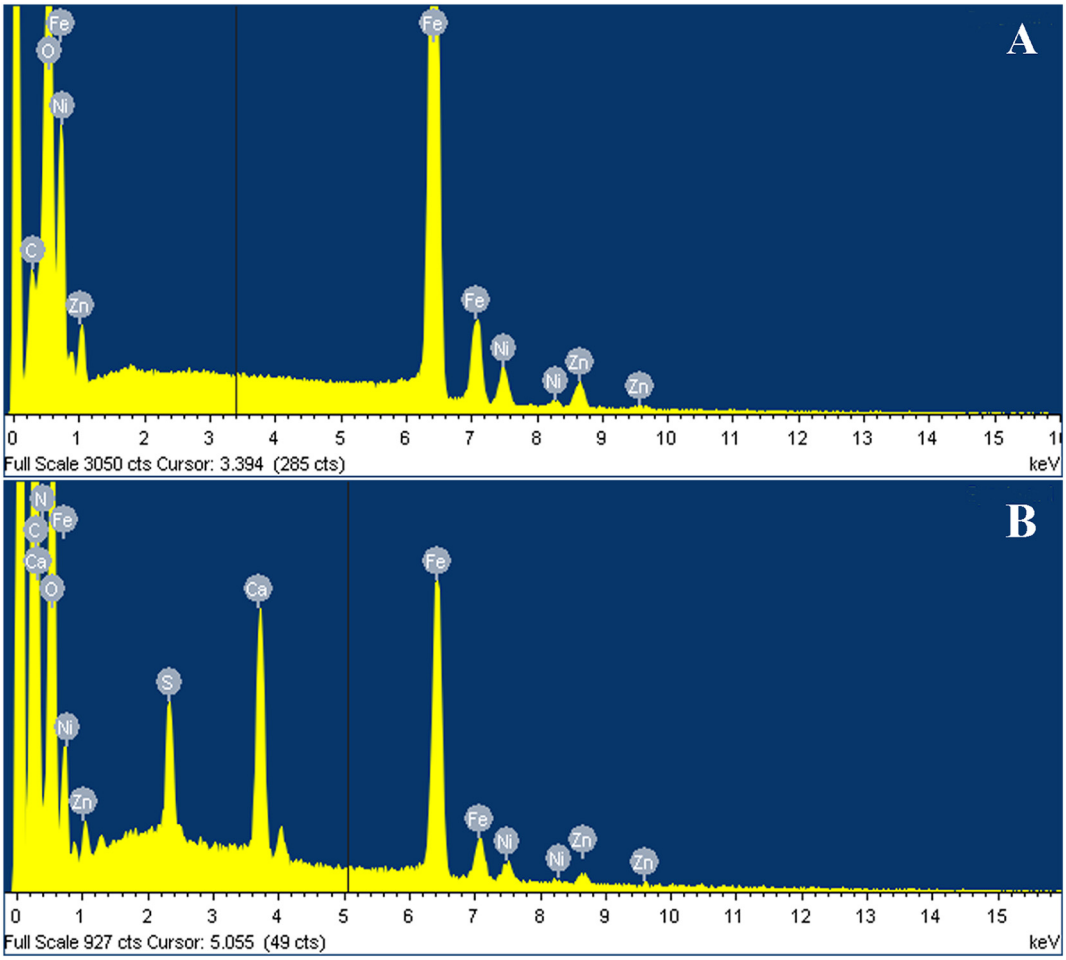

Fig. 8. EDX spectra of (A) $Ni_{0.2}Zn_{0.2}Fe_{2.6}O_4$ and (B) CMC/P(PTA)/$Ni_{0.2}Zn_{0.2}Fe_{2.6}O_4$.

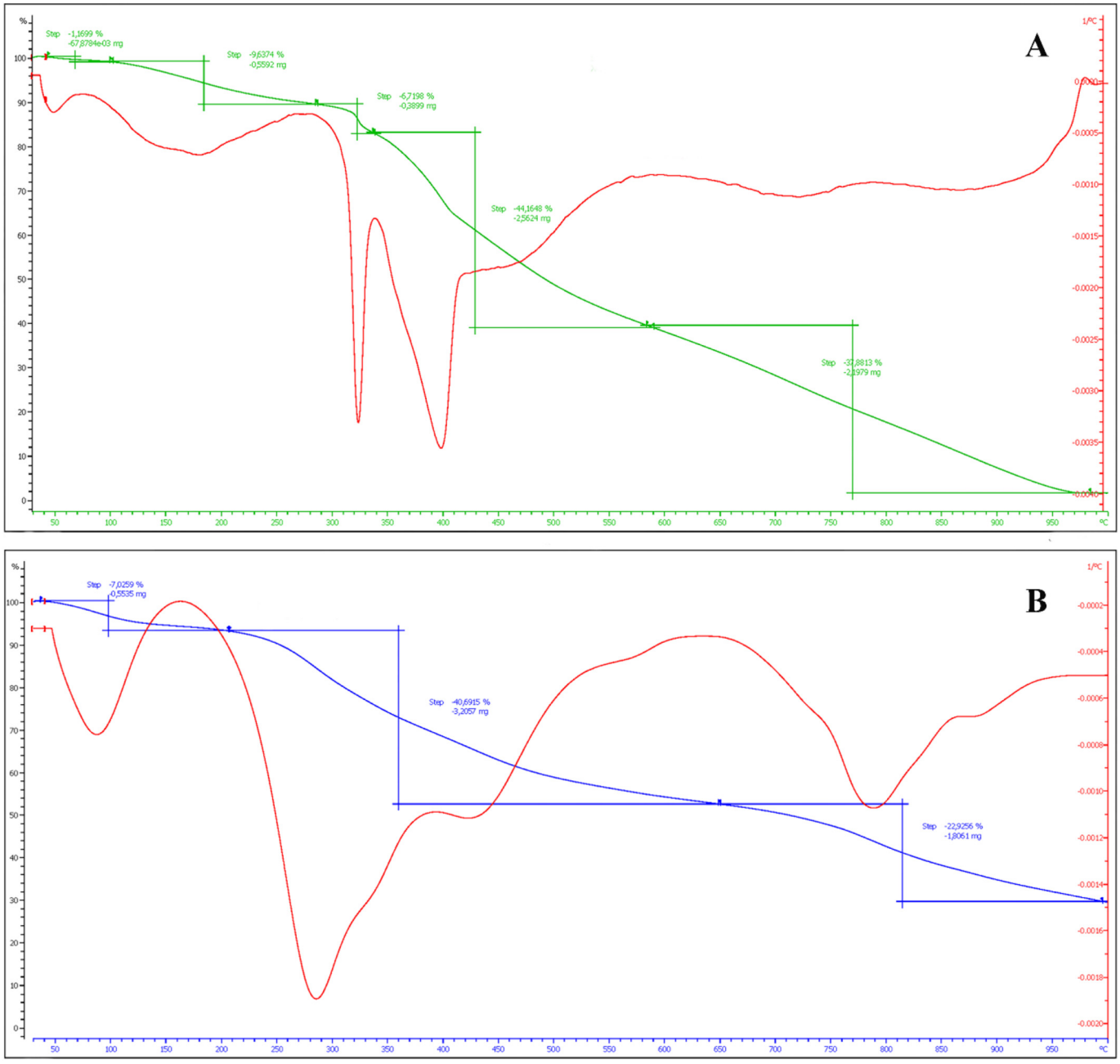

Fig. 9. TGA/DTGA curves of (A) P(PTA) and (B) CMC/P(PTA)/$Ni_{0.2}Zn_{0.2}Fe_{2.6}O_4$.

where K_1 (1/min) and K_2 (g/mg min) respectively refer to PFO rate constant and PSO rate constant, and K_i (1/min) shows the rate constant of IPD. Moreover, C provides data about the thickness of the boundary layer. Notably, the greater value of C is related to the influence of the boundary layer diffusion.

The initial rate of adsorption (h) can be obtained using K_2 and q_e values via the following equation:

$$h = K_2 q_e^{\ 2} \tag{8}$$

Non-linear regression analysis of the empirical data can be used to acquire the kinetic models constant values. The obtained kinetic parameters are presented in Table 1. The coefficient of determination (R^2) and Chi-square (χ^2) was also employed to evaluate the conformity between the experimental data and the computed values. χ^2 is defined as follows:

$$\chi 2 = \sum_{i=1}^{n} \frac{\left(q_{e,\,exp} - q_{e,cal}\right)^2}{q_{e,cal}} \tag{9}$$

where $q_{e,exp}$ and $q_{e,cal}$ respectively refer to the experimental and computed adsorbent capacities, and n shows data point numbers.

The kinetic parameters in Table 1 show that the R^2 values of 0.9629, 0.9564, and 0.9686 respectively acquired by PSO model for Nd^{+3}, Tb^{+3}, and Dy^{+3} are greater than those of PFO model (0.8831, 0.8538, and 0.8803). The values of χ^2 are also lower than those of PFO model. The values of q_e computed by PSO model are in agreement with the values

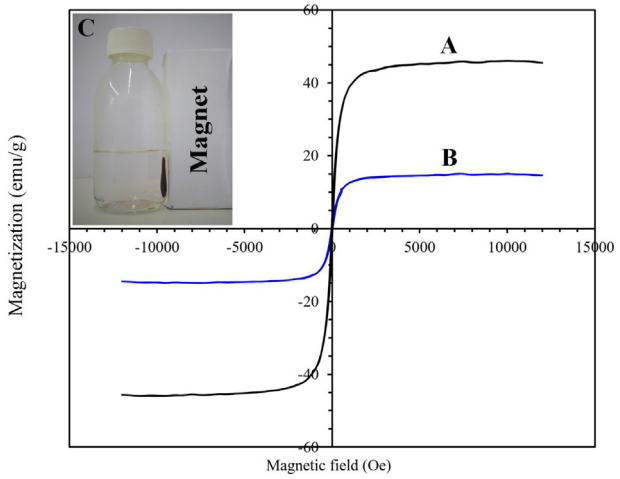

Fig. 10. Magnetization curves of (A) $Ni_{0.2}Zn_{0.2}Fe_{2.6}O_4$ and (B) CMC/P(PTA)/$Ni_{0.2}Zn_{0.2}Fe_{2.6}O_4$; (C) magnetic separation of the ions-loaded adsorbent.

of the experimental q_e, implying the chemisorption of the process. The R^2 and χ^2 values obtained by fitting IPD model to the empirical data show that it is also appropriate for explaining the adsorption kinetic of Nd^{+3}, Tb^{+3}, and Dy^{+3} onto the CMC/P(PTA)/$Ni_{0.2}Zn_{0.2}Fe_{2.6}O_4$. Thus, it can be mentioned that Nd^{+3}, Tb^{+3}, and Dy^{+3} adsorption processes follow both IPD and PSO kinetic models.

3.5. Adsorbent dosage effect

Nd^{+3}, Tb^{+3}, and Dy^{+3} ions adsorption onto the CMC/P(PTA)/$Ni_{0.2}Zn_{0.2}Fe_{2.6}O_4$ was studied using 30 mg/L initial ions concentration at pH = 5.5 within 90 min. As can be seen in Fig. 11C, by an enhancement in adsorbent dosage in the range of 0.01 to 0.07 g, adsorption efficiency increases. The reason is that the metal ions compete for confined adsorption sites at lower adsorbent dosage. However, by increasing the adsorbent dosage, a greater surface area and more empty sites are available; therefore, adsorption efficiency increases [32]. The maximum adsorption efficiency is 98.15% for Nd^{+3}, 97.6% for Tb^{+3}, and 99.42% for Dy^{+3} using 0.06 g of the adsorbent. The adsorption efficiency of the ions smoothly increases with the adsorbent up to 0.07 g. Consequently, 0.06 g of the adsorbent was considered as an optimum dosage for further experiments.

3.6. Initial concentration effect

The initial adsorbate concentration is considered as an essential driving force to overcome the adsorbate mass transfer resistance between the solid and aqueous phases. The initial concentration influence of Nd^{+3}, Tb^{+3}, and Dy^{+3} on the adsorption efficiency is presented in Fig. 11D. The adsorption efficiency respectively decreases from 98.15 to 16.74, 97.6 to 21.45, and 99.42 to 21.76% for Nd^{+3}, Tb^{+3}, and Dy^{+3}. By calculating the amount of q_e, it was seen that by enhancing initial concentration from 30 to 300 mg/L, q_e increased from 24.52 to 41.88, 24.76 to 53.62, and 24.87 to 54.33 mg/g for Nd^{+3}, Tb^{+3}, and Dy^{+3},

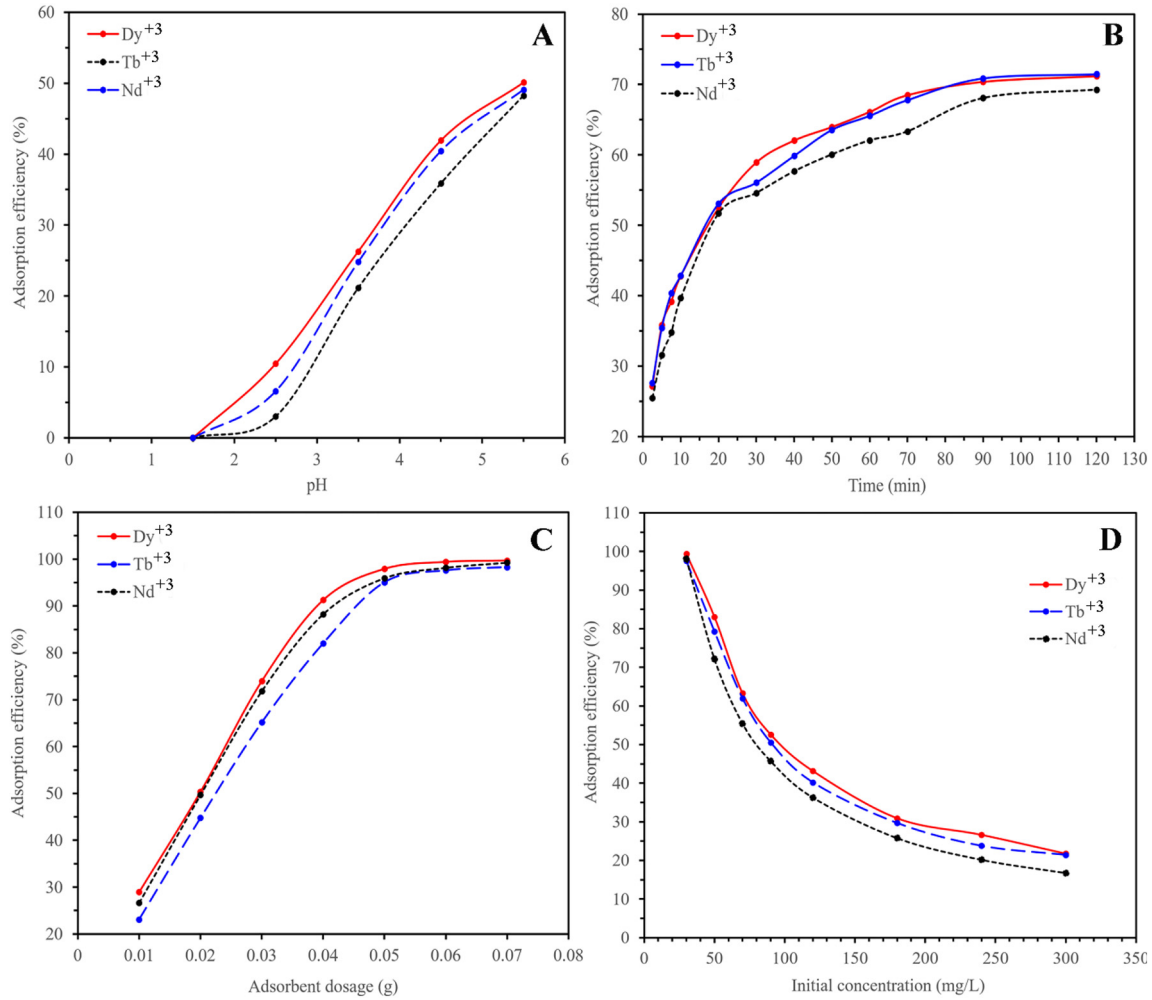

Fig. 11. Effects of (A) pH, (B) contact time, (C) adsorbent dosage, and (D) initial concentration on the adsorption of the ions.

respectively. These results show that Nd^{+3}, Tb^{+3}, and Dy^{+3} adsorption is dependent on the concentration of the metal ions since it supplies the major driving force for overcoming limitations of mass transfer between the solid and the aqueous phases. The adsorption is not influenced by the initial ion concentration when the concentration of the ion is low that is owing to the great number of binding sites while being easily accessible for adsorption. The value of adsorption efficiency decreases at higher ion concentration for a constant content of adsorbent because the quantity of the accessible sites of adsorption on the surface of the adsorbent decreases and therefore their saturation takes place easily. As a result, by occupying valence forces via exchanging or sharing electron and complexation, more mass transfer from the liquid stage occurs, which is fairly known as a slow process [33].

3.7. Adsorption isotherms

For the optimization of adsorbent usage in an adsorption process, knowing that how solutes interact with adsorbent is so important. In this case, adsorption isotherms can explain the interaction between adsorbate quantity adsorbed onto adsorbent and dissolved adsorbate concentration at equilibrium state. In this paper, Freundlich and Langmuir isotherm models were applied for fitting the obtained data at equilibrium and evaluating the adsorption properties of Nd^{+3}, Tb^{+3}, and Dy^{+3} onto the CMC/P(PTA)/$Ni_{0.2}Zn_{0.2}Fe_{2.6}O_4$. The nonlinear forms of Langmuir and Freundlich are respectively defined by Eqs. (10) and (11) [34,35].

$$q_e = \frac{b\ qm\ Ce}{(1 + bCe)} \tag{10}$$

$$q_e = K\ C_e{}^{1/n} \tag{11}$$

The isotherm parameters including q_m (the maximum capacity at saturation state (mg/g)), b (constant of Langmuir (L/mg)), K (capacity of adsorption ($mg^{1-1/n}\ L^{1/n}/g$)), and 1 / n (adsorption intensity) are shown in Table 2. The means of the dimensionless factor ($R_L = \frac{1}{1 + bC_i}$) can be used to appraise the desirability of the adsorption process in the Langmuir model as following: irreversible ($R_L = 0$), favorable ($0 < R_L < 1$), linear ($R_L = 1$), and unfavorable ($R_L > 1$) adsorption [36]. According to the Langmuir adsorption constants (Table 2), the R_L values of 0.001, 0.0022, and 0.0005 respectively acquired for Nd^{+3}, Tb^{+3}, and Dy^{+3} are between 0 and 1 that show the adsorption of the ions onto the adsorbent is favorable. In addition, the results of the adsorption isotherms presented in Table 2 indicate that the 1 / n values of 0.09, 0.13, and 0.12 for Nd^{+3}, Tb^{+3}, and Dy^{+3}, respectively, obtained from Freundlich model are representative of highly curved isotherms due to the values of $1 / n < 0.7$. The results show that the experimental data for Nd^{+3}, Tb^{+3}, and Dy^{+3} adsorption onto the CMC/P(PTA)/$Ni_{0.2}Zn_{0.2}Fe_{2.6}O_4$ are fitted with Freundlich isotherm model with R^2 values of 0.9709, 0.9482, and 0.9632, respectively, that are higher than those acquired by Langmuir isotherm model. The lower values of χ^2 also confirm the obtained results for each ion. In the present study, the results of fitting experimental data show that the adsorption of the metal ions is performed by the sites of the adsorbent that are heterogeneous, indicating non-uniform and multi-layer adsorption. A comparison of the adsorption capacity of different adsorbents is represented in Table 3.

Table 1
Kinetic constants for adsorption of the ions by the CMC/P(PTA)/$Ni_{0.2}Zn_{0.2}Fe_{2.6}O_4$.

		Nd^{+3}	Tb^{+3}	Dy^{+3}
PFO	K_1 (1/min)	0.116	0.132	0.126
	q_e (mg/g)	31.15	32.29	32.71
	R^2	0.8831	0.8538	0.8803
	χ^2	7.24	8.77	7.52
PSO	K_2 (g/mg min)	0.0043	0.0049	0.0047
	q_e (mg/g)	34.85	35.80	36.27
	h (mg/g min)	5.22	6.28	6.18
	R^2	0.9629	0.9564	0.9686
	χ^2	2.3	2.61	1.97
IPD	K_i (1/min)	11.16	11.02	11.20
	R^2	0.9737	0.9782	0.9676
	χ^2	1.63	1.31	2.03

Table 2
Isotherm constants for adsorption of the ions by the CMC/P(PTA)/$Ni_{0.2}Zn_{0.2}Fe_{2.6}O_4$.

		Nd^{+3}	Tb^{+3}	Dy^{+3}
Langmuir	b (L/mg)	3.28	1.51	6.391
	q_m (mg/g)	36.59	42.87	43.76
	R_L	0.001	0.0022	0.0005
	R^2	0.5679	0.5398	0.5771
	χ^2	16.7	43.21	47.31
Freundlich	K ($mg^{1-1/n}\ L^{1/n}/g$)	24.23	23.7	26.13
	1 / n	0.09	0.13	0.12
	R^2	0.9709	0.9482	0.9632
	χ^2	1.12	4.86	4.12

3.8. Ionic strength effect

The existence of salts as the most available materials in real samples as an interfering agent can affect the adsorption efficiency of the target ion that leads to strengthen or weaken its adsorption. Thus, in the present study, the $NaNO_3$ solutions with various concentrations (0.02, 0.04, 0.06, 0.08, and 0.1 M) were utilized to evaluate the ionic strength influence on Nd^{+3}, Tb^{+3}, and Dy^{+3} ions adsorption onto the CMC/P(PTA)/

Table 3
Comparison of the adsorption capacity of Nd^{+3}, Tb^{+3}, and Dy^{+3} onto various adsorbents.

Adsorbent	q_m (mg/g)			Reference
	Nd^{+3}	Tb^{+3}	Dy^{+3}	
Fe_3O_4-C_{18}-chitosan-DETA	27.1		28.3	[37]
EDTA functionalized chitosan	74			[38]
Phosphonic acid functionalized silica microspheres	45			[39]
γ-Fe_2O_3-NH_4OH@SiO_2(APTMS)		46.5	23.2	[40]
GA-g-PAM/SiO_2	12.24			[41]
Zr@XG-ZA	14.01[a]			[42]
EDASiDGA	16.15			[43]
Oxidized multi-walled carbon nanotubes			78.12	[44]
Carbon black derived from recycled tires	0.67			[5]
3D GO-CZ	9.68			[45]
Macroporous polymeric resin (TVEX-PHOR)		24.93		[46]
TA-MWCNTs		8.55		[47]
YZ		44.5		[48]
Poly(acrylamide-expanded perlite) [P (AAm-EP)]		118.3		[49]
P(HEMA-Hap)-phy		49.27		[50]
Supported biomass on zeolite (SBZ)		5.07		[51]
Acryloyl–phenyl thiourea		74.23		[52]
Hybrid Lewis base ligands functionalized alumina-silica			125.4	[53]
MIL-101-PMIDA	70.9			[54]
CA@Fe_3O_4 NPs	41			[55]
11-Molybdo-vanadophosphoric acid supported on Zr modified mesoporous silica SBA-15			50	[56]
MPS (22 nm)-2NH-2COOH			44.8	[57]
o-CNCs-IIPs			28.97	[58]
o-CNCs/o-MWCNTs-IIPs			38.7	[58]
o-CNCs/GO-IIPs			41.79	[58]
Imprinted mesoporous silica materials			22.33	[59]
CMC/P(PTA)/$Ni_{0.2}Zn_{0.2}Fe_{2.6}O_4$	39.82[a]	50.32[a]	48.23[a]	This study

[a] Calculated from Freundlich isotherm.

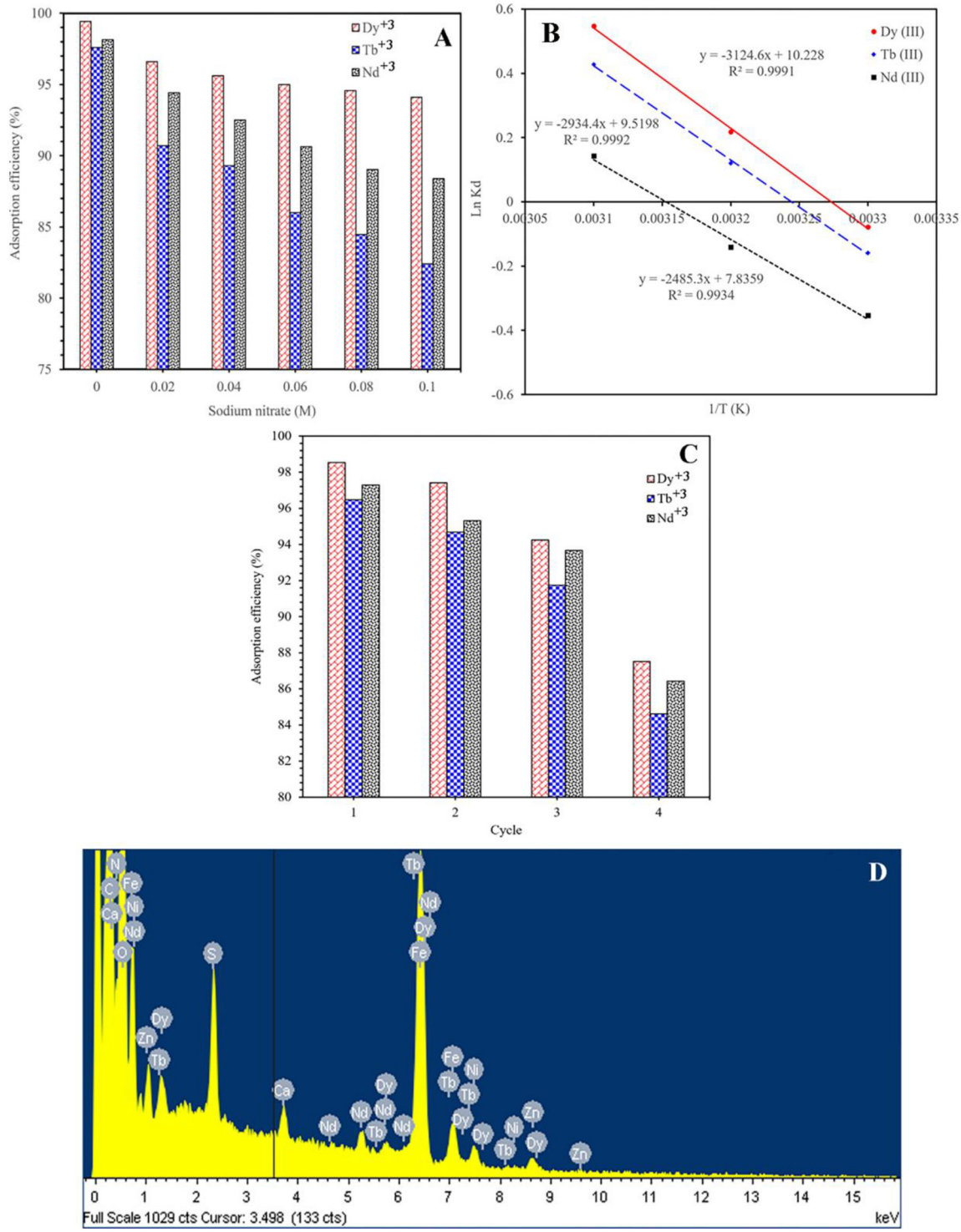

Fig. 12. (A) Effect of ionic strength on the adsorption of the ions, (B) Ln K_d versus 1 / T for calculation of enthalpy and entropy changes, (C) reusability of the CMC/P(PTA)/$Ni_{0.2}Zn_{0.2}Fe_{2.6}O_4$ for adsorption of the ions, and (D) EDX spectrum of the CMC/P(PTA)/$Ni_{0.2}Zn_{0.2}Fe_{2.6}O_4$ after adsorption of the ions.

$Ni_{0.2}Zn_{0.2}Fe_{2.6}O_4$ under the optimum conditions. The results in Fig. 12A indicate a reduction in the adsorption efficiency with an enhancement in the concentration of $NaNO_3$ from 0.02 to 0.1 M that may be explained by the occurrence of competition between the Na^+ cations from the salt and cationic ions for the occupation of the adsorbent active sites. The adsorption efficiency of Dy^{+3} decreases from 96.6 to 94.1% that is lower than those obtained for Nd^{+3} and Tb^{+3}, indicating that the concentration of $NaNO_3$ has higher negative effect on the adsorption of Nd^{+3} and Tb^{+3}, specifically Nd^{+3}.

3.9. Temperature effect and evaluation of thermodynamic parameters

The parameters of thermodynamic (ΔH^o (kJ/mol), ΔS^o (kJ/mol K), and ΔG^o (kJ/mol)) were evaluated at 25, 35, and 45 °C to consider the effect of temperature on the performance of adsorption and find the adsorption mechanism by the following equations [60]:

$$K_d = q_e / C_e \quad (12)$$

Table 4
Effect of temperature on the adsorption of the ions at 90 mg/L and thermodynamic parameters.

Adsorption efficiency (%)			
Temperature (°C)	Nd^{+3}	Tb^{+3}	Dy^{+3}
25	45.72	50.58	52.61
35	51.05	57.51	59.89
45	58.08	64.8	67.5

Thermodynamic parameters				
	Temperature (°C)	Nd^{+3}	Tb^{+3}	Dy^{+3}
K_d	25	0.702	0.853	0.925
	35	0.869	1.128	1.244
	45	1.154	1.534	1.728
ΔH° (kJ/mol)		20.66	24.40	25.97
ΔS° (kJ/mol K)		0.065	0.079	0.085
ΔG° (kJ/mol)	25	0.877	0.394	0.193
	35	0.359	−0.308	−0.559
	45	−0.861	−1.131	−1.446

$$\text{Ln } K_d = \Delta S^\circ/R - \Delta H^\circ/RT \quad (13)$$

$$\Delta G^\circ = -RT \text{ Ln } K_d \quad (14)$$

where R (8.314 J/mol K) shows the gas constant, T shows the temperature (K), and K_d refers to the distribution coefficient. C_e shows the equilibrium concentration of ion in the solution (mg/L). As can be seen in Table 4, adsorption efficiency increases for all metal ions by an increase in temperature. ΔH^o and ΔS^o values in Eq. (13) were respectively acquired from the slope and intercept of the Ln K_d versus 1 / T plot (Fig. 12B). The thermodynamic parameters are presented in Table 4. K_d value increases by enhancing the temperature that indicates the process is endothermic in nature. The values of ΔG^o are low that indicate the strong adsorptive forces, spontaneous adsorption process, and better adsorption at a higher temperature. The adsorption of the ions is not spontaneous at low temperature. $\Delta H^o > 0$ reveals that the ions adsorption is endothermic, and their adsorption efficiency increases with increasing temperature. $\Delta S^o > 0$ demonstrates that there is a good affinity between the ions and the adsorbent, and randomness increases at the interface of the solid-solution during the process. In conclusion, the thermodynamic parameters reveal endothermic adsorption process, an affinity of the adsorbent for the ions, and spontaneous nature of Nd^{+3}, Tb^{+3}, and Dy^{+3} adsorption onto the adsorbent by rising temperature.

3.10. Reusability studies

One of the main parameters in the adsorption process is adsorbent reusability as it makes the process economically feasible. To evaluate the reusability of the CMC/P(PTA)/$Ni_{0.2}Zn_{0.2}Fe_{2.6}O_4$, 50 mL of 0.2 M HNO_3 was applied as the eluent. First, metal ions adsorption was done by the addition of 0.06 g of the adsorbent into 50 mL solution of 30 mg/L of metal ions at optimum conditions. The adsorbent loaded with the ions was separated by an external magnetic field, washed several times with DW and finally dried at 40 °C. Then, the desorption process was performed by using the eluent for 2 h. After the desorption process, the metal ions in the solutions were measured, and the adsorbent was neutralized and further used for the ions adsorption in the cycles. Nd^{+3}, Tb^{+3}, and Dy^{+3} ions were desorbed from the adsorbent >82, 84, and 88%, respectively. Four cycles of adsorption-desorption were performed to evaluate the reuse efficiency of the adsorbent. The results in Fig. 12C show that the CMC/P(PTA)/$Ni_{0.2}Zn_{0.2}Fe_{2.6}O_4$ adsorption efficiency respectively decreases from 97.29 to 86.43, 96.47 to 84.61, and 98.54 to 87.52% for Nd^{+3}, Tb^{+3}, and Dy^{+3} after the fourth cycle that indicates metal ions may chemically bond with the groups on the adsorbent surface.

3.11. Competitive adsorption

To evaluate competitive adsorption of Nd^{+3}, Tb^{+3}, and Dy^{+3} in the ternary system of 30 mg/L (1:1:1), 0.06 g of the CMC/P(PTA)/$Ni_{0.2}Zn_{0.2}Fe_{2.6}O_4$ (the same as a single system) was used. According to the value of q_{mix}/q_0, three kinds of influences can occur in a multicomponent system as following:

- Antagonism ($q_{mix}/q_0 < 1$): effect of mixture of component in solution is less than its individual effect.
- Synergism ($q_{mix}/q_0 > 1$): effect of mixture of component in solution is greater than its individual effect.
- Non-interaction ($q_{mix}/q_0 = 1$): effect of mixture of component in solution is neither less nor more than that of its individual effect.

where q_{mix} and q_0 are respectively the adsorption capacities of each ion in the mixture and single systems.

The value of q_{mix}/q_0 was respectively obtained to be 0.2, 0.38, and 0.41 for Nd^{+3}, Tb^{+3}, and Dy^{+3}. The obtained results indicate that the q_{mix}/q_0 value for all ions is <1 in the ternary mixture; therefore, the existence of each ion shows an antagonism effect on the other ions adsorption. The adsorption efficiency for Nd^{+3}, Tb^{+3}, and Dy^{+3} respectively decreased to 19.4, 37.6, and 40.9%. EDX spectrum was also recorded after the adsorption process, and the result is presented in Fig. 12D. The existence of Nd^{+3}, Tb^{+3}, and Dy^{+3} peaks in the spectrum strongly confirms the successful adsorption of the ions by the CMC/P(PTA)/$Ni_{0.2}Zn_{0.2}Fe_{2.6}O_4$.

4. Conclusion

In this research, the novel biodegradable nanoporous P(PTA) was synthesized by polycondensation reaction of TMAPD in {[1,3-(pr)2im]Br} ionic liquid as green media. Then, the CMC/$Ni_{0.2}Zn_{0.2}Fe_{2.6}O_4$ magnetic bionanocomposite containing the P(PTA) was fabricated. The successful synthesis of the products was approved by FE-SEM, EDX, NMR, XRD, FT-IR, and VSM techniques. The prepared bionanocomposite showed favorable magnetization value of 14.88 emu/g that was enough to be easily separated by a magnetic field from aqueous medium. Then, it was used to investigate the adsorption of Nd^{+3}, Tb^{+3}, and Dy^{+3}. For obtaining the maximum adsorption efficiency of the ions at the concentration of 30 mg/L, the optimum conditions were obtained at pH = 5.5, the adsorbent dosage of 0.06 g, and contact time of 90 min. The adsorption efficiency values of 98.15, 97.6, and 99.42% were respectively obtained for Nd^{+3}, Tb^{+3}, and Dy^{+3} at optimum conditions. The adsorption kinetics followed PSO and IPD models, and Freundlich model was suitable for fitting the adsorption data of the metal ions obtained at equilibrium. The adsorption efficiency for the ions greatly decreased in the presence of $NaNO_3$ as ionic strength. The thermodynamic parameters revealed that the spontaneous nature of Nd^{+3}, Tb^{+3}, and Dy^{+3} adsorption onto the adsorbent can be occurred by increasing temperature. The competitive adsorption of the ions showed that the existence of each ion had antagonism effect on the other ions adsorption. The results show that the CMC/P(PTA)/$Ni_{0.2}Zn_{0.2}Fe_{2.6}O_4$ is an efficient and potential adsorbent with a favorable performance for practical applications in Nd^{+3}, Tb^{+3}, and Dy^{+3} ions adsorption process.

CRediT authorship contribution statement

Hamedreza Javadian: Investigation, Formal analysis, Writing - original draft, Writing - review & editing. **Montserrat Ruiz:** Investigation, Supervision. **Mehdi Taghavi:** Investigation, Formal analysis. **Ana Maria Sastre:** Conceptualization, Supervision.

Declaration of competing interest

The authors declare that there is no conflict of interest regarding the publication of this article.

Acknowledgments

This work has been supported by the Spanish Ministry of Economy and Competitiveness (Ref. CTM2017-83581-R). Hamedreza Javadian acknowledges the financial support received (Ref. BES-2015-072506).

References

[1] I. Liatsou, M. Efstathiou, I. Pashalidis, Adsorption of trivalent lanthanides by marine sediments, J. Radioanal. Nucl. Chem. 304 (2015) 41–45.
[2] I. Anastopoulos, A. Bhatnagar, E.C. Lima, Adsorption of rare earth metals: a review of recent literature, J. Mol. Liq. 221 (2016) 954–962.
[3] J. Jacinto, B. Henriques, A.C. Duarte, C. Vale, E. Pereira, Removal and recovery of critical rare earth elements from contaminated waters by living *Gracilaria gracilis*, J. Hazard. Mater. 344 (2018) 531–538.
[4] J. Ponou, L.P. Wang, G. Dodbiba, K. Okaya, T. Fujita, K. Mitsuhashi, T. Atarashi, G. Satoh, M. Noda, Recovery of rare earth elements from aqueous solution obtained from vietnamese clay minerals using dried and carbonized parachlorella, J. Environ. Chem. Eng. 2 (2014) 1070–1081.
[5] Y.R. Smith, D. Bhattacharyya, T. Willhard, M. Misra, Adsorption of aqueous rare earth elements using carbon black derived from recycled tires, Chem. Eng. J. 296 (2016) 102–111.
[6] V.N. Rychkov, E.V. Kirillov, S.V. Kirillov, V.S. Semenishchev, G.M. Bunkov, M.S. Botalov, D.V. Smyshlyaev, A.S. Malyshev, Recovery of rare earth elements from phosphogypsum, J. Clean. Prod. 196 (2018) 674–681.
[7] V. Fernandez, Rare-earth elements market: a historical and financial perspective, Resour. Policy 53 (2017) 26–45.
[8] M. Alemrajabi, A.C. Rasmuson, K. Korkmaz, K. Forsberg, Recovery of rare earth elements from nitrophosphoric acid solutions, Hydrometallurgy 169 (2017) 253–262.
[9] A. Battsengel, A. Batnasan, A. Narankhuu, K. Haga, Y. Watanabe, A. Shibayama, Recovery of light and heavy rare earth elements from apatite ore using sulphuric acid leaching, solvent extraction and precipitation, Hydrometallurgy 179 (2018) 100–109.
[10] L. Jiang, W. Zhang, C. Luo, D. Cheng, J. Zhu, Adsorption toward trivalent rare earth element from aqueous solution by zeolitic imidazolate frameworks, Ind. Eng. Chem. Res. 55 (2016) 6365–6372.
[11] Z.V.P. Murthy, A. Choudhary, Separation and estimation of nanofiltration membrane transport parameters for cerium and neodymium, Rare Metals 31 (2012) 500–506.
[12] L. Fan, C. Luo, Z. Lv, F. Lu, H. Qiu, Removal of Ag^{+} from water environment using a novel magnetic thiourea-chitosan imprinted Ag^{+}, J. Hazard. Mater. 194 (11) (2011) 193–201.
[13] G. Cravotto, S. Tagliapietra, B. Robaldo, M. Trotta, Chemical modification of chitosan under high-intensity ultrasound, Ultrason. Sonochem. 12 (2005) 95–98.
[14] K. Kurita, Controlled functionalization of the polysaccharide chitin, Prog. Polym. Sci. 26 (2001) 1921–1971.
[15] N.K. Patel, V.K. Sinha, Synthesis, characterization and optimization of water-soluble chitosan derivatives, Int. J. Polym. Mater. Polym. Biomater. 58 (2009) 548–560.
[16] S. Zhao, F. Zhou, L. Li, M. Cao, D. Zuo, H. Liu, Removal of anionic dyes from aqueous solutions by adsorption of chitosan-based semi-IPN hydrogel composites, Compos. Part B 43 (2012) 1570–1578.
[17] D.W. Cho, B.H. Jeon, C.M. Chon, Y. Kim, F.W. Schwartz, E.S. Lee, H. Song, A novel chitosan/clay/magnetite composite for adsorption of Cu(II) and As(V), Chem. Eng. J. 200-202 (34) (2012) 654–662.
[18] J. Lu, F. Yan, J. Texter, Advanced applications of ionic liquids in polymer science, Prog. Polym. Sci. 34 (2009) 431–448.
[19] M. Taghavi, M. Ghaemy, S.M. AminiNasab, M. Hassanzadeh, Influence of ionic liquid on selective polycondensation of a new diamine-bisphenol: synthesis and properties of polyamides and their composites with modified nanosilica, Polymer 54 (2013) 3828–3840.
[20] A.M. Bochek, N.M. Zabivalova, E.N. Brazhnikova, M.S. Anferova, V.K. Lavrent'ev, Chitosan—polyamide composite nanofibers produced by needleless electrospinning, Fibre Chem. 50 (2019) 391–395.
[21] D.L. Francisco, L.B. Paiva, W. Aldeia, Advances in polyamide nanocomposites: a review, Polym. Compos. 40 (2019) 851–870.
[22] Y.S. Vygodskii, E.I. Lozinskaya, A.S. Shaplov, K.A. Lyssenko, M.Y. Antipin, Y.G. Urman, Implementation of ionic liquids as activating media for polycondensation processes, Polymer 45 (2004) 5031–5045.
[23] D. Ni, Z. Lin, P. Xiaoling, W. Xinqing, G. Hongliang, Preparation and characterization of nickel-zinc ferrites by a solvothermal method, Rare Metal Mater. Eng. 44 (9) (2015) 2126–2131.
[24] R. Rahmawati, M. Gilang Permana, B. Harison, B. Yuliarto Nugraha, D. Kurniadi Suyatman, Optimization of frequency and stirring rate for synthesis of magnetite (Fe_3O_4) nanoparticles by using coprecipitation-ultrasonic irradiation methods, Procedia Eng. 170 (2017) 55–59.
[25] A.S.A. Bakr, Y.M. Moustafa, E.A. Motawea, M.M. Yehia, M.M.H. Khalil, Removal of ferrous ions from their aqueous solutions onto $NiFe_2O_4$–alginate composite beads, J. Environ. Chem. Eng. 3 (2015) 1486–1496.
[26] S.A. Elfeky, S. Ebrahim Mahmoud, A. Fahmy Youssef, Applications of CTAB modified magnetic nanoparticles for removal of chromium (VI) from contaminated water, J. Adv. Res. 8 (4) (2017) 435–443.
[27] V. Gopalakannan, N. Viswanathan, Synthesis of magnetic alginate hybrid beads for efficient chromium(VI) removal, Int. J. Biol. Macromol. 72 (2015) 862–867.
[28] P. Kampalanonwat, P. Supaphol, The study of competitive adsorption of heavy metal ions from aqueous solution by aminated polyacrylonitrile nanofiber mats, Energy Procedia 56 (2014) 142–151.
[29] A. Afkhami, M. Saber-Tehrani, H. Bagheri, Simultaneous removal of heavy-metal ions in wastewater samples using nano-alumina modified with 2,4-dinitrophenylhydrazine, J. Hazard. Mater. 181 (2010) 836–844.
[30] H. Javadian, B. Babzadeh Koutenaei, E. Shekarian, F. Zamani Sorkhrodi, R. Khatti, M. Toosi, Application of functionalized nano HMS type mesoporous silica with N-(2-aminoethyl)-3-aminopropyl methyldimethoxysilane as a suitable adsorbent for removal of Pb (II) from aqueous media and industrial wastewater, J. Saudi Chem. Soc. 21 (2017) S219–S230.
[31] H. Javadian, M. Torabi Angaji, M. Naushad, Synthesis and characterization of polyaniline/γ-alumina nanocomposite: a comparative study for the adsorption of three different anionic dyes, J. Ind. Eng. Chem. 20 (2014) 3890–3900.
[32] T.T.N. Le, V.T. Le, M.U. Dao, Q.V. Nguyen, T.T. Vu, M.H. Nguyen, D.L. Tran, H.S. Le, Preparation of magnetic graphene oxide/chitosan composite beads for effective removal of heavy metals and dyes from aqueous solutions, Chem. Eng. Commun. 206 (2019) 1337–1352.
[33] K.M. Seema, B.B. Mamba, J. Njuguna, R.Z. Bakhtizin, A.K. Mishra, Removal of lead (II) from aqueous waste using (CD-PCL-TiO_2) bio-nanocomposites, Int. J. Biol. Macromol. 109 (2018) 136–142.
[34] H. Javadian, Adsorption performance of suitable nanostructured novel composite adsorbent of poly(N-methylaniline) for removal of heavy metal from aqueous solutions, J. Ind. Eng. Chem. 20 (2014) 4344–4352.
[35] H. Javadian, Application of kinetic, isotherm and thermodynamic models for the adsorption of Co(II) ions on polyaniline/polypyrrole copolymer nanofibers from aqueous solution, J. Ind. Eng. Chem. 20 (2014) 4233–4241.
[36] S. Liu, B. Huang, L. Chai, Y. Liu, G. Zeng, X. Wang, W. Zeng, M. Shang, J. Deng, Z. Zhou, Enhancement of As(V) adsorption from aqueous solution by a magnetic chitosan/biochar composite, RSC Adv. 7 (2017) 10891–10900.
[37] E. Liu, X. Zheng, X. Xu, F. Zhang, E. Liu, Y. Wang, C. Li, Y. Yan, Preparation of diethylenetriamine-modified magnetic chitosan nanoparticles for adsorption of rare-earth metal ions, New J. Chem. 41 (2017) 7739–7750.
[38] J. Roosen, K. Binnemans, Adsorption and chromatographic separation of rare earths with EDTA- and DTPAfunctionalized chitosan biopolymers, J. Mater. Chem. A 2 (2014) 1530–1540.
[39] I.V. Melnyk, V.P. Goncharyk, L.I. Kozhara, G.R. Yurchenko, A.K. Matkovsky, Y.L. Zub, B. Alonso, Sorption properties of porous spray-dried microspheres functionalized by phosphonic acid groups, Microporous Mesoporous Mater. 153 (2012) 171–177.
[40] T. Kegl, I. Ban, A. Lobnik, A. Košak, Synthesis and characterization of novel γ-Fe_2O_3-NH_4OH@SiO_2(APTMS) nanoparticles for dysprosium adsorption, J. Hazard. Mater. 378 (2019), 120764.
[41] S. Iftekhar, V. Srivastava, A. Casas, M. Sillanpää, Synthesis of novel GA-g-PAM/SiO_2 nanocomposite for the recovery of rare earth elements (REE) ions from aqueous solution, J. Clean. Prod. 170 (2018) 251–259.
[42] S. Iftekhar, V. Srivastava, S. Ben Hammouda, M. Sillanpää, Fabrication of novel metal ion imprinted xanthan gum-layered double hydroxide nanocomposite for adsorption of rare earth elements, Carbohydr. Polym. 194 (2018) 274–284.
[43] T. Ogata, H. Narita, M. Tanaka, Rapid and selective recovery of heavy rare earths by using an adsorbent with diglycol amic acid group, Hydrometallurgy 155 (2015) 105–109.
[44] S.M.A. Koochaki-Mohammadpour, M. Torab-Mostaedi, A. Talebizadeh-Rafsanjani, F. Naderi-Behdani, Adsorption isotherm, kinetic, thermodynamic, and desorption studies of lanthanum and dysprosium on oxidized multiwalled carbon nanotubes, J. Dispers. Sci. Technol. 35 (2014) 244–254.
[45] X. Xu, X.-Y. Jiang, F.-P. Jiao, X.-Q. Chen, J.-G. Yu, Tunable assembly of porous three-dimensional graphene oxide-corn zein composites with strong mechanical properties for adsorption of rare earth elements, J. Taiwan Inst. Chem. Eng. 85 (2018) 106–114.
[46] H.A. Madbouly, N.E. El-Hefny, Y.A. El-Nadi, Adsorption and separation of terbium (III) and gadolinium(III) from aqueous nitrate medium using solid extractant, Sep. Sci. Technol. (2019) 1–13.
[47] S. Tong, S. Zhao, W. Zhou, R. Li, Q. Jia, Modification of multi-walled carbon nanotubes with tannic acid for the adsorption of La, Tb and Lu ions, Microchim. Acta 174 (2011) 257–264.
[48] D. Baybaş, U. Ulusoy, Polyacrylamide–clinoptilolite/Y-zeolite composites: characterization and adsorptive features for terbium, J. Hazard. Mater. 187 (1) (2011) 241–249.
[49] R. Akkaya, Synthesis and characterization of a new low-cost composite for the adsorption of rare earth ions from aqueous solutions, Chem. Eng. J. 200 (2012) 186–191.
[50] R. Akkaya, Terbium adsorption onto polyhydroxyethylmethacrylate–hydroxyapatite composite and its modified composition by phytic acid, Desalin. Water Treat. 52 (2014) 1440–1447.
[51] Ó. Barros, L. Costa, F. Costa, A. Lago, V. Rocha, Z. Vipotnik, B. Silva, T. Tavares, Recovery of rare earth elements from wastewater towards a circular economy, Molecules 24 (2019) 1005.
[52] N.S. Reddy, K.M. Rao, S.V. Krishna, C.S. Ha, Synthesis of 1–acryloyl–3–phenyl thiourea based pH sensitive hydrogels for removal of samarium and terbium, Macromol. Res. 24 (2016) 494–501.

[53] M.R. Awual, N.H. Alharthi, Y. Okamoto, M.R. Karim, M.E. Halim, M.M. Hasan, M.M. Rahman, M.M. Islam, M.A. Khaleque, M.C. Sheikh, Ligand field effect for dysprosium(III) and lutetium(III) adsorption and EXAFS coordination with novel composite nanomaterials, Chem. Eng. J. 320 (2017) 427–435.
[54] Y.R. Lee, K. Yu, S. Ravi, W.S. Ahn, Selective adsorption of rare earth elements over functionalized Cr-MIL-101, Appl. Mater. Interfaces 10 (2018) 23918–23927.
[55] R.M. Ashour, R. El-Sayed, A.F. Abdel-Magied, A.A. Abdel-Khalek, M.M. Ali, K. Forsberg, A. Uheida, M. Muhammed, J. Dutta, Selective separation of rare earth ions from aqueous solution using functionalized magnetite nanoparticles: kinetic and thermodynamic studies, Chem. Eng. J. 327 (2017) 286–296.
[56] H. Aghayan, A. Mahjoub, A. Khanchi, Samarium and dysprosium removal using 11-molybdo-vanadophosphoric acid supported on Zr modified mesoporous silica SBA-15, Chem. Eng. J. 225 (2013) 509–519.
[57] T. Kaneko, F. Nagata, S. Kugimiya, K. Kato, Optimization of carboxyl-functionalized mesoporous silica for the selective adsorption of dysprosium, J. Environ. Chem. Eng. 6 (2018) 5990–5998.
[58] X. Zheng, Y. Zhang, T. Bian, Y. Zhang, Z. Li, J. Pan, Oxidized carbon materials cooperative construct ionic imprinted cellulose nanocrystals films for efficient adsorption of Dy(III), Chem. Eng. J. 381 (2020), 122669.
[59] X. Zheng, E. Liu, F. Zhang, Y. Yan, J. Pan, Efficient adsorption and separation of dysprosium from NdFeB magnets in an acidic system by ion imprinted mesoporous silica sealed in a dialysis bag, Green Chem. 18 (2016) 5031–5040.
[60] K. Zhu, Y. Duan, F. Wang, P. Gao, H. Jia, C. Ma, C. Wang, Silane-modified halloysite/Fe_3O_4 nanocomposites: simultaneous removal of Cr(VI) and Sb(V) and positive effects of Cr(VI) on Sb(V) adsorption, Chem. Eng. J. 311 (2017) 236–246.

ANNEX IV

Synthesis of calcium alginate/novel selectively synthesized biodegradable poly(pyrimidine-thiophene-amide) with free hydroxyl groups in ionic liquid as green media /$Ni_{0.2}Zn_{0.2}Fe_{2.6}O_4$ magnetic bionanocomposite powder: Adsorption properties towards rare earth elements

Synthesis of calcium alginate/novel selectively synthesized biodegradable poly(pyrimidine-thiophene-amide) with free hydroxyl groups in ionic liquid as green media/$Ni_{0.2}Zn_{0.2}Fe_{2.6}O_4$ magnetic bionanocomposite powder: Adsorption properties towards rare earth elements

Hamedreza Javadian[a,*], Montserrat Ruiz[b], Mehdi Taghavi[c], Ana Maria Sastre[a]

[a]Department of Chemical Engineering, ETSEIB, Universitat Politècnica de Catalunya, Diagonal 647, 08028 Barcelona, Spain

[b]Department of Chemical Engineering, EPSEVG, Universitat Politècnica de Catalunya, Av. Víctor Balaguer, s/n, 08800 Vilanova i la Geltrú, Spain

[c]Department of Chemistry, Faculty of Science, Shahid Chamran University of Ahvaz, 61357-43337, Iran

[*]Corresponding author.

Email addresses: Hamedreza.javadian@yahoo.com; Hamedreza.javadian@upc.edu

Abstract

In this paper, a novel biodegradable polyamide, namely poly(pyrimidine-thiophene-amide) (P(PTA)), was synthesized by polycondensation reaction of 5,5'-(thiophen-2-ylmethylene)bis(2-aminopyrimidine-4,6-diol) (TMAPD) with terephthalic acid in 1,3-dipropyl imidazolium bromide {[1,3-$(pr)_2$im]Br} ionic liquid as green media. Then, calcium alginate/P(PTA)/$Ni_{0.2}Zn_{0.2}Fe_{2.6}O_4$ (CA/P(PTA)/$Ni_{0.2}Zn_{0.2}Fe_{2.6}O_4$) magnetic bionanocomposite was synthesized for Nd^{+3}, Tb^{+3}, and Dy^{+3} ions adsorption in single aqueous solutions. The results of FE-SEM, NMR, FT-IR, XRD, TGA, and VSM indicated the successful synthesis of the products. The value of saturation magnetization of the bionanocomposite was reported to be 15.28 emu/g, indicating a fast magnetic response. According to the experimental results, it can be stated that the adsorption data were efficiently fitted by pseudo-second-order (PSO) kinetic model. Adsorption isotherms were also evaluated by fitting with Freundlich and Langmuir isotherm models. A better fit for Tb^{+3} and Dy^{+3} ions adsorption was achieved by Freundlich model, while Langmuir isotherm fitted the adsorption data of Nd^{+3}. Moreover, ΔG°, ΔH°, and ΔS° values presented that the ions adsorption onto the adsorbent was feasible and endothermic and occurred spontaneously under the investigated conditions. The obtained results indicated that

the CA/P(PTA)/$Ni_{0.2}Zn_{0.2}Fe_{2.6}O_4$ can be considered as a potential adsorbent for Nd^{+3}, Tb^{+3}, and Dy^{+3} ions efficient adsorption.

Keywords: Calcium alginate, Poly(pyrimidine-thiophene-amide), Magnetic, Bionanocomposite, Adsorption, Rare earth elements.

1. Introduction

Rare Earth Elements (REEs) are extensively utilized in numerous innovative implements, for example, TVs, laser, liquid crystal displays (LCDs), screens, fluorescent lamps, particular magnets and numerous others [1-3]. Owing to concentration on the extraction of REEs in a couple of nations, especially China, western countries consider the recycling of REEs as a vital object. After publishing a report by the European Commission in 2010 concerning the definition of fourteen elements, including REEs, as critical elements for EU economy, the attentions have been heightening for gathering and recycling wastes that contain such critical elements, and numerous mandates have been forcing to back up these goals in the EU-27 [4].

The aforementioned reasons clarify why recycling the wastes of electrical and electronic equipment (WEEE) and particular magnets is receiving developing consideration. Besides, the quantity of such wastes created in western nations is not only enormous but also develops yearly. Thus, a genuine secondary mine, known as urban mine, is created for the recovery of base, valuable and REEs [5].

In this manner, various techniques have been carried out for REEs recovery, for example, co-precipitation, solvent extraction, ion exchange, hydrometallurgy, adsorption, and so on [6]. It is noticeable that adsorption has been demonstrated to be a high applicable method for the treatment of water containing ions because of being an uncomplicated operation, highly efficient and cost-effective [7]. So far, a variety of adsorbents including resin, inorganic nanoparticles, biomaterials, and functional polymeric materials have been applied for recovering REEs and heavy metals [8,9]. The low adsorption capacity of the adsorbents is one of the reasons that motivates investigators to prepare alternative adsorbents with better performance.

Alginate, as a natural polymer, is the derivation of various types of brown algae. The properties of alginate such as biocompatibility, low cost, and capability of carboxyl groups of alginate for the formation of complexes with ions such as cobalt alginate (Co-Alg_2), nickel alginate (Ni-Alg_2), and copper alginate (Cu-Alg_2) makes it as potential adsorbent [10]. The transformation of alginate aqueous solution into hydrogel can be taken place by adding metallic

divalent cations. Numerous researches have reported the important role of the porous structure of ionotropic metal alginates for metal ions adsorption from aqueous media [11].

Polyamides (PAs), known as one of the polymeric materials possessing high performance, are commonly characterized by high melting point, good mechanical properties, good chemical resistance, and thermo-oxidative stability that are gathered all together to provide an extensive range of applications [12,13]. During recent years, many researchers have tried to use several procedures to enhance the processability of PAs using structural amendment without any negative effects on their remarkable chemical, mechanical, and thermal properties in order to retain aromatic PAs application at the center of scientific research. Introduction of heteroaromatic rings, aliphatic parts, cardo moieties, bulky pendant groups, and non-coplanar structural segments in the polymer backbone not only prevents their alignment and interrupts the hydrogen bonding but also enhances their processability [14].

Ionic Liquids (ILs) are considered as low melting salts that demonstrate a new kind of advanced and technological ionic solvents that can be considered to be used in a specific application. [15,16]. Studying the dialkylimidazolium based ILs has gained substantial attention as promising alternative green solvents and catalysts in polymer synthesis. Hence, they have been considerably expanded, and consequently a various number of alternatives are accessible or even commercially available. There have been numerous reports on the effective formation of PAs with high molecular weight by the polycondensation processes in ILs [17].

In the present study, the novel CA/P(PTA)/$Ni_{0.2}Zn_{0.2}Fe_{2.6}O_4$ was synthesized by the gelation process of sodium alginate in the presence of a novel biodegradable polyamide (poly(pyrimidine-thiophene-amide) (P(PTA))) synthesized by the polycondensation reaction of 5,5'-(thiophen-2-ylmethylene)bis(2-aminopyrimidine-4,6-diol) (TMAPD) with terephthalic acid in 1,3-dipropyl imidazolium bromide {[1,3-$(pr)_2$im]Br} ionic liquid as green media and the hydrothermally synthesized $Ni_{0.2}Zn_{0.2}Fe_{2.6}O_4$ and then used for Nd^{+3}, Tb^{+3}, and Dy^{+3} ions adsorption from aqueous media. FE-SEM, NMR, FT-IR, XRD, TGA, and VSM methods were utilized to characterize the products. To receive the optimum adsorption conditions, pH, adsorbent dosage, contact time, ionic strength, and initial metal ions concentration as effective parameters on the adsorption process were investigated. Kinetic and isotherm models for fitting the adsorption data were evaluated, and to test the reusability of the

CA/P(PTA)/$Ni_{0.2}Zn_{0.2}Fe_{2.6}O_4$, the adsorption-desorption cycle was experimented four times via the identical adsorbent.

2. Materials and methods

2.1. Materials and reagents

Sodium alginate was bought from PanReac AppliChem. $Dy(NO_3)_3.5H_2O$ was purchased from Alfa Aesar. $Nd(NO_3)_3.6H_2O$, $Tb(NO_3)_3 \cdot 6H_2O$, $Zn(NO_3)_2.6H_2O$, $Fe(NO_3)_3.9H_2O$, $Ni(NO_3)_2 \cdot 6H_2O$, glutaraldehyde, 2-amino-4,6-dihydroxypyrimidine, 2-thiophenecarboxaldehyde, terephthalic acid, triphenyl phosphite (TPP), dimethyl sulfoxide (DMSO), and methanol were bought from Sigma-Aldrich. The 1000 mg/L stock solutions of each ion were made via dissolving the salts in deionized water (DW). 0.1 M HNO_3 or 0.1 M NaOH was utilized for adjustment of the initial pH of the test solutions.

2.2. Synthesis of $Ni_{0.2}Zn_{0.2}Fe_{2.6}O_4$ magnetic nanoparticles

The $Ni_{0.2}Zn_{0.2}Fe_{2.6}O_4$ magnetic nanoparticles were synthesized by the hydrothermal method. A mixed solution of 0.2 M Ni^{2+}, 0.2 M Zn^{2+} and 2.6 M Fe^{3+} was prepared in HCl solution, and then NaOH solution was added into the mixed solution under nitrogen gas, and the value of the pH of the mixture was adjusted to 10.5. To this mixture, 0.3 g of CTAB was added, and then it was placed into an autoclave (Teflon-lined stainless steel) at 200 °C of an oven for 8 h for hydrothermal treatment. In the following, the temperature of the autoclave was naturally decreased to the room temperature (RT), and the precipitate was collected and rinsed several times using DW to reach neutral pH. Finally, the obtained particles were dried at 50 °C.

2.3. Synthesis of the ionic liquid (1,3-dipropyl imidazolium bromide)

The RT Ionic Liquid (IL) was synthesized based on the procedure that was introduced in the literature [18].

2.4. Monomer synthesis (5,5'-(thiophen-2-ylmethylene)bis(2-aminopyrimidine-4,6-diol (TMAPD))

TMAPD was synthesized according to the following procedure: A mixture of 2.54 g (0.02 mol) 2-amino-4,6-dihydroxypyrimidine, 1 mL (0.01 mol) 2-thiophenecarboxaldehyde, and 20 mL DMSO was stirred for 6 h at 110 °C. After completion of the reaction tested by thin-layer chromatography, the temperature of the solution was decreased to the RT, and the violet powder obtained by pouring the solution into 400 mL of cold DW (-5 °C) was filtered, rinsed several times using DW and then dried using vacuum oven at 100 °C. The reaction yield was 92 % (3.20 g), and the obtained compound has not shown sharp melting point and started to be decomposed

above 300 ˚C. FT-IR (KBr, cm^{-1}): 3153-3477 (stretching of O-H and NH_2), 3049 (stretching of C-H aromatic), 2944 (stretching of C-H aliphatic), 1651 (stretching of C=N), 1586 (stretching of C=C), 1232 (C-N) and 1163 (C-O). ^{1}H NMR (DMSO-*d*$_6$, δ in ppm) (**Fig. 1**): 5.33 (s, 1H, CH), 6.61 (s, 4H, -NH_2), 6.78-6.80 (d, 1H, Ar-H, *J*= 5.6 Hz), 6.93-6.94 (d, 1H, Ar-H, *J*= 5.6 Hz), 7.42-7.44 (d, 1H, Ar-H, *J*= 5.2 Hz), 10.95-11.28 (m, 4H, broad, hydroxy pyrimidine). ^{13}C NMR (100 MHz, (DMSO-*d*$_6$, δ in ppm) (**Fig. 2**): 30.98, 115.41, 128.27, 128.55, 137.86, 140.13, 143.76, 170.77.

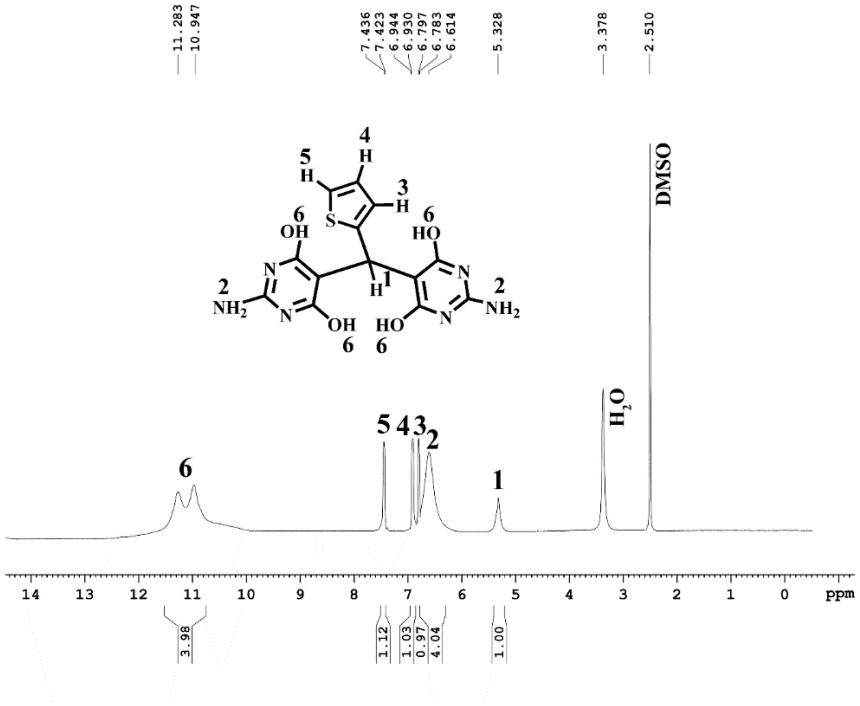

Fig. 1. ^{1}H NMR of the monomer.

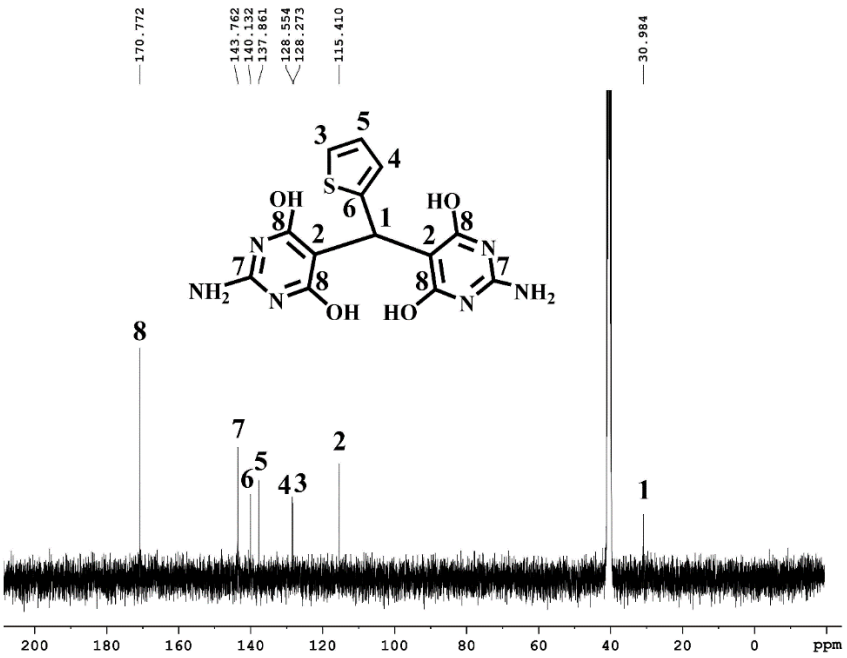

Fig. 2. ^{13}C NMR of the monomer.

2.5. Synthesis of the biodegradable P(PTA) by polycondensation reaction of TMAPD in TPP/IL

The synthesis of the biodegradable P(PTA) was carried out from a compound containing multi polar thiophene, amine, and free hydroxyl chelating groups. It was particularly synthesized from the diamine-phenol compound in 1,3-dipropyl imidazolium bromide as an ionic liquid without using toxic triphenyl phosphite/N-methylpyrolidone/pyridine/LiCl that is needed in the ordinary direct polycondensation. The P(PTA) was achieved by polycondensation of TMAPD using TPP-IL as catalyst and solvent by the following procedure: A flask of three-necked round-bottomed with the volume of 50 mL was fitted with a mechanical stirrer, a water cooled condenser, and argon gas, and then a mixture containing 1 mmol TMAPD, 1 mmol terephthalic acid, 0.7 g 1,3-dipropyl imidazolium bromide {[1,3-(pr)$_2$im]Br} as IL, and 1.29 mmol TPP was placed. The solution became sticky as the reaction continued at 110 $^{\circ}$C for 2.5 h. In the following, the reaction mixture temperature was decreased to the RT, and the precipitation of the obtained P(PTA) was performed using 100 mL of methanol. After the precipitate filtration, the hot water was used for washing it. Afterward, the precipitate was further refined in a Soxhlet apparatus using methanol for 24 h to eliminate the oligomers with low molecular weight. FT-IR (KBr, cm^{-1}): 3164-3337 (stretching of O-H and NH_2), 3054 (stretching of C-H aromatic), 2958 (stretching of C-H aliphatic), 1683 (stretching of C=O amide), 1641 (stretching of C=N), 1593 (stretching of

C=C), 1215 (C-N) and 1167 (C-O). ^{1}H NMR (DMSO-d_6, δ in ppm) (**Fig. 3**): 5.37 (s, 1H, CH), 7.25-7.27 (m, 2H, Ar-H), 7.44 (s, 1H, Ar-H), 7.99-8.00 (d, 2H, Ar-H, J= 3.2 Hz), 8.06-8.08 (d, 2H, Ar-H, J= 5.2 Hz), 11.01 (s, 1H, OH amide), 11.32 (m, 4H, broad, hydroxy pyrimidine).

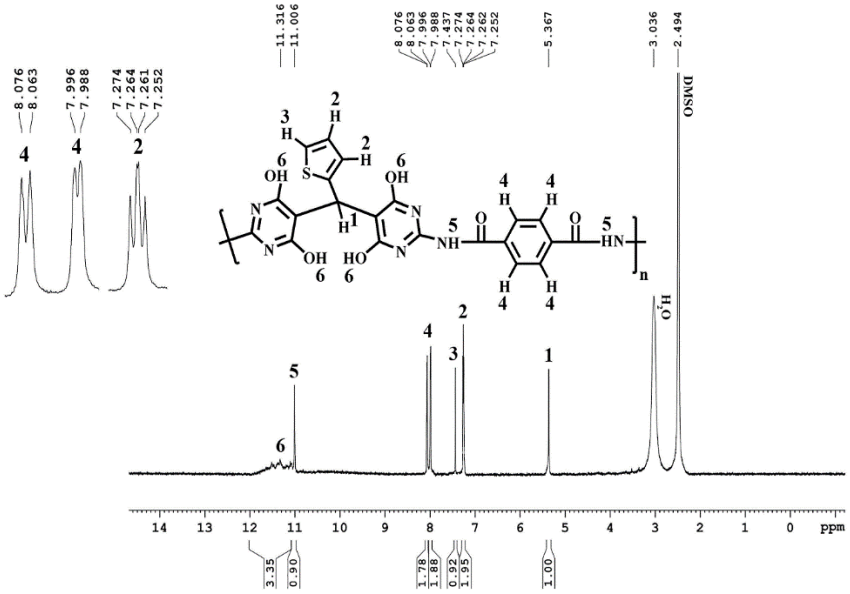

Fig. 3. ^{1}H NMR of the polymer.

2.6. Synthesis of CA/P(PTA)/$Ni_{0.2}Zn_{0.2}Fe_{2.6}O_4$ magnetic nanocomposite

Sodium alginate powder was dissolved in DW with a concentration of 1.5 % (w/v) to prepare a sodium alginate solution. 0.5 g of P(PTA) and 0.7 g of $Ni_{0.2}Zn_{0.2}Fe_{2.6}O_4$ were fully dispersed in the sodium alginate solution with vigorous stirring for 24 h to achieve a homogeneous solution, A. Afterwards, solution A was added dropwise to the solution of $CaCl_2$ (0.05 M) and 2 % glutaraldehyde for gelation process, and then the mixture was mixed for 24 h. The desired product was collected by an external magnetic field, rinsed several times using DW until reaching the solution pH to 7, and dried at 50 ˚C. Finally, it was powdered.

2.7. Characterization and analyses

To analyze the morphology and chemical characterization of the products, FE-SEM and EDX were respectively applied using Zeiss Neon-40, Germany. 400 MHz and 100 MHz of Bruker Advance DRX instrument were respectively used to record ^{1}H NMR and ^{13}C NMR spectra by DMSO-d_6 as a solvent. FT-IR spectrophotometer (PerkinElmer, USA) was employed to identify the functional groups of the products. XRD (GBC MMA instrument) was used to characterize the crystallinity of the product in the range of 2θ = 10–70˚ at RT. To record the thermal decomposition properties of the products, a thermogravimetric analyzer (TGA) (Mettler

TGA/SDTA 851e/LF/1100 thermobalance) under N_2 atmosphere at a rate of 10 °C/min was applied. The magnetic properties of the products were studied by a vibrating sample magnetometer (VSM, Daghigh Kavir Corporation, Iran).

2.8. Adsorption experiments

The experiments related to batch adsorption of the ions using the CA/P(PTA)/$Ni_{0.2}Zn_{0.2}Fe_{2.6}O_4$ were performed by a laboratory shaker adjusted at 180 rpm. To explore the influence of solution pH, the pH values of the metal ions solutions (30 mg/L) were adjusted between 1.5 to 5.5 using a pH meter. Each solution containing 0.03 g of the adsorbent was shaken for 20 min at 25 °C. In order to perform kinetic experiments, the mixtures of 0.03 g of the adsorbent and 30 mg/L solutions of each ion with the volume of 50 mL were agitated at various times (2.5–70 min). To evaluate the influence of adsorbent dosage, various quantities of the adsorbent from 0.01 to 0.06 g were utilized while the pH of the solutions was kept constant at optimized value. For isotherm evaluation, 0.04 g of the adsorbent and the solutions with the concentrations between 30–300 mg/L were utilized at RT. The influence of ionic strength was taken into consideration in the presence of $NaNO_3$ with the concentration in the range of 0.02-0.1 M. To assess the influence of temperature on the ions adsorption, the tests at various temperatures (25, 35, 45 °C) were conducted. After ending the adsorption process, the samples were removed from the shaker, and the adsorbent was collected using an external magnet. Agilent 4100 MP-AES Spectrometer was used to measure the ions concentration in the solution. The adsorption efficiency and adsorption capacity of the metal ions by the CA/P(PTA)/$Ni_{0.2}Zn_{0.2}Fe_{2.6}O_4$ were computed by the bellowing equations:

$$\text{Adsorption efficiency (\%)} = (C_0 - C_e)/C_o \times 100 \quad (1)$$

$$q_e = (C_0 - C_e) \times V/m \quad (2)$$

$$q_t = (C_0 - C_t) \times V/m \quad (3)$$

Where q_e and q_t (mg/g) refer to the quantities of metal ion that were respectively adsorbed onto the adsorbent at equilibrium and adsorption time t (min). Moreover, C_0 and C_e respectively refer to the initial and equilibrium concentrations of metal ion (mg/L). C_t demonstrates the concentration of metal ion in solution at time t. V shows the volume (L) of the solution, and m refers to the weight (g) of the adsorbent.

2.9. Batch reusability study

Reusability experiments were done by separation of the loaded adsorbent from the adsorption solution. In the following, the adsorbent was rinsed several times using DW and contacted with 50 mL of 0.2 M HNO_3 for 2 h in order to desorb Nd^{+3}, Tb^{+3}, and Dy^{+3}. After separating the adsorbent using an external magnet, the ions in the solutions were determined using Agilent 4100 MP-AES Spectrometer.

3. Results and discussion

3.1. Products characterization

Fig. 4 indicates the XRD pattern of the $Ni_{0.2}Zn_{0.2}Fe_{2.6}O_4$. The peaks at 2θ = 18.13°, 30.07°, 35.50°, 37.08°, 43.07°, 53.95°, 56.96°, and 63.89° are in accordance with the standard pattern of nickel zinc ferrite (JCPDS 08-0234) [19]. The Full Width at Half Maximum (FWHM) of the strongest reflection of the XRD pattern was used to estimate the average crystal size based on the Scherrer equation as following [20]:

$$D = k\lambda/\beta \cos\theta \quad (4)$$

Where k refers to the function of shape (value = 0.89), λ shows the X-ray wavelength of the radiation, β refers the Full Width at Half Maximum (FWHM) at 2θ = 35.50°, and θ shows the diffraction angle. Based on the Scherrer equation, the D value was 27.68 nm.

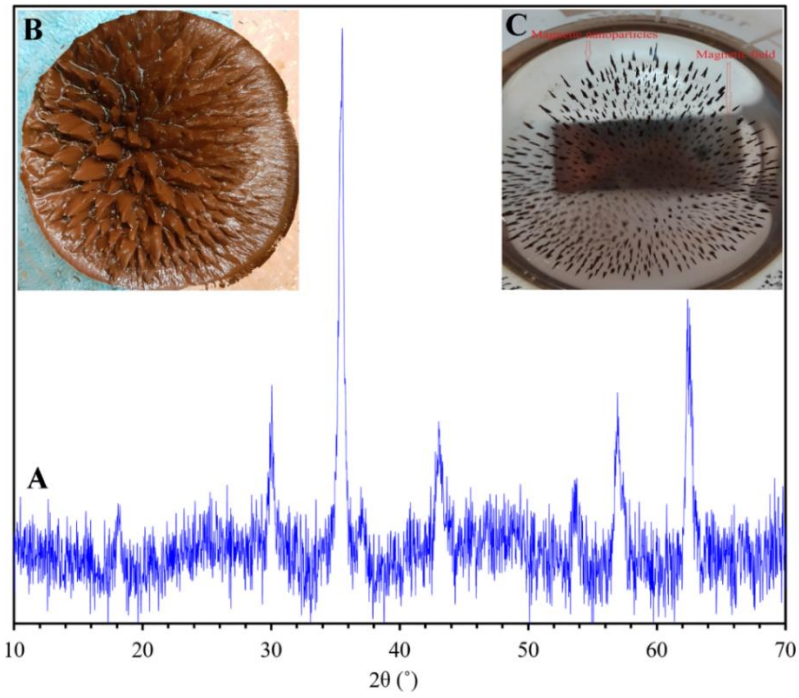

Fig. 4. (A) XRD pattern of $Ni_{0.2}Zn_{0.2}Fe_{2.6}O_4$ nanopartciles; Photo of $Ni_{0.2}Zn_{0.2}Fe_{2.6}O_4$ nanoparticles (B) before drying and (C) in the solution under magnetic field after drying.

The FE-SEM image of the $Ni_{0.2}Zn_{0.2}Fe_{2.6}O_4$ in **Fig. 5A** represents that the synthesized particles are almost spherical in shape and homogenous in distribution with a diameter less than 100 nm. **Fig. 5B** shows the distribution of the magnetic nanoparticles and P(PTA) on the surface of the CA or embedding with the CA that confirms the successful synthesis of the CA/P(PTA)/$Ni_{0.2}Zn_{0.2}Fe_{2.6}O_4$ magnetic bionanocomposite.

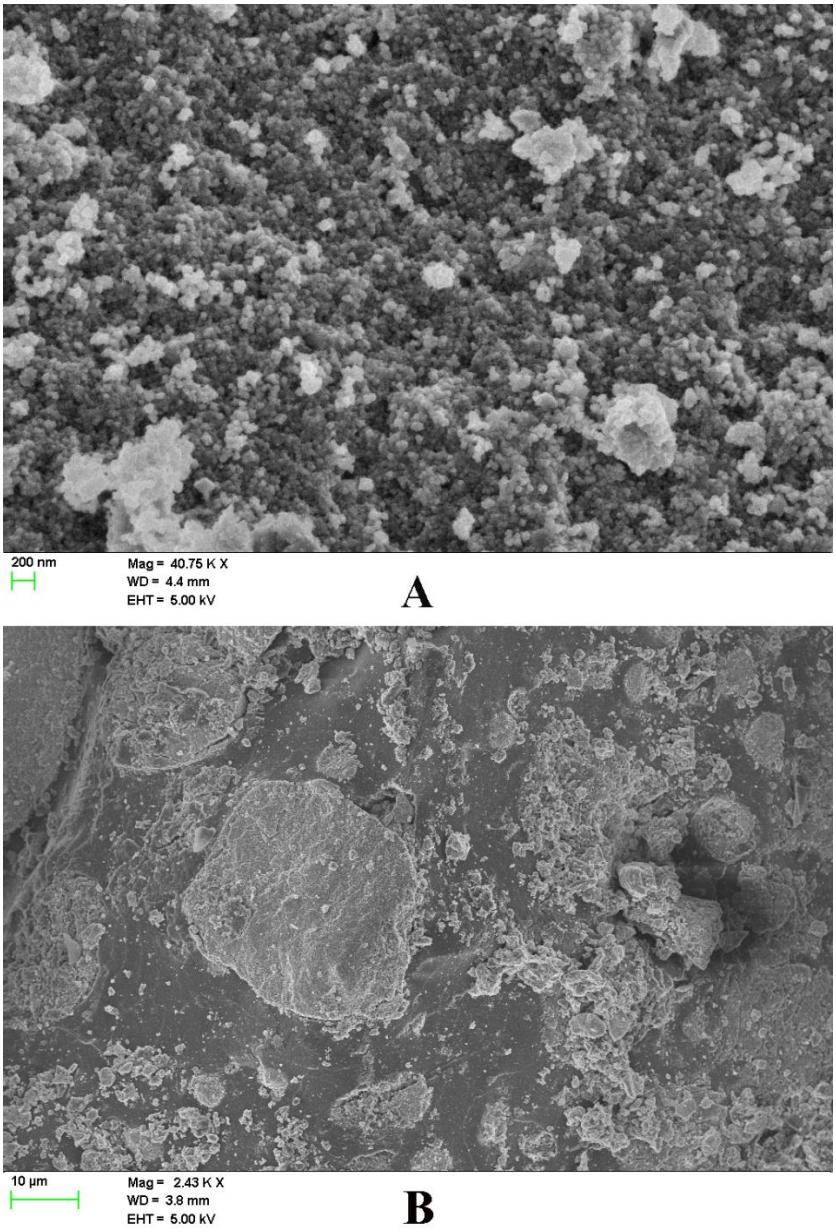

Fig. 5. FE-SEM images of (A) $Ni_{0.2}Zn_{0.2}Fe_{2.6}O_4$ and (B) CA/P(PTA)/$Ni_{0.2}Zn_{0.2}Fe_{2.6}O_4$.

Fig. 6 indicates the FT-IR spectrum for CA, $Ni_{0.2}Zn_{0.2}Fe_{2.6}O_4$, P(PTA) and CA/P(PTA)/$Ni_{0.2}Zn_{0.2}Fe_{2.6}O_4$. The FT-IR spectrum of CA in **Fig. 6A** shows a peak at 3389 cm^{-1}

related to the stretching vibration of O-H. The peaks at 1622, 1423, and 1052 cm^{-1} are characterized by the asymmetrical and symmetrical stretching of carboxyl groups, and C-O-C stretching, respectively [21]. The FT-IR spectrum of the $Ni_{0.2}Zn_{0.2}Fe_{2.6}O_4$ in **Fig. 6B** shows a broad absorption band around 3424 cm^{-1} and less intensive band at 1633 cm^{-1} related to the O-H stretching vibration [22]. The peaks at 2925 and 2853 cm^{-1} are assigned to the anti-symmetric and symmetric C-H vibrations of CTAB, respectively [23]. It can be mentioned that the band at 567 cm^{-1} relates to inherent metal stretching vibrations at the tetrahedral site (Fe-O), while the value of 478 cm^{-1} is attributed to the stretching of octahedral metal (M-O) [22]. In **Fig. 6C**, the peaks (cm^{-1}) related to the P(PTA) are as follows: 3164-3337 (stretching of O-H and NH_2), 3054 (stretching of C-H aromatic), 2958 (stretching of C-H aliphatic), 1683 (stretching of C=O amide), 1641 (stretching of C=N), 1593 (stretching of C=C), 1215 (C-N) and 1167 (C-O). **Fig. 6D** shows the existence of the peaks related to CA, P(PTA) and $Ni_{0.2}Zn_{0.2}Fe_{2.6}O_4$, confirming the successful synthesis of the CA/P(PTA)/$Ni_{0.2}Zn_{0.2}Fe_{2.6}O_4$.

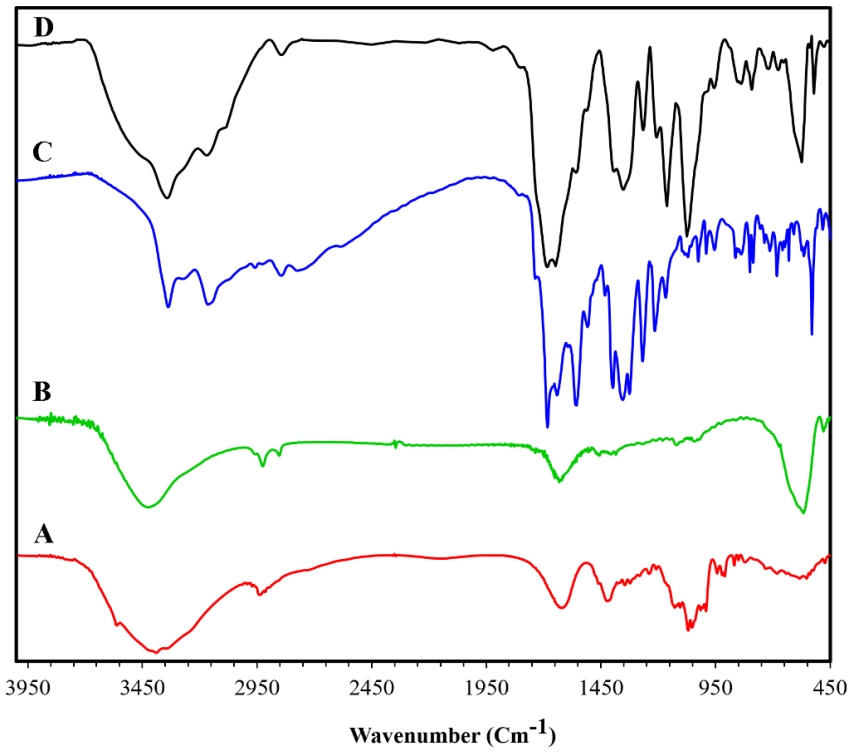

Fig. 6. FT-IR spectra of (A) CA, (B) $Ni_{0.2}Zn_{0.2}Fe_{2.6}O_4$, (C) P(PTA), and (D) CA/ P(PTA)/$Ni_{0.2}Zn_{0.2}Fe_{2.6}O_4$.

EDX was recorded to analyze the elements of the products and the obtained results are presented in **Fig. 7**. **Fig. 7A** illustrates Ni, Zn, Fe, and O peaks that confirm the formation of the $Ni_{0.2}Zn_{0.2}Fe_{2.6}O_4$. The elemental analysis of the nanocomposite in **Fig. 7B** represents similar peaks available in **Fig. 7A** along with the new peaks of N, S, and Ca due to the presence of P(PTA) and CA. Sodium peak is not seen in the spectrum of the CA/P(PTA)/$Ni_{0.2}Zn_{0.2}Fe_{2.6}O_4$, suggesting that sodium ions were completely released from the matrix of sodium alginate into the solution during the crosslinking reaction process of sodium alginate with calcium.

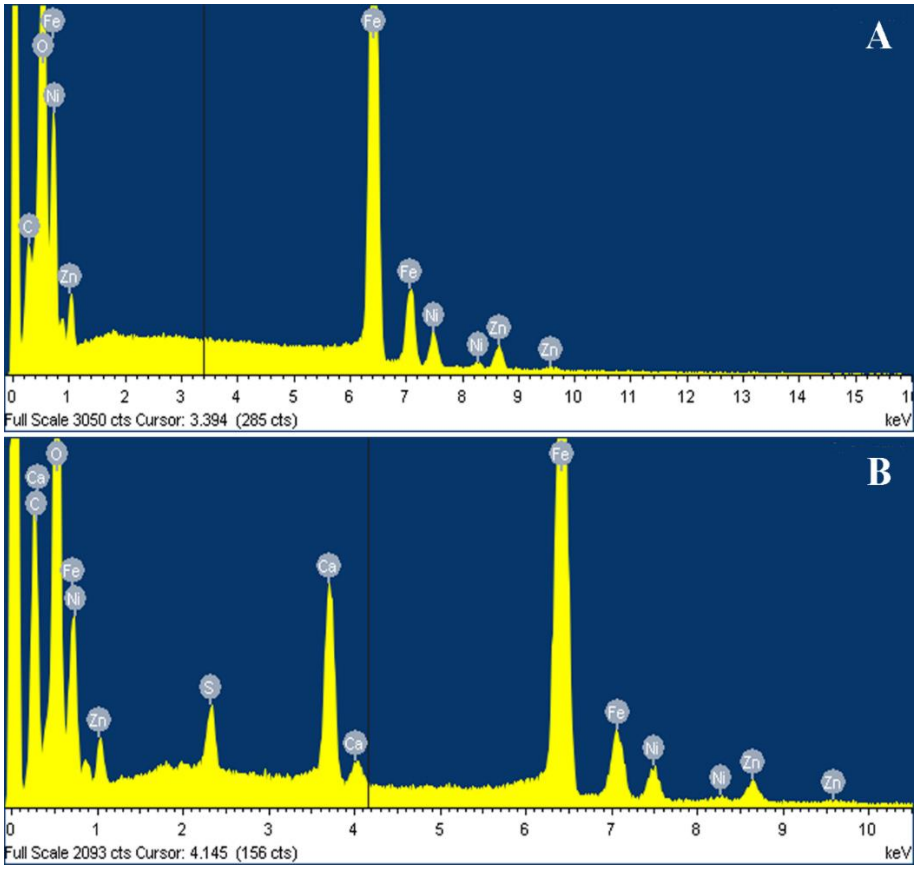

Fig. 7. EDX spectra of (A) $Ni_{0.2}Zn_{0.2}Fe_{2.6}O_4$ and (B) CA/P(PTA)/$Ni_{0.2}Zn_{0.2}Fe_{2.6}O_4$.

The thermo-stability of the resulting P(PTA) in **Fig. 8A** shows five different weight-loss steps in the TGA curve of the P(PTA). Obviously, the first step (around 100 ˚C) with a weight loss of 1.17 % can be attributed to water evaporation. The second step (from around 100 to 290 ˚C) with the amount of 9.6 % weight loss can be attributed to the preliminary degradation of aliphatic groups of P(PTA). At the third step, ranging between 300 and 330 ˚C, the aromatic groups of the P(PTA) are degrading gradually, and the forth step with the weight loss of 44.16 %

corresponds to their further decomposition. The final step can be related to the complete degradation of the polymer residue and its conversion to CO_2 and H_2O. **Fig. 8B** shows the TGA curve of the CA/P(PTA)/$Ni_{0.2}Zn_{0.2}Fe_{2.6}O_4$. The thermal stability of the nanocomposite increases in comparison with the pure P(PTA). It is obvious that the temperature of decomposition is shifted to higher temperature due to the existence of inorganic material in the matrix of the polymer, indicating that the thermal stability of the composite increases with $Ni_{0.2}Zn_{0.2}Fe_{2.6}O_4$ loading.

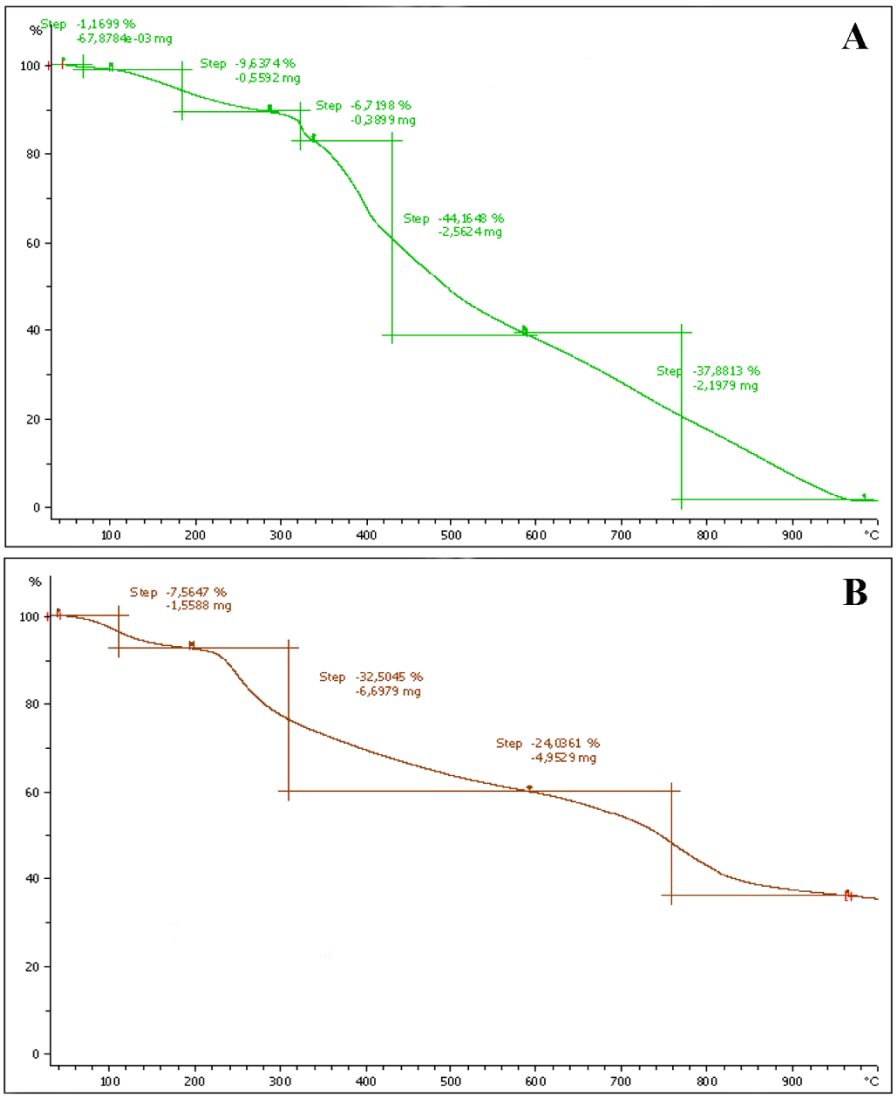

Fig. 8. TGA curves of (A) P(PTA) and (B) CA/P(PTA)/$Ni_{0.2}Zn_{0.2}Fe_{2.6}O_4$.

According to the magnetic hysteresis loops in **Fig. 9A**, the value of 45.87 emu/g obtained for the magnetic saturation of the $Ni_{0.2}Zn_{0.2}Fe_{2.6}O_4$ indicates its superparamagnetic behavior. It is obvious from **Fig. 9B** that combining the magnetic nanoparticles with the CA and P(PTA) leads

to a reduction in saturation magnetization from 45.78 to 15.28 emu/g. Despite this difference, the CA/P(PTA)/$Ni_{0.2}Zn_{0.2}Fe_{2.6}O_4$ could be easily separated from aqueous solution by an external magnetic field to avoid secondary pollution. As indicated in **Fig. 9C**, the metals-loaded adsorbent is easily separated by applying an external magnetic field from the solution.

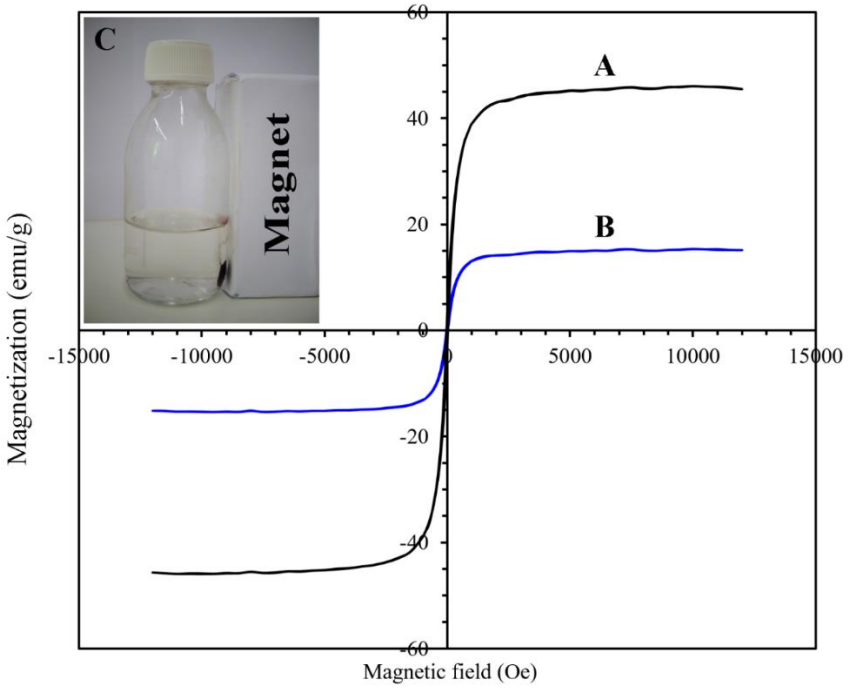

Fig. 9. Magnetization curves of (A) $Ni_{0.2}Zn_{0.2}Fe_{2.6}O_4$ and (B) CA/P(PTA)/$Ni_{0.2}Zn_{0.2}Fe_{2.6}O_4$; (C) Magnetic separation of the ions-loaded adsorbent.

3.2. Effect of pH

One of the essential parameters in the adsorption process is the initial pH value of the solution that must be optimized to reach favorable adsorption efficiency. In this research study, the influence of pH on Nd^{+3}, Tb^{+3}, and Dy^{+3} ions adsorption efficiency was studied in the range of 1.5-5.5. The experiments at pH > 5.5 were not studied due to the precipitation of the ions in the solutions at pH values higher than 5.5. According to the results in **Fig. 10A**, the adsorption efficiency values of Nd^{+3}, Tb^{+3}, and Dy^{+3} at low pH values are low because of the fact that the active sites of the CA/P(PTA)/$Ni_{0.2}Zn_{0.2}Fe_{2.6}O_4$ are protonated, causing the limitation of the available active sites for the ions adsorption. Amine groups are also partially protonated at low pH values. Consequently, electrostatic repulsion forces cause limitation in the interaction between the protonated amine groups and the metal ions. The active sites protonation decreases at higher pH values owing to the decrease in the concentration of H^+ ions, leading to higher

adsorption efficiency [24]. According to the results, pH=5.5 was considered as an optimum value for performing further adsorption tests.

3.3. Effect of contact time

From the experimental data presented in **Fig. 10B**, the equilibrium state of the adsorption process occurs after approximately 50 min of contact time. At first, the rate of reaction is relatively fast, and the adsorption efficiency for Nd^{+3}, Tb^{+3}, and Dy^{+3} respectively reaches to 60.59, 55.92 and 57.31 % in the first 2.5 min, and then a lower rate is seen and eventually no more notable adsorption is obtained beyond 50 min. In the beginning of the process, Nd^{+3}, Tb^{+3}, and Dy^{+3} ions adsorption efficiency is high owing to the fact that a greater adsorbent surface area is accessible for the ions adsorption. In continuation of the process, the formation of a monolayer by the adsorbed ions leads to exhaustion in the adsorbent capacity, and then the rate of metal ions transportation from the adsorbent exterior sites to its interior sites controls the uptake rate of the ions. It could be also noted that by considering the constant number of the active adsorption sites and the adsorption of only one ion by each active site in a monolayer, a rapid uptake of the ions by the adsorbent surface takes place initially that decreases in the following by intensifying the competition of the ions in the solution for occupying and decreasing the available active sites [25].

3.4. Adsorption kinetics

To explore the kinetics of adsorption, nonlinear pseudo-first order (PFO), PSO, and intra-particle diffusion (IPD) models were applied according to Eqs. (5), (6), and (7), respectively [26,27].

$$q_t = q_e\,(1 - \exp^{-K_1 t}) \quad (5)$$

$$q_t = K_2 q_e^2 t / 1 + K_2 q_e t \quad (6)$$

$$q_t = K_i t^{0.5} + C \quad (7)$$

Where K_1 (1/min) refers to the PFO rate constant, K_2 (g/mg min) shows PSO rate constant, K_i (1/min) refers the rate constant of IPD, and C provides data about the thickness of the boundary layer: the greater value of C is related to the influence of the boundary layer diffusion.

The initial adsorption rate (h) can be computed using K_2 and q_e values by the following equation:

$$h = K_2 q_e^2 \quad (8)$$

The validity of each model was compared by Chi-square (χ^2) according to Eqs. (9), since the coefficient of determination (R^2) may not be reasonable to select the best adsorption model in view of the fact that it only presents the fit between equations and experimental data, while the

correlation between predicted and experimental values of the adsorption capacity is explained by χ^2. The lower values of χ^2 indicate a better fit.

$$\chi^2 = \sum_{i=1}^{n} \frac{(q_{e,exp} - q_{e,cal})^2}{q_{e,cal}} \quad (9)$$

Where n refers to the number of data points. $q_{e,exp}$ and $q_{e,cal}$ are respectively related to the experimental and computed adsorbent capacities.

Table 1. Kinetic constants for adsorption of the ions by the CA/P(PTA)/$Ni_{0.2}Zn_{0.2}Fe_{2.6}O_4$.

		Nd^{+3}	Tb^{+3}	Dy^{+3}
PFO	K_1 (1/min)	0.343	0.314	0.329
	q_e (mg/g)	45.38	44.69	45.37
	R^2	0.8249	0.8927	0.8794
	χ^2	6.67	4.58	5.03
PSO	K_2 (g/mg min)	0.01274	0.01158	0.01195
	q_e (mg/g)	48.05	47.43	48.13
	h (mg/g min)	29.41	26.05	27.68
	R^2	0.9878	0.9974	0.9964
	χ^2	0.46	0.11	0.15
IPD	K_i (1/min)	9.58	9.98	9.88
	R^2	0.8999	0.8708	0.8745
	χ^2	3.81	5.52	5.24

Table 1 presents the kinetic parameters acquired by modeling the experimental data. The values of R^2 by fitting the experimental data with PSO model are higher than those obtained by PFO and IPD models. Furthermore, the comparison between the experimental equilibrium adsorption capacity ($q_{e,exp}$) and the computed equilibrium adsorption capacity ($q_{e,cal}$) shows that the quantities given by the PSO model are more alike than those provided by PFO and IPD models, describing the adsorption process by chemisorption mechanism via electrostatic attraction. Based on the IPD model, q_t versus $t^{0.5}$ should follow a linear plot that passes through the origin if it is the sole rate-limiting step [28]. As stated by the results, it may be deduced that IPD is not only the rate-limiting factor. The χ^2 values acquired from PSO model (0.11–0.67) in comparison with the values obtained from PFO (4.63–9.64) and IPD (4.83-5.8) models are lower that strongly confirm the PSO equation as the best model to describe Nd^{+3}, Tb^{+3}, and Dy^{+3} ions adsorption onto the CA/P(PTA)/$Ni_{0.2}Zn_{0.2}Fe_{2.6}O_4$.

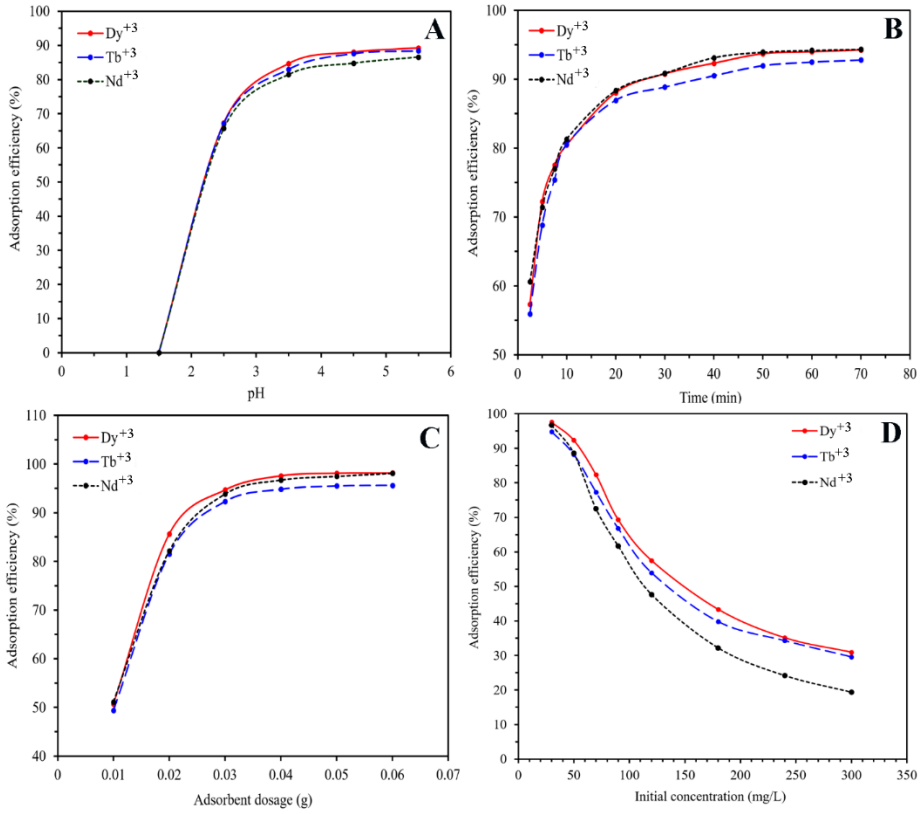

Fig. 10. Effects of (A) pH, (B) contact time, (C) initial concentration, and (D) adsorbent dosage on the adsorption of the ions.

3.5. Effect of adsorbent dosage

One of the major factors that has a considerable influence on the ions adsorption is adsorbent dosage, determining the adsorbent potential via the number of accessible active binding sites for the ions adsorption at a given initial concentration. The influence of adsorbent dosage on Nd^{+3}, Tb^{+3}, and Dy^{+3} ions adsorption is illustrated in **Fig. 10C**. It is clear that adsorption efficiency for Nd^{+3}, Tb^{+3}, and Dy^{+3} ions respectively enhances from 51.14 to 98.11, 49.33 to 95.62, and 50.66 to 98.15 % by enhancing the dosage of adsorbent from 0.01 to 0.04 g. The increase in the ions adsorption by enhancing the adsorbent dosage is due to enhancement in the number of active sites and available surface area [29]. Obtaining the maximum adsorption efficiency means that the equilibrium state is reached, and this is achieved by using 0.04 g of the adsorbent for Nd^{+3}, Tb^{+3}, and Dy^{+3}. The ions adsorption efficiency is not remarkably changed by increasing the adsorbent dosage beyond 0.04 g.

3.6. Effect of concentration

The capacity of adsorption of the CA/P(PTA)/$Ni_{0.2}Zn_{0.2}Fe_{2.6}O_4$ was investigated by the influence of Nd^{+3}, Tb^{+3}, and Dy^{+3} initial concentration, and the results are presented in **Fig. 10D**. As presented in **Fig. 10D**, enhancement in the initial concentration of the ions leads to the reduction in adsorption efficiency from 96.73 to 19.33, 94.82 to 29.59, and 97.58 to 30.95 % for Nd^{+3}, Tb^{+3}, and Dy^{+3}, respectively, while adsorption capacity at equilibrium for Nd^{+3}, Tb^{+3}, and Dy^{+3} by the CA/P(PTA)/$Ni_{0.2}Zn_{0.2}Fe_{2.6}O_4$ increases. At the initial concentration of 300 mg/L, the capacity of adsorption for Nd^{+3}, Tb^{+3}, and Dy^{+3} ions obtained at 25 °C was respectively calculated to be 72.49, 110.95, and 116.05 mg/g. At low initial concentration of the ions in the solution, the ratio of surface area and the total available adsorption sites to the initial number of the ions in the solution is relatively high that leads the adsorption of the ions to be independent of the initial concentration of the ions, thus, the ions are easily adsorbed. At higher initial concentration, limitation in the total available adsorption sites results in a decrease in the adsorption efficiency of the ions [30]. The increase in q_e at higher initial concentration could be related to enhancement in driving force.

3.7. Adsorption isotherms

Nonlinear Langmuir and Freundlich models were utilized to fit the adsorption data. Langmuir model hypothesis is mentioned as follows: uniform and equivalent active sites on adsorbent surface, the adsorption process in the monomolecular layer, and no fundamental interaction between adsorbed substances on the surface of adsorbent. Freundlich model hypothesizes the multilayer adsorption onto the heterogeneous surface of the adsorbent. They are presented by the following equations [31,32]:

$$q_e = \frac{b\ q_m\ C_e}{(1+bCe)} \quad \text{(Langmuir)} \qquad (10)$$

$$q_e = K\ C_e^{1/n} \quad \text{(Freundlich)} \qquad (11)$$

Where q_e and q_m (mg/g) respectively refer to the equilibrium and maximum adsorption capacities. C_e (mg/L) shows the equilibrium concentration of the adsorbate, and b (L/mg) and K ($mg^{1-1/n}\ L^{1/n}/g$) respectively show the Langmuir and Freundlich adsorption constants. Moreover, n demonstrates the heterogeneity factor. A value of $n > 1$ shows that adsorption is favorable.

The dimensionless factor (R_L) illustrates the intrinsic characteristics of the Langmuir model that is expressed as follows:

$$R_L = \frac{1}{1+bC_i} \qquad (12)$$

Where C_i (mg/L) is the highest initial metal concentration.

Table 2. Isotherm constants for adsorption of the ions by the CA/P(PTA)/$Ni_{0.2}Zn_{0.2}Fe_{2.6}O_4$.

		Nd^{+3}	Tb^{+3}	Dy^{+3}
Langmuir	b (L/mg)	0.88	0.199	0.364
	q_m (mg/g)	71.44	98.34	99.91
	R_L	0.004	0.016	0.009
	R^2	0.9563	0.8428	0.7989
	χ^2	8.4	112.03	157.44
Freundlich	K ($mg^{1-1/n}$ $L^{1/n}$/g)	44.4	36.58	43.18
	n	8.45	4.91	5.54
	R^2	0.8534	0.9812	0.9877
	χ^2	28.24	13.37	9.64

The coefficient of determination (R^2) values and the achieved parameters are revealed in **Table 2**. According to the values of R_L, there are four cases that are mentioned as following: the process of adsorption with $R_L = 0$ is irreversible. It is linear if $R_L = 1$ while it is favorable if $0 < R_L < 1$. In contrast, it is unfavorable if $R_L > 1$ [33]. The values of R_L for Nd^{+3}, Tb^{+3}, and Dy^{+3} calculated by Eq. (12) are between 0 and 1, suggesting that the adsorption process of the ions by the CA/P(PTA)/$Ni_{0.2}Zn_{0.2}Fe_{2.6}O_4$ is favorable. The n value for Nd^{+3}, Tb^{+3}, and Dy^{+3} is 8.45, 4.91, and 5.54, respectively, showing a strong interaction between the CA/P(PTA)/$Ni_{0.2}Zn_{0.2}Fe_{2.6}O_4$ and the metal ions. It is apparent from the obtained results that Freundlich model better fits the experimental data than Langmuir model for both Tb^{+3} and Dy^{+3} ions adsorption that indicates the adsorption of Tb^{+3} and Dy^{+3} ions is multilayer adsorption, and the adsorption of the ions takes place on a non-uniform surface. In contrast, the best fit for Nd^{+3} adsorption data is obtained by Langmuir model according to the values of R^2 and χ^2, indicating that the adsorption of Nd^{+3} is monolayer adsorption. The value of the maximum monolayer adsorption capacity (q_m) of Nd^{+3} calculated by Langmuir model at 25 ˚C is 71.44 mg/g, which is close to the experimental data. A comparison of the adsorption capacity of different adsorbents is represented in **Table 3**.

Table 3. Comparison of the adsorption capacity of Nd^{+3}, Tb^{+3}, and Dy^{+3} onto various adsorbents.

Adsorbent	q_m (mg/g)			Reference
	Nd^{+3}	Tb^{+3}	Dy^{+3}	
Fe_3O_4-C_{18}-chitosan-DETA	27.1		28.3	[34]
EDTA functionalized chitosan	74			[35]
Phosphonic acid functionalized silica microspheres	45			[36]
γ-Fe_2O_3-NH_4OH@SiO_2 (APTMS)			23.2	[37]
Cellulose functionalized with thiourea	73			[38]
MIL-101-PMIDA	70.9			[39]
A layered thiostannate, $(Me_2NH_2)_{1.33}(Me_3NH)_{0.67}Sn_3S_7 \cdot 1.25H_2O$ (FJSM-SnS)	126			[40]
Oxidized multi-walled carbon nanotubes			78.12	[41]
Lanthanide-ion imprinted polymers	126.5			[42]
Macroporous polymeric resin (TVEX-PHOR)		24.93		[43]
TA-MWCNTs		8.55		[44]
PAAm–YZ		42.9		[45]
Poly(acrylamide-expanded perlite) [P(AAm-EP)]		118.3		[46]
P(HEMA–Hap)		109.66		[47]
Poly(amidoxime-hydroxamic acid) resins		125		[48]
CaHAP/NF		130.43		[49]
Acryloyl–phenyl thiourea		74.23		[50]
Hybrid Lewis base ligands functionalized alumina-silica			125.4	[51]
CA@Fe_3O_4 NPs	41			[52]
11-Molybdo-vanadophosphoric acid supported on Zr modified mesoporous silica SBA-15			50	[53]
MPS (22 nm)-2NH-2COOH			44.8	[54]
o-CNCs/GO-IIPs			48.14	[55]
Imprinted mesoporous silica materials			22.33	[56]
CA/P(PTA)/$Ni_{0.2}Zn_{0.2}Fe_{2.6}O_4$	72.49	108.82[a]	113.08[a]	This study

[a] Calculated from Freundlich isotherm

3.8. Effect of ionic strength

Fig. 11A expresses ionic strength influence on Nd^{+3}, Tb^{+3}, and Dy^{+3} ions adsorption. The results show a significant effect of $NaNO_3$ on Nd^{+3}, Tb^{+3}, and Dy^{+3} ions adsorption onto the adsorbent. When 0.02 M $NaNO_3$ is used, the adsorbent efficiency for the adsorption of Nd^{+3}, Tb^{+3}, and Dy^{+3} ions from the solution decreases from 96.73 to 91.53, 94.82 to 88.83, and 97.58 to 93.3 %, respectively. By increasing $NaNO_3$ concentration from 0.02 to 0.1 M, a significant decrease in the ability of the adsorbent to adsorb the ions is seen due to the competition of Na^+ from the dissolution of $NaNO_3$ with the ions for interacting with the functional groups on the adsorbent surface [57]. In the case of Nd^{+3} and Tb^{+3}, the order of adsorption efficiency is $Nd^{+3} > Tb^{+3}$ at low concentration of $NaNO_3$, while it changes to $Tb^{+3} > Nd^{+3}$ at higher concentration of $NaNO_3$. This result suggests that ion exchange interaction could be the mechanism of the adsorption process of Nd^{+3}, Tb^{+3}, and Dy^{+3} by the CA/P(PTA)/$Ni_{0.2}Zn_{0.2}Fe_{2.6}O_4$.

3.9. Temperature effect on the adsorption and evaluation of thermodynamic parameters

Various temperatures of 25, 35, and 45 ˚C were applied for the batch adsorption of the ions by 0.04 g of the CA/P(PTA)/$Ni_{0.2}Zn_{0.2}Fe_{2.6}O_4$ at the concentration of 90 mg/L and pH = 5.5. The results presented in **Table 4** show that rising temperature from 25 to 45 ˚C leads to an increase in adsorption efficiency from 61.71 to 69.15 %, 66.79 to 77.25 %, and 69.33 to 79.73 % for Nd^{+3}, Tb^{+3}, and Dy^{+3}, respectively. These observations are mostly as a result of an increase in the surface activity that propose the endothermic process of adsorption between Nd^{+3}, Tb^{+3}, and Dy^{+3} and the CA/P(PTA)/$Ni_{0.2}Zn_{0.2}Fe_{2.6}O_4$.

The parameters of thermodynamic, namely Gibbs free energy (ΔG°, kJ/mol), enthalpy (ΔH°, kJ/mol), and entropy (ΔS°, kJ/mol K) were computed using the equations as following [58]:

$$K_d = q_e/C_e \quad (13)$$

$$\text{Ln } K_d = \Delta S^\circ/R - \Delta H^\circ/RT \quad (14)$$

$$\Delta G^\circ = - RT \text{ Ln } K_d \quad (15)$$

Where K_d refers to the distribution coefficient, and C_e shows the equilibrium concentration of ion in the solution (mg/L). R demonstrates the gas constant (8.314 J/mol K), and T indicates the temperature (K). The values of ΔH° and ΔS° in **Table 4** were computed based on the slope and intercept of the plot of Ln K_d versus 1/T, respectively (**Fig. 11B**).

Table 4. Effect of temperature on the adsorption of the ions at 90 mg/L and thermodynamic parameters.

Temperature (°C)	Adsorption efficiency (%)		
	Nd^{+3}	Tb^{+3}	Dy^{+3}
25	61.71	66.79	69.33
35	65.10	71.78	73.90
45	69.15	77.25	79.73
Thermodynamic parameters			
	Nd^{+3}	Tb^{+3}	Dy^{+3}
ΔH° (kJ/mol)	13.72	21.78	23.03
ΔS° (kJ/mol K)	0.051	0.079	0.084
Temperature (°C)			
25	-1.736	-2.284	-2.574
ΔG° (kJ/mol) 35	-2.168	-2.961	-3.236
45	-2.725	-3.823	-4.211

The value of ΔG° is negative and small that rises with increasing the temperature, which indicates a reduction in Gibbs energy in the adsorption process. The ΔG° negative values demonstrate that the process is naturally spontaneous and feasible. The positive ΔH° values confirm the endothermic nature of adsorption, and the values of $\Delta S^{\circ} > 0$ describe an increase in the randomness at the CA/P(PTA)/$Ni_{0.2}Zn_{0.2}Fe_{2.6}O_4$-solution interface during the adsorption process [58]. The parameters of thermodynamic show the possibility of applying the CA/P(PTA)/$Ni_{0.2}Zn_{0.2}Fe_{2.6}O_4$ for Nd^{+3}, Tb^{+3}, and Dy^{+3} ions adsorption.

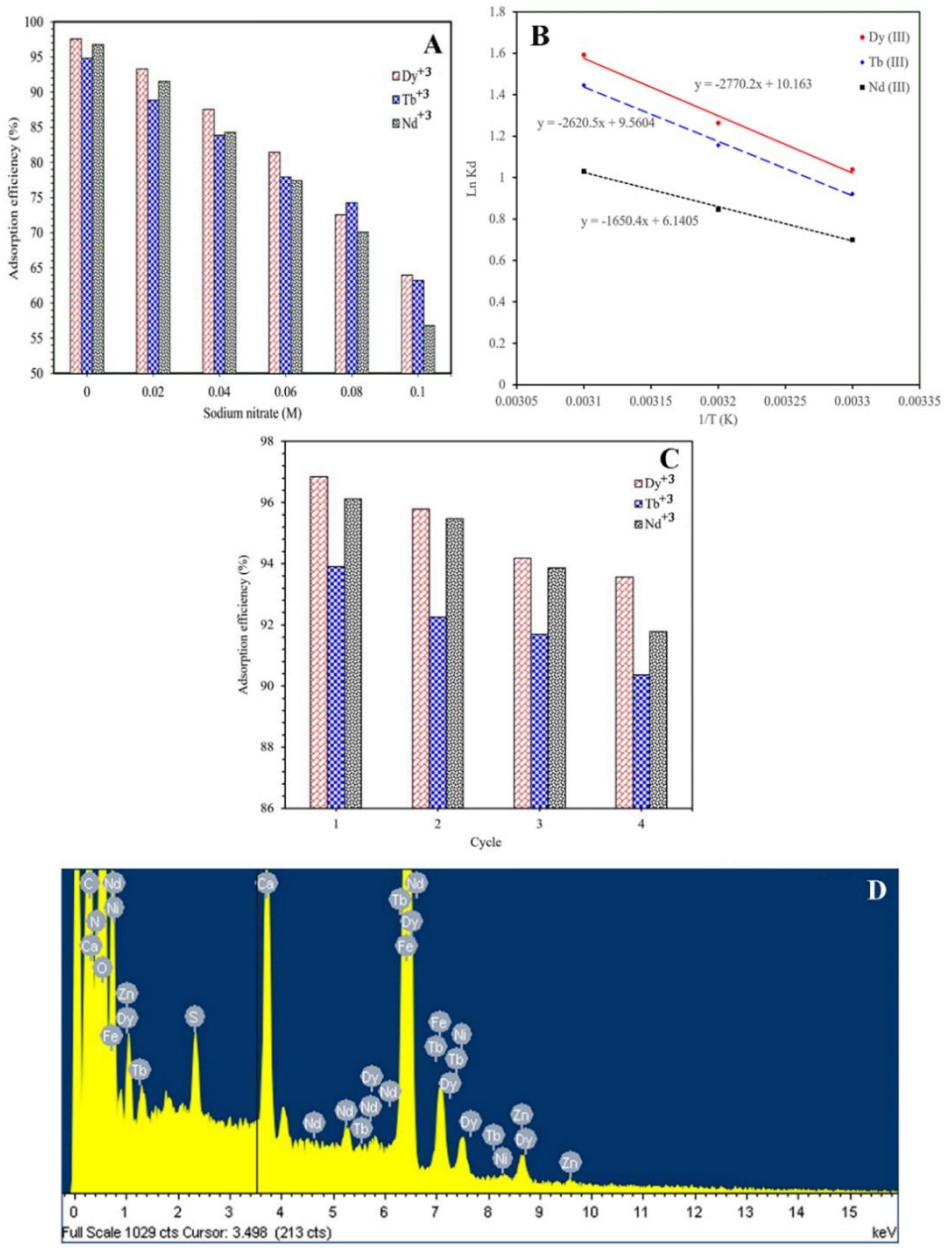

Fig. 11. (A) Effect of ionic strength on the adsorption of the ions, (B) Ln K_d versus 1/T for calculation of enthalpy and entropy changes, (C) Reusability of the CA/P(PTA)/$Ni_{0.2}Zn_{0.2}Fe_{2.6}O_4$ for adsorption of the ions, and (D) EDX spectrum of the CA/P(PTA)/$Ni_{0.2}Zn_{0.2}Fe_{2.6}O_4$ after adsorption of the ions.

3.10. Reusability studies

The regeneration of the adsorbent is a significant parameter in designing an adsorption process. To explore the reusability of the adsorbent, desorption test was performed using 0.2 M HNO_3 solution. Firstly, the CA/P(PTA)/$Ni_{0.2}Zn_{0.2}Fe_{2.6}O_4$ was loaded with 30 mg/L solutions of Nd^{+3},

Tb^{+3}, and Dy^{+3}. The concentration of each metal was determined by the Agilent 4100 MP-AES Spectrometer after the separation of the loaded adsorbent with an external magnet. The loaded CA/P(PTA)/$Ni_{0.2}Zn_{0.2}Fe_{2.6}O_4$ was rinsed completely using DW and then dried at 40 ˚C. Secondly, 50 mL of HNO_3 solution was used for the desorption process at RT at 180 rpm for 2 h. After finishing the process, the concentration of each metal in the solution was calculated. Four adsorption-desorption cycles were performed to test the reusability of the CA/P(PTA)/$Ni_{0.2}Zn_{0.2}Fe_{2.6}O_4$. Nd^{+3}, Tb^{+3}, and Dy^{+3} ions were desorbed from the adsorbent > 89, 91, and 95 %, respectively. As illustrated in **Fig. 11C**, after the fourth cycle, the adsorption performance for Nd^{+3}, Tb^{+3}, and Dy^{+3} declined from 96.12 to 91.78, 93.91 to 90.36, and 96.85 to 93.56 %, respectively. The results represent an efficient regeneration of the CA/P(PTA)/$Ni_{0.2}Zn_{0.2}Fe_{2.6}O_4$ by 0.2 M HNO_3 solution and reutilization with an insignificant decline in its adsorption efficiency that could confirm the economy of the adsorption process.

3.11. Competitive adsorption

To evaluate competitive adsorption of Nd^{+3}, Tb^{+3}, and Dy^{+3} ions in the ternary system of 30 mg/L (1:1:1), 0.04 g of the CA/P(PTA)/$Ni_{0.2}Zn_{0.2}Fe_{2.6}O_4$ (the same as a single system) was used. According to the value of q_{mix}/q_0, three kinds of influences, namely antagonism, synergism, and non-interaction, can occur in a multi-component system as following:

- Antagonism ($q_{mix}/q_0 < 1$): the influence of the component mixture in solution is lower than its influence in a single mode.
- Synergism ($q_{mix}/q_0 > 1$): the influence of the component mixture in solution is higher than its influence in a single mode.
- Non-interaction ($q_{mix}/q_0 = 1$): the influence of the component mixture in solution is neither less nor more compared with its influence in a single mode.

Where q_{mix} and q_0 are the adsorption capacities of each ion in the mixture and single systems, respectively.

The value of q_{mix}/q_0 for each ion was respectively calculated to be 0.23, 0.51, and 0.51 for Nd^{+3}, Tb^{+3}, and Dy^{+3}. The obtained results indicate that the q_{mix}/q_0 value for all ions is less than 1 in a ternary mixture. Therefore, the presence of each ion shows antagonism influence on the adsorption of other ions in the process. The adsorption efficiency for Nd^{+3}, Tb^{+3}, and Dy^{+3} ions decreased to 22.3, 48.05, and 50.28 %, respectively. EDX spectrum was also recorded after the adsorption process and the result is demonstrated in **Fig. 11D**. The existence of Nd^{+3}, Tb^{+3}, and

Dy^{+3} peaks in the spectrum strongly confirms the successful adsorption of these ions by the CA/P(PTA)/$Ni_{0.2}Zn_{0.2}Fe_{2.6}O_4$.

4. Conclusion

In this study, the CA/P(PTA)/$Ni_{0.2}Zn_{0.2}Fe_{2.6}O_4$ magnetic bionanocomposite was synthesized and characterized using various methods including FE-SEM, NMR, FT-IR, XRD, TGA, and VSM. The adsorption efficiency of the synthesized adsorbent was investigated by conducting comprehensive experiments of Nd^{+3}, Tb^{+3}, and Dy^{+3} ions adsorption from aqueous solution. The optimum ions adsorption was achieved at pH = 5.5 and 30 mg/L of the ions with the adsorbent dosage of 0.04 g. The adsorption kinetic of the ions onto the adsorbent was well explained by the PSO in comparison with PFO and IPD models. In addition, the equilibrium adsorption data were tested by Langmuir and Freundlich isotherm models. The data of Tb^{+3} and Dy^{+3} were well described by Freunlich model. In the case of Nd^{+3} adsorption, Langmuir was found to fit the data superior to Freunlich model, and maximum adsorption capacity was 71.44 mg/g. The calculation of the parameters of thermodynamic including ΔH°, ΔG°, and ΔS° showed that Nd^{+3}, Tb^{+3}, and Dy^{+3} ions adsorption was endothermic. 0.2 M HNO_3 was used as eluent for the desorption of the ions, and the results of adsorption-desorption cycles indicated that the adsorption efficiency of the CA/P(PTA)/$Ni_{0.2}Zn_{0.2}Fe_{2.6}O_4$ respectively decreased from 96.12 to 91.78, 93.91 to 90.36, 96.85 to 93.56 % for Nd^{+3}, Tb^{+3}, and Dy^{+3} after the 4th cycle.

Acknowledgments

This work has been supported by the Spanish Ministry of Economy and Competitiveness (Ref. CTM2017-83581-R). Hamedreza Javadian acknowledges the financial support received (Ref. BES-2015-072506).

References

[1] Z. Zhao, X. Sun, Y. Dong, Synergistic Effect of doped functionalized ionic liquids in silica hybrid material for rare earth adsorption, Ind. Eng. Chem. Res. 55 (2016) 2221−2229.

[2] W. Bonificio, D.R. Clarke, Rare-earth separation using bacteria, Environ. Sci. Technol. Lett. 3 (2016) 180-184.

[3] C. Li, Z. Zhuang, F. Huang, Z. Wu, Y. Hong, Z. Lin, Recycling rare earth elements from industrial wastewater with flowerlike nano-$Mg(OH)_2$, ACS Applied Materials & Interfaces 5 (19) (2013) 9719-25.

[4] European Commission, 2010, Critical raw materials for the EU. Report of the ad-hoc Working Group on defining critical raw materials. http://ec.europa.eu/enterprise/policies/rawmaterials/files/docs/report-b_en.pdf (accessed 17.01.17).

[5] C. Tunsu, M. Petranikova, M. Gergorić, C. Ekberg, T. Retegan, Reclaiming rare earth elements from end-of-life products: A review of the perspectives for urban mining using hydrometallurgical unit operations, Hydrometallurgy 156 (2015) 239-258.

[6] M. Wang, X. Li, W. Hua, L. Shen, X. Yu, X. Wang, Electrospun poly(acrylic acid)/silica hydrogel nanofibers scaffold for highly efficient adsorption of lanthanide ions and its photoluminescence performance, ACS Appl. Mater. Interfaces. 8 (2016) 23995-24007.

[7] A.A. Zaki, T. El-Zakla, M.A.E. Geleel, Modeling kinetics and thermodynamics of Cs^{+} and Eu^{3+} removal from waste solutions using modified cellulose acetate membranes. J. Membr. Sci. 401-402 (2012) 1-12.

[8] Y. Zhu, Y. Zheng, A. Wang, A simple approach to fabricate granular adsorbent for adsorption of rare elements. Int. J. Biol. Macromol. 72 (2015) 410-420.

[9] F. Zhao, E. Repo, Y. Meng, X. Wang, D. Yin, M. Sillanpaa, An EDTA-β-cyclodextrin material for the adsorption of rare earth elements and its application in preconcentration of rare earth elements in seawater. J. Colloid Interface Sci. 2016, 465, 215-224.

[10] H. Ren, Z. Gao, D. Wu, J. Jiang, Y. Sun, C. Luo, Efficient Pb(II) removal using sodium alginate–carboxymethylcellulose gel beads: Preparation, characterization, and adsorption mechanism, Carbohydr. Polym. 137 (2016) 402–409.

[11] N.M. Mahmoodi, Magnetic ferrite nanoparticle–alginate composite: Synthesis, characterization and binary system dye removal, J. Taiwan Inst. Chem. Eng. 44 (2013) 322–330.

[12] J.A. Reglero Ruiz, M. Trigo-López, F.C. García, J.M. García, Functional aromatic polyamides, Polymers 9(9) 2017 414.

[13] K. Marchildon, Polyamides – Still strong after seventy years, Macromol. React. Eng. 5 (2011) 22-54.

[14] M. Ghaemy, B. Aghakhani, M. Taghavi, S.M. AminiNasab, M. Mohseni, Synthesis and characterization of new imidazole and fluorene–bisphenol based polyamides: Thermal, photophysical and antibacterial properties, React. Funct. Polym. 73 (2013) 555-563.

[15] D. Mecerreyes, Applications of ionic liquids in polymer science and technology. Springer, 2015.

[16] J. Lu, F. Yan, J. Texter, Advanced applications of ionic liquids in polymer science, Prog. Polym. Sci. 34 (2009) 431-448.

[17] E.I. Lozinskaya, A.S. Shaplov, M.V. Kotseruba, L.I. Komarova, K.A. Lyssenko, M.Y. Antipin, D.G. Golovanov, Y.S. Vygodskii, "One-pot" synthesis of aromatic poly(1,3,4-oxadiazole)s in novel solvents—ionic liquids. J Polym Sci Pol Chem 44 (2006) 380–394.

[18] Y.S. Vygodskii, E.I. Lozinskaya, A.S. Shaplov, K.A. Lyssenko, M.Y. Antipin, Y.G. Urman, Implementation of ionic liquids as activating media for polycondensation processes, Polymer 45 (2004) 5031–5045.

[19] D. Ni, Z. Lin, P. Xiaoling, W. Xinqing, G. Hongliang, Preparation and characterization of nickel-zinc ferrites by a solvothermal method, Rare Metal Mat Eng. 44(9) (2015) 2126-2131.

[20] K. Nejati, R. Zabihi, Preparation and magnetic properties of nano size nickel ferrite particles using hydrothermal method, Chem. Cent. J. 6 (2012) 23.

[21] R. Fabryanty, C. Valencia, F. Edi Soetaredjo, J. Nyoo Putro, S. Permatasari Santoso, A. Kurniawan, Y.H. Ju, S. Ismadji, Removal of crystal violet dye by adsorption using bentonite-alginate composite, J. Environ. Chem. Eng. 5 (2017) 5677-5687.

[22] A.S.A. Bakr, Y.M. Moustafa, E.A. Motawea, M.M. Yehia, M.M.H. Khalil, Removal of ferrous ions from their aqueous solutions onto $NiFe_2O_4$–alginate composite beads, J. Environ. Chem. Eng. 3 (2015) 1486–1496.

[23] S.A. Elfeky, S. Ebrahim Mahmoud, A. Fahmy Youssef, Applications of CTAB modified magnetic nanoparticles for removal of chromium (VI) from contaminated water, J. Adv. Res. 8(4) (2017) 435–443.

[24] Y. Song, L.Y. Yang, Y. Wang, D. Yu, J. Shen, X. Ouyang, Highly efficient adsorption of Pb(II) from aqueous solution using amino-functionalized SBA-15/calcium alginate microspheres as adsorbent, Int. J. Biol. Macromol. 125 (2019) 808-819.

[25] P. Chakravarty, N.S. Sarma, H.P. Sharma, Removal of Pb (II) from aqueous solution using heartwood of Areca catechu powder, Desalination 256 (2010) 16–21.

[26] H. Javadian, M. Torabi Angaji, M. Naushad, Synthesis and characterization of polyaniline/γ-alumina nanocomposite: A comparative study for the adsorption of three different anionic dyes, J. Ind. Eng. Chem. 20 (2014) 3890-3900.

[27] H. Javadian, P. Vahedian, M. Toosi, Adsorption characteristics of Ni(II) from aqueous solution and industrial wastewater onto Polyaniline/HMS nanocomposite powder, Appl. Surf. Sci. 284 (2013) 13-22.

[28] M.L.F.A. De Castro, M.L.B. Abad, D.A.G. Sumalinog, R.R.M. Abarca, P. Paoprasert, M.D.G. de Luna, Adsorption of methylene blue dye and Cu(II) ions on EDTA-modified bentonite: Isotherm, kinetic and thermodynamic studies, Sustain. Environ. Res. 28 (2018) 197-205.

[29] Z.H. Hua, A. Mohamed Omer, X. Ouyang, D. Yu, Fabrication of carboxylated cellulose nanocrystal/sodium alginate hydrogel beads for adsorption of Pb(II) from aqueous solution, Int. J. Biol. Macromol. 108 (2018) 149–157.

[30] G. Zhou, Y. Wang, R. Zhou, C. Wang, Y. Jin, J. Qiu, C. Hua, Y. Cao, Synthesis of amino-functionalized bentonite/$CoFe_2O_4$@MnO_2 magnetic recoverable nanoparticles for aqueous Cd^{2+} removal, Sci. Total Environ. 682 (2019) 505-513.

[31] H. Javadian, F. Ghorbani, H. Tayebi, S.M. Hosseini Asl, Study of the adsorption of Cd (II) from aqueous solution using zeolite-based geopolymer, synthesized from coal fly ash; kinetic, isotherm and thermodynamic studies, Arab. J. Chem. 8 (2015) 837-849.

[32] H. Javadian, M. Ghasemi, M. Ruiz, A.M. Sastre, S.M. Hosseini Asl, M. Masomi, Fuzzy logic modeling of Pb (II) sorption onto mesoporous NiO/$ZnCl_2$-*Rosa Canina-L* seeds activated carbon nanocomposite prepared by ultrasound-assisted co-precipitation technique, Ultrason. Sonochem. 40 (2018) 748-762.

[33] H. Javadian, M. Taghavi, Application of novel Polypyrrole/thiol-functionalized zeolite Beta/MCM-41 type mesoporous silica nanocomposite for adsorption of Hg^{2+} from aqueous solution and industrial wastewater: Kinetic, isotherm and thermodynamic studies, Appl. Surf. Sci. 289 (2014) 487–494.

[34] E. Liu, X. Zheng, X. Xu, F. Zhang, E. Liu, Y. Wang, C. Li, Y. Yan, Preparation of diethylenetriamine-modified magnetic chitosan nanoparticles for adsorption of rare-earth metal ions, New J. Chem. 41 (2017) 7739-7750.

[35] J. Roosen, K. Binnemans, Adsorption and chromatographic separation of rare earths with EDTA- and DTPAfunctionalized chitosan biopolymers. J Mater Chem A. 2 (2014) 1530–1540.

[36] I.V. Melnyk, V.P. Goncharyk, L.I. Kozhara, G.R. Yurchenko, A.K. Matkovsky, Y.L. Zub, B. Alonso, Sorption properties of porous spray-dried microspheres functionalized by phosphonic

acid groups, Microporous Mesoporous Mater. 153 (2012) 171–177.

[37] T. Kegl, I. Ban, A. Lobnik, A. Košak, Synthesis and characterization of novel γ-Fe_2O_3-NH_4OH@SiO_2(APTMS) nanoparticles for dysprosium adsorption, J. Hazard. Mater. 378 (2019) 120764.

[38] A. Negrea, A. Gabor, C.M. Davidescu, M. Ciopec, P. Negrea, N. Duteanu, A. Barbulescu, Rare earth elements removal from water using natural polymers, Sci Rep. 8 (2018) 316.

[39] Y.R. Lee, K. Yu, S. Ravi, W.S. Ahn, Selective adsorption of rare earth elements over functionalized Cr-MIL-101. Appl Mater Interfaces. 10 (2018) 23918-23927.

[40] X-H. Qi, K-Z Du, M-L Feng, Y-J Gao, X-Y. Huang, M.G. Kanatzidis, Layered $A_2Sn_3S_7 \cdot 1.25H_2O$ (*A* = organic cation) as efficient ion-exchanger for rare earth element recovery, J. Am. Chem. Soc. 2017, 139, 12, 4314-4317.

[41] S.M.A. Koochaki-Mohammadpour, M. Torab-Mostaedi, A. Talebizadeh-Rafsanjani, F. Naderi-Behdani, Adsorption isotherm, kinetic, thermodynamic, and desorption studies of lanthanum and dysprosium on oxidized multiwalled carbon nanotubes. J Dispers Sci Technol 35 (2014) 244–254.

[42] M.M. Yusoff, N.R. Nik Mostapa, Md. Shaheen Sarkar, T.K. Biswas, Md. Lutfor Rahman, S.E. Arshad, M.S. Sarjadi, A.D. Kulkarni, Synthesis of ion imprinted polymers for selective recognition and separation of rare earth metals, J. Rare Earth 35 (2017) 177-186.

[43] H.A. Madbouly, N.E. El-Hefny, Y.A. El-Nadi, Adsorption and separation of terbium(III) and gadolinium(III) from aqueous nitrate medium using solid extractant, Sep Sci Technol. (2019) 1-13.

[44] S. Tong, S. Zhao, W. Zhou, R. Li, Q. Jia, Modification of multi-walled carbon nanotubes with tannic acid for the adsorption of La, Tb and Lu ions, Microchim Acta 174 (2011) 257–264.

[45] D. Baybaş, U. Ulusoy, Polyacrylamide–clinoptilolite/Y-zeolite composites: Characterization and adsorptive features for terbium, J Hazard Mater 187(1) (2011) 241–249.

[46] R. Akkaya, Synthesis and characterization of a new low-cost composite for the adsorption of rare earth ions from aqueous solutions, Chem Eng J 200 (2012) 186–191.

[47] R. Akkaya, Terbium adsorption onto polyhydroxyethylmethacrylate–hydroxyapatite composite and its modified composition by phytic acid, Desalin Water Treat 52 (2014) 1440-1447.

[48] F.A. Alakhras, K.A. Dari, M.S. Mubarak, Synthesis and chelating properties of some Poly (Amidoxime-hydroxamic Acid) resins toward some trivalent lanthanide metal ions, J Appl Polym Sci 97(2) (2005) 691–696.

[49] M.A. Attia, S.I. Moussa, R.R. Sheha, H.H. Someda, E.A. Saad, Hydroxyapatite/$NiFe_2O_4$ superparamagnetic composite: Facile synthesis and adsorption of rare elements, Appl. Radiat. Isot. 145 (2019) 85-94.

[50] N.S. Reddy, K.M. Rao, S.V. Krishna, C.S. Ha, Synthesis of 1–acryloyl–3–phenyl thiourea based pH sensitive hydrogels for removal of samarium and terbium. Macromol. Res. 24 (2016) 494–501.

[51] M.R. Awual, N.H. Alharthi, Y. Okamoto, M.R. Karim, M.E. Halim, M.M. Hasan, M.M. Rahman, M.M. Islam, M.A. Khaleque, M.C. Sheikh, Ligand field effect for Dysprosium(III) and Lutetium(III) adsorption and EXAFS coordination with novel composite nanomaterials, Chem. Eng. J. 320 (2017) 427-435.

[52]] R.M. Ashour, R. El-Sayed, A.F. Abdel-Magied, A.A. Abdel-Khalek, M.M. Ali, K. Forsberg, A. Uheida, M. Muhammed, J. Dutta, Selective separation of rare earth ions from aqueous solution using functionalized magnetite nanoparticles: kinetic and thermodynamic studies, Chem. Eng. J. 327 (2017) 286–296.

[53] H. Aghayan, A. Mahjoub, A. Khanchi, Samarium and dysprosium removal using 11-molybdo-vanadophosphoric acid supported on Zr modified mesoporous silica SBA-15, Chem. Eng. J. 225 (2013) 509–519.

[54] T. Kaneko, F. Nagata, S. Kugimiya, K. Katob, Optimization of carboxyl-functionalized mesoporous silica for the selective adsorption of dysprosium, J Environmen Chem Eng 6 (2018) 5990-5998.

[55] X. Zheng, Y. Zhang, T. Bian, Y. Zhang, Z. Li, J. Pan, Oxidized carbon materials cooperative construct ionic imprinted cellulose nanocrystals films for efficient adsorption of Dy(III), Chem Eng J 381 (2020) 122669.

[56] X. Zheng, E. Liu, F. Zhang, Y. Yan, J. Pan, Efficient adsorption and separation of dysprosium from NdFeB magnets in an acidic system by ion imprinted mesoporous silica sealed in a dialysis bag, Green Chem. 18 (2016) 5031–5040.

[57] K. Srinivasa Rao, G. Roy Chaudhury, B.K. Mishra, Kinetics and equilibrium studies for the removal of cadmium ions from aqueous solutions using Duolite ES 467 resin, Int. J. Miner. Process. 97 (2010) 68–73.
[58] S. He, C. Han, H. Wang, W. Zhu, S. He, D. He, Y. Luo, Uptake of arsenic(V) using alumina functionalized highly ordered mesoporous SBA-15 (Alx-SBA-15) as an effective adsorbent, J. Chem. Eng. Data. 60 (2015) 1300-1310.

ANNEX V

One-step hydrothermal synthesis of green synthesized poly(pyrimidine-thiophene-amide) as novel polyamide in imidazolium based ionic liquid as green media/$Ni_{0.2}Zn_{0.2}Fe_{2.6}O_4$ nanocomposite: Investigation on Nd^{+3}, Tb^{+3}, and Dy^{+3} adsorption

One-step hydrothermal synthesis of green synthesized poly(pyrimidine-thiophene-amide) as novel polyamide in imidazolium based ionic liquid as green media/$Ni_{0.2}Zn_{0.2}Fe_{2.6}O_4$ nanocomposite: Investigation on Nd^{+3}, Tb^{+3}, and Dy^{+3} adsorption

Hamedreza Javadian[a,*], Montserrat Ruiz[b], Mehdi Taghavi[c], Ana Maria Sastre[a]

[a]Department of Chemical Engineering, ETSEIB, Universitat Politècnica de Catalunya, Diagonal 647, 08028 Barcelona, Spain

[b]Department of Chemical Engineering, EPSEVG, Universitat Politècnica de Catalunya, Av. Víctor Balaguer, s/n, 08800 Vilanova i la Geltrú, Spain

[c]Department of Chemistry, Faculty of Science, Shahid Chamran University of Ahvaz, 61357-43337, Iran

[*]Corresponding author.

Email addresses: Hamedreza.javadian@yahoo.com; Hamedreza.javadian@upc.edu

Abstract

In this research, the poly(pyrimidine-thiophene-amide) (P(PTA)) as a novel polyamide was synthesized by polycondensation reaction of 5,5'-(thiophen-2-ylmethylene)bis(2-aminopyrimidine-4,6-diol) (TMAPD) with terephthalic acid in 1,3-dipropyl imidazolium bromide {[1,3-$(pr)_2$im]Br} ionic liquid as green media. Then, the hydrothermal method was used to produce the magnetic P(PTA)/$Ni_{0.2}Zn_{0.2}Fe_{2.6}O_4$ (M-P(PTA)). The analyses of the products were carried out by FE-SEM, NMR, XRD, TGA, VSM, and FT-IR techniques. The saturation magnetization of the nanocomposite by VSM analysis was found to be 50.44 emu/g. The adsorbent capability for the simultaneous adsorption of Nd^{+3}, Tb^{+3}, and Dy^{+3} rare earth elements was investigated. The adsorption efficiency for 50 mg/L of Nd^{+3}, Tb^{+3}, and Dy^{+3} was 95.67, 97.48, and 98.41 %, respectively, at pH=5.5 by using 0.15 g of the M-P(PTA) within 130 min. The kinetic adsorption data were effectively fitted with pseudo-second-order (PSO). Tb^{+3} and Dy^{+3} equilibrium data were favorably modeled with Freundlich model while Langmuir model was appropriate for modeling Nd^{+3} adsorption.

Keywords: Poly(pyrimidine-thiophene-amide), Magnetic, Nanocomposite, Adsorption, Rare earth elements.

1. Introduction

Lanthanide elements together with yttrium and scandium are named as rare earth elements (REEs) and are extensively utilized in a variety of industrial applications like automotive catalytic converters, high strength permanent magnets, electronic tools, lasers, and superconductors [1]. It is essential that the production of REEs be in balance with their consumption all around the world. As long as this balance might be disturbed owing to the high demands of REEs for high-tech applications, their production, recovery, and recycling are considered as significant matters in the aspects of geopolitics and economy [2]. Recycling rates in terms of the base metals such as aluminum, iron, and copper, and costly metals namely gold, silver, platinum-group metals are being highly obtained. In spite of the presence of many scientific research articles (mainly lab-scale) written on attempts performed on recycling of REEs, the recycling quantity of the REEs was only under 1% in 2011 because of ineffective gathering, technological difficulties, and unavailability of motivations [3]. Amongst all conventional methods, adsorption can be regarded as an inexpensive, simple and eco-friendly method that is highly efficient for metals recovery from aqueous media [4]. It can be considered as a competitive substitution to solvent extraction because of not using organic solvents [5]. Many investigations have been conducted for adsorption of REEs from aqueous media by utilizing adsorbents, such as carbons [6], porous silica [7], metal organic frameworks [8], metal oxides [9], polymers [10], and biomaterials [11].

Synthetic polyamides (PAs) were generally known as the primary engineering plastics and are still by far considered as the most significant kind of these groups of materials [12,13]. However, commercial synthesis of these polymers mainly demonstrates inadequate solubility and great temperatures of melting point, leading to a reduction in their processability and limitation in additional usages. Consequently, new studies have put their attention on developing structurally changed PAs with enhances solubility and improved processability [14].

Due to the worsening of the environment, there is a great need for the improvement of new methodologies for polymerization using environmentally eco-friendly media and giving sufficient solubility to polymerization which could substitute the highly polar solvents which are volatile, mostly flammable, poisonous, dangerous and harmful [15]. Effective utilization of green solvents of ionic liquids (ILs) offers new and significant chemical and physical properties. However, their extremely low vapor pressure, non-volatility, great thermal stability, and

inflammability has primarily attracted the consideration of many researchers. Furthermore, their appropriate polarity (owing to their ionic nature) also makes them suitable for dissolving different polar and non-polar inorganic, organometallic, organic, and great molecular-weight polymeric compounds, which causes their utilization as catalysts and solvents in different kinds of reactions. ILs have recently attracted significant attention of polymer researchers, and different polycondensation reactions have been achieved in ionic media. Researches have demonstrated the creation of high molecular-weight PAs by reacting various diamines with a dicarboxylic acid in ILs [16].

Generally, adsorbents are separated from aqueous media by filtration or high-speed centrifugation, and there is a difficulty for the rapid separation of adsorbent from high volume solutions. To solve this problem, magnetic adsorbents can be utilized due to their easy separation from aqueous media by applying an external field [17]. Magnetic nanocomposites are generally simple, cost-effective and environmentally friendly in comparison to the other adsorbents [18]. Thus, by using adsorbents combined with nanotechnology and magnetic separation technique, metal ions can be ideally separated.

In this research, a novel polyamide (poly(pyrimidine-thiophene-amide) (P(PTA))) was synthesized by polycondensation reaction of 5,5'-(thiophen-2-ylmethylene)bis(2-aminopyrimidine-4,6-diol) (TMAPD) with terephthalic acid in 1,3-dipropyl imidazolium bromide {[1,3-$(pr)_2$im]Br} ionic liquid as green media and then, the P(PTA)/$Ni_{0.2}Zn_{0.2}Fe_{2.6}O_4$ (M-P(PTA)) magnetic nanocomposite was prepared by hydrothermal method and used as an adsorbent for adsorption of the rare earth elements. The impact of main factors including contact time, adsorbent dosage, and primary concentration on Nd^{+3}, Tb^{+3}, and Dy^{+3} ions adsorption was investigated. The nanocomposite was tested in the consecutive adsorption-desorption cycles to evaluate its reusability.

2. Materials and methods

2.1. Materials and reagents

$Dy(NO_3)_3.5H_2O$ was purchased from Alfa Aesar. $Nd(NO_3)_3.6H_2O$, $Tb(NO_3)_3 \cdot 6H_2O$, $Zn(NO_3)_2.6H_2O$, $Fe(NO_3)_3.9H_2O$, $Ni(NO_3)_2 \cdot 6H_2O$, glutaraldehyde, 2-amino-4,6-dihydroxypyrimidine, 2-thiophenecarboxaldehyde, terephthalic acid, triphenyl phosphite (TPP), dimethyl sulfoxide (DMSO), and methanol were bought from Sigma-Aldrich. The stock solution

of 1000 mg/L was made by dissolving the salts in deionized water (DW). Appropriate molarity of HNO_3 or NaOH was applied to adjust the pH of the solutions to the favorable value.

2.2. Synthesis of the ionic liquid (1,3-dipropyl imidazolium bromide)

Room temperature ionic liquid (IL) was synthesized based on the reported procedure [19].

2.3. Monomer synthesis (5,5'-(thiophen-2-ylmethylene)bis(2-aminopyrimidine-4,6-diol (TMAPD))

TMAPD was synthesized according to the following procedure: A mixture of 2.54 g (0.02 mol) 2-amino-4,6-dihydroxypyrimidine, 1 mL (0.01 mol) 2-thiophenecarboxaldehyde, and 20 mL DMSO was mixed for 6 h at 110 °C. While the reaction tested by thin-layer chromatography was completed, the temperature of the solution was decreased to the temperature of room and the violet powder obtained by pouring the solution into 400 mL of cold DW (-5 °C) was filtered, rinsed many times using DW and then dried using vacuum oven at 100 °C. The reaction yield was 92 % (3.20 g), and the obtained compound have not shown sharp melting point, and started to be decomposed above 300 °C. FT-IR (KBr, cm^{-1}): 3153-3477 (stretching of O-H and NH_2), 3049 (stretching of C-H aromatic), 2944 (stretching of C-H aliphatic), 1651 (stretching of C=N), 1586 (stretching of C=C), 1232 (C-N) and 1163 (C-O). ^{1}H NMR (DMSO-d_6, δ in ppm) (**Fig. 1**): 5.33 (s, 1H, CH), 6.61 (s, 4H, -NH_2), 6.78-6.80 (d, 1H, Ar-H, J= 5.6 Hz), 6.93-6.94 (d, 1H, Ar-H, J= 5.6 Hz), 7.42-7.44 (d, 1H, Ar-H, J= 5.2 Hz), 10.95-11.28 (m, 4H, broad, hydroxy pyrimidine). ^{13}C NMR (100 MHz, (DMSO-d_6, δ in ppm) (**Fig. 2**): 30.98, 115.41, 128.27, 128.55, 137.86, 140.13, 143.76, 170.77.

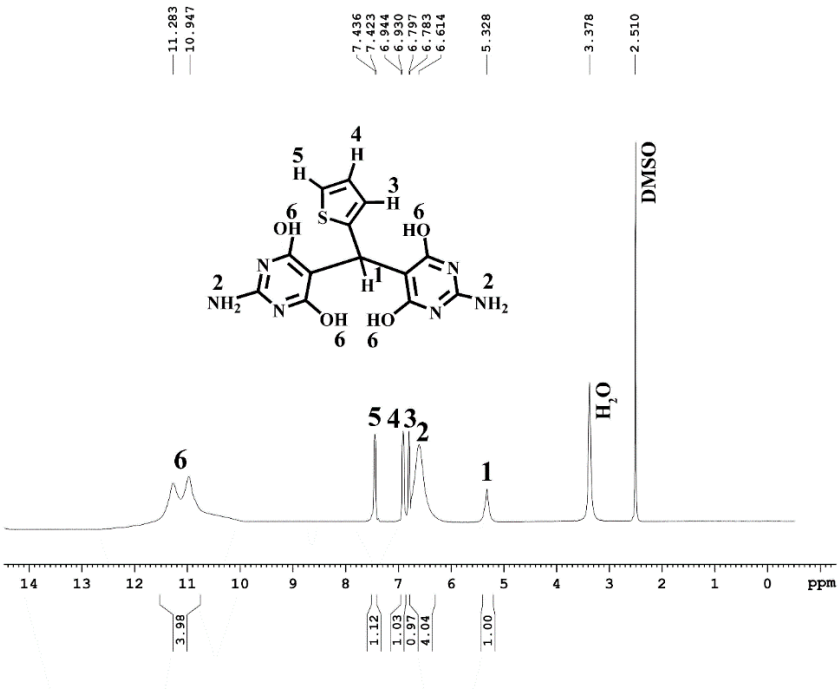

Fig. 1. ^{1}H NMR of the monomer.

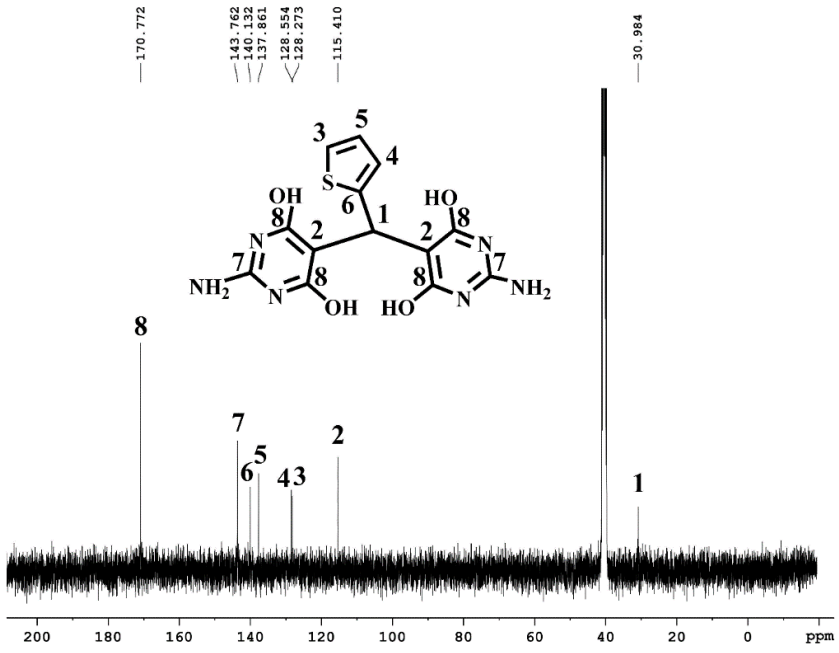

Fig. 2. ^{13}C NMR of the monomer.

2.4. Synthesis of the P(PTA) by polycondensation reaction of TMAPD in TPP/IL

Synthesis of the P(PTA) was carried out from a compound containing multi polar thiophene, amine, and free hydroxyl chelating groups. It was particularly fabricated from the diamine-phenol compound in 1,3-dipropyl imidazolium bromide as an ionic liquid without using toxic triphenyl phosphite/N-methylpyrolidone/pyridine/LiCl that is needed in the ordinary direct polycondensation. The P(PTA) was achieved by polycondensation of TMAPD using TPP-IL as catalyst and solvent by the following procedure: A flask of three-necked round-bottomed with the volume of 50 mL was fitted with a mechanical stirrer, a water cooled condenser, and argon gas and then, a mixture containing 1 mmol TMAPD, 1 mmol terephthalic acid, 0.7 g 1,3-dipropyl imidazolium bromide {[1,3-$(pr)_2$im]Br} as IL, and 1.29 mmol TPP was placed. The solution became sticky as the reaction continued at 110 °C for 2.5 h. In the following, the reaction mixture temperature was decreased to the temperature of the room, and the precipitation of the obtained P(PTA) was performed using 100 mL of methanol. Then, after the precipitate filtration, the hot water was used for washing it. Afterward, the precipitate was further refined in a Soxhlet apparatus using methanol for 24 h to eliminate the oligomers with low molecular weight. FT-IR (KBr, cm^{-1}): 3164-3337 (stretching of O-H and NH_2), 3054 (stretching of C-H aromatic), 2958 (stretching of C-H aliphatic), 1683 (stretching of C=O amide), 1641 (stretching of C=N), 1593 (stretching of C=C), 1215 (C-N) and 1167 (C-O). ^{1}H NMR (DMSO-d_6, δ in ppm) (**Fig. 3**): 5.37 (s, 1H, CH), 7.25-7.27 (m, 2H, Ar-H), 7.44 (s, 1H, Ar-H), 7.99-8.00 (d, 2H, Ar-H, J= 3.2 Hz), 8.06-8.08 (d, 2H, Ar-H, J= 5.2 Hz), 11.01 (s, 1H, OH amide), 11.32 (m, 4H, broad, hydroxy pyrimidine).

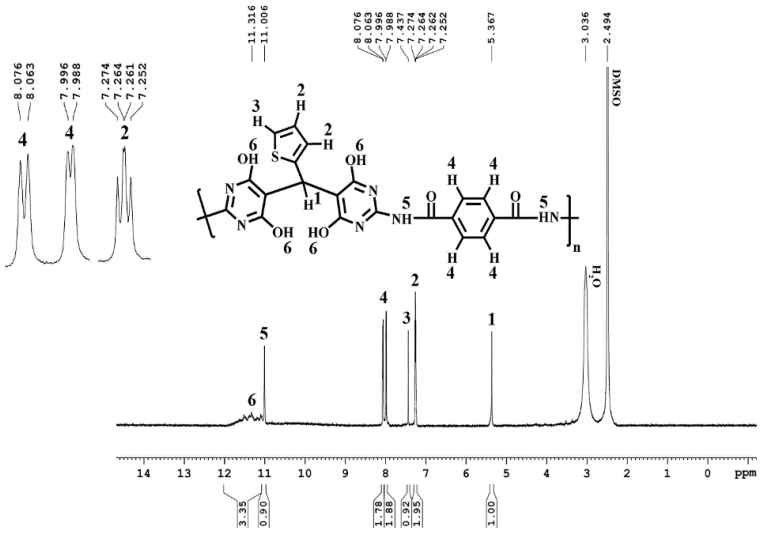

Fig. 3. ^{1}H NMR of the polymer.

2.5. Synthesis of M-P(PTA) nanocomposite

The M-P(PTA) nanocomposite was synthesized by the hydrothermal method as follows: 1.8 g of the P(PTA) was added to the solution of HCl and N,N-Dimethylformamide containing 0.2 M Ni^{2+}, 0.2 M Zn^{2+} and 2.6 M Fe^{3+}. In the following, NaOH solution was added into the mixed solution under nitrogen gas and the mixture pH value was set to 10.5. 0.3 g of CTAB and 4 mL glutaraldehyde were added to the mixture and then it was placed into an autoclave (Teflon-lined stainless steel) at 200 °C of an oven for 8 h. The temperature of the autoclave was naturally decreased to the temperature of the room, and the product was collected and rinsed with DW several times to reach neutral pH. Finally, the composite was dried at 50 °C.

2.5. Instruments

The crystalline structure of the prepared products was tested by XRD (GBC MMA instrument) at room temperature with CuKα characteristic radiation (λ = 0.154 nm). The XRD pattern was step-scanned in 2θ range of 10-70 at the rate of 5°/min. The morphology and particle size of the formulated products were studied using FE-SEM (TESCAN MIRA3, Czech Republic) while the voltage of acceleration was 15 kV. FT-IR (PerkinElmer, USA) in the rage of 4000-400 cm^{-1} was used for the determination of the functional groups of the products. To record ^{1}H NMR at 400 MHz and ^{13}C NMR at 100 MHz in DMSO-d_6 as a solvent, the Bruker Advance DRX tool (Germany) was used. The magnetic properties of the M-P(PTA) was investigated by a Vibrating Sample Magnetometer (VSM, Daghigh Kavir Corporation, Iran). For this purpose, a given amount of the M-P(PTA) was put in the magnetometer and balanced before quantifications. Magnetic field intensity (H) was increased in the range of −12000 Oe to +12000 Oe at 27 °C to determine the magnetic properties of the product that was defined in term of saturation magnetization. To record the thermal decomposition properties of the product, a thermogravimetric analyzer (TGA) (Mettler TGA/SDTA 851e/LF/1100 thermobalance) under air atmosphere at rate=10 °C/min was applied.

2.7. Adsorption experiments

The adsorption of Nd^{+3}, Tb^{+3}, and Dy^{+3} ions onto the M-P(PTA) was evaluated by batch experiments in the closed flasks containing 50 mL of the single solutions of the ions with the concentration of 50 mg/L. The experiments were performed at pH=5.5, and pH increase beyond 5.5 was not investigated to prevent the metals precipitation of the metals in OH form. The impact

of adsorbent dosage was evaluated from 0.05 to 0.19 g. To study the adsorption kinetic of the ions onto the adsorbent, the solutions containing 50 mg/L of the ions were contacted with 0.13 g of the adsorbent at different contact time (2.5 to 150 min). The isotherm tests were performed by the addition of 0.15 g of the adsorbent to the solutions with the primary concentrations in the scale of 50-300 mg/L. After adsorption process, the sorbent was magnetically separated from the solution, and the concentration of the ions was determined by an ICP-OES (Agilent 720, Agilent, USA).

The equilibrium amounts of adsorbed Nd^{+3}, Tb^{+3}, and Dy^{+3} (q_e, mg/g) were computed by the equation in the following:

$$q_e = \frac{(C_0 - C_e) \times V}{m} \quad (1)$$

Where C_0 and C_e (mg/L) respectively correspond to the primary concentration and concentration of the ions at equilibrium while V (L) and m (g) respectively refer to is the solution volume and the M-P(PTA) mass.

The adsorption efficiency of the ions was computed using the equation in the following:

$$\text{Adsorption efficiency (\%)} = \frac{C_0 - C_e}{C_0} \times 100 \quad (2)$$

3. Results and discussion

3.1. Products analyses

The M-P(PTA) FE-SEM image at different magnifications indicated in **Fig. 4** reveals that the shape of the synthesized particles is nearly spherical with homogenous distribution and diameter less than 100 nm, confirming the formation of the nanocomposite.

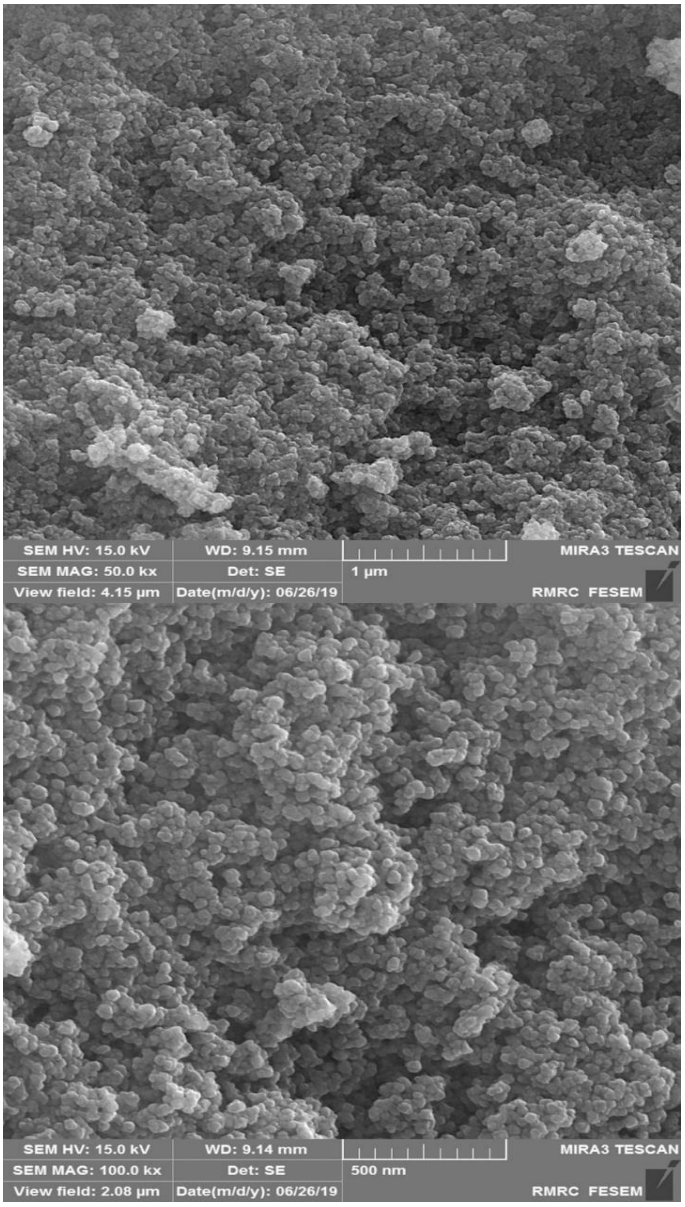

Fig. 4. FE-SEM images of the M-P(PTA).

Fig. 5 indicates the XRD pattern of the M-P(PTA). The peaks at 2θ = 18.19, 30.01, 35.36, 36.96, 42.98, 53.32, 56.82 and 63.73 are in accordance with the standard pattern of nickel zinc ferrite (JCPDF 08-0234) [20]. Full Width at Half Maximum (FWHM) of the strongest reflection of the XRD pattern was used to estimate the average size of crystal based on the Scherrer equation (Eq. (3)) [21]:

$$D = k\lambda/\beta \cos \theta \quad (3)$$

Where k shows the shape function (where k= 0.89), λ refer to the radiation X-ray wavelength, β refers to the Full Width at Half Maximum (FWHM) at 2θ=35.33 while θ shows the diffraction angle. Based on the Scherrer equation, the value of D was computed to be about 31.62 nm.

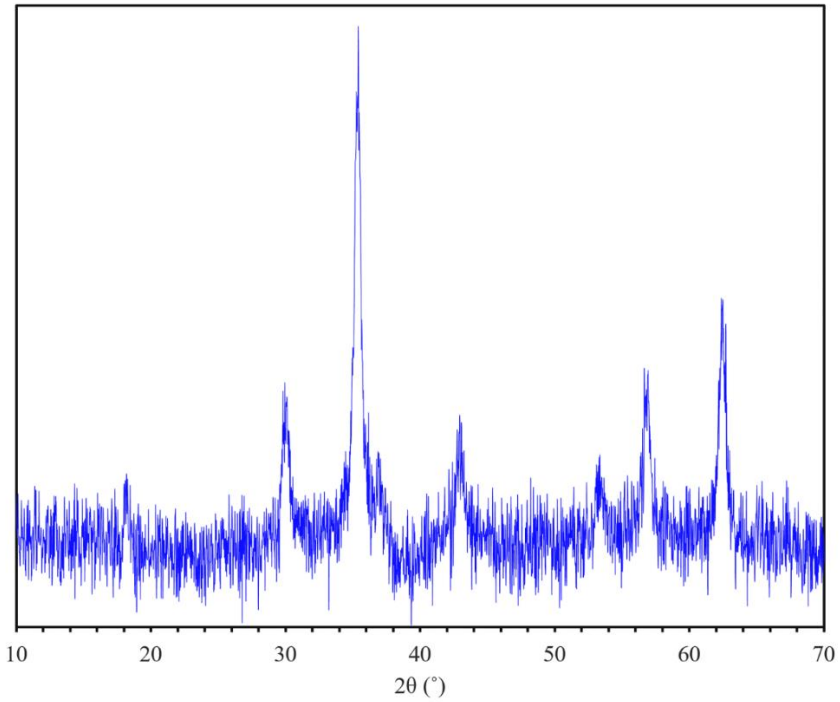

Fig. 5. XRD pattern of the M-P(PTA).

Fig. 6 indicates the FT-IR spectrum for the P(PTA) and M-P(PTA). The peaks in the FT-IR spectrum of the P(PTA) in **Fig. 6A** are as follows: 3164-3337 (stretching of O-H and NH_2), 3054 (stretching of C-H aromatic), 2958 (stretching of C-H aliphatic), 1683 (stretching of C=O amide), 1641 (stretching of C=N), 1593 (stretching of C=C), 1215 (C-N) and 1167 (C-O). **Fig. 6B** shows a band at 576 cm^{-1} which is corresponded to inherent metal stretching vibrations at the tetrahedral site (Fe-O), while the band at about 481 cm^{-1} is related to the stretching of octahedral metal (M-O) [22]. The comparison of the spectrum of P(PTA) spectrum with the M-P(PTA) spectrum expresses the successful preparation of the M-P(PTA).

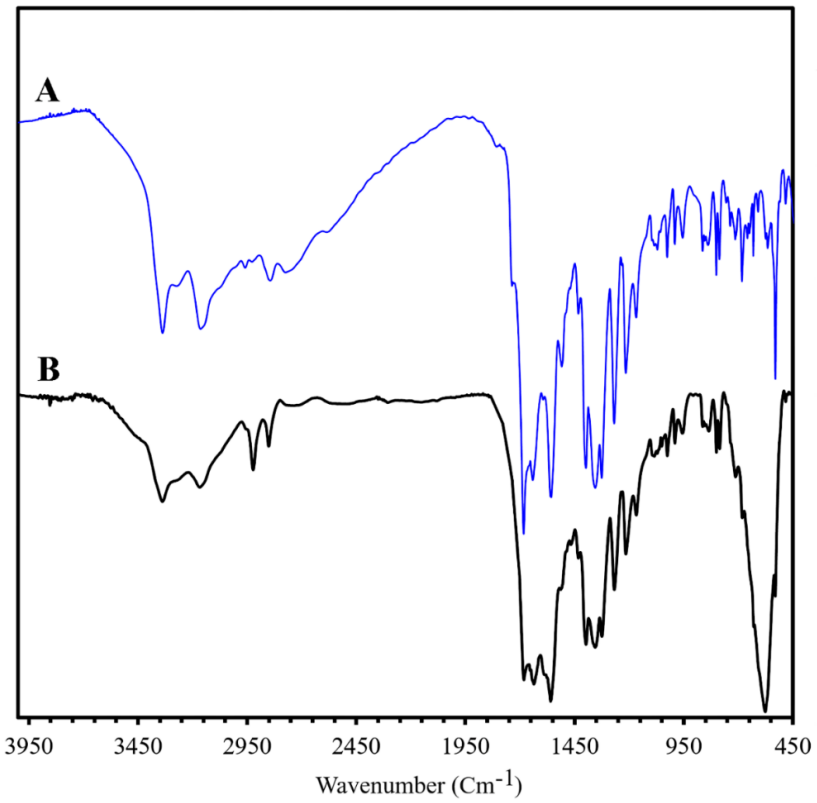

Fig. 6. FT-IR spectra of (A) P(PTA) and (B) M-P(PTA).

EDX was recorded to analyze the elements of the product and the result is presented in **Fig. 7**. It shows N, C, O, Ni, Zn, Fe and S peaks that confirm the formation of the M-P(PTA).

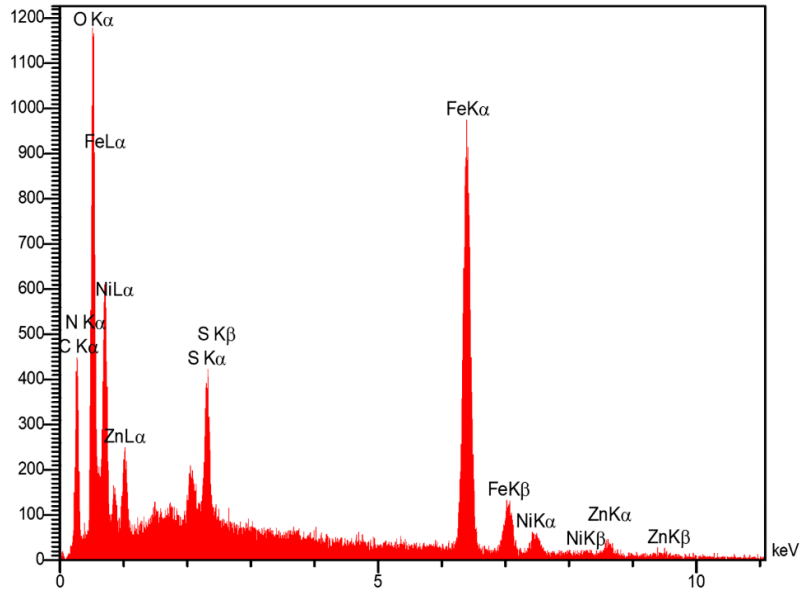

Fig. 7. EDX spectrum of the M-P(PTA).

The thermo-stability of the P(PTA) and M-P(PTA) recorded by TGA under the atmosphere of N_2 at rate=10 ˚C/min is presented in **Fig. 8**. As it is illustrated in **Fig. 8A**, there are three different weight-loss steps in the TGA curve of the P(PTA). Obviously, the first step (around 100 ˚C) with a weight loss of 1.17 % can be attributed to water evaporation. The second step between 100 and 290 ˚C with the amount of 9.6 % that could be due to the preliminary degradation of aliphatic groups of P(PTA). At the third step ranging between 300 and 330 ˚C, the aromatic groups of the P(PTA) are degrading gradually and the forth step with the weight loss of 44.16 % corresponded to their further decomposition. The final step could be related to the complete degradation of the polymer residue and its conversion to CO_2 and H_2O. **Fig. 8B** shows the TGA curve of the M-P(PTA). The thermal stability of the nanocomposite has enhanced compared to pure P(PTA). It is obvious that the temperature of decomposition is moved to higher temperatures due to the inorganic material existence in the matrix of the polymer, indicating that the thermal stability of the composite increases with $Ni_{0.2}Zn_{0.2}Fe_{2.6}O_4$ loading.

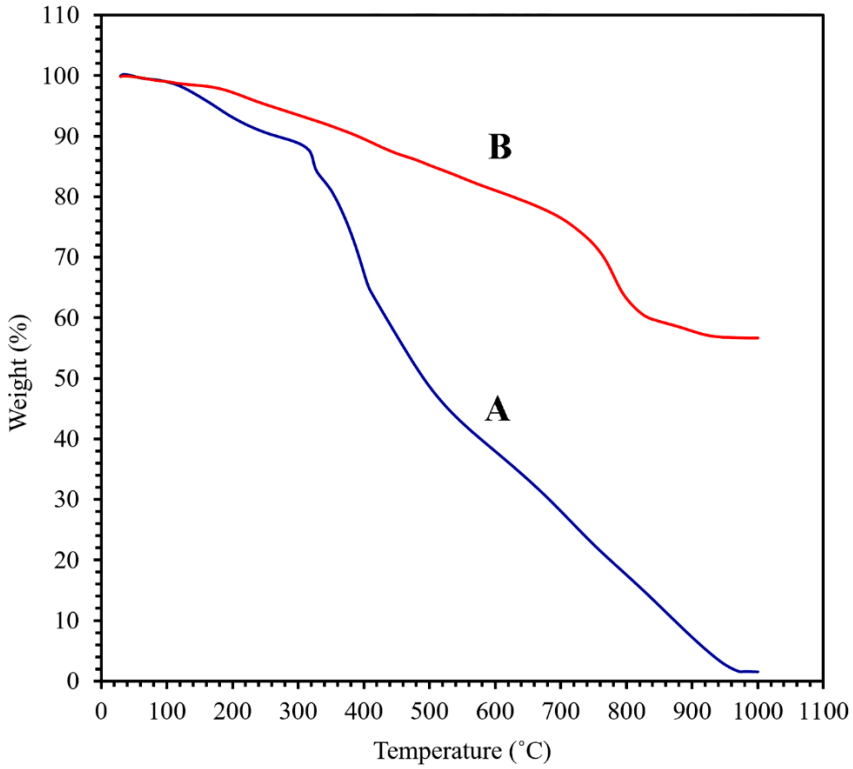

Fig. 8. TGA curves of (A) P(PTA) and (B) M-P(PTA).

According to the magnetic hysteresis loops in **Fig. 9**, the magnetic saturation for the M-P(PTA) is about 50.49 emu/g that indicates the superparamagnetic behavior of the synthesized

products. This high magnetization value shows that the metals-loaded M-P(PTA) can be simply taken apart from aqueous solution via performing an external magnetic field.

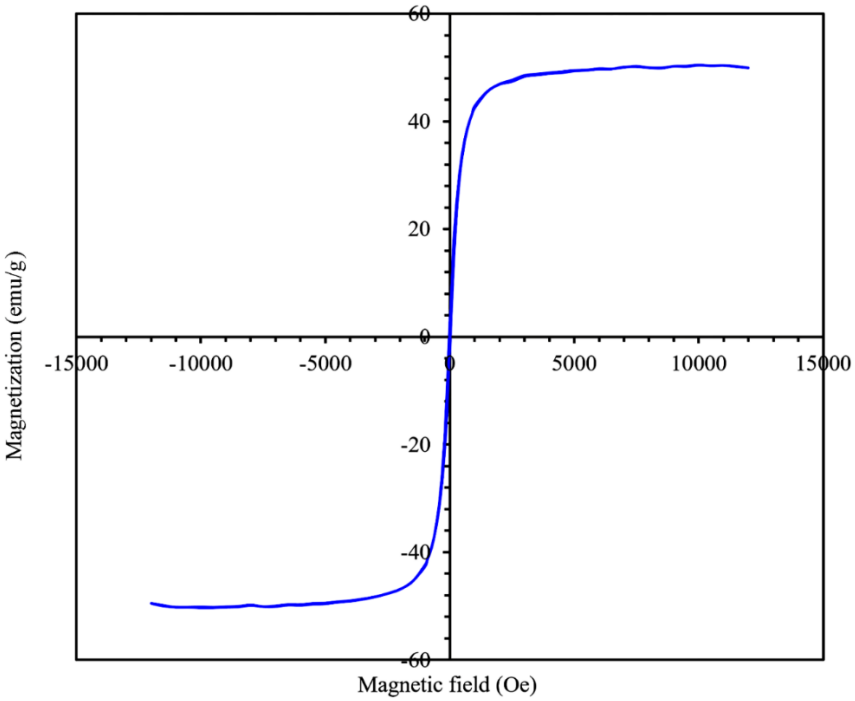

Fig. 9. Magnetization curve of M-P(PTA).

3.2. Contact time effect and batch adsorption kinetic studies

The dependency of Nd^{+3}, Tb^{+3}, and Dy^{+3} ions adsorption efficiency to contact time is presented in **Fig. 10** that expresses increasing contact time leads to an increase in adsorption efficiency until reaching the maximum value. The adsorption efficiency for Nd^{+3}, Tb^{+3}, and Dy^{+3} is 75.15, 77.15 and 78.49 %, respectively, within 60 min, and the maximum value of adsorption efficiency for each metal is achieved in 130 min, and more increase in contact time has no more significant changes in adsorption efficiency.

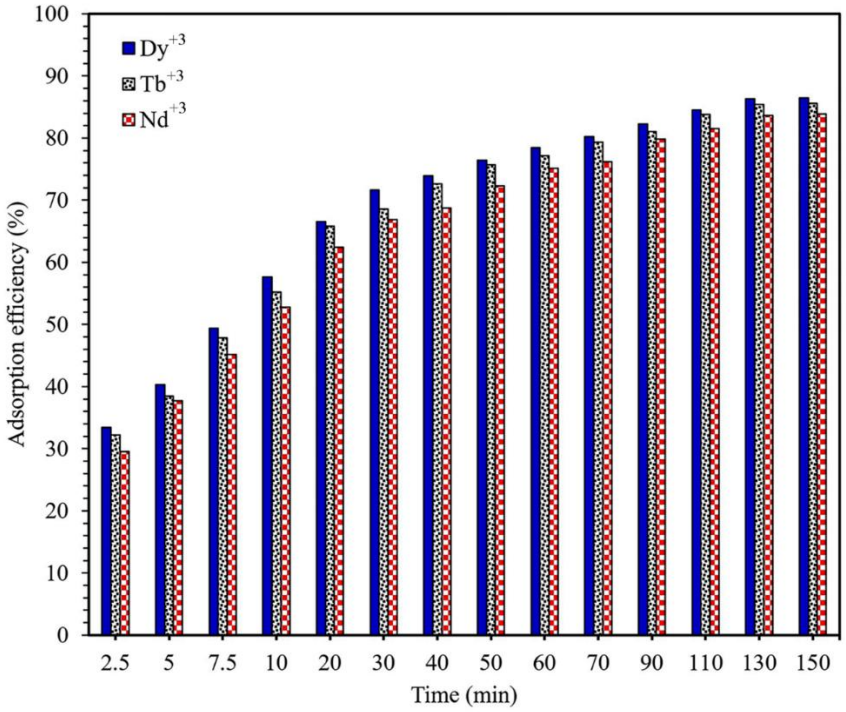

Fig. 10. Effects of contact time on the adsorption of the ions.

The non-linear pseudo-first-order (PFO), PSO, and intra-particle diffusion (IPD) models were employed to model Nd^{+3}, Tb^{+3}, and Dy^{+3} adsorption kinetic data. The equations are as follows [23]:

$q_t = q_e\,(1 - \exp^{-K1t})$ Pseudo-first-order (4)

$q_t = K_2 q_e^2 t/1 + K_2 q_e t$ Pseudo-second-order (5)

$q_t = K_i t^{0.5} + C$ Intra-particle diffusion (6)

Where K1 is the constant of PFO rate (h^{-1}), K_2 (g/mgh) is the constant of PSO rate and K_i also shows the rate constant of IPD. Moreover, C provides information about the thickness of the boundary layer while a greater C value is related to the diffusion effect of the boundary layer.

The initial adsorption rate (h) can be obtained using K_2 and q_e values based on the equation in the following:

$h = K_2 q_e^2$ (7)

The validity of each model was compared by chi-square (χ^2) according to Eqs. (7) [24], since the coefficient of determination (R^2) may not be reasonable to select the best adsorption model in view of the fact that it only presents the fit between equations linear forms and empirical data while the correlation among empirical and anticipated adsorption capacity values is defined by χ^2. The lower values of χ^2 indicate a better fit.

$$\chi^2 = \sum_{i=1}^{n} \frac{(q_{e,exp} - q_{e,cal})^2}{q_{e,cal}} \quad (8)$$

Where n shows the data point numbers while $q_{e,exp}$ and $q_{e,cal}$ respectively refer to the empirical and computed adsorbent capacities.

Table 1. Kinetic constants for adsorption of the ions by the M-P(PTA).

		Nd^{+3}	Tb^{+3}	Dy^{+3}
Pseudo-first-order	K (min^{-1})	0.121	0.1273	0.1349
	q_e ($mg.g^{-1}$)	14.69	15.13	15.31
	R^2	0.8954	0.9011	0.9023
	χ^2	1.30	1.24	1.18
Pseudo-second-order	k_2 ($g.mg^{-1}.min^{-1}$)	0.0100	0.0105	0.0112
	q_e ($mg.g^{-1}$)	16.15	16.55	16.68
	h ($mg.g^{-1}.min^{-1}$)	2.61	2.87	3.12
	R^2	0.9771	0.9787	0.9800
	χ^2	0.28	0.26	0.24
Intra-particle diffusion	K_{id} (min^{-1})	4.55	4.53	4.44
	R^2	0.9496	0.9376	0.9307
	χ^2	0.63	0.78	0.84

The values of kinetic parameters are presented in **Table 1.** As it is obvious, the highest values of R^2 and the lowest values of χ^2 obtained by PSO show that the main mechanism for controlling the adsorption of Nd^{+3}, Tb^{+3}, and Dy^{+3} onto the M-P(PTA) is chemisorption. The plots of IPD model showed that the adsorption of the metal is a multi-stage process. The stages were related to the strong electrostatic forces of attractions among the functional groups of the adsorbent and the ions, and gradual adsorption by the diffusion of the ions into the adsorbent pores until the occupation of most or all of the active sites. In addition, IPD model was not the sole rate-limiting step, as the related plots do not pass through the origin. Thus, intra-particle diffusion along with other mechanisms controls the rate of adsorption [25,26].

3.3. Adsorbent dosage effect

To define the capacity of adsorbent for a specified metal ion initial concentration, the adsorbent dosage is considered as an essential parameter in the adsorption process. As can be seen in **Fig. 11**, by enhancing the adsorbent dosage in the scale of 0.05 to 0.19 g, the adsorption efficiency for Nd^{+3}, Tb^{+3}, and Dy^{+3} increases up to 95.67, 97.48 and 98.41 %, respectively. Increasing dosage higher than 0.15 g has no influence on the adsorption of the metals. It is expected that the number of active sites becomes greater by increasing adsorbent dosage, leading to an increase in

adsorption efficiency. Also, the active surface area of the adsorbent is enlarged by increasing adsorbent dosage [27]. Accordingly, a positive impact of higher adsorbent dosage on adsorption performance is confirmed.

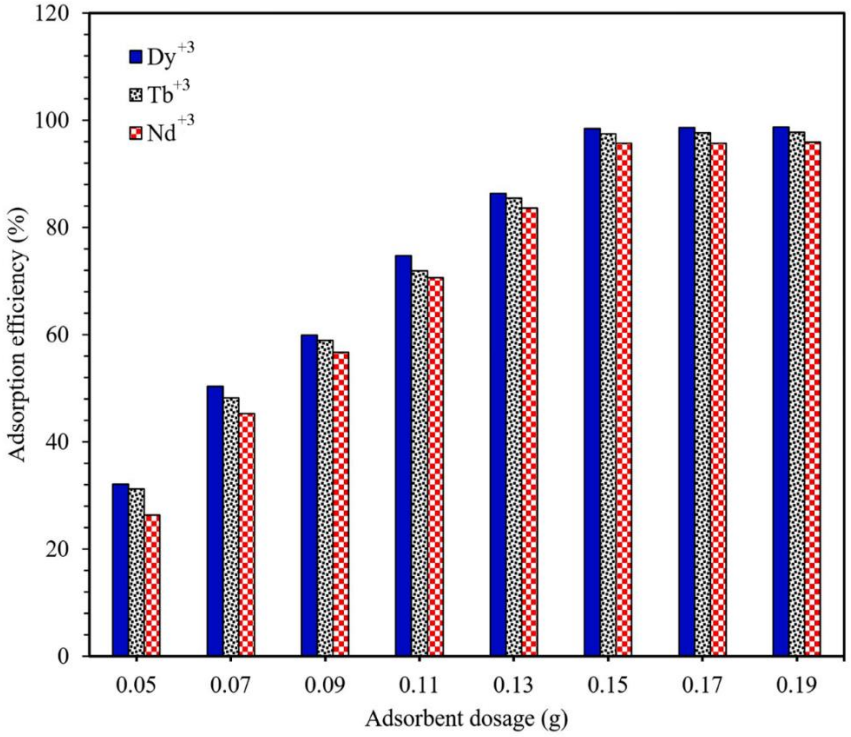

Fig. 11. Effects of adsorbent dosage on the adsorption of the ions.

3.4. Primary concentration effect and batch adsorption isotherm studies

As it is illustrated in **Fig. 12**, by increasing primary concentration from 50 to 300 mg/L, adsorption efficiency declines from 95.67 to 18.39 %, 97.48 to 25.19 %, and 98.41 to 26.43 % for Nd^{+3}, Tb^{+3}, and Dy^{+3}, respectively. The easy adsorption of the ions at low initial concentration is as a result of the high surface area and easy accessibility of the adsorption sites. The decrease in the adsorption efficiency of the ions could be related to the confinement of the total existing adsorption sites at higher initial concentrations [28].

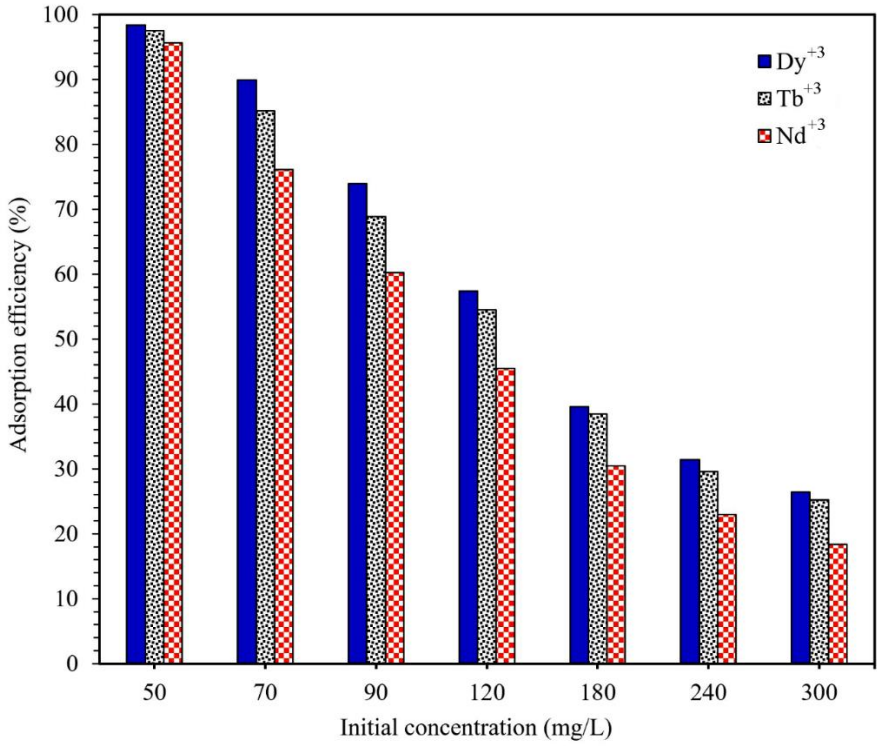

Fig. 12. Effect of initial concentration on the adsorption of the ions.

Langmuir and Freundlich models were used to fil the equilibrium data that are respectively related to the monolayer and multilayer adsorption. The nonlinear Langmuir and Freundlich models were utilized according to Eqs. (9) and (10), respectively [29].

$$q_e = \frac{b\ q_m\ C_e}{(1+bC_e)} \quad (9)$$

$$q_e = K\ C_e^{1/n} \quad (10)$$

Where q_e and q_m (mg/g) respectively show the adsorption at equilibrium and the maximum capacity of adsorption. C_e (mg/L) also refers to the equilibrium concentration of the adsorbate while b (L/mg) and K (L/mg) respectively show the constants of Langmuir and Freundlich adsorption. n also shows the factor of heterogeneity. The adsorption is favorable if $n > 1$.

The R_L as a dimensionless factor is defined to show the inherent attributes of the Langmuir model that is described in the following:

$$R_L = \frac{1}{1+bC_i} \quad (11)$$

Where C_i (mg/L) shows the greatest primary metal concentration.

Generally, R_L has four different values and four cases are defined based on them: the adsorption process is irreversible if $R_L = 0$; if $R_L = 1$, the adsorption process is linear; if $0 < R_L < 1$, the adsorption process is favorable; and if $R_L > 1$, the adsorption process is unfavorable [30]. The coefficient of determination (R^2) values and the related factors are presented in **Table 2**.

Table 2. Isotherm constants for adsorption of the ions by M-P(PTA).

		Nd^{+3}	Tb^{+3}	Dy^{+3}
Langmuir	b ($mg.L^{-1}$)	3.07	1.75	2.47
	q_m ($mg.g^{-1}$)	18.30	22.81	24.00
	R_L	0.0011	0.0019	0.0014
	R^2	0.9859	0.7335	0.7885
	χ^2	0.01	2.76	2.7
Freundlich	K ((mg/g)(l/mg)1/n)	16.04	16.07	17.30
	n	36.10	12.74	13.38
	R^2	0.8571	0.9813	0.9625
	χ^2	0.13	0.19	0.48

The values of R_L of Nd^{+3}, Tb^{+3}, and Dy^{+3} calculated by Eq. (11) are in the range of 0 to 1, which proposed that the metal ions adsorption processes by the M-P(PTA) are favorable. The n value is 36.10, 12.74, and 13.38 for Nd^{+3}, Tb^{+3}, and Dy^{+3}, respectively, showing a strong interaction between the M-P(PTA) and the metal ions. According to the values of R^2 and χ^2, it is obvious that the experimental data of Tb^{+3} and Dy^{+3} are fitted well with Freundlich, indicating multilayer adsorption, and the adsorption of the ions takes place on non-uniform surfaces. In the case of Nd^{+3}, Langmuir isotherm is able to model the adsorption data favorably. Consequently, the adsorption of the ion is monolayer adsorption. A comparison of the adsorption capacity of different adsorbents is represented in **Table 3**.

Table 3. Comparison of the adsorption capacity of Nd^{+3}, Tb^{+3}, and Dy^{+3} onto various adsorbents.

Adsorbent	q_m (mg/g)			Reference
	Nd^{+3}	Tb^{+3}	Dy^{+3}	
Fe_3O_4-C_{18}-chitosan-DETA	27.1		28.3	[31]
γ-Fe_2O_3-NH_4OH@SiO_2(APTMS)		46.5	23.2	[32]
GA-g-PAM/SiO_2	12.24			[33]
Zr@XG-ZA	14.01[a]			[34]
EDASiDGA	16.15			[35]
Carbon black derived from recycled tires	0.67			[36]
3D GO-CZ	9.68			[37]
Macroporous polymeric resin (TVEX-PHOR)		24.93		[38]
TA-MWCNTs		8.55		[39]
YZ		44.5		[40]
P(HEMA-Hap)-phy		49.27		[41]
Supported biomass on zeolite (SBZ)		5.07		[42]
CA@Fe_3O_4 NPs	41			[43]
MPS (22 nm)-2NH-2COOH			44.8	[44]
o-CNCs-IIPs			28.97	[45]
o-CNCs/o-MWCNTs-IIPs			38.7	[45]
o-CNCs/GO-IIPs			41.79	[45]
Imprinted mesoporous silica materials			22.33	[46]
M-P(PTA)	18.68	24.57[a]	25.89[a]	This study

[a] Calculated from Freundlich isotherm

3.5. Ionic strength effect

The metal ions adsorption can be influenced by co-ions presence in the solution. **Fig. 13** shows the results of the percentage of the ions adsorbed onto the P(PTA) in the presence of NaCl with the concentration ranging from 0.02 to 0.1 M. As indicated in **Fig. 13**, the adsorption efficiency of the ions is influenced by NaCl existence in the solution. A decrease is observed by increasing the concentration of NaCl, and adsorption efficiency decreases from 92.98 to 67.42 % for Nd^{+3}, 95.33 to 81.7 % for Tb^{+3}, and 97.47 to 87.41 % for Dy^{+3}. This behavior corresponds to the Na^+ ions that compete with the Nd^{+3}, Tb^{+3}, and Dy^{+3} in the adsorption process for the available active sorption sites of the M-P(PTA) [47]. In addition, an increase in Na^+ concentration in the solution may cause the inhibition of Nd^{+3}, Tb^{+3}, and Dy^{+3} approach to the active sites of the M-P(PTA).

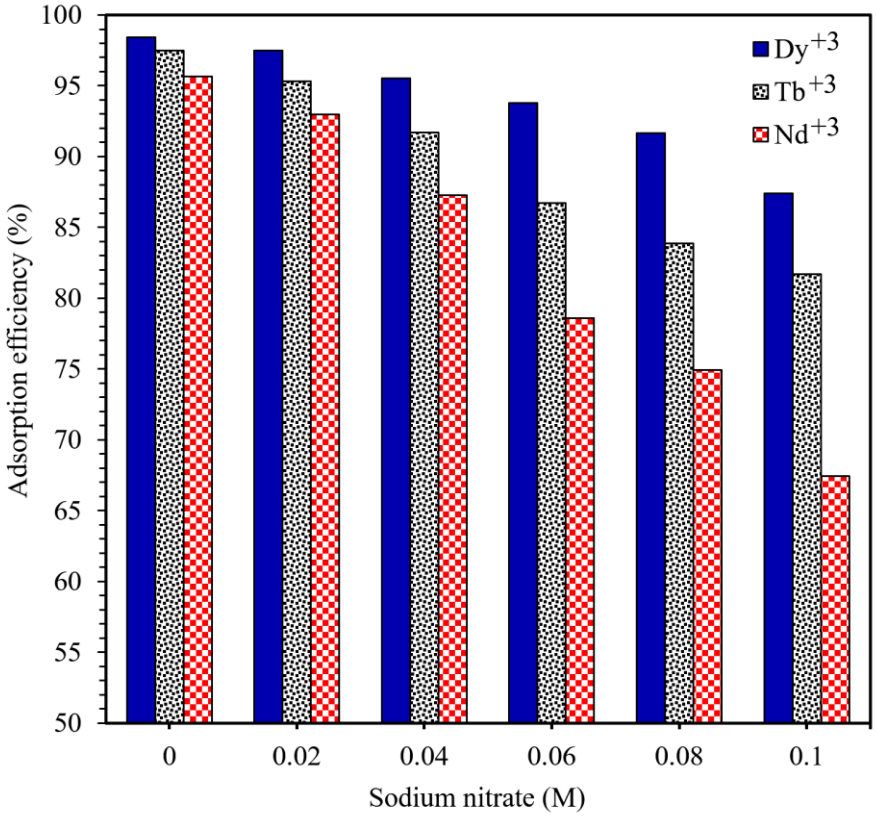

Fig. 13. Effect of ionic strength on the adsorption of the ions

3.6.Temperature effect on the adsorption and evaluation of thermodynamic parameters

The influences of solution temperature on the adsorption efficiency of the ions using the M-P(PTA) as an adsorbent has been investigated by changing temperature ranged from 25 to 45 ˚C, and the results were presented in **Table 4**. It is obvious that the ions adsorption efficiency increases with an increase in the temperature in a certain temperature range. This increase might be resulted from the effective collision between the ions molecules and the M-P(PTA) particles in a certain temperature range leading to the enhanced adsorption efficiency. To assess the feasibility of an adsorption process, thermodynamic parameters such as the standard free energy change (ΔG^0), standard enthalpy change (ΔH^0), and standard entropy change (ΔS^0) can be calculated using the following equations:

$$K_d = q_e/C_e \quad (12)$$

$$\text{Ln } K_d = \Delta S^\circ/R - \Delta H^\circ/RT \quad (13)$$

$$\Delta G^\circ = - RT \text{ Ln } K_d \quad (14)$$

Where K_d refers to the distribution coefficient, and C_e shows the equilibrium concentration of ion in the solution (mg/L). R demonstrates the gas constant (8.314 J/mol K), and T indicates the

temperature (K). The values of ΔH° and ΔS° in **Table 4** were computed based on the slope and intercept of the plot of Ln K_d versus 1/T, respectively (**Fig. 14**).

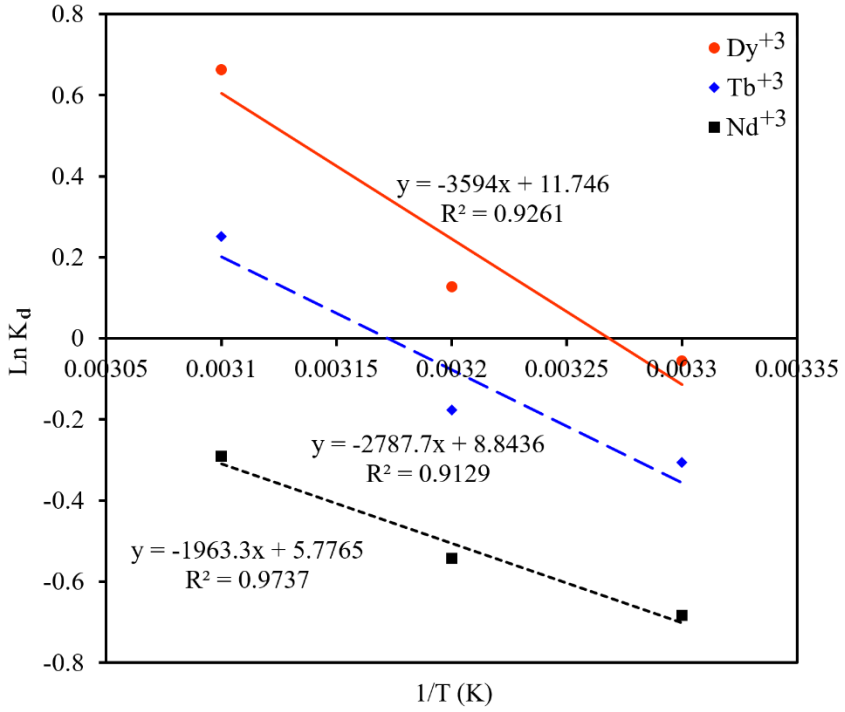

Fig. 14. Ln K_d versus 1/T for calculation of enthalpy and entropy changes.

The values of ΔG^0 are positive at all temperatures in the case of Nd^{+3} that suggest the non-spontaneous adsorption of Nd^{+3} onto the M-P(PTA), while the values obtained for Tb^{+3} and Dy^{+3} show the spontaneity of the adsorption process at higher temperatures. The positive values of ΔH^0 indicate that the adsorption process of the ions is endothermic. The positive values for ΔS^0 confirm the increased randomness at the solid/solution interface during the adsorption of the ions onto the surface of the M-P(PTA).

Table 4. Effect of temperature on the adsorption of Nd (III), Tb (III), and Dy (III) at 90 mg/L and thermodynamic parameters.

Temperature (°C)	Adsorption efficiency (%)		
	Nd^{+3}	Tb^{+3}	Dy^{+3}
25	60.22	68.83	73.94
35	63.53	71.54	77.32
45	69.16	79.41	85.34

Thermodynamic parameters				
		Nd^{+3}	Tb^{+3}	Dy^{+3}
ΔH° (kJ/mol)		16.32	23.18	29.88
ΔS° (kJ/mol K)		0.048	0.074	0.098
	Temperature (°C)			
ΔG° (kJ/mol)	25	1.694	0.759	0.137
	35	1.391	0.452	-0.328
	45	0.770	-0.664	-1.753

3.7. Reusability studies

For studying the reusability of the adsorbent, 0.15 g of the M-P(PTA) treated with 50 mg/L of Nd^{+3}, Tb^{+3}, and Dy^{+3} in a 50 mL single solution at pH = 5.5, agitation rate of 180 rpm and contact time of 130 min were used. The ions-loaded M-P(PTA) were magnetically separated and rinsed with deionized water for removing any ions that were not absorbed. Then, the M-P(PTA) was treated with 50 mL of 0.2 M HNO_3 for 2.5 h. The ions final concentration was evaluated using an ICP-OES. The reusability of the M-P(PTA) was tested by the same adsorbent in four adsorption-desorption cycles. As can be seen in **Fig. 15**, lower adsorption efficiency is obtained by increasing cycles for all ions. After four cycles, the adsorption efficiency for Nd^{+3}, Tb^{+3}, and Dy^{+3} by the M-P(PTA) is 84.64, 86.37, and 88.75 %, respectively. The decrease in adsorption efficiency could be owing to the strong chemical bonds among the ions and the functional groups that cause incomplete desorption of the ions. The obtained results imply that the regeneration and recycling of the M-P(PTA) could be successfully performed after repeatedly applying for Nd^{+3}, Tb^{+3}, and Dy^{+3} adsorption process.

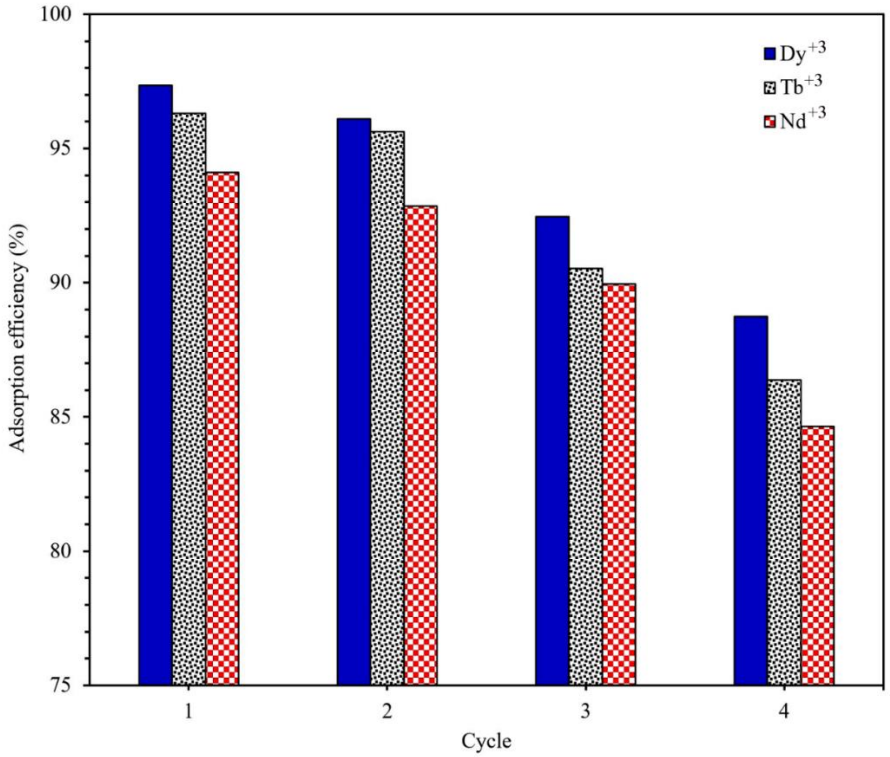

Fig. 15. Reusability of the M-P(PTA) for adsorption of the ions.

3.8. Competitive adsorption

To evaluate competitive adsorption of Nd^{+3}, Tb^{+3}, and Dy^{+3} in the ternary system of 50 mg/L (1:1:1), 0.15 g of the M-P(PTA) (the same as a single system) was used. According to the value of q_{mix}/q_0, three kinds of influences such as antagonism, synergism, and non-interaction can occur in a multi-component system as following:

- Antagonism ($q_{mix}/q_0 < 1$): the influence of the component mixture in solution is lower than its influence in a single mode.
- Synergism ($q_{mix}/q_0 > 1$): the influence of the component mixture in solution is higher than its influence in a single mode.
- Non-interaction ($q_{mix}/q_0 = 1$): the impact of the component mixture in solution is neither less nor more compared with its influence in a single mode.

  Where q_{mix} and q_0 are the adsorption capacities of each ion in the mixture and single systems, respectively.

The value of q_{mix}/q_0 for each ion was calculated to be 0.15, 0.33, and 0.35 for Nd^{+3}, Tb^{+3}, and Dy^{+3}, respectively. The obtained results indicate that the q_{mix}/q_0 value for each ion is less than 1 in a ternary mixture; therefore, the existence of each ion shows antagonism influence on

the adsorption of other ions in the process. The adsorption efficiency for Nd^{+3}, Tb^{+3}, and Dy^{+3} ions decreased to 14.32, 32.46, and 34.64 %, respectively. EDX spectrum was also recorded after the adsorption process and the result is shown in **Fig. 16**. The existence of Nd^{+3}, Tb^{+3}, and Dy^{+3} in the spectrum strongly confirms the successful adsorption of these ions by the M-P(PTA).

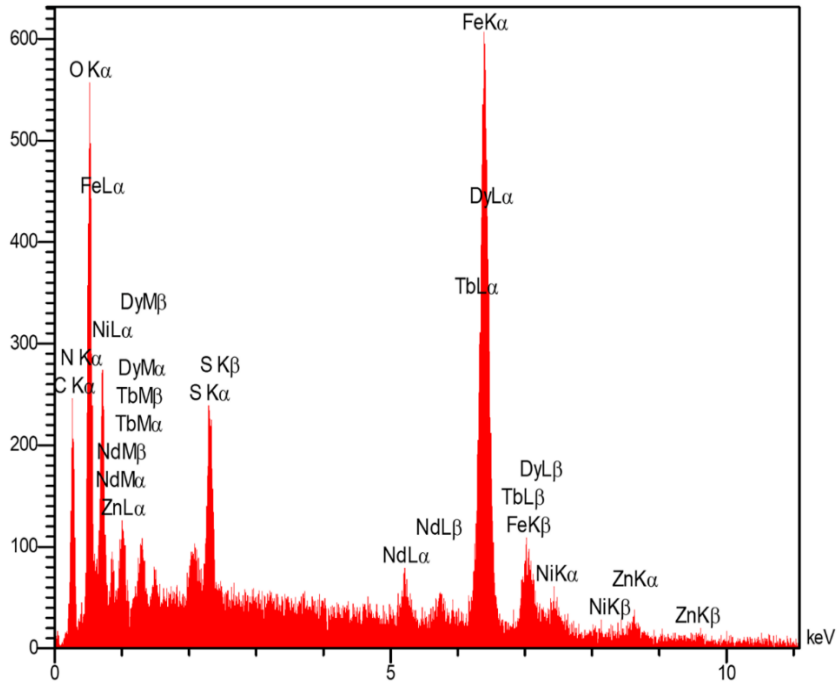

Fig. 16. EDX spectrum of M-P(PTA) after adsorption of the ions.

4. Conclusion

The goal of this research was to create the magnetic nanocomposite of the novel M-P(PTA). The production of the samples was confirmed by FE-SEM, NMR, FT-IR, XRD, and VSM techniques. It was tested for the simultaneous adsorption of Nd^{+3}, Tb^{+3}, and Dy^{+3}. The results showed that at pH = 5.5, the value of adsorption efficiency within 130 min for Nd^{+3}, Tb^{+3}, and Dy^{+3} was 95.67, 97.48, and 98.41 %, respectively. The competitive adsorption indicated antagonism influence of each ion on the adsorption of other ions in the process. PSO model was found to be appropriate for modeling the adsorption kinetic data. Freundlich model respectively fitted the adsorption equilibrium data of Tb^{+3} and Dy^{+3} with R^2 of 0.9813 and 0.9625 while Nd^{+3} data was modeled well with Langmuir model with R^2 of 0.9859. Using the adsorbent in four adsorption-desorption cycles led to a decrease in adsorption efficiencies of Nd^{+3}, Tb^{+3}, and Dy^{+3}.

Consequently, it can be used as a potential recyclable adsorbent for the purpose of rare earth elements adsorption, especially Nd^{+3}, Tb^{+3}, and Dy^{+3}.

Acknowledgments

This work has been supported by the Spanish Ministry of Economy and Competitiveness (Ref. CTM2017-83581-R). Hamedreza Javadian acknowledges the financial support received (Ref. BES-2015-072506).

References

[1] G. Yuqian, Z. Shimin, Z. Kaiya, W. Zhiwei, X. Shuxia, L. Zhenpu, W. Kun, Adsorption of La^{3+} and Ce^{3+} by poly-γ-glutamic acid crosslinked with polyvinyl alcohol, J. Rare Earth, 33 (2015) 884-891.

[2] K. Binnemans, P. Tom Jones, Rare earths and the balance problem, J. Sustain. Metall. 1 (2015) 29–38.

[3] K. Binnemans, P. Tom Jones, B. Blanpain, T. Van Gerven, Y. Yang, A. Walton, M. Buchert, Recycling of rare earths: a critical review, J. Clean. Prod. 51 (2013) 1-22.

[4] D. Ouyang, Y. Zhuo, L. Hu, Q. Zeng, Y. Hu, Z. He, Research on the adsorption behavior of heavy metal ions by porous material prepared with silicate tailings, Minerals, 9(5) (2019) 291.

[5] J. Xu, R. Koivula, W. Zhang, E. Wiikinkoski, S. Hietala, Risto Harjula, Separation of cobalt, neodymium and dysprosium using amorphous zirconium phosphate, Hydrometallurgy 175 (2018) 170–178.

[6] A.N. Turanov, V.K. Karandashev, V.M. Masalov, A.A. Zhokhov, G.A. Emelchenko, Adsorption of lanthanides(III), uranium(VI) and thorium(IV) from nitric acid solutions by carbon inverse opals modified with tetraphenylmethylenediphospine dioxide, J. Colloid Interface Sci. 405 (2013) 183-188.

[7] J. Florek, F. Chalifour, F. Bilodeau, D. Lariviere, F. Kleitz, Nanostructured hybrid materials for the selective recovery and enrichment of rare earth elements, Adv. Funct. Mater. 24 (2014) 2668-2676.

[8] X. Zhao, M. Wong, C. Mao, T.X. Trieu, J. Zhang, P. Feng, X. Bu, Size-selective crystallization of homochiral camphorate metaleorganic frameworks for lanthanide separation, J. Am. Chem. Soc. 136 (2014) 12572-12575.

[9] M.P. Moloney, J. Causse, C. Loubat, A. Grandjean, Sodium “activation” of silano-phosphonate modified mesoporous TiO_2 leading to improved rare-earth element extraction, Eur. J. Inorg. Chem. 2014 (2014) 2268-2277.
[10] M.-R. Huang, H.-J. Lu, X.-G. Li, Synthesis and strong heavy-metal ion sorption of copolymer microparticles from phenylenediamine and its sulfonate, J. Mater. Chem. 22 (2012) 17685-17699.
[11] F. Wang, J. Zhao, F. Pan, H. Zhou, X. Yang, W. Li, H. Liu, Adsorption properties toward trivalent rare earths by alginate beads doping with silica, Industrial Eng. Chem. Res. 52 (2013) 3453-3461.
[12] J.A. Reglero Ruiz, M. Trigo-López, F.C. García, J.M. García, Functional aromatic polyamides, Polymers, 9(9) (2017) 414.
[13] K. Marchildon, Polyamides – Still strong after seventy years, Macromol. React. Eng. 5 (2011) 22-54.
[14] S.M. Amininasab, A. Rashidi, M. Taghavi, Z. Shami, Preparation and characterization of novel thermostable polyamides bearing different photoactive pendent architectures with antibacterial properties, Chin. J. Polym. Sci. 34 (2016) 766–776.
[15] J. Lu, F. Yan, J. Texter, Advanced applications of ionic liquids in polymer science. Prog. Polym. Sci. 34 (2009) 431–448.
[16] M. Ghaemy, M. Hassanzadeh, S.M. Amini Nasab, M. Taghavi, Ionic liquids in the synthesis of high-performance fluorinated polyamides with backbones containing derivatives of imidazole and carbazole rings, Polym. J. 45 (2013) 622–630.
[17] J.-S. Wang, R.-T. Peng, J.-H. Yang, Y.-C. Liu, X.-J. Hu, Preparation of ethylenediamine-modified magnetic chitosan complex for adsorption of uranyl ions, Carbohydr. Polym. 84 (2011) 1169–1175.
[18] Y. Hua, J. Xiao, Q. Zhang, C. Cui, C. Wang, Facile synthesis of surface-functionalized magnetic nanocomposites for effectively selective adsorption of cationic dyes, Nanoscale Res Lett. 13 (2018) 99.
[19] Y.S. Vygodskii, E.I. Lozinskaya, A.S. Shaplov, K.A. Lyssenko, M.Y. Antipin, Y.G. Urman, Implementation of ionic liquids as activating media for polycondensation processes, Polymer 45 (2004) 5031–5045.

[20] D. Ni, Z. Lin, P. Xiaoling, W. Xinqing, G. Hongliang, Preparation and Characterization of Nickel-Zinc Ferrites by a Solvothermal Method, Rare Metal Mat. Eng. 44(9) (2015) 2126-2131.

[21] A. Bahadur, A. Saeed, M. Shoaib, S. Iqbal, M. Imran Bashir, M. Waqas, M. Nasir Hussain, N. Abbas, Eco-friendly synthesis of magnetite (Fe_3O_4) nanoparticles with tunable size: Dielectric, magnetic, thermal and optical studies, Mater. Chem. Phys. 198 (2017) 229-235.

[22] A.S.A. Bakr, Y.M. Moustafa, E.A. Motawea, M.M. Yehia, M.M.H. Khalil, Removal of ferrous ions from their aqueous solutions onto $NiFe_2O_4$–alginate composite beads, J. Environ. Chem. Eng. 3 (2015) 1486–1496.

[23] P. Nanta, K. Kasemwong, W. Skolpap, Isotherm and kinetic modeling on superparamagnetic nanoparticles adsorption of polysaccharide, J. Environ. Chem. Eng. 6 (2018) 794-802.

[24] F. Ciesielczyk, P. Bartczak, T. Jesionowski, Removal of cadmium(II) and lead(II) ions from model aqueous solutions using sol–gel-derived inorganic oxide adsorbent, Adsorption 22 (2016) 445–458.

[25] A.C. Martins, O. Pezoti, A.L. Cazetta, K.C. Bedin, D.A.S. Yamazaki, G.F.G. Bandoch, T. Asefa, J.V. Visentainer, V.C. Almeida, Removal of tetracycline by NaOH-activated carbon produced from macadamia nut shells: kinetic and equilibrium studies, Chem. Eng. J. 260 (2015) 291–299.

[26] S. Ben-Ali, I. Jaouali, S. Souissi-Najar, A. Ouederni, Characterization and adsorption capacity of raw pomegranate peel biosorbent for copper removal, J. Clean. Prod. 142 (2017) 3809–3821.

[27] Z. Liu, Z. Zhang, F. Hu, X. Duan, X. Ye, Adsorption performance and micro-structural morphology of a novel magnetic composite adsorbent for removing Cd^{2+} from water, Microchem. J. 146 (2019) 1209-1217.

[28] O.-H. Kwon, J.-O. Kim, D.-W. Cho, R. Kumar, S. Han Baek, M.B. Kurade, B.-H. Jeon, Adsorption of As(III), As(V) and Cu(II) on zirconium oxide immobilized alginate beads in aqueous phase, Chemosphere 160 (2016) 126-133

[29] N. Boukhalfa, M. Boutahala, N. Djebri, A. Idris, Kinetics, thermodynamics, equilibrium isotherms, and reusability studies of cationic dye adsorption by magnetic alginate/oxidized multiwalled carbon nanotubes composites Int. J. Biol. Macromol. 123 (2019) 539-548.

[30] A. Mohammadinezhad, G. Bagheri Marandi, M. Farsadrooh, H. Javadian, Synthesis of poly(acrylamide-co-itaconic acid)/MWCNTs superabsorbent hydrogel nanocomposite by ultrasound-assisted technique: Swelling behavior and Pb (II) adsorption capacity Ultrason. Sonochem. 49 (2018) 1-12.

[31] E. Liu, X. Zheng, X. Xu, F. Zhang, E. Liu, Y. Wang, C. Li, Y. Yan, Preparation of diethylenetriamine-modified magnetic chitosan nanoparticles for adsorption of rare-earth metal ions, New J. Chem. 41 (2017) 7739-7750.

[32] T. Kegl, I. Ban, A. Lobnik, A. Košak, Synthesis and characterization of novel γ-Fe_2O_3-NH_4OH@SiO_2(APTMS) nanoparticles for dysprosium adsorption, J. Hazard. Mater. 378 (2019) 120764.

[33] S. Iftekhar, V. Srivastava, A. Casas, M. Sillanpää, Synthesis of novel GA-g-PAM/SiO_2 nanocomposite for the recovery of rare earth elements (REE) ions from aqueous solution. J Clean Prod. 170 (2018) 251-259.

[34] S. Iftekhar, V. Srivastava, S. Ben Hammouda, M. Sillanpää, Fabrication of novel metal ion imprinted xanthan gum-layered double hydroxide nanocomposite for adsorption of rare earth elements, Carbohydr Polym. 194 (2018) 274–284.

[35] T. Ogata, H. Narita, M. Tanaka, Rapid and selective recovery of heavy rare earths by using an adsorbent with diglycol amic acid group, Hydrometallurgy. 155 (2015) 105-109.

[36] Y.R. Smith, D. Bhattacharyya, T. Willhard, M. Misra, Adsorption of aqueous rare earth elements using carbon black derived from recycled tires, Chem Eng J 296 (2016) 102–111.

[37] X. Xu, X-Y. Jiang, F-P. Jiao, X-Q. Chen, J-G. Yu, Tunable assembly of porous three-dimensional graphene oxide-corn zein composites with strong mechanical properties for adsorption of rare earth elements, J Taiwan Inst Chem Eng 85 (2018) 106-114.

[38] H.A. Madbouly, N.E. El-Hefny, Y.A. El-Nadi, Adsorption and separation of terbium(III) and gadolinium(III) from aqueous nitrate medium using solid extractant, Sep Sci Technol. (2019) 1-13.

[39] S. Tong, S. Zhao, W. Zhou, R. Li, Q. Jia, Modification of multi-walled carbon nanotubes with tannic acid for the adsorption of La, Tb and Lu ions, Microchim Acta 174 (2011) 257–264.

[40] D. Baybaş, U. Ulusoy, Polyacrylamide–clinoptilolite/Y-zeolite composites: Characterization and adsorptive features for terbium, J Hazard Mater 187(1) (2011) 241–249.

[41] R. Akkaya, Terbium adsorption onto polyhydroxyethylmethacrylate–hydroxyapatite composite and its modified composition by phytic acid, Desalin Water Treat 52 (2014) 1440-1447.

[42] Ó. Barros, L. Costa, F. Costa , A. Lago, V. Rocha, Z. Vipotnik, B. Silva, T. Tavares, Recovery of rare earth elements from wastewater towards a circular economy, Molecules 24 (2019) 1005.

[43] R.M. Ashour, R. El-Sayed, A.F. Abdel-Magied, A.A. Abdel-Khalek, M.M. Ali, K. Forsberg, A. Uheida, M. Muhammed, J. Dutta, Selective separation of rare earth ions from aqueous solution using functionalized magnetite nanoparticles: kinetic and thermodynamic studies, Chem. Eng. J. 327 (2017) 286–296.

[44] T. Kaneko, F. Nagata, S. Kugimiya, K. Kato, Optimization of carboxyl-functionalized mesoporous silica for the selective adsorption of dysprosium, J. Environ. Chem. Eng. 6 (2018) 5990-5998.

[45] X. Zheng, Y. Zhang, T. Bian, Y. Zhang, Z. Li, J. Pan, Oxidized carbon materials cooperative construct ionic imprinted cellulose nanocrystals films for efficient adsorption of Dy(III), Chem Eng J 381 (2020) 122669.

[46] X. Zheng, E. Liu, F. Zhang, Y. Yan, J. Pan, Efficient adsorption and separation of dysprosium from NdFeB magnets in an acidic system by ion imprinted mesoporous silica sealed in a dialysis bag, Green Chem. 18 (2016) 5031–5040.

[47] I. Ghodbane, L. Nouri, Q. Hamdaoui, M. Chiha, Kinetic and equilibrium study for the sorption of cadmium (II) ions from aqueous phase by eucalyptus bark. J Hazard Mater 152 (2007) 148–158.